# The Response of Submerged Structures to Underwater Blast

**Andreas Schiffer**

Exeter College
University of Oxford

Department of Engineering Science
Parks Road, OX1 3PJ, Oxford, U.K.

Submitted for the degree of
D.Phil in Engineering Science

Hilary term 2013

**The Response of Submerged Structures to Underwater Blast**

Andreas Schiffer, Exeter College, University of Oxford
For the degree of D.Phil. in Engineering Science, Trinity Term 2013

The response of submerged structures subject to loading by underwater blast waves is governed by complex interactions between the moving or deforming structure and the surrounding fluid and these phenomena need to be thoroughly understood in order to design structural components against underwater blast.

This thesis has addressed the response of simple structural systems to blast loading in shallow or deep water environment. Analytical models have been developed to examine the one-dimensional response of both water-backed and air-backed submerged rigid plates, supported by linear springs and loaded by underwater shock waves. Cavitation phenomena as well as the effect of initial static fluid pressure are explicitly included in the models and their predictions were found in excellent agreement with detailed FE simulations.

Then, a novel experimental apparatus has been developed, to reproduce controlled blast loading in initially pressurised liquids. It consists of a transparent water shock tube and allows observing the structural response as well as the propagation of cavitation fronts initiated by fluid-structure interaction in a blast event. This experimental technique was then employed to explore the one-dimensional response of monolithic plates, sandwich panels and double-walled structures subject to loading by underwater shock waves. The performed experiments provide great visual insight into the cavitation process and the experimental measurements were found to be in good agreement with analytical predictions and dynamic FE results.

Finally, underwater blast loading of circular elastic plates has been investigated by theroretically modelling the main phenomena of dynamic plate deformation and fluid-structure interaction. In addition, underwater shock experiments have been performed on circular composite plates and the obtained measurements were found in good correlation with the corresponding analytical predictions. The validated analytical models were then used to determine the optimal designs of circular elastic plates which maximise the resistance to underwater blast.

# Acknowledgements

It would never have been possible to write this doctoral thesis without the help and support of the kind people around me, to only some of whom it is possible to give acknowledgment here.
First and foremost, I would like to express my deepest gratitude to my principal supervisor, Dr. Vito Tagarielli, for his constant support, motivation, patience and guidance. His extensive knowledge and wisdom, as well as his joy and passion for science have been the inspiration on my path to the completion of this research work and have encouraged me to become a passionate researcher who loves science and the scientific approach of solving problems.
I am also extremely grateful to my second supervisor, Dr. Nik Petrinic, for his personal support and advice, as well as for providing a stimulating and welcoming academic and social environment. Without his tireless commitment I would never have got the great opportunity to do research in such an exciting field of engineering.
I also thank Prof. Alan Cocks for good advice and stimulating conversations which have been invaluable on academic and personal level.
Furthermore, I would like to acknowledge the Engineering and Physical Sciences Research Council (EPSRC) and the Defence Science and Technology Laboratory (DStl) for their financial support that made this research project possible.
I would never forget the constant help and assistance of my labmates at the Impact Engineering Laboratory, Antonio Pellegrino, Ettore Barbieri, Petros Siegkas, Simone Falco, Robert Gerlach, Kov Murugaratnam, Ben Cousins and Phillip Anderson, not to mention all the fun we had together during the last years. In addition, I am grateful to Jens Wiegand for his co-operation and his technical advice on the use of laboratory equipment. I would like to thank Stuart Carter and all the technicians from the group‘s workshop who helped machining the bits and pieces that were so vital for my experimental work.
I am thankful to my fellow graduate students at Exeter College for providing me with plenty happyness and making my mind relax during the hard times of my thesis.
Last but not least, I would like to thank my parents and my two brothers for personal support and encouragement throughout my life.

# Published work

The work presented in this thesis was extracted from research articles published (or prepared) by the author prior to completion of this DPhil course and a full list of these publications is provided below.

**Publications in peer-reviewed journals:**

1. Schiffer A., Tagarielli V.L., Petrinic N. and Cocks A.C.F., 2012. *The Response of Submerged Rigid Plates to Blast Loading: Analytical Models and Finite Element Predictions.* Journal of Applied Mechanics, 79: 061014 (14 pages).
   (corresponding to Chapter 3)
2. Schiffer A. and Tagarielli V.L., 2012. *The response of rigid plates to blast in deep water: fluid-structure interaction experiments.* Proceedings of the Royal Society A, 468: 2807-2828.
   (corresponding to Chapter 4)
3. Schiffer A. and Tagarielli V.L., 2013. *One-dimensional Response of Sandwich Plates to Underwater Blast: Fluid-Structure Interaction Experiments and Simulations.* submitted to Journal of the Mechanics and Physics of Solids, May 2013.
   (corresponding to Chapter 5)
4. Schiffer A. and Tagarielli V.L., 2013. *The One-dimensional Response of a Water-Filled Hull to Underwater Blast: Experiments and Simulations.* submitted to International Journal of Impact Engineering, May 2013.
   (corresponding to Chapter 6)
5. Schiffer A. and Tagarielli V.L., 2013. *Analytical models for the dynamic response of elastic composite plates subject to underwater blast.* submitted to Journal of the Mechanics and Physics of Solids, June 2013.
   (corresponding to Chapter 7)
6. Schiffer A. and Tagarielli V.L., 2013. *The Response of Circular Composite Plates to Underwater Blast: Experiments and Modelling.* submitted to International Journal of Solids and Structures, July 2013.
   (corresponding to Chapter 8)

**Publications in conference proceedings:**

7. Schiffer A., Tagarielli V.L., Cocks A.C.F. and Petrinic N., 2012. *The Response of Composite Plates to Underwater Blast.* Proceedings of the ASME International Mechanical Engineering Congress & Exposition, Houston, Texas, USA, November 2012. (corresponding to Chapters 7 and 8)
8. Schiffer A. and Tagarielli V.L., 2012. *One-dimensional Response of Submerged Plates to Underwater Blast*. European Solid Mechanics Conference, Graz, Austria, July 2012. (corresponding to Chapters 3, 4 and 5)
9. Schiffer A. and Tagarielli V.L., 2013. *The One-dimensional Response of Sandwich Plates Subject Blast in Deep and Shallow Water*. International Mechanical Engineering Congress & Exposition, San Diego, California, USA, November 2013. (corresponding to Chapter 5).

# Contents

**Abstract** i

**Acknowledgements** ii

**Published work** iii

**Table of Contents** v

**List of Figures** x

**List of Tables** xxi

**Notation** xxii

**Chapter 1 Introduction** 1

1.1 Motivation and Background ..... 1

1.2 Innovations in the design of naval ships and submarines ..... 2

1.3 Design of structures subject to underwater blast ..... 4

1.4 Objectives of the thesis ..... 7

**Chapter 2 Literature Review** 10

2.1 Review of existing literature ..... 10

2.1.1 Underwater explosions ..... 10

2.1.2 FSI: physical background and predictive modelling ..... 14

2.1.3 Underwater blast experiments ..... 21

2.2 Outline of the thesis ..... 25

**Chapter 3 The Response of Rigid Plates to Deep Water Blast: Analytical Models and Finite Element Predictions 27**

3.1 Introduction ..... 27

3.2 Analytical models ..... 28

3.2.1 Summary of the Taylor model for a free-standing monolithic plate ..... 29

3.2.2 Stage I response for a spring-supported rigid plate ..... 31

3.2.3 Stage II response: effects of cavitation ..... 34

3.3 Finite Element Calculations ..... 47

3.4 Comparison of analytical and FE predictions ..... 50

3.4.1 Problem 1: closing front and breaking front propagation ..... 51

3.4.2 Problem 1: pressure and velocity histories ..... 53

3.4.3 Problem 2: closing front and breaking front propagation ..... 56

3.4.4 Problem 2: pressure and velocity histories ..... 57

3.5 Sensitivity of the response to $\kappa$, $\psi$ and $\overline{p}_{st}$ ..... 59

3.6 Conclusions ..... 64

**Chapter 4 The Response of Rigid Plates to Blast in Deep Water: Fluid-structure interaction Experiments 67**

4.1 Introduction ..... 67

4.2 Problem definition ..... 68

4.3 Experimental apparatus ..... 69

4.3.1 Transparent shock tube and instrumentation ..... 69

4.3.2 Generation of the shock wave ..... 74

4.3.3 Propagation of shock waves in the compliant tube ..... 78

4.4 Results and discussion ..... 79

4.4.1 Response of fluid ..... 79

4.4.2 Response of the specimen ..... 90

4.4.3 Sensitivity of impulse to mass and initial static pressure ..... 92

4.5 Conclusions ..... 94

**Chapter 5 The One-dimensional Response of Sandwich Plates to Blast in Deep and Shallow Water 97**

5.1 Introduction ..... 97

5.2 Specimen design and manufacture ..... 98

5.3 Experimental technique ..... 101

5.4 Finite element models ..... 103

5.5 Results ..... 107

5.5.1 Fluid response ..... 107

5.5.2 Structural response ..... 116

5.6 Discussion ..... 121

5.6.1 Comparison of $I_{f,max}$ and $\varepsilon_c$ between air-backed and water-backed sandwich plates ..... 122

5.6.2 Effect of initial hydrostatic fluid pressure on $I_{f,max}$ and $\varepsilon_c$ ..... 126

5.6.3 Effect of normalised core strength $\bar{\sigma}_c$ on applied impulse $\bar{I}_{f,\max}$ and core crush $\varepsilon_c$ ..... 127

5.7 Conclusions ..... 132

**Chapter 6 The One-dimensional Response of Double-walled Structures Subject to Underwater Blast 134**

6.1 Introduction ..... 134

6.2 Problem definition ..... 135

6.3 Fluid-structure interaction experiments ..... 136

6.3.1 Laboratory setup ..... 136

6.3.2 Specimen design and manufacture ..... 138

6.3.3 Outline of the experimental study ..... 140

6.4 Finite element models ..... 142

6.5 Results and discussion ..... 144

6.5.1 Fluid response ..... 145

6.5.2 Structural response ..... 150

6.5.3 Sensitivity of applied impulse and core crush to the gap width ..... 156

6.6 Conclusions ..... 161

**Chapter 7 Analytical Models for the Response of Elastic Circular Plates to Underwater Blast 164**

7.1 Introduction ..... 164

7.2 Analytical models ..... 165

7.2.1 Pressure pulse loading ..... 166

a) Phase 1: wave propagation phase ( $0 \le t \le t_1$ ). ..... 167

b) Phase 2: retardation phase ( $t > t_1$ ). ..... 175

7.2.2 Underwater blast loading ..... 176

7.3 Finite element models ..... 183

7.3.1 Material models ..... 184

7.3.2 Details on the FE models ..... 185

7.4 Comparison and discussion of results ..... 187

7.4.1 Impulsive loading ..... 187

7.4.2 Underwater blast loading ..... 194

7.5 Conclusions ..... 205

**Chapter 8 The Response of Circular Composite Plates to Underwater Blast: Experiments and Predictive Model Validation 207**

8.1 Introduction ..... 207

8.2 Underwater shock experiments ..... 208

8.2.1 Description of composite specimens ..... 208

8.2.2 Experimental technique ..... 210

8.3 Finite element models ..... 212

8.4 Results and Discussion ..... 212

8.4.1 The cavitation process ..... 214

8.4.2 Dynamic plate deflection ..... 218

8.5 Conclusions ..... 224

**Chapter 9 Conclusions 226**

9.1 The one-dimensional response of rigid plates subject to blast in deep and shallow water ..... 227

9.2 The one-dimensional response of sandwich plates subject to blast in deep and shallow water ..... 229

9.3 The one-dimensional response of double-walled structures to underwater blast ..... 230

9.4 The response of circular elastic plates to underwater blast ..... 231

Appendix A Description of structural loading subsequent to first cavitation (Phase 2 response) ..... 234

Appendix B Review of lamina theory ..... 237

# List of Figures

Fig. 1.1: (a) Extensive hull damage of the USS Cole after detonation of an explosive charge mid-ship; (b) photograph taken from the USS Tripoli during repair after the ship struck a sea mine. ..... 2

Fig. 1.2: Current applications of composite materials in naval ships and submarines [2]. The abbreviations C, TD and D denote 'concept', 'technology demonstrator' and 'developed (in-service)'. ..... 3

Fig. 2.1: Pressure versus time history measured at a distance 18 m from a 136 kg TNT charge fired 15 m below the surface; reproduced from Cole [5]. ..... 12

Fig. 2.2: Characteristics of primary and secondary pressure pulses at a stand-off distance of 10 m from a 1000 kg TNT charge deotonated at a water depth of 1000 m; the characteric time periods and pressure values were calculated using the formulas given in Slifko [6]. ..... 14

Fig. 2.3: High-speed photographic sequence of a monolithic beam impacted by a foam projectile [10]. ..... 16

Fig. 2.4: Schematic of the water shock tube developed by Deshpande et al. [36]. ..... 23

Fig. 2.5: Schematic of the test method developed by Wadley et al. [44] to investigate the blast performance of sandwich panels. ..... 24

Fig. 3.1: Sketches of problem geometry, reference system, boundary conditions and loading case, for Problem 1 (a) and Problem 2 (b). ..... 31

Fig. 3.2: (a) Schematic illustration of the phenomena of initial cavitation, emergence and propagation of BFs, development of a CF. (b) Detail of the fluid conditions at a propagating CF. ..... 36

Fig. 3.3: Non-dimensional regime charts for Problem 1. The curves show the transitions between different regimes for two different values of non-dimensional static pressure: (a) $\overline{p}_{st} = 0$ and (b) $\overline{p}_{st} = 0.6$ ..... 44

Fig. 3.4: Non-dimensional regime charts for Problem 2. The curves show the transitions between different regimes for two different values of non-dimensional static pressure: (a) $\overline{p}_{st} = 0$ and (b) $\overline{p}_{st} = 0.07$ ..... 47

Fig. 3.5: Schematic of the Abaqus/Explicit FE model used to investigate the 1D water-backed plate response (Problem 2). FE simulations for Problem 1 follow a similar scheme, with the fluid column attached to the plate's back face absent. ..... 49

Fig. 3.6: Normalised rise time $\overline{t}_r^{FE} = t_r^{FE} / \theta$ (a) and peak pressure $\overline{p}_0^{FE} = p_0^{FE} / p_0$ (b) of the incident shock wave as functions of the mesh size used in the FE calculations. ..... 50

Fig. 3.7: Non-dimensional time versus position charts illustrating, for Problem 1, emergence of cavitation in the fluid attached to the plate's front face and subsequent propagation of breaking fronts and closing fronts: (a) effect of non-dimensional stiffness and (b) effect of the initial static pressure. ..... 52

Fig. 3.8: Analytical and FE predictions of non-dimensional front face pressure and plate velocity time histories for Problem 1: (a) *regime* 1, (b) *regime* 2 and (c) *regime* 3..... 55

Fig. 3.9: Non-dimensional time versus position charts illustrating, for Problem 2, emergence of cavitation in the fluid attached to the plate's front face and subsequent propagation of breaking fronts and closing fronts: (a) effect of non-dimensional stiffness and (b) effect of the initially applied pressure..... 56

Fig. 3.10: Analytical and FE predictions of the non-dimensional front face pressure, back face pressure and plate velocity histories for Problem 2: (a) *regime* 1, (b) *regime* 2, (c) *regime* 3 and (d) *regime* 4..... 58

Fig. 3.11: (a) Problem 1: Partial and total non-dimensional impulse imparted to the front face as a function of non-dimensional stiffness $\kappa$ for selected values of $\overline{p}_{st}$ . (b) Problem 1: Partial and total non-dimensional impulse imparted to the front face as a function of the non-dimensional parameter $\psi$ for selected values of $\overline{p}_{st}$ . ..... 63

Fig. 3.12: (a) Problem 2: Partial and total non-dimensional impulse imparted to the front face as a function of non-dimensional stiffness $\kappa$ for selected values of $\overline{p}_{st}$ . (b) Problem 2: Total non-dimensional impulse applied to the front face as a function of the non-dimensional parameter $\psi$ for selected values of $\overline{p}_{st}$. $\overline{I}_t = \overline{I}_p$ in this case..... 63

Fig. 4.1: Free body diagram of rigid plates for the two problems under investigation: (a) air-backed plate and (b) water-backed plate. Plates are loaded by exponentially decaying pressure waves in initially pressurised water. ..... 69

Fig. 4.2: Sketch of the apparatus employed in this study to explore the response of (a) air-backed unsupported rigid plates and (b) water-backed unsupported rigid plates..... 71

Fig. 4.3: Photographs of the laboratory setup for the case of an experiment in water-backed configuration. ..... 73

Fig. 4.4: Impact of the striker on a piston in contact with pressurised water (a); sketch of the compound steel-foam striker employed in this study (b). ..... 77

Fig. 4.5: Comparison between theoretical predictions and experimental measurements of the incident pressure versus time histories in water at (a) atmospheric pressure and (b) higher initial static pressure. ..... 78

Fig. 4.6: High-speed photographs for experiment 1 ( $p_{st} = 0.1\,\text{MPa}$ , $\psi = 1.13$ , $p_0 = 14.9\,\text{MPa}$ ): (a) shock wave reaches the specimen; (b) onset of cavitation and propagation of a breaking front (BF); (c) further propagation of the BF and increase of strain in the liquid; (d)

emergence of a closing front (CF) at the fluid-structure interface; (e) complete collapse of the cavitation zone. ..... 82

Fig. 4.7: High-speed photographs for experiment 2 ( $p_{st} = 2.7\,\text{MPa}$ , $\psi = 1.13$ , $p_0 = 11.9\,\text{MPa}$ ): (a) shock wave reaches the specimen; (b) onset of cavitation and propagation of two breaking fronts (BF); (c) propagation of one of the BFs and emergence of a closing front (CF); (d) further propagation of the CF; (e) complete collapse of the cavitation zone. ..... 83

Fig. 4.8: (a) Measurements and analytical predictions of closing front and breaking front trajectories in a time versus distance chart for experiments 1 ( $p_{st} = 0.1\,\text{MPa}$ ), experiment 2 ( $p_{st} = 2.7\,\text{MPa}$ ) and experiment 3 ( $p_{st} = 0.9\,\text{MPa}$ ), all of which conducted in air-backed configuration with $\psi = 1.13$ . (b) Similar information for experiment 4 ( $p_{st} = 0.1\,\text{MPa}$ ) and experiment 5 ( $p_{st} = 1.1\,\text{MPa}$ ) both of which performed in water-backed configuration with $\psi = 0.91$ ..... 84

Fig. 4.9: High-speed photographs for experiment 4 ( $p_{st} = 0.1\,\text{MPa}$ , $\psi = 0.91$ , $p_0 = 15.1\,\text{MPa}$ ): (a) shock wave reaches the specimen; (b) onset of cavitation and propagation of two breaking fronts (BF); (c) propagation of one of the BFs and emergence of a closing front (CF); (d) further propagation of the CF and cavitation at the specimen‘s back face; (e) complete collapse of the cavitation zone. ..... 86

Fig. 4.10: High-speed photographs for experiment 5 ( $p_{st} = 1.1\,\text{MPa}$ , $\psi = 0.91$ , $p_0 = 13.1\,\text{MPa}$ ): (a) shock wave reaches the specimen; (b) onset of cavitation and propagation of two breaking fronts (BF); (c) emergence of a closing front (CF); (d) further propagation of the CF; (e) complete collapse of the cavitation zone. ..... 87

Fig. 4.11: Volumetric strain field in the water adjacent to the air-backed specimen in experiment 7 ( $\psi = 1.94$ , $p_{st} = 0.1\,\text{MPa}$ , $p_0 = 14.7\,\text{MPa}$ ) measured at three specific instants

corresponding to the high-speed photographs; the continuous lines represent analytical predictions obtained with the models presented in Chapter 3. ..... 89

Fig. 4.12: (a) Time histories of the non-dimensional impulse $\bar{I}_f = I_f / (2 p_0 \theta)$ for experiment 1 ( $p_{st} = 0.1\text{MPa}$ ) and experiment 2 ( $p_{st} = 2.7\,\text{MPa}$ ) conducted in air-backed configuration with $\psi = 1.13$ ; analytical predictions are included. (b) Similar information for experiment 4 ( $p_{st} = 0.1\text{MPa}$ ) and experiment 5 ( $p_{st} = 1.1\text{MPa}$ ) conducted in water-backed specimen configuration with $\psi = 0.91$ ; analytical predictions are compared to measurements. ..... 91

Fig. 4.13: (a) Maximum non-dimensional impulse $\bar{I}_{f,\max}$ as a function of $\psi$ for experiments performed with both air-backed and water-backed plates at $p_{st} = 0.1\text{MPa}$ ; analytical predictions are included for comparison. (b) $\bar{I}_{f,\max}$ as a function of the non-dimensional static pressure $\bar{p}_{st}$ , for experiments performed on both air-backed and water-backed plates; two different choices of $\psi$ are considered and measurements are compared with analytical predictions. ..... 94

Fig. 5.1: Measurements of the nominal compressive stress versus strain response obtained from quasi-static compression tests with (a) specimens 1 and 2 (Alporas) and (b) specimens 3-5 (Rohacell). ..... 100

Fig. 5.2: (a) Schematic of the laboratory setup used for performing underwater shock experiments on a water-backed sandwich specimen and (b) details of the specimen geometry. ..... 102

Fig. 5.3: (a) Schematic of the FE model used to simulate the 1D response of a water-backed sandwich plate subjected to loading by a shock wave at the front face sheet with initially unpressurised fluid-columns. The FE models for air-backed sandwich plates follow a similar scheme, with the fluid column attached to the plate's back face sheet absent. (b) Detail of the

mesh used for a simulation performed for a water-backed experiment with specimen 1 (Alporas foam core, see Table 5.1).....107
Fig. 5.4: (a) High-speed photographic sequence for experiment 1 (Alporas foam): (1) shock wave reaches the water-backed sandwich specimen; (2) onset of cavitation and propagation of two breaking fronts (BF); (3) emergence of a closing front (CF); (4) complete collapse of the cavitated region; (b) similar information for experiment 2 (Rohacell foam). .....110
Fig. 5.5: Measurements and FE predictions of closing front (CF) and breaking front (BF) trajectories plotted in a time versus distance chart for experiments 1 and 2, both conducted in water-backed configuration; analytical predictions for a rigid plate of mass equal to the total sandwich ($M = 24.5\,\mathrm{g}$, $p_0 = 11.4\,\mathrm{MPa}$, $p_{st} = 0.1\,\mathrm{MPa}$, $\theta = 0.145\,\mathrm{ms}$) are included for comparison.....112
Fig. 5.6: (a) High-speed photographic sequence for experiment 3 (Alporas foam): (1) shock wave reaches the air-backed sandwich specimen; (2) onset of cavitation and propagation of a breaking front (BF); (3) emergence of a closing front (CF); (4) further propagation of the closing front (CF); (b) similar information for experiment 4 (Rohacell foam).....113
Fig. 5.7: Measurements and FE predictions of closing front (CF) and breaking front (BF) trajectories plotted in a time versus distance chart for experiments 3 and 4, both performed in air-backed configuration; analytical predictions for a monolithic plate of mass equal to the total sandwich ($M = 24.4\,\mathrm{g}$, $p_{st} = 0.1\,\mathrm{MPa}$, $p_0 = 11.1\,\mathrm{MPa}$, $\theta = 0.145\,\mathrm{ms}$) are included for comparison.....115
Fig. 5.8: Measurements of the point of first cavitation (cavitation distance) plotted against the normalised core strength $\bar{\sigma}_c$ for experiments conducted with specimens 1-5 in both air-backed and water-backed configurations; analytical predictions (Liang et al. [29]) are included for comparison. .....116

Fig. 5.9: (a) Measured time histories of front and back face velocities for experiment 1 ( $p_{st} = 0.1\text{MPa}$ , $p_0 = 11.4\,\text{MPa}$ , $\theta = 0.145\,\text{ms}$ ) and experiment 5 ( $p_{st} = 1.05\,\text{MPa}$ , $p_0 = 8.8\,\text{MPa}$ , $\theta = 0.12\,\text{ms}$ ) both performed on specimen 1 (Alporas foam) in water-backed configuration; (b) displacement versus time histories for the same experiments; FE predictions for experiment 1are included in both figures. ..... 119

Fig. 5.10: (a) Measured time histories of front and back face velocities for experiment 2 ( $p_{st} = 0.1\text{MPa},\ p_0 = 11.4\,\text{MPa}$ , $\theta = 0.145\,\text{ms}$ ) and experiment 6 ( $p_{st} = 0.72\,\text{MPa}$ , $p_0 = 9.2\,\text{MPa}$ , $\theta = 0.12\,\text{ms}$ ) both conducted with specimen 4 (Rohacell foam) in water-backed configuration; (b) displacement versus time histories for the same experiments; FE predictions for experiment 2 are included in both figures. ..... 120

Fig. 5.11: (a) Measurements and FE predictions of front and back face velocities as functions of time for experiment 3 ( $p_{st} = 0.1\text{MPa}$ , $p_0 = 8.1\text{MPa}$ , $\theta = 0.11\,\text{ms}$ ) performed on *specimen 1* (Alporas foam) in air-backed configuration; (b) displacement versus time histories for the same experiment. ..... 121

Fig. 5.12: Sensitivity of core crush $\varepsilon_c$ to shock intensity $I_0 = 2p_0\theta$ measured for experiments performed on specimen 1 (Alporas foam) and specimen 2 (Rohacell foam), both of which tested in air-backed and water-backed configuration; FE predictions are included for comparison..... 124

Fig. 5.13: Experimental measurements and FE predictions of the non-dimensional impulse $\bar{I}_{f,\max}$ as functions of the parameter $\psi$ for experiments performed on *specimen 1* (Alporas foam) and *specimen 4* (Rohacell foam) in both air-backed and water-backed configuration; analytical predictions for monolithic plates of mass equal to the total sandwich (dotted curves) are included for comparison. ..... 125

Fig. 5.14: (a) Sensitivity of the non-dimensional impulse $\bar{I}_{f,\max}$ to the normalised static pressure $\bar{p}_{st}^{*} = p_{st} / p_0$ measured for experiments performed in water-backed configuration on specimen 1 (Alporas foam) and specimen 2 (Rohacell foam) with pressure waves of $p_0 = 8.8 - 9.2\,\text{MPa}$ and $\theta = 0.12\,\text{ms}$ ($\psi \approx 2.9$ in all experiments); FE predictions are included for comparison; (b) measurements and FE predictions of the core crush $\bar{\varepsilon}_c = \varepsilon_c / \varepsilon_D$ as functions of $\bar{p}_{st}^{*}$ for the same set of experiments. ..... 127

Fig. 5.15: Measurements and FE predictions of (a) the non-dimensional impulse $\bar{I}_{f,\max}$ and (b) core crush $\bar{\varepsilon}_c = \varepsilon_c / \varepsilon_D$ as functions of the normalised core strength $\bar{\sigma}_c = \sigma_c / p_0$ for Rohacell foam-cored sandwich plates (*specimens* 3, 4 and 5) in contact with water at atmospheric pressure ( $p_{st} = 0.1\text{MPa}$ ) and loaded by shock waves of decay time $\theta = 0.12\,\text{ms}$ . ..... 130

Fig. 5.16: Measurements and FE predictions of (a) the non-dimensional impulse $\bar{I}_{f,\max}$ and (b) core crush $\bar{\varepsilon}_c = \varepsilon_c / \varepsilon_D$ as functions of the normalised core strength $\bar{\sigma}_c = \sigma_c / p_0$ for Alporas foam-cored sandwich plates (*specimens* 1 and 2) in contact with water at atmospheric pressure ( $p_{st} = 0.1\text{MPa}$ ) on both sides and loaded by shock waves of decay time $\theta = 0.12\,\text{ms}$ . ..... 131

Fig. 6.1: Sketches of problem geometry and loading case of (a) monolithic double-hulls and (b) sandwich double-hulls. ..... 136

Fig. 6.2: (a) Schematic of the experimental apparatus used to perform underwater blast experiments on a structural system representative of a monolithic double-hull with motion of the inner hull constraint to zero. Experiments on free-standing inner hulls are performed with anvil and distance bush absent. (b) Specimen geometry of outer skin specimen in monolithic design and (c) in sandwich construction. ..... 138

Fig. 6.3: Schematic of the FE model used to simulate the 1D response of a sandwich double-hull. The FE models for monolithic double-hulls follow a similar scheme, but with the core and the back face sheet absent. ..... 144

Fig. 6.4: Sequence of high-speed photographs for experiment 3 showing the response of a monolithic double-hull with a stationary inner hull specimen consequent to underwater shock loading ( $p_0 = 11.6\,\text{MPa}$ , $\theta = 0.14\,\text{ms}$ , areal mass of the outer skin was $m_F = 43.0\,\text{kgm}^{-2}$ ). ..... 146

Fig. 6.5: Sequence of high-speed photographs for experiment 7 showing the response of a sandwich double-hull with a rigid, stationary inner hull specimen consequent to underwater shock loading ( $p_0 = 11.6\,\text{MPa}$ , $\theta = 0.14\,\text{ms}$ , areal mass of the outer skin was $m_F = 42.3\,\text{kgm}^{-2}$ ). ..... 147

Fig. 6.6: Sequence of high-speed photographs for experiment 12 showing the response of a monolithic double-hull with an unsupported inner hull specimen consequent to underwater shock loading ( $p_0 = 12.0\,\text{MPa}$ , $\theta = 0.14\,\text{ms}$ , $m_F = 43.0\,\text{kgm}^{-2}$ , $m_F / m_B = 0.5$ ) ..... 149

Fig. 6.7: Sequence of high-speed photographs for experiment 16 showing the response of a sandwich double-hull with an unsupported inner hull specimen consequent to underwater shock loading ( $p_0 = 11.5\,\text{MPa}$ , $\theta = 0.14\,\text{ms}$ , $m_F = 42.5\,\text{kgm}^{-2}$ , $m_F / m_B = 0.5$ ). ..... 150

Fig. 6.8: Test series 2, stationary inner hull ( $\psi_F = 3.4$ , $D = 120\,\text{mm}$ ): (a) Measurements and FE predictions of the non-dimensional impulse applied on the inner hull $\bar{I}_B(t)$ as functions of time; results obtained with both monolithic and sandwich double-hulls are included. (b) FE predictions of the non-dimensional impulse imparted to the outer skin $\bar{I}_F(t)$ for the same set of experiments. ..... 152

Fig. 6.9: Measurements and FE predictions of the compressive core strain $\varepsilon_c(t)$ as functions of time for for test series 2 ($\psi_F = 3.4$, $D = 120\,\text{mm}$); sandwich plates with different types of core are compared. ..... 153

Fig. 6.10: Measurements and FE predictions of the impulse imparted to outer skin and inner hull specimens, $\bar{I}_F(t)$ and $\bar{I}_B(t)$, respectively, as functions of time for experiments conducted with unsupported inner hull specimens ($D = 60\,\text{mm}$, $\psi_F = 3.4$, $\psi_B = 1.8$): (a) monolithic double-hull (experiment 12); (b) sandwich double-hull (experiment 16); $\psi_F = 3.4$, $\psi_B = 1.8$ and $D = 60\,\text{mm}$ in both experiments. ..... 156

Fig. 6.11: Test series 1, stationary inner hull ($\psi_F = 3.4$): (a) effect of the water gap width $D$ on the maximum non-dimensional impulse imparted to the outer skin and inner hull, $\bar{I}_{\text{F,max}}$ and $\bar{I}_{\text{B,max}}$, respectively; measurements are indicated by full circles and the solid and dashed curves represent FE predictions. (b) Measurements and FE predictions of the core crush $\varepsilon_c^{pl}$ as functions of the water gap width $D$. ..... 158

Fig. 6.12: Test series 3, unsupported inner hull ($m_F/m_B = 0.5$, $\psi_F = 3.4$, $\psi_B = 1.8$): (a) Measurements and FE predictions of $\bar{I}_{\text{F,max}}$ and $\bar{I}_{\text{B,max}}$ as functions of the water gap width $D$ for monolithic double-hulls; (b) similar information for the experiments performed with sandwich-double hulls. ..... 160

Fig. 6.13: Test series 4, unsupported inner hull ($m_F/m_B = 3.4$, $\psi_F = 1.9$, $\psi_B = 6.3$): (a) Measurements and FE predictions of $\bar{I}_{\text{F,max}}$ and $\bar{I}_{\text{B,max}}$ as functions of the water gap width $D$ for the case of monolithic double-hulls. ..... 161

Fig. 7.1: Dynamic plate deformation consequent to pressure pulse loading: (a) initial configuration; (b) propagation of a flexural wave with the wave front located at $\zeta$; (c) the wave front reaches the plate's centre point and Phase 1 response terminates. ..... 167

Fig. 7.2: Free body diagrams of the circular plate in deformed configuration: (a) section through the whole structure; (b) circular sector.....174

Fig. 7.3: Central deflection versus time histories of laminated composite plates (*Material 1*) subject to impulsive loading with initial velocity $v_0 = 85\,\mathrm{ms}^{-1}$ for two different geometries: (a) $R = 150\,\mathrm{mm}$, $h = 8\,\mathrm{mm}$ ($\bar{h} = 0.053$) and (b) $R = 100\,\mathrm{mm}$, $h = 8\,\mathrm{mm}$ ($\bar{h} = 0.08$); analytical predictions are compared to FE simulations.....188

Fig. 7.4: Impulsive loading of circular plates made from elastic isotropic material (*Material 2*): analytical and FE predictions of the maximum central deflection $w_0^{\max}$ as functions of imparted impulse $I$; contours of aspect ratio $\bar{h} = h/R$ are included for four selected geometries, all of which of thickness $h = 8\,\mathrm{mm}$.....189

Fig. 7.5: Design chart for circular elastic plates subject to impulsive loading; contours of normalised central deflection $\bar{w}_0^{\max} = w_0^{\max}/R$ (solid curves, underlined values) and areal mass $\bar{\mu}_{imp} = ER\mu/I^2$ (dashed curves) are included.....191

Fig. 7.6: (a) Analytical and FE predictions of the normalised maximum centre deflection $\bar{w}_0^{\max}$ as functions of the normalised impulse $\hat{I}$ for circular plates made from elastic isotropic material (*Material 2*); contours of aspect ratio $h/R$ are included for three selected geometries, all of which of thickness $h = 10\,\mathrm{mm}$. The solid curves represent analytical predictions performed by loading the plates impulsively according to the Taylor impulse, while the dashed curves denote those obtained from the analytical model developed in this thesis. (b) Analytical predictions of the response time $\hat{t}_{\max}$ as a function of $\hat{I}$ for the case of impulsive loading. .....194

Fig. 7.7: (a) Central deflection versus time histories of circular plates made from composite laminate (*Material 1*, $h = 8\,\mathrm{mm}$, $R = 300\,\mathrm{mm}$) and subjected to loading by an underwater shock

wave of $p_0 = 75\,\text{MPa}$ and $\theta = 0.15\,\text{ms}$; analytical predictions are compared to FE simulations for two different layups. (b) Similar information for underwater blast loading with $p_0 = 130\,\text{MPa}$ and $\theta = 0.15\,\text{ms}$. (c) Plate deformation and fluid pressure fields for five selected time frames obtained from the FE simulation corresponding to the loading case used in (a); analytical predictions (dashed curves) are included. FE scale: 75 MPa (red) – 0 MPa (blue), cavitation zones are highlighted in grey. ..... 197

Fig. 7.8: Comparison between analytical and FE predictions of the maximum central deflection $w_0^{\max}$ plotted as functions of the impulse $I_0 = 2p_0\theta$ for underwater blast loading of elastic isotropic plates (*Material 2*, $h$ = 10 mm, $\theta = 0.15\,\text{ms}$); contours of $\bar{h} = h/R$ are included for five different geometries. ..... 198

Fig. 7.9: Analytical predictions of the maximum centre deflections $\bar{w}_0$ as functions of the normalised peak pressure $\bar{p}_0$ for circular isotropic plates with contours of (a) non-dimensional radius $\bar{R}$, (b) aspect ratio $\bar{h}$ and (c) acoustic impedance $\bar{\alpha}$. ..... 201

Fig. 7.10: (a) Design chart for circular isotropic plates subject to underwater blast loading with $\bar{\alpha} = 0.15$ and with constained normalised deflection $\bar{w}_0 = 0.1$; contours of non-dimensional peak pressure $\bar{p}_0 = p_0/E$ (solid curves, underlined values) and areal mass $\bar{\mu} = \mu/\left(\theta\sqrt{E\rho}\right)$ (dashed curves) are included. (b) Similar design chart for a fixed maximum centre deflection of $\bar{w}_0 = 0.2$ ..... 204

Fig. 7.11: Variation of the normalised peak pressure $\bar{p}_0$ sustained by the optimal designs and the 'worst case designs', $\bar{p}_0^{\max}$ and $\bar{p}_0^{\min}$, respectively, as a function of the non-dimensional areal mass $\bar{\mu} = \mu/\left(\theta\sqrt{E\rho}\right)$ for $\bar{\alpha} = 0.15$ and fixed central deflections of $\bar{w}_0 = 0.1$ and $\bar{w}_0 = 0.2$. ..... 205

Fig. 8.1: Schematic of the experimental apparatus used to perform underwater blast experiments on circular composite plates.....212

Fig. 8.2: Post-test photographs showing shear failure of CRP plates consequent to blast loading: (a) experiment 3, $p_0 = 10.8\,\text{MPa}$, $\theta = 0.14\,\text{ms}$; (b) experiment 2, $p_0 = 9.4\,\text{MPa}$, $\theta = 0.12\,\text{ms}$. .....214

Fig. 8.3: Selected high-speed photographs for experiment 1 ( $p_0 = 7.2\,\text{MPa}$, $\theta = 0.12\,\text{ms}$ ) performed on a CRP plate; fluid pressure contour plots extracted from corresponding FE simulations are included for comparison; FE scale: 7.2 MPa (red) – 0 MPa (blue); cavitation zones are highlighted in dark grey.....216

Fig. 8.4: Sequcence of high-speed photographs for experiment 2 ( $p_0 = 9.4\,\text{MPa}$, $\theta = 0.12\,\text{ms}$ ) performed on a CRP composite plate: (a) incident wave reaches the specimen; (b) elastic specimen deformation; (c) plate failure and appearance of two cavitation zones, both expanding by propagation of breaking fronts (BF); (d) coalescence of both cavitation zones and emergence of a closing front (CF); (e)-(f) collapse of cavitation bubbles by propagation of a CF.....217

Fig. 8.5: (a) High-speed photographic sequence for experiment 5 ( $p_0 = 6.8\,\text{MPa}$, $\theta = 0.14\,\text{ms}$ ) showing the dynamic elastic deformation of a CRP plate; (b) contour plots of fluid pressure obtained from the corresponding FE simulations for four selected time frames; composite plies are oriented parallel and perpendicular to the section plane; FE scale: 6.8 MPa (red) – 0 MPa (blue); cavitation zones are highlighted in dark grey.....220

Fig. 8.6: Time histories of the measured centre deflection for two selected experiments performed on GRP plates: (a) experiment 8, $p_0 = 9.0\,\text{MPa}$, $\theta = 0.12\,\text{ms}$; (b) experiment 10, $p_0 = 7.0\,\text{MPa}$, $\theta = 0.14\,\text{ms}$; analytical and FE predictions are included for comparison. .....221

Fig. 8.7: Analytical predictions of maximum centre deflection $\bar{w}_0^{\max}$ as a function of the non-dimensional peak pressure of the incident shock wave $\bar{p}_0 = p_0/E$ for the plate geometries and pressure pulse characteristics used in experiments 4 – 14; experimental measurements obtained from these experiments are included for comparison (full and empty markers). ....224

# List of Tables

Table 1.1: Existing literature on the response of submerged structures to underwater blast as well as research contributions from this thesis. ..... 9

Table 4.1: Details of selected experiments performed in this study. ..... 80

Table 5.1: Properties and dimensions of the sandwich foam cores considered in this study .. 99

Table 5.2: Details of selected experiments performed in this study ..... 108

Table 6.1: Core properties and dimensions of the sandwich specimens considered in this study ..... 139

Table 6.2: List of experiments conducted with rigid, stationary inner hull specimens, reporting masses of the outer skin specimens, widths of water gaps as well as the characteristics of the loading pressure pulses. ..... 141

Table 6.3: List of experiments conducted with rigid, unsupported inner hull specimens, reporting masses of the specimens, withs of water gaps as well as the characteristics of the loading pressure pulses. ..... 142

Table 8.1: Constituent material properties ..... 210

Table 8.2: Elastic properties of the equivalent transversely isotropic lamina used to model CRP and GRP plates. ..... 210

Table 8.3: Details of experiments performed in this study ..... 214

# Notation

## General notation rules

Overdots denote derivatives with respect to time (e.g. $\dot{u}$ , $\ddot{w}$ , $\dot{w}$ , etc.).
Overbars denote normalised (non-dimensional) quantities (e.g. $\overline{w}$ , $\overline{v}$ , etc.).

## Coordinate Systems

| | | |
|---|---|---|
| $x, y, z$ | ... | cartesian coordinates |
| $r, \varphi, z$ | ... | cylindrical coordinates |
| $u$ | ... | dispacement in $x$- or $r$-direction |
| $v$ | ... | dispacement in $y$- or $\varphi$-direction |
| $w$ | ... | dispacement in $z$-direction |

## Symbols

### Lower case roman letters

| | | |
|---|---|---|
| $a_c$ | ... | radial expansion of cavitation zone |
| $c$ | ... | thickness of sandwich core |
| $\Delta c$ | ... | core compression |
| $\Delta c_F$ | ... | final core compression |
| $c_w$ | ... | speed of sound in fluid |
| $c_{BF}$ | ... | velocity of breaking front |
| $c_{CF}$ | ... | velocity of closing front |
| $d_S$ | ... | diameter of striker |
| $d_c$ | ... | diameter of sandwich core |
| $d_p$ | ... | pore size of foam |
| $d_F$ | ... | diameter of foam cylinder (Chapter 4) |
| $h$ | ... | plate thickness |
| $\overline{h}$ | ... | aspect ratio |
| $h_f$ | ... | thickness of front face sheet |

$h_b$ ... thickness of back face sheet

$k$ ... linear spring stiffness

$k_Y$ ... yield ratio

$l_e$ ... element size in FE model

$l_s$ ... plastic shock width

$m$ ... total mass per unit area

$m_c$ ... mass per unit area of sandwich core

$m_f$ ... mass per unit area of front face sheet

$m_b$ ... mass per unit area of back face sheet

$m_{S,P}$ ... mass per unit area of striker-piston system

$m_F$ ... mass per unit area of outer skin

$m_B$ ... mass per unit area of inner hull

$p$ ... pressure (general)

$p_b$ ... pressure applied on the back face of the structure

$p_f$ ... pressure applied on the front face of the structure

$p_{f,1a}$ ... front face pressure for Phase 1a (Chapter 7)

$p_{f,1b}$ ... back face pressure for Phase 1a (Chapter 7)

$p_{f,\max}$ ... peak front face pressure

$p'$ ... absolute pressure applied on the back face of the structure (Chapter 3)

$p_c$ ... cavitation pressure

$p_c^0$ ... initial pressure stress in hydrostatic compression

$p_0$ ... peak pressure of shock wave

$p_{in}$ ... pressure wave travelling towards the plate (incident wave)

$p_{in}^{1D}$ ... analytical predictions of the loading pressure wave for Phase 2 (Chapter 7)

$p_{out}$ ... pressure wave reflected from the fluid-structure interface

$p_{rare}$ ... rarefaction wave

$p_{CF}$ ... pressure of uncavitated fluid at the closing front

$p_{CF,in}$ ... pressure wave train approaching the closing front

$p_{CF,out}$ ... pressure wave train reflected from the closing front

$p_{I,in}$ ... pressure wave train approaching the fluid-structure interface in Stage I

$p_{I,out}$ ... pressure wave train travelling away from the fluid-structure interface in Stage I

$p_{II,in}$ ... pressure wave train approaching the fluid-structure interface in Stage II

$p_{II,out}$ ... pressure wave train travelling away from the fluid-structure interface (Stage II)

$p_B$ ... dynamic pressure applied on the inner hull

$p_F^b$ ... dynamic pressure applied on the back face of the outer skin

$p_F^f$ ... dynamic pressure applied on the front face of the outer skin

$p'_{st}$ ... ficticious initial hydrostatic pressure

$p_{st,c}$ ... critical static pressure

$p_{st}$ ... initial hydrostatic pressure

$\overline{p}_{st}^*$ ... normalised static pressure

$s, r$ ... auxiliary quantities (Chapter 3)

$t$ ... time

$\Delta t$ ... time increment

$\Delta t_i$ ... interframe time

$t_c$ ... time of the onset of cavitation in the front water column

$t'_c$ ... time of the onset of cavitation in the back water column

$t_{rest}$ ... time of arrest of breaking front

$t_{\max}$ ... time at which the structure reaches the peak displacment

$t_I$ ... time of Stage I termination (Chapter 3)

$t_1$ ... time of Phase 1 termination (Chapter 7)

$t_b$ ... rise time of back face sheet velocity

$u_f$ ... displacement of front face sheet

$u_b$ ... displacement of back face sheet

$v_{CF}$ ... particle velocity of uncavitated fluid at the closing front

$v_{CF,in}$ ... particle velocity of wave train approaching the closing front

$v_{CF,out}$ ... particle velocity of wave train reflected from the closing front

$v$ ... plate velocity (general)

$v_0$ ... initial plate velocity

$v_b$ ... velocity of back face sheet

$v_{com}$ ... common velocity of face sheets

$v_f$ ... velocity of front face sheet

$v_{f,0}$ ... velocity imparted to the front face (Taylor prediction)

$v_{f,\max}$ ... maximum front face sheet velocity

$v_{\max}$ ... maximum plate velocity

$v_w$ ... fluid particle velocity

$v_c$ ... velocity of cavitated fluid

$\Delta v$ ... velocity jump

$v_F$ ... final velocity of back face sheet

$v_S$ ... velocity of striker

$w_B$ ... plate deflection due to bending

$w_S$ ... plate deflection due to shearing

$w_0$ ... total centre deflection

$w_0^{\max}$ ... maximum centre deflection

$w_{B0}$ ... plate centre deflection due to bending

$w_{S0}$ ... plate centre deflection due to shearing

$x_{rest}$ ... position of arrest of breaking front

$x_{BF}$ ... position of breaking front

$x_{CF}$ ... position of closing front

$x_c,\ z_c$ ... position of the onset of cavitation

$\Delta x_i$ ... pixel size

## Upper case roman letters

$\mathbf{A}$ ... stiffness matrix of laminate in material coordinates

$\hat{\mathbf{A}}$ ... stiffness matrix of laminate in the $(r,\varphi,z)$ coordinate system

$\mathbf{D}$ ... bending stiffness matrix of laminate in material coordinates

$\hat{\mathbf{D}}$ ... bending stiffness matrix of laminate in the $(r,\varphi,z)$ coordinate system

$A_P$ ... cross-sectional area of piston

$A, B, C$ ... auxiliary quantities (Chapter 3)

$D, F, G$ ... auxiliary quantities (Chapter 3)

$D$ ... width of water gap

$E$ ... Young's modulus of isotropic material

$E_1, E_2, E_3$ ... Young's moduli in fibre, transverse and through-thickness directions

$E_c$ ... Young's modulus of core material

$E_f$ ... Young's modulus of fibres

$E_m$ ... Young's modulus of matrix material

$G_{12}$ ... in-plane shear modulus

$G_{23}, G_{13}$ ... transverse shear moduli (in material coordinates)

$G_{rz}$ ... transverse shear moduli in the $(r,\varphi,z)$ coordinate system

$H_f$ ... height of water column (FEM)

$I$ ... imparted impulse (general)

$I_p$ ... maximum partial impulse (Chapter 3)

$I_t$ ... maximum total impulse (Chapter 3)

$I_f$ ... impulse imparted to the front face of the structure

$I_{f,\max}$ ... maximum impulse imparted to the front face of the structure

$\hat{I}_t$ ... normalised impulse for impulsive loading (Chapter 7)

$I_b$ ... impulse imparted to the back face sheet

$I_0$ ... impulse applied on a stationary plate

$I_F$ ... impulse imparted to the outer skin

$I_B$ ... impulse imparted to the inner hull

$I_{FF}$ ... impulse imparted to a rigid plate of mass equal to the front face sheet

$I_{TOT}$ ... impulse imparted to a rigid plate of mass equal to the total sandwich

$I_{F,\max}$ ... maximum impulse imparted to the outer skin

$I_{B,\max}$ ... maximum impulse imparted to the inner hull

$K_w$ ... bulk modulus of fluid

$L$ ... length of fluid column

$M_f$ ... mass of front face sheet

$M_b$ ... mass of back face sheet

$M_F$ ... mass of outer skin

$M_B$ ... mass of inner hull

$M_P$ ... mass of piston

$M_S$ ... mass of striker

$M_r, M_t$ ... bending moments (per unit width) in radial and tangential direction

$M_{rt}$ ... twisting moment (per unit width)

$\tilde{M}_r, \tilde{M}_t$ ... average bending moments (per unit width) in radial and tangential direction

$N_r, N_t$ ... in-plane forces (per unit width) in radial and tangential direction

$N_{rt}$ ... in-plane shear force (per unit width)

$\tilde{N}_r, \tilde{N}_t$ ... average in-plane forces (per unit width) in radial and tangential direction

$P_F, P_M$ ... loading functions (Chapter 7)

$P_{F,1a}, P_{M,1a}$ ... loading functions for Phase 1a (Chapter 7)

$P_{F,1b}, P_{M,1b}$ ... loading functions for Phase 1b (Chapter 7)

$P_{F,2}, P_{M,2}$ ... loading functions for Phase 2 (Chapter 7)

$Q_{rz}$ ... transverse shear force (per unit width)

$R$ ... plate radius

$V_w$ ... volume of fluid

$V_c$ ... volume of cavitated fluid

$Y$ ... multiplier in Cowper-Symonds overstress power law

$Z$ ... acoustic impedance of solid

$Z_w$ ... acoustic impedance of fluid

## Lower case greek letters

$\bar{\alpha}$ ... non-dimensional acoustic impedance

$\beta$ ... viscosity parameter

$\gamma_{rz}, \gamma_{tz}$ ... transverse shear deformations in $(r, \varphi, z)$ coordinates

$\gamma_{rz0}$ ... transverse shear deformation at the clamped boundary

$\gamma_{rt}$ ... in-plane shear deformation

$\varepsilon_c$ ... core strain

$\varepsilon_{cY}$ ... yield strain of the core material

$\varepsilon_c^{pl}$ ... plastic core strain

$\varepsilon_D$ ... densification strain

$\varepsilon_V$ ... volumetric strain

$\dot{\varepsilon}$ ... strain rate

$\dot{\varepsilon}^{pl}$ ... plastic strain rate

$\varepsilon_r, \varepsilon_t$ ... in-plane strains in radial and tangential direction

$\zeta$ ... position of flexural wave front

$\eta$ ... strain in cavitated fluid

$\theta$ ... decay time of shock wave

$\kappa$ ... non-dimensional stiffness

$\kappa_r, \kappa_t$ ... bending curvatures in radial and tangential direction

$\kappa_{rt}$ ... twisting curvature

$\lambda$ ... auxiliary variable (Chapter 3)

$\mu$ ... mass per unit area (Chapters 7 and 8)

$\nu$ ... Poisson's ratio of isotropic material

$\nu_p$ ... plastic Poisson's ratio

$\nu_f$ ... Poisson's ratio of fibres

$\nu_m$ ... Poisson's ratio of matrix material

$\nu_{12}$ ... Poisson's ratio associated to transverse strain in 2-direction due to applied stress in 1-direction

$\nu_{21}$ ... Poisson's ratio associated to transverse strain in 1-direction due to applied stress in 2-direction

$\nu_{13}$ ... Poisson's ratio associated to transverse strain in 3-direction due to applied stress in 1-direction

$\nu_{23}$ ... Poisson's ratio associated to transverse stress in 3-direction due to applied stress in 2-direction

$\rho$ ... density of solid

$\rho_f$ ... density of fibres

$\rho_m$ ... density of matrix material

$\rho_w$ ... density of fluid

$\rho_c$ ... density of sandwich core

$\rho_F$ ... density of foam

$\sigma_H$ ... hydrostatic stress field

$\sigma_c$ ... compressive strength of sandwich core

$\sigma_c^0$ ... initial yield stress in uniaxial compression

$\sigma_Y$ ... yield stress

$\varphi_f$ ... volume fraction of fibres

$\psi$ ... FSI parameter related to the total areal mass

$\psi_f$ ... FSI parameter related to the areal mass of the front face sheet

$\psi_F$ ... FSI parameter related to the areal mass of the outer skin

$\psi_B$ ... FSI parameter related to the areal mass of the inner hull

# Abbreviations

FSI ... fluid-structure interaction

BF ... breaking front

CF ... closing front

FE ... finite element

CRP ... carbon fibre reinforced polymer

GRP ... glass fibre reinforced polymer

UD ... uni-directional

# Chapter 1

# Introduction

## 1.1 Motivation and Background

The response of submerged structures to underwater blast is a major consideration in the design and construction of naval ships and submarines. Underwater detonation of an explosive charge gives rise to propagation of spherical shock waves [1], impinging on surrounding structures and leading to dynamic deformation or failure. Figure 1.1 (a) shows severe damage of the USS Cole after detonation of an explosive charge in close proximity to the vessel, tearing a hole of approximately 10 m radius in the hull mid-ship. The photograph illustrated in Fig. 1.1 (b) was taken from the USS Tripoli after the ship struck an underwater sea mine, resulting in extensive hull failure by tensile tearing and shearing below the water line.

Each repair or maintenance interval results in high service costs, long repair times and in temporary loss of military equipment. Blast-resistant structural designs as well as optimal material selections are main drivers to mitigate increasing repair and maintenance costs in the operation of naval ships and submarines.



Fig. 1.1: (a) Extensive hull damage of the USS Cole after detonation of an explosive charge mid-ship; (b) photograph taken from the USS Tripoli during repair after the ship struck a sea mine.

## 1.2 Innovations in the design of naval ships and submarines

During the last decades new trends have emerged in the design of naval ships and submarines: structures originally made from steel, aluminium, bronze or other high-density castings have been increasingly replaced by composite materials. Composites were first used after World War II for a range of non-critical components in smaller boats but applications were limited due to poor fabrication quality and low stiffness. However, advances in design and manufacture of composite materials remarkably improved their mechanical performance and led to a widespread use of composites in military marine vehicles and commercial craft. This trend continues today because of the need to reduce maintenance, repair and fuel consumption costs as well as to improve operational performance (e.g. low magnetic signature, buoyancy requirements, range) while maintaining structural strength and stiffness.

A summary of the wide range of applications for composites in naval ships and submarines is illustrated in Fig. 1.2 [2]; the letters C, TD, and D denote concept, technology demonstrator

and fully developed, respectively. Although naval applications for composites have become extremely widespread, the replacement process is still relatively slow since ship designers and builders have great experience and confidence in the use of metals, which have proven to perform well in most static, dynamic and impact loading cases. Moreover, simple design rules as well as analytical tools to predict failure modes and shock resistance have been established for metallic naval structures throughout the last decades but essentially don't exist for composites to date. In addition, experimental data on underwater shock performance of composite structures is extremely scarce owing to the expense and difficulty of large-scale underwater blast tests. As a consequence, safety factors are much higher (typically between 5 and 10) than those used for metallic designs, resulting in detrimental effects on the strength-to-weight benefit offered by composites.

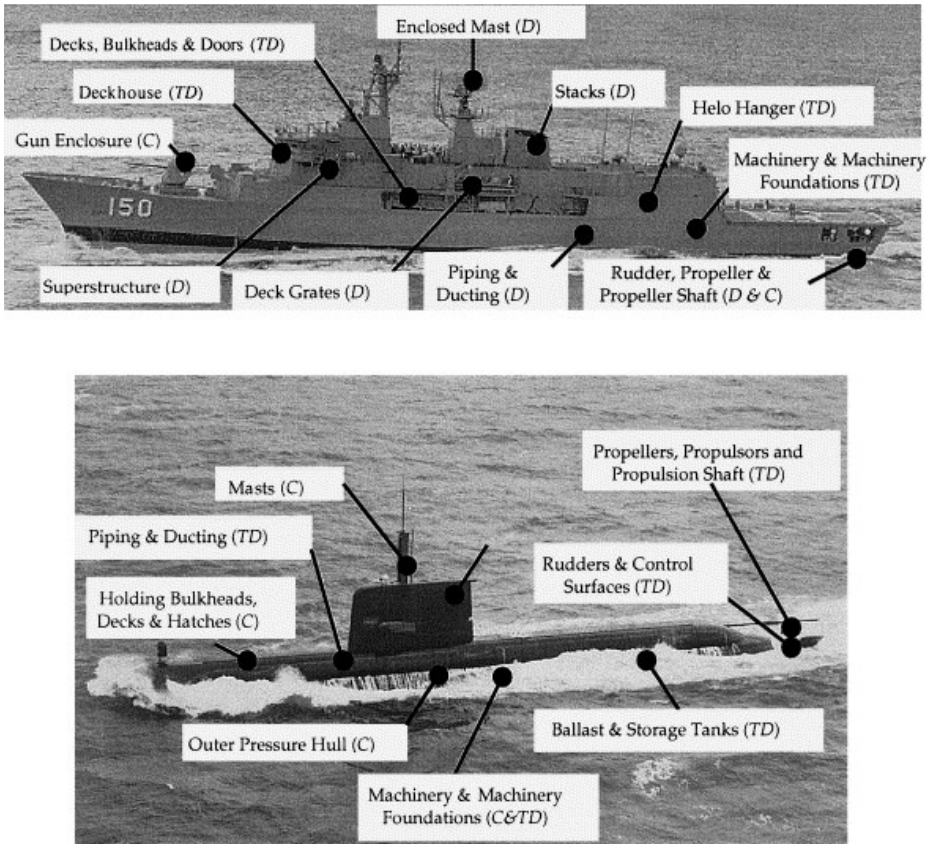



Fig. 1.2: Current applications of composite materials in naval ships and submarines [2]. The abbreviations C, TD and D denote 'concept', 'technology demonstrator' and 'developed (in-service)'.

Concurrent to the introduction of composite materials, sandwich panels, comprising of a crushable core (e.g. foams, honeycomb structures, lattice materials, etc.) and two face sheets, have attracted the attention of designers in the field of light-weight vessel construction.

Although sandwich panels were originally used as stiff and light-weight construction materials for static applications, there is currently a trend to employ sandwich constructions for impact and blast mitigation because of their ability to absorb kinetic energy via mechanical deformation processes in the core. Particularly for underwater blast, sandwich plates experience lower blast impulses than monolithic designs of equal mass, with the reductions a consequence of fluid-structure interaction (FSI). This topic has been the scope of recent research activities, and useful guidelines for the design of blast-resistant submerged sandwich structures have already been established. However, some questions in the design of blast resistant sandwich plates still remain unanswered. In particular, only limited information exists on the response of water-backed sandwich plates subject to underwater blast. Moreover, it is still unclear how sandwich structures perform when subjected to deep explosions, which is of primary interest to designers of blast resistant submarine applications.

## 1.3 Design of structures subject to underwater blast

Fluid-structure interaction consequent to blast loading of submerged structures has many unique characteristics and is governed by complex physics. When blast waves impinge on surrounding submerged structures, the ensuing structural motion leads to a tensile (rarefaction) wave radiated from the loaded surface. Such tensile wave can trigger cavitation if the pressure in the surrounding water drops below the vapour pressure. The cavitation zone spreads in the water with supersonic speed [3] and becomes visible in form of rapidly

growing and collapsing gas bubbles. Cavitation phenomena significantly affect wave propagation as well as structural loading and need to be thoroughly understood in order to design submerged structures against underwater blast.

The complexity of fluid-structure interaction problems renders the computation of analytical solutions extremely difficult and can only be obtained for simple cases [4]. Therefore, predicting the response of complex structural systems to underwater explosions is limited to the use of numerical methods. Due to the great progress in computing technology during the last decades, fully coupled numerical simulations are now extensively used in the design of naval structures and are increasingly supplanting time-consuming and costly large-scale tests. Although there is a vast array of numerical techniques capable of handling continuum mechanics problems (e.g. finite element method, finite volume method, finite difference method, etc.) the finite element method (FEM) has become widespread in the design of submerged structures subject to underwater blast. Modern FE packages (e.g. ABAQUS, ANSYS) provide modelling functionalities to the user capable of simulating the generation of explosive shock waves, wave propagation in the fluid, shock loading of the structure, fluid-structure interaction and the effects of cavitation. However, FE models have inherent deficiencies to reproduce the discontinuous rise in pressure at the shock front of the blast wave leading to inevitable distortion of the wave front and attenuation of the pressure amplitude. In an FE scheme, pressure discontinuities can only be approximated with good accuracy by using a very fine mesh in the fluid domain, which hampers the solution process and can lead to long computation times.

To overcome the computational expense associated with fully-coupled FE simulations, designers of naval ships and submarines often neglect the surrounding fluid and employ purely structural FE models, in which shock wave loading is mimicked by a pressure loading

history deduced from empirical relations or simplified analytical models. Other solution approaches are based on impulsive loading assumptions, justified by the discrepancy between the duration of the shock impulse and the structural response time. Such numerical models do not include the whole complexity of the physics arising from FSI phenomena and are therefore limited to specific problem characteristics and loading cases.

Although FE simulations are suitable for modelling complex FSI problems, they do not provide a solid foundation for understanding the underlying physics. Analytical solutions of simplified FSI problems, such as impact of planar shock waves on submerged rigid plates or sandwich panels, provide great insight into the cavitation process and how this affects the structural response. In addition, analytical solutions are computed much faster than FE models and can be employed in iterative algorithms, in which problem geometry, loading pressure pulse and material parameters are continually adjusted in order to find optimal structural designs. Several authors have used analytical FSI models to construct design charts for the selection of light-weight and blast-resistant geometries. On the other hand, being based on the assumption of negligible hydrostatic fluid pressure, the analytical models in the current literature cannot be used in the design of structures exposed to the threat of explosions in deep water.

In addition to predictive modelling techniques, large-scale explosive test methods are commonly used in the shipbuilding industry in order to probe the shock resistance of naval constructions. Although such tests provide important information on survivability, damage tolerance and failure modes consequent to underwater blast loading, they are time-consuming, cost-intensive and require adequate control and safety measures. Because of these issues, laboratory-scale test methods have been developed which are capable of simulating

underwater blast in a safe and controlled manner. Although these test methods are capable of measuring the dynamic response of structural components, they do not allow measuring the effects of increased initial hydrostatic pressure on the blast response of the component, which is a major concern for deep water applications. In addition, none of the experimental techniques to date allow observation of the cavitation process in the water, which need to be understood in order to predict duration and intensity of the shock impulse imparted to the structure.

## 1.4 Objectives of the thesis

Table 1.1 presents a synopsis of existing literature on fundamental FSI problems relevant for the design of blast-resistant submerged components and allocates their contributions to air-backed and water-backed applications. It can be seen from this table that, although considerable experimental, theoretical and numerical effort has been devoted to study the underwater blast response of various structural systems, some fundamental problems have been left unaddressed by the research community. In particular, the response of water-backed structures subject to underwater blast as well as the effect of an elevated initial hydrostatic fluid pressure on the structural response are still unexplored topics in the current literature but are vital considerations in the design of submarine applications.

The objective of this thesis is to fill some gaps in the current knowledge of FSI in underwater blast, with a focus on unravelling the underlying physics by providing a clear physical picture of cavitation processes and their interactions with surrounding structures in a blast event.

To achieve this, it is instructive to begin with the simplest of problems listed in Table 1.1, namely the 1D response of monolithic plates to underwater blast. Starting from the pioneering

work of Taylor [4], the theory will be extended to the problem of a spring-supported rigid plate, in contact with water on one or both sides and loaded by pressure pulses propagating in initially pressurised water.

Then, the 1D response of free-standing water-backed and air-backed monolithic plates will be examined by simulating underwater blast at a laboratory scale and observing the structural response as well as the cavitation phenomena in the water. Experimental results will serve to validate the developed analytical models and to examine the dependence of blast performance on initial static pressure and structural mass. Subsequently, the developed experimental method is employed to investigate the 1D response of sandwich plates and double-walled structural systems to underwater blast. Finite element simulations will be performed to gain more insight into FSI and to validate the results obtained from the corresponding experiments.

Next, it will be demonstrated to what extent the 1D analytical models can represent the 3D response of real-life structures. In the process, an analytical FSI model for the dynamic response of circular elastic plates to underwater blast will be developed, based on predictions computed with 1D analytical FSI models.

Finally, the underwater blast response of circular composite plates will be interrogated using the developed experimental apparatus. Observations of the cavitation process as well as measurements of the dynamic plate deflection will be compared with predictions performed with FE and analytical models.

Table 1.1: Existing literature on the response of submerged structures to underwater blast as well as research contributions from this thesis.

| | | **air-backed** | | **water-backed** | |
|---|---|---|---|---|---|
| | | shallow water $p_{st} \approx 0$ | deep water $p_{st} \neq 0$ | shallow water $p_{st} \approx 0$ | deep water $p_{st} \neq 0$ |
| **1D monolithic plates** | experimental | **Chapter 4** | **Chapter 4** | **Chapter 4** | **Chapter 4** |
| | numerical/ analytical | Taylor (1941)<br>**Chapter 3** | **Chapter 3** | **Chapter 3** | **Chapter 3** |
| **1D sandwich plates** | experimental | Deshpande et al. (2006)<br>Wadley et al. (2008)<br>**Chapter 5** | **Chapter 5** | **Chapter 5** | **Chapter 5** |
| | numerical/ analytical | Deshpande & Fleck (2005)<br>Hutchinson & Xue (2005)<br>Liang et al. (2007) | **?** | **?** | **?** |
| **Circular composite plates** | experimental | Latourte et al. (2011)<br>LeBlanc & Shukla (2011)<br>**Chapter 8** | **?** | **?** | **?** |
| | numerical/ analytical | **Chapter 7** | **?** | **Chapter 7** | **?** |

# Chapter 2

# Literature Review

## 2.1 Review of existing literature

The current literature on underwater blast loading is examined in this section to underpin the work presented in this thesis. First, a review of underwater explosion phenomena will be given. Then, attention will be focussed on current theoretical and numerical predictive models for the response of submerged structures to underwater blast. Finally, the existing experimental methods for blast loading of submerged structural components will be summarised, including both large-scale testing of real-size components and blast experiments at laboratory scale.

### 2.1.1 Underwater explosions

The physical phenomena associated to underwater explosions are well established due to extensive research carried out during World War II. A comprehensive summary of experimental and theoretical work on underwater explosions conducted during the 1940s is given in Cole [5] and the main physical processes are briefly sketched in the following.

The underwater detonation of an explosive charge converts the original explosive material into a gas at very high temperature and pressure. During this process a detonation wave is generated, propagating in the explosive material with supersonic speed. The detonation wave can be described as a shock wave immediately followed by a reaction zone in which the chemical transformation takes place. Once the detonation process is completed, the enormous pressure of the reaction gases is transmitted to the surrounding water as a shock wave propagating in all directions. In close proximity to the detonation point the generated pressures are so large that the wave speed becomes dependent upon the surrounding pressure field, causing the shape of the wave to change with the magnitude of pressure and displacement of water as it propagates. The velocity of wave propagation can be several times higher than the speed of sound in water ($c_w \simeq 1490\,\mathrm{ms}^{-1}$ at 18°C); however, this value is being approached quite quickly as the wave advances outwards and the pressure drops to a level for which the rate of propagation is no longer affected by the magnitude of pressure.

The gases generated in the blast event form an expanding bubble, displacing the surrounding water. At later times, the gas pressure falls below the equilibrium pressure, determined by superposition of atmospheric and hydrostatic pressure, owing to the inertia of the outward flowing water. This negative pressure gradient forces the surrounding water to decelerate and to invert its velocity, contracting the boundary of the bubble. The inertia of the water together with the elasticity of the gas in the bubble, represent an oscillating system that permits repeated cycles of expansions and contractions of the gas bubble boundary. As a result, successive disturbances are transmitted to the water in form of secondary pressure pulses which become progressively weaker and normally only the primary shock wave is of significance [5]. The pressure versus time history plotted in Fig. 2.1 was measured 18 m away

from a 136 kg TNT charge fired 15 m below the water surface and shows the relation between primary shock wave, bubble pulse duration and secondary pressure pulse.

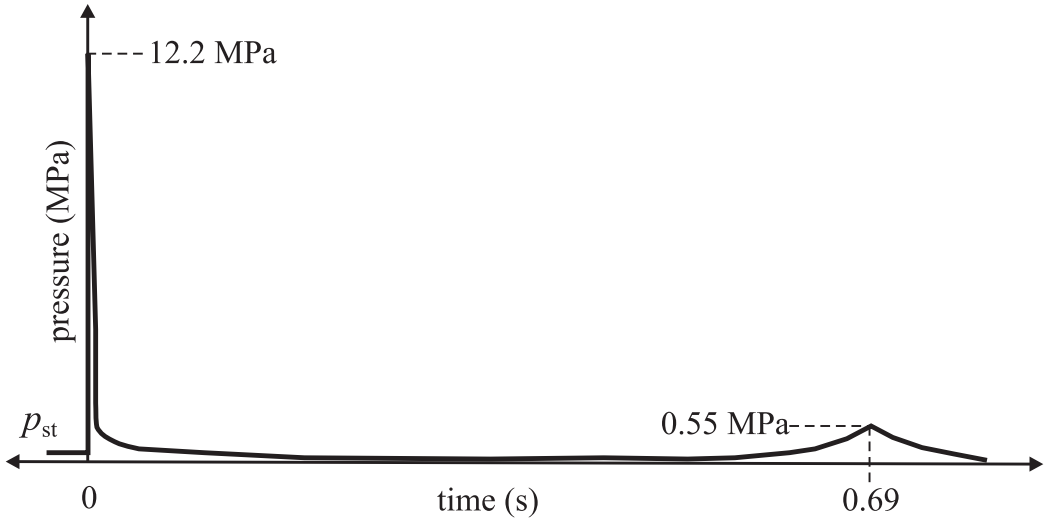



Fig. 2.1: Pressure versus time history measured at a distance 18 m from a 136 kg TNT charge fired 15 m below the surface; reproduced from Cole [5].

At sufficient distance from the detonation point, the pressure versus time history associated with the passage of the primary shock wave (see Fig. 2.1) at a point in the water can be written as

$$p(t) = p_0 \mathrm{e}^{-t/\theta} \tag{2.1}$$

where the peak pressure $p_0$ and the decay time $\theta$ depend upon the mass and type of explosive material as well as on the distance from the point of detonation. The dependency of $p_0$ and $\theta$ on the stand-off distance $R_{\mathrm{exp}}$ and mass of explosive $M_{\mathrm{exp}}$ can be described by the power law relations

$$p_0 = K_1 \left( \frac{M_{\mathrm{exp}}}{R_{\mathrm{exp}}} \right)^{\alpha_1} \quad ; \quad \theta = K_2 M_{\mathrm{exp}}^{1/3} \left( \frac{M_{\mathrm{exp}}^{1/3}}{R_{\mathrm{exp}}} \right)^{\alpha_2} \tag{2.2}$$

where $K_1$, $K_2$, $\alpha_1$ and $\alpha_2$ are material constants which can be taken from Table 2 in Swistak [1] ($K_1 = 52.4$, $K_2 = 0.084$, $\alpha_1 = 1.13$ and $\alpha_2 = -0.23$ for an underwater TNT explosion ).

The bubble pulse durations of underwater explosions strongly depend on the depth of water as well as on the proximity of boundary surfaces. Slifko [6] examined the dependence of the pressure pulse characteristics upon depth and stand-off distance for TNT and HBX-3 charges fired at water depths between 150 m and 4300 m. Simple relations based on dynamic pressure measurements were established which allowed concluding that all pressure pulse characteristics can be written as functions of depth and stand-off distance. The peak pressure of the primary shock wave was found to be independent from depth and decreases with increased distance from the explosion, while the characteristic durations were functions of depth alone.

Primary and secondary pressure pulses experienced by a fluid element at a distance of 10 m from a 1000 kg TNT charge detonated at a depth of 1000 m are illustrated in Fig. 2.2. The pressure pulse characteristics were calculated by using the power law scaling relations presented in Slifko [6]. It should be noted that the duration of the first bubble period, defined as the time between both pressure spikes in Fig. 2.2, is approximately ten times shorter than what reported in Fig. 2.1 for a shallow water explosion. Another interesting aspect of deep explosions is the occurrence of a negative pressure phase (relative to the ambient pressure), as a consequence of increased hydrostatic pressure acting on the oscillating bubble boundary.

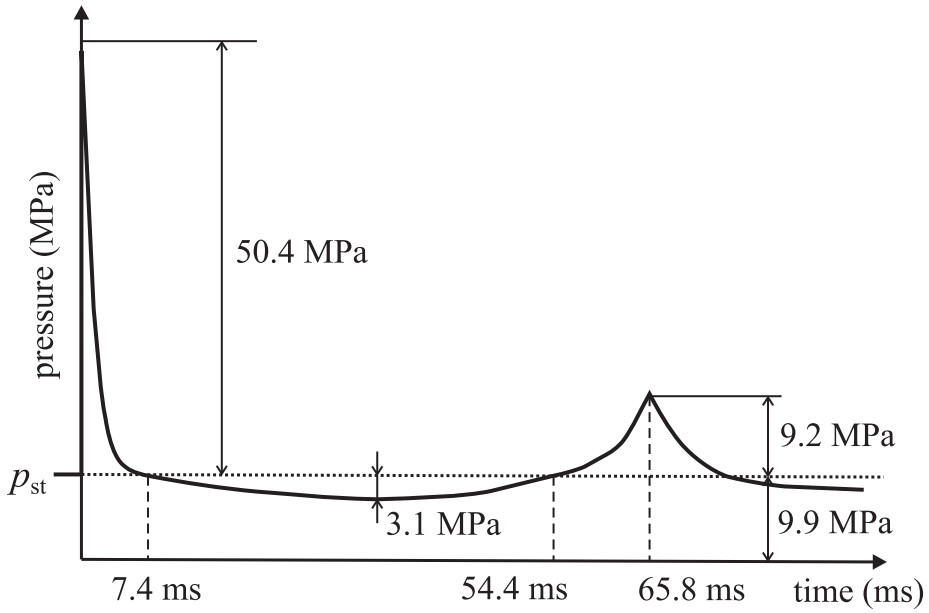



Fig. 2.2: Characteristics of primary and secondary pressure pulses at a stand-off distance of 10 m from a 1000 kg TNT charge deotonated at a water depth of 1000 m; the characteric time periods and pressure values were calculated using the formulas given in Slifko [6].

### 2.1.2 FSI: physical background and predictive modelling

Submerged structural components surrounding the point of detonation are subjected to intense dynamic loads, triggered by impingement of the primary shock wave. The ensuing dynamic response is dictated by the emergence of elastic and plastic waves propagating in the solid and can be considerably different to the static loading case. This discrepancy can be attributed to interia effects, possible strain-rate dependency of the material behaviour as well as the occurrence of different deformation and failure mechanisms when the structure is loaded dynamically.

Before attempting to establish predictive models for underwater blast problems, it is instructive to understand the main phenomena of the dynamic structural response consequent to impulsive transverse loads. A large body of literature exists on the dynamic behaviour of structures made from ductile materials. In typical blast loading scenarios, the effect of material elasticity often plays a minor role because their deformation is dominated by large

plastic strains. Therefore, the introduction of a rigid-ideally plastic material model is adequate in most dynamic loading cases. Although the first investigations on the static behaviour of structures commenced in the late 19$^{th}$ century, studies of dynamic loading cases are much more recent and date back to World War II. Early theoretical work on the transient response of thin plates subject to transverse dynamic loads was carried out by Hudson [7] and Wang & Hopkins [8] who established theoretical models for the dynamic plastic response of thin plates subject to impulsive loads.

In his book *Structural Impact*, N. Jones [9] gives a comprehensive account of the dynamic behaviour of beams, plates and shells made from ductile materials which may be idealised as rigid-perfectly plastic. Starting from the basic principles of static plastic deformation, Jones presents analytical models and generates exact solutions for simple dynamic structural problems in order to provide insight into the main physical phenomena, such as the formation of stationary or travelling plastic hinges during the plastic collapse process. The theoretical models presented in this publication can be used to predict the maximum central deflection as well as the onset of failure for basic structural problems and account for the effects of finite displacements, transverse shear and rotary inertia.

Concerning the prediction of the dynamic response of composite plates, only limited work is reported in the current literature. Composites are inhomogeneous, anisotropic and elastic solids and exhibit a response which is deeply different to that of ductile structures [9]. This was demonstrated, for example, in an experimental study by Tagarielli et al. [10] who examined the elastic response of fully-clamped monolithic composite beams and sandwich panels to transverse projectile impact at mid-span. They observed that dynamic beam deformation is dictated by propagation of a flexural wave emanating from the edge of the projectile and propagating towards the supports, as shown in Fig. 2.3.

These observations were used to motivate simple analytical models for predicting the maximum mid-span deflections of monolithic and sandwich beams [11]. However, such models were based on isotropic elastic material behaviour and thus did not account for the anisotropy of fibre reinforced composites.

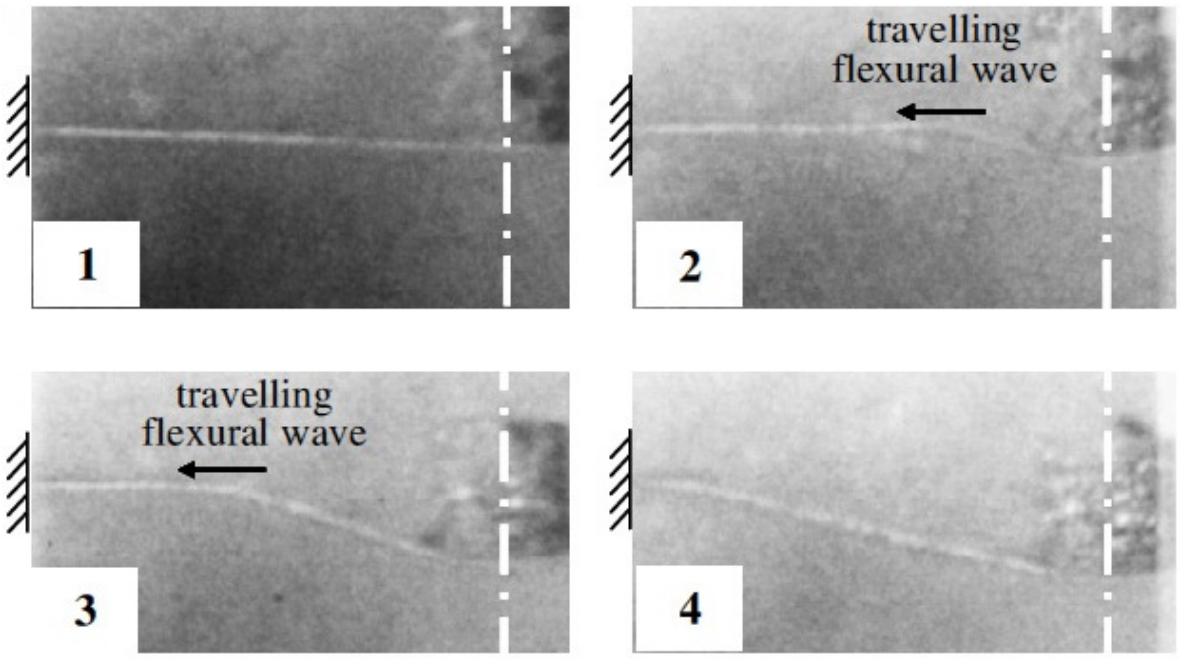



Fig. 2.3: High-speed photographic sequence of a monolithic beam impacted by a foam projectile [10].

Sandwich plates comprising of PVC foam cores and face sheets made from carbon or glass fibre reinforced polymers are widely used in marine and aerospace applications. Hoo Fatt & Palla [12] investigated the dynamic behaviour of such sandwich panels and developed analytical models to predict dynamic deformation as well as failure initiation consequent to impulsive pressure loading. In this paper, the overall response of the sandwich is modelled in two sequential stages: (i) core-crush phase with propagation of stress waves in through-thickness direction and (ii) a plate shearing and bending phase, with a transverse shear wave propagating in the sandwich.

The impact of underwater blast waves on surrounding structures produces a response which elicits not only dynamic deformation processes but also complex FSI phenomena. Due to the fact that such loading scenarios are relatively uncommon in most engineering problems, FSI in underwater blast has been a widely unexplored field until it attracted the attention of several research groups during World War II.

The pioneering work on FSI dates back to the early 1940s; Taylor [4] investigated the response of a rigid free-standing plate loaded by an exponentially decaying planar shock wave as given in eq. (2.1). Upon arrival of the incident wave at the fluid-structure interface the plate is set in motion and continuity between the plate and the adjacent fluid particles causes a tensile (rarefaction) wave to be radiated from the fluid-structure interface and propagating into the fluid. The amplitude of the rarefaction wave scales with the plate's velocity and forces the fluid pressure at the interface to drop below the vapour pressure. As a consequence, the water cavitates at the interface and structural loading ceases. The response of the plate is dictated by the Taylor FSI parameter defined as

$$\psi = \frac{\rho_w c_w \theta}{m} \tag{2.3}$$

where $\rho_w$ and $c_w$ are density and speed of sound in the fluid, respectively, $\theta$ represents the decay time of the blast wave and $m$ is the mass per unit area of the plate. Taylor [4] concluded that the momentum transmitted to the structure in the blast event is reduced by decreasing the plate's mass, i.e. increasing the parameter $\psi$ in eq.(2.3): lighter plates respond to blast loading with higher acceleration, promoting cavitation processes to initiate at earlier times in the response.

The pressure at which fluids cavitate depends on their thermodynamic conditions but also on impurities and dissolved gases, as well as on the presence of fluid-solid interfaces, which can trigger nucleation of cavitation in the presence of tensile hydrostatic stress in the fluid. Some experiments [13] have shown that distilled, de-ionised, degassed and filtered water in laboratory conditions can achieve a tensile strength up to 9 MPa; on the other hand, this value drops to very close to zero for the case of sea or lake water, and it is reasonable to neglect the tensile strength of water in comparison to the intense compressive shock waves experienced during blast events.

In his book *Cavitation and Bubble Dynamics*, C.E. Brennen [14] gives a comprehensive account of the theoretical background of cavitation in liquids.

The main phenomena of the cavitation process need to be thoroughly understood when studying the response of structures subject to underwater blast. Theoretical work by Kennard [3] provided great insight into this; he found that 'breaking fronts' (BFs) emerge from the point of first cavitation, propagating outwards with supersonic speed and generating an expanding pool of cavitated water. Subject to the conditions in the uncavitated water ahead of the cavitation boundary, such BFs can arrest, invert their motion and become 'closing fronts' (CFs), reducing the volume of cavitated fluid.

Bleich and Sandler [15] developed mathematical models to examine the evolution of cavitation boundaries consequent to shock loading of a rigid plate floating on a liquid half-space.

A significant part of the recent blast loading literature has concentrated on the shock resistance of sandwich structures. Such structures are potential candidates for the construction of naval hulls because they exhibit excellent stiffness-to-weight properties and provide blast

mitigation owing to dissipative deformation mechanisms in the core. Both composite and metallic sandwich panels are common construction materials in the shipbuilding industry. Composite sandwich panels possess large stiffness-to-weight ratios and typically consist of fibre-reinforced polymer face sheets and a core made from honeycomb [16], polymer foam [17-19] or balsa wood [19]. Metallic sandwich designs are normally used for more cost-sensistive applications and are in many cases slightly heavier than composite sandwiches of similar strength. Development of new light-weight metallic sandwich core materials, such as metallic foams [20] and pyramidal lattice cores [21], has been the scope of recent research activities.

Early work on underwater blast loading of sandwich panels was conducted by Xue & Hutchinson [22] who performed FE simulations in order to examine the response of monolithic and sandwich plates by imparting the front face sheet an initial velocity in accordance to the Taylor impulse [4]. The study showed that well-designed sandwich panels can sustain considerably higher blast impulses than monolithic designs of equal mass. Similar results are reported in more recent numerical studies [23, 24].

Other authors developed analytical models to examine the response of sandwich plates subject to underwater blast and to understand the effects of the ensuing FSI phenomena. Fleck & Deshpande [25] proposed an analytical model for the response of clamped metallic sandwich beams subject to impulsive underwater blast loads with the impulse imparted to the structure estimated from the Taylor analysis [4]. Subsequently, Qiu et al. [26] extended these models [25] to examine the impulsive shock response of clamped circular metallic sandwich plates.

However, in many cases, the Taylor analysis is not suitable for estimating the impulse imparted to a submerged sandwich plate in the event of an underwater explosion. Deshpande & Fleck [27] and Hutchinson & Xue [28] developed analytical models for the 1D response of sandwich plates subject to loading by an underwater blast wave. Both studies found that the

cavitation process is different to that of a monolithic plate [4]: in the case of a sandwich plate, the cavitation process initiates at a finite distance from the fluid-structure interface, owing to the support provided by the core. Their models are based on the assumption that a layer of water attaches to the front face sheet, effectively increasing its mass and hence the momentum transmitted to the plate. They concluded that the impulse imparted to a sandwich plate lies between the Taylor predictions [4] for a free-standing plate of mass equal to the total sandwich (upper bound) and the face sheet only (lower bound).

Then later, Liang et al. [29] approached the same problem and found that the attached-layer-assumption [27, 28] can lead to significant underestimation of momentum transmitted to the sandwich plate, indicating that FSI plays a more complex role than initially assumed. To overcome this discrepancy, they refined this theory by accounting for re-attachment of cavitated water to the structure during the phase of core compression. Moreover, they noted that the distance of the first cavitation plane from the fluid-structure interface can be approximated by

$$\overline{x}_c = \frac{x_c}{c_w \theta} \approx 4.8 \left( \frac{\sigma_c}{p_0} \right)^{1.1} \left( 0.24 - 0.015\psi + 0.0012\psi^2 \right) \tag{2.4}$$

for a limited range of parameters, $0 < \sigma_c / p_0 < 0.35$ and $0 < \psi < 8$ ($\sigma_c$ is the collapse strength of the foam core).

Although the FSI models outlined above [27-29] capture the early stages of the cavitation process with good accuracy, they do not take detailed account of the subsequent contraction of the cavitation zone driven by pressure waves travelling in the water layer trapped between the front face sheet and the cavitation boundary.

The importance of such FSI phenomena was recognised by McMeeking et al. [30] who investigated underwater blast loading of sandwich plates in more detail by explicitly modelling the motion of the cavitation boundaries. They assumed that the cavitation zone

reaches the fluid-structure interface and collapses subsequently by propagation of a reconstitution wave (equivalent to a closing front [3]) reflected from the wet face of the sandwich.

The analytical models outlined above have treated the cavitation process in a manner suitable for specific core topologies and can only be used for a limited range of problems. While such models capture the onset of cavitation with good accuracy, the subsequent response in which the cavitation zone collapses is only treated with crude approximations. In addition, none of the references quoted herein considered the effects of a non-negligible hydrostatic pressure in the water prior to the blast event which is vital for designing structural components against deep water blast. Moreover, most of the current design guidelines have been developed to aid the selection of blast resistant designs and materials for components in contact with water on one face only but cannot be used for water-backed FSI problems. More sophisticated analytical models are needed which are capable to predict the response of air-backed and water-backed structures subject to blast in deep or shallow water without the need of simplifying assumptions for the cavitation process. Such models will be developed in this thesis for the 1D response of both air-backed and water-backed rigid plates, supported by linear springs and loaded by underwater shock waves.

### 2.1.3 Underwater blast experiments

During the last decades large-scale explosive test facilities have been extensively used in the naval shipbuilding industry to guarantee that safety-critical components withstand extreme conditions such as intense dynamic loading by shock waves generated in an underwater blast event. Early experimental work on underwater blast loading was conducted during World War

II. A large part of this research was published in 1951 by the U.S. Office of Naval Research (ONR) [31].

Nowadays, the use of composite materials in naval constructions has become extremely widespread, because they offer benefits in terms of weight, magnetic signature and corrosion resistance. Since the 1980s several studies have focussed on exploring damage and failure of naval composite structures subject to underwater blast. Hall [32] investigated the underwater shock resistance of large-scale composite hulls by underwater detonation of an explosive charge in the proximity of the submerged test structure. Mouritz et al. [33] developed an explosive test rig able to generate intense blast waves a water-filled pit and used it to investigate damage and failure of both water-backed and air-backed hulls made from glass-fibre reinforced composites (GRP). Recently, Ramajeyathilagam & Vendhan [34] performed underwater explosion tests on air-backed rectangular steel plates by mounting the test structures on a sealed box fixture prior blast loading in a water-filled shock tank. Further details on the methodology of underwater explosion tests on plane plates are summarised in Rajendran et al. [35].

Large-scale tests provide important information on survivability, damage tolerance and failure modes exhibited by naval structures when loaded by underwater shock waves. On the other hand, they are time-consuming, cost-intensive and require adequate control and safety measures. Because of these issues, recent advances in experimental methods have focussed on simulating underwater blast loading in a laboratory environment. Deshpande et al. [36] developed an experimental apparatus able to generate realistic underwater blast waves in a water-filled steel shock tube by firing a steel projectile at a water piston, as illustrated in Fig. 2.4. They used this technique to examine the 1D response of monolithic plates and sandwich panels and found that the momentum transmitted to the structure in a blast event can be

considerably reduced by employing the sandwich construction, consistent with the conclusions of previous theoretical and numerical studies [27, 28].

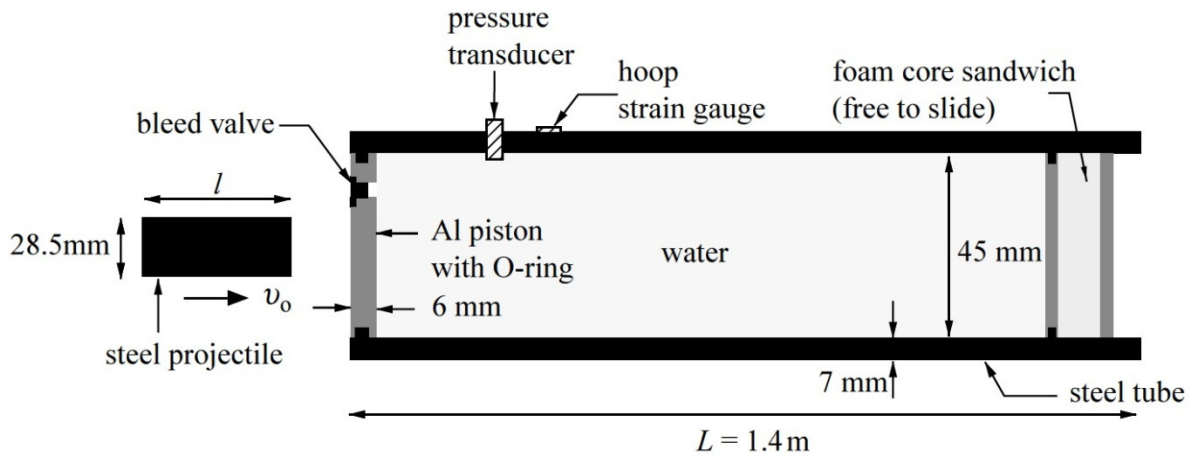



Fig. 2.4: Schematic of the water shock tube developed by Deshpande et al. [36].

This experimental method [36] was then employed by Kazemahvazi et al. [37] to investigate dynamic failure of clamped circular copper plates subject to underwater blast. Later, McShane et al. [38] used the same apparatus to probe the performance of free-standing sandwich plates with metallic lattice cores by measuring transmitted momentum and permanent core compression.

Espinosa et al. [39] followed a similar approach and designed a divergent shock tube to investigate dynamic deformation of circular clamped monolithic plates subject to underwater blast and used scaling rules to mimic the response of real-size naval constructions. Plate deformation histories were measured by observing shadow Moire fringes with a high-speed camera. Subsequently, Mori et al. [40, 41] and Latourte [42] employed the apparatus developed by Espinosa et al. [39] to characterise failure modes and damage mechanisms of monolithic plates and sandwich panels and provided experimental evidence for the benefits of sandwich construction in terms of blast resistance.

LeBlanc and Shukla [43] also used a water-filled shock tube to examine underwater blast loading of clamped GRP composite plates but with the blast wave generated by internal detonation of an explosive charge.

Wadley et al. [44] designed an underwater explosive test rig able to generate blast waves in a water-filled cardboard cylinder by detonation of an explosive sheet, as illustrated in Fig. 2.5.

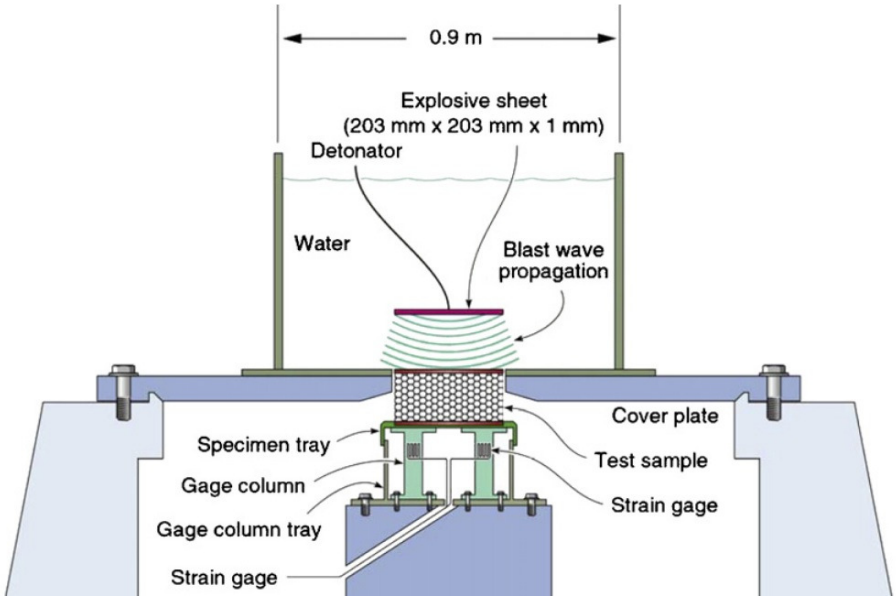



Fig. 2.5: Schematic of the test method developed by Wadley et al. [44] to investigate the blast performance of sandwich panels.

Although the test methods outlined above are capable of measuring the dynamic response of simple structural systems, they do not allow measuring the effects of increased initial hydrostatic pressure which is of great importance for the design of submarine applications resistant to blast loading in deep water. In addition, while cavitation was observed by several authors [45-47] for the purpose of examining the destructive action of collapsing cavitation bubbles on contiguous structural surfaces, none of the references quoted above report direct observation of propagating cavitation fronts consequent to blast loading of submerged structures. Although a vast range of components in marine applications are in contact with water on both sides during operation (e.g. fins, double hulls [48], etc.), only very little is

known about the shock response of water-backed structural systems. When water-backed structures are subjected to underwater explosions, the ensuing FSI phenomena can be deeply different and guidelines developed for air-backed components can no longer be used.

The work presented in this thesis will cover these gaps in the current literature. To achieve this, an experimental apparatus capable of reproducing underwater blast loading under increased hydrostatic fluid pressure will be developed. This apparatus will be used to observe the structural response as well as the evolution of cavitation phenomena in the water consequent to blast loading of both water-backed and air-backed structures. The results of these experiments will be presented in Chapters 4, 5, 6 and 8, together with predictions obtained from analytical models and detailed FE simulations.

## 2.2 Outline of the thesis

The literature review presented in the previous section provides a synopsis of the milestones within the current blast loading literature but also pinpoints shortcomings in the understanding of fundamental FSI phenomena. The aim of this work is to fill some gaps in the literature by undertaking a rigorous experimental, theroretical and numerical study of the main physical processes governing the response of structures subject to underwater blast. In particular, this thesis will address the following problems:

- In Chapter 3, 1D analytical models will be derived for the underwater blast response of a rigid spring-supported plate, in contact with water on one side (air-backed problem) or both sides (water-backed problem). The response will be characterised by defining different regimes of behaviour and the sensitivity of the applied impulse to structural mass and initial hydrostatic pressure will be examined.

- An experimental shock tube apparatus capable of simulating blast loading in initially pressurised water will be developed in Chapter 4, in order to probe the one-dimensional response of water-backed or air-backed monolithic plates to underwater blast. In the process, experimental evidence for the existence of propagating breaking fronts and closing fronts, as predicted by Kennard [3], will be provided via direct observation of the cavitation process.
- The developed experimental apparatus will then be used to investigate the 1D response of sandwich plates and double-walled structures to underwater blast. The results obtained from these experiments will be presented in Chapters 5 and 6, respectively, together with predictions obtained from corresponding FE simulations.
- Predictive analytical models for the dynamic deformation of circular elastic plates to underwater blast will be developed in Chapter 7. The accuracy of these models will be validated against 3D FE simulations and experimental results obtained from FSI experiments, which will be presented in detail in Chapter 8.

Finally, in Chapter 9, the major conclusions of this thesis will be summarised and directions for future studies will be given.

# Chapter 3

# The Response of Rigid Plates to Deep Water Blast: Analytical Models and Finite Element Predictions

## 3.1 Introduction

In this chapter the 1D response to blast loading of a rigid plate supported by a linear spring, in contact with a liquid on one or both sides is investigated. Analytical models will be constructed capable of capturing the cavitation process in the fluid and its effects on the plate's response; theoretical predictions will be compared with results of detailed FE simulations. The sensitivity of the imparted blast impulse to structural mass, spring stiffness and initial hydrostatic will be explored and non-dimensional performance charts will be constructed to aid structural design and material selection of components exposed to the threat of an explosion in water.

## 3.2 Analytical models

Underwater detonation of an explosive charge gives rise to propagation of spherical shock waves, travelling at the speed of sound in the medium, $c_w$. At sufficient distance from the point of detonation, these waves can be treated as 1D planar waves and their shape can be described by an exponentially decaying pressure versus time pulse, such that the pressure at an arbitrary point in the liquid (of coordinate $x$), and at an arbitrary time $t$ can be described by

$$p_{in}(x,t) = p_0 e^{-(t-x/c_w)/\theta} \tag{3.1}$$

for a wave travelling in the positive $x$-direction. The peak pressure $p_0$ and the decay time $\theta$ are set by the characteristics of the blast [1]. When the shock wave (3.1) reaches a fluid-structure interface located at $x=0$, the pressure field in the fluid is modified by wave reflection. In the case of a stationary interface, the wave gets fully reflected and the reflected wave, travelling in the negative $x$-direction, can be written as

$$p_{out}(x,t) = p_0 e^{-(t+x/c_w)/\theta} \tag{3.2}$$

The interface pressure is given by $p_{in}(0,t) + p_{out}(0,t)$ and results in an imparted impulse

$$I_0 = 2\int_0^\infty p_0 e^{-t/\theta} dt = 2p_0\theta \tag{3.3}$$

Assume that the structure consists of a rigid, unsupported plate. Impingement of the pressure wave (4.1) on its wet surface sets the plate in motion and compatibility dictates that the plate and the fluid at the interface possess the same velocity $v(t)$; plate motion results in a rarefaction wave of magnitude

$$p_{rare}(x,t) = -\rho_w c_w v(t + x/c_w) \tag{3.4}$$

emanating from the interface and travelling in the negative $x$-direction. The pressure field in the fluid is given by superposition as

$$p(x,t) = p_{st} + p_{in} + p_{out} + p_{rare} = p_{st} + p_0\, e^{-(t-x/c_w)/\theta} + p_0\, e^{-(t+x/c_w)/\theta} - \rho_w c_w v\left(t + x/c_w\right) \quad (3.5)$$

where $p_{st}$ represents the hydrostatic pressure in the fluid prior to the blast event.

The tensile rarefaction wave can cause the pressure to drop to the value of the cavitation pressure of the fluid $p_c$, at a location $x_c$ and time $t_c$. The value of the cavitation pressure $p_c$ is negligible in typical underwater blast events, compared to $p_0$, which is typically on the order of 100 MPa; we shall therefore assume in the following that $p_c = 0$, in line with the assumptions of previous studies in this field [24, 27-29]. Both the motion of the rigid plate and the pressure field in the fluid are significantly affected by the occurrence of cavitation, and eq. (3.5) needs to be modified. Accordingly, we define as 'Stage I' the response preceding the instant of first cavitation in the water, while we term as 'Stage II' the response subsequent to first cavitation.

### 3.2.1 Summary of the Taylor model for a free-standing monolithic plate

The 1D problem of an unsupported rigid plate loaded on one side by an exponentially decaying shock wave was solved by Taylor [4] for vanishing initial static pressure, $p_{st} = 0$. Here we briefly summarise this solution.

Consider a rigid plate of mass per unit area *m*, loaded by a shock wave as given by eq. (3.1); equilibrium dictates

$$m\ddot{u} = 2\, p_0\, e^{-(t/\theta)} - \rho_w c_w \dot{u} \quad (3.6)$$

where $u(t)$ denotes the displacement of the plate and dots denote differentiation with respect to time.

Equation (4.2) can be solved with initial conditions $u(0)=0$ and $v(0)=\dot{u}(0)=0$; this gives

$$v(t)=\frac{2p_0\theta}{m(\psi-1)}\left(e^{-t/\theta}-e^{-\psi t/\theta}\right) \tag{3.7}$$

where $\psi$ is a non-dimensional parameter defined as

$$\psi=\frac{\rho_w c_w \theta}{m} \tag{3.8}$$

which can be regarded as a non-dimensional measure of the inverse of the plate mass, for a given explosion. The interface pressure field in the fluid is obtained by substitution of eq. (3.7) into eq. (3.5) evaluated at $x=0$; this yields

$$p(0,t)=2p_0 e^{-t/\theta}-\frac{2p_0\psi}{\psi-1}\left(e^{-t/\theta}-e^{-\psi t/\theta}\right). \tag{3.9}$$

It was shown by Taylor that first cavitation for an unsupported, blast-loaded rigid plate always takes place at the fluid-structure interface at time

$$t_c=\frac{\ln(\psi)\theta}{\psi-1} \tag{3.10}$$

and a zone of cavitated water spreads from the interface into the fluid at $t>t_c$; loading of the structure ceases and the plate moves at constant velocity. The impulse transmitted to the plate is obtained by time integration of the interface pressure up to the cavitation time $t_c$

$$I_t=\int_0^{t_c}\left[2p_0 e^{-t/\theta}-\frac{2p_0\psi}{\psi-1}\left(e^{-t/\theta}-e^{-\psi t/\theta}\right)\right]dt=I_0\psi^{-\frac{\psi}{\psi-1}} \tag{3.11}$$

where $I_0=2p_0\theta$ is a reference impulse, corresponding to the impulse that would be imparted to a stationary plate by the incident wave (eq. (3.3)).

### 3.2.2 Stage I response for a spring-supported rigid plate

In this section we proceed to derive the governing equations for the two problems sketched in Fig. 3.1 and described below:

(i) *Problem 1:* A rigid plate of mass per unit area *m* is supported by a linear spring and is in contact with water at initial uniform pressure $p_{st}$. The plate is loaded by an exponentially decaying shock wave propagating in water towards the structure (Fig. 3.1 a).

(ii) *Problem 2.* A rigid plate of mass per unit area *m* is supported by a linear spring and is in contact with water at initial uniform pressure $p_0$ on both sides. The plate is loaded by an exponentially decaying shock wave on one side (Fig. 3.1 b).

In the following we will indicate the side of the rigid plate loaded by the incident wave as 'front face', while 'back face' will denote the opposite side.

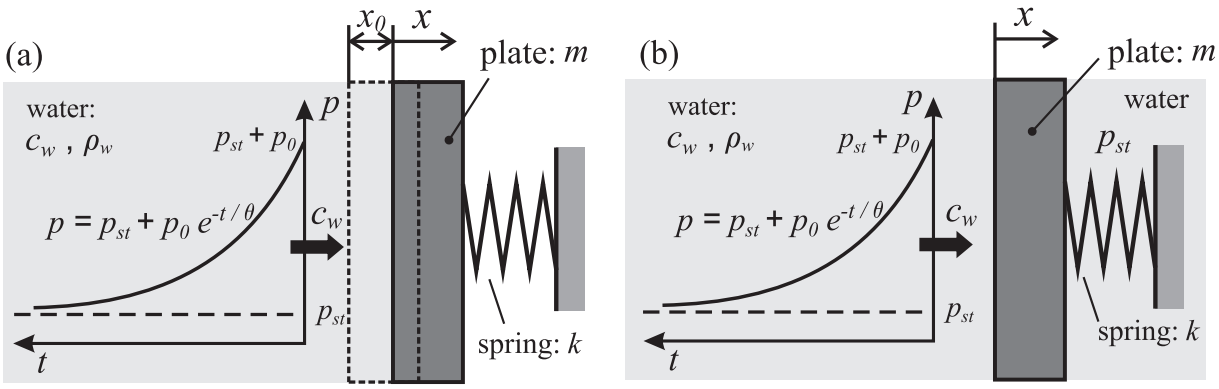



Fig. 3.1: Sketches of problem geometry, reference system, boundary conditions and loading case, for Problem 1 (a) and Problem 2 (b).

We define the parameters

$$\begin{aligned} &\bar{t} = t/\theta;\ \bar{x} = x/(c_w\theta);\ \bar{u}(\bar{t}) = u/(c_w\theta);\ \bar{v}(\bar{t}) = vm/I_0; \\ &\bar{p}(\bar{x},\bar{t}) = p/p_0;\ \bar{v}_w(\bar{x},\bar{t}) = v_w m/I_0;\ \bar{I}_t = I_t/I_0;\ \bar{p}_{st} = p_{st}/p_0 \end{aligned} \tag{3.12}$$

representing the non-dimensional time, position, plate displacement, plate velocity, pressure field, particle velocity field, transmitted impulse, initial pressure, respectively ($v_w(x,t)$ is the particle velocity field in the water). In the following we proceed to determine the non-dimensional particle velocity and pressure fields $\bar{v}_w(\bar{x},\bar{t})$ and $\bar{p}(\bar{x},\bar{t})$ for the two problems described above, prior to cavitation in the fluid.

**a) Problem 1: Stage I response**

Consider the problem of a rigid plate in contact with water on the front face, as sketched in Fig. 3.1 (a); let us assume that the plate is initially in equilibrium under the action of $p_{st}$ and of the spring reaction. In a coordinate system where $x=0$ corresponds to this initial equilibrium position (Fig. 3.1 a), the equation of motion for the rigid plate is given by

$$m\ddot{u} + ku = 2p_0\, e^{-(t/\theta)} - \rho_w c_w \dot{u} \tag{3.13}$$

where $k$ is the stiffness of the supporting spring, per unit area of the plate. The solution of eq. (3.13) is found by imposing the initial conditions $u(0)=0$ and $\dot{u}(0)=0$. In terms of the non-dimensional parameters (3.12), we find

$$\bar{u}(\bar{t}) = A\left[2\psi s\, e^{-\bar{t}} - e^{-0.5\psi\bar{t}(1+s)}(\psi s - \psi + 2) - e^{-0.5\psi\bar{t}(1-s)}(\psi s + \psi - 2)\right] \tag{3.14}$$

after defining the non-dimensional stiffness

$$\kappa = \frac{k\,m}{\rho_w^2\, c_w^2} \tag{3.15}$$

and the auxiliary quantities

$$A = \frac{p_0\theta}{c_w m\psi s\left(\kappa\psi^2 - \psi + 1\right)};\ \ s = \sqrt{1-4\kappa}. \tag{3.16}$$

The non-dimensional plate velocity follows as

$$\overline{v}\left(\overline{t}\right)=-B\left[4s\,e^{-\overline{t}}+e^{-0.5\psi\overline{t}(1+s)}\left(\psi-\psi s^2-2s-2\right)+e^{-0.5\psi\overline{t}(1-s)}\left(\psi s^2-\psi-2s+2\right)\right];$$
$$B=\frac{1}{4s\left(\kappa\psi^2-\psi+1\right)}. \tag{3.17}$$

The absolute fluid pressure field is calculated by substituting the expression for the plate velocity into eq. (3.5); in non-dimensional terms, we find

$$\overline{p}\left(\overline{x},\overline{t}\right)=\overline{p}_{st}+e^{-(\overline{t}-\overline{x})}+e^{-(\overline{t}+\overline{x})}+C\left[4s\,e^{-(\overline{t}+\overline{x})}+e^{-0.5\psi(\overline{t}+\overline{x})(1+s)}\left(\psi-\psi s^2-2s-2\right)+\right.$$
$$\left.+e^{-0.5\psi(\overline{t}+\overline{x})(1-s)}\left(\psi s^2-\psi-2s+2\right)\right] \tag{3.18}$$

with

$$C=\frac{\psi}{2s\left(\kappa\psi^2-\psi+1\right)}. \tag{3.19}$$

The non-dimensional velocity field in water $\overline{v}_w\left(\overline{x},\overline{t}\right)$ is obtained by superposition of the particle velocity fields associated with the incident, reflected and rarefaction waves

$$\overline{v}_w\left(\overline{x},\overline{t}\right)=\frac{1}{2\psi}\left[e^{-(\overline{t}-\overline{x})}-e^{-(\overline{t}+\overline{x})}\right]-B\left[4s\,e^{-(\overline{t}+\overline{x})}+e^{-0.5\psi(\overline{t}+\overline{x})(1+s)}\left(\psi-\psi s^2-2s-2\right)+\right.$$
$$\left.+e^{-0.5\psi(\overline{t}+\overline{x})(1-s)}\left(\psi s^2-\psi-2s+2\right)\right]. \tag{3.20}$$

Note that $v_w\left(0,\overline{t}\right)=v\left(\overline{t}\right)$, due to continuity at the fluid-structure interface.

### b) Problem 2: Stage I response

Now consider the problem sketched in Fig. 3.1 (b), where there is now liquid on both sides of the plate. Loading of the plate by the incident shock wave (4.1) sets the plate in motion and this results in radiation of a pressure wave at the plate's back face. The interface pressure at the back face (see Fig. 3.1 b) is given by

$$p'\left(t\right)=p_{st}+\rho_w c_w v\left(t\right) \tag{3.21}$$

The equation of motion of the plate can be written as

$$m\ddot{u}+ku=2p_0\,e^{-(t/\theta)}-2\rho_w c_w\dot{u} \tag{3.22}$$

and is solved with initial conditions $u(0)=0$ and $\dot{u}(0)=v(0)=0$. In non-dimensional form this gives

$$\bar{u}(\bar{t}) = D\left[2\psi r e^{-\bar{t}} - e^{-\psi\bar{t}(1+r)}(\psi r-\psi+1) - e^{-\psi\bar{t}(1-r)}(\psi r+\psi-1)\right] \tag{3.23}$$

where

$$D = \frac{p_0\theta}{c_w m\psi r\left(\kappa\psi^2-2\psi+1\right)};\ r=\sqrt{1-\kappa}. \tag{3.24}$$

The non-dimensional plate velocity $\bar{v}(\bar{t})$, pressure field $\bar{p}(\bar{x},\bar{t})$ and particle velocity field $\bar{v}_w(\bar{x},\bar{t})$ follow as

$$\bar{v}(\bar{t}) = -F\left[2re^{-\bar{t}} - e^{-\psi\bar{t}(1+r)}(\psi r-\psi+1)(r+1) + e^{-\psi\bar{t}(1-r)}(\psi r+\psi-1)(r-1)\right], \tag{3.25}$$

$$\begin{aligned}\bar{p}(\bar{x},\bar{t}) = \bar{p}_{st} + e^{-(\bar{t}-\bar{x})} + e^{-(\bar{t}+\bar{x})} + G\Big[2re^{-(\bar{t}+\bar{x})} - e^{-\psi(\bar{t}+\bar{x})(1+r)}(r+1)(\psi r-\psi+1) + \\ + e^{-\psi(\bar{t}+\bar{x})(1-r)}(r-1)(\psi r+\psi-1)\Big],\end{aligned} \tag{3.26}$$

$$\begin{aligned}\bar{v}_w(\bar{x},\bar{t}) = \frac{1}{2\psi}\left[e^{-(\bar{t}-\bar{x})} - e^{-(\bar{t}+\bar{x})}\right] - F\Big[2re^{-(\bar{t}+\bar{x})} - e^{-\psi(\bar{t}+\bar{x})(1+r)}(r+1)(\psi r-\psi+1) + \\ + e^{-\psi(\bar{t}+\bar{x})(1-r)}(r-1)(\psi r+\psi-1)\Big]\end{aligned} \tag{3.27}$$

after defining the auxiliary parameters

$$F = \frac{1}{2s\left(\kappa\psi^2-2\psi+1\right)};\ G = \frac{\psi}{s\left(\kappa\psi^2-2\psi+1\right)}. \tag{3.28}$$

### 3.2.3 Stage II response: effects of cavitation

In this section we derive the Stage II response for a spring-supported rigid plate, accounting for the effects of water cavitation, for both Problem 1 and Problem 2. The analysis is performed with the assumption that the water response can be described by a linear elastic, reversible pressure versus volumetric strain constitutive relation for $p>0$. In contrast, we assume that for $p<0$ the fluid is unable to sustain any pressure; this yields

$$p = \begin{cases} -K_w \varepsilon_V = -c_w{}^2 \rho_w \varepsilon_V & \text{for } p > 0 \\ 0 & \text{for } p \le 0 \end{cases} \tag{3.29}$$

where $K_w$ denotes the bulk modulus of water.

The pressure field in the water attached to the plate's front face is given in Stage I by eqs. (3.18) and (3.26) as a function of time and distance from the fluid-structure interface, for problems 1 and 2, respectively. The presence, in both these expressions, of a negative pressure term associated with the rarefaction wave can cause the pressure to drop to zero, at time $t_c$, at a general position $x_c$ ($x_c = 0$ for the 'Taylor' problem described in Section 3.2.1). The general sequence of events following cavitation, at time $t_c$, has been outlined by several authors [3, 30] and is illustrated in Fig. 3.2 (a):

- water cavitates at time $t_c$ and at a position $x_c$ ($x_c \le 0$ for the choice of coordinate system in Fig. 3.2 a);
- two breaking fronts emanate from the point of first cavitation $x_c$ and travel in the positive and negative *x*-directions; 'breaking fronts' are defined as interfaces separating regions of cavitated and uncavitated water. The directions in which these fronts propagate is such to leave cavitated water behind them. It was shown by Kennard [3] that the velocity of propagation of a breaking front is always greater than the speed of sound in the fluid.
- depending upon the pressure and particle velocity in the fluid immediately ahead and behind the breaking fronts, these fronts can arrest and remain stationary or invert their direction of motion; in the latter case, we will denote them as 'closing fronts'. Kennard [3] has shown that closing fronts always move at subsonic speeds.

For the two problems described in Section 3.2.2, two breaking fronts originate at time $t_c$ at a position $x_c$ and travel into opposite directions (see Fig. 3.2 a). It will be shown below that the

breaking front travelling towards the blast event (in the negative $x$-direction) will never arrest. In contrast, the breaking front travelling towards the plate's front face can either arrest before the fluid-structure interface (at a position $x_{rest}$ and time $t_{rest}$) and invert its direction of motion, becoming a closing front, or reach the fluid-structure interface. In this last case, the breaking front can either arrest at the interface or be reflected as a closing front.

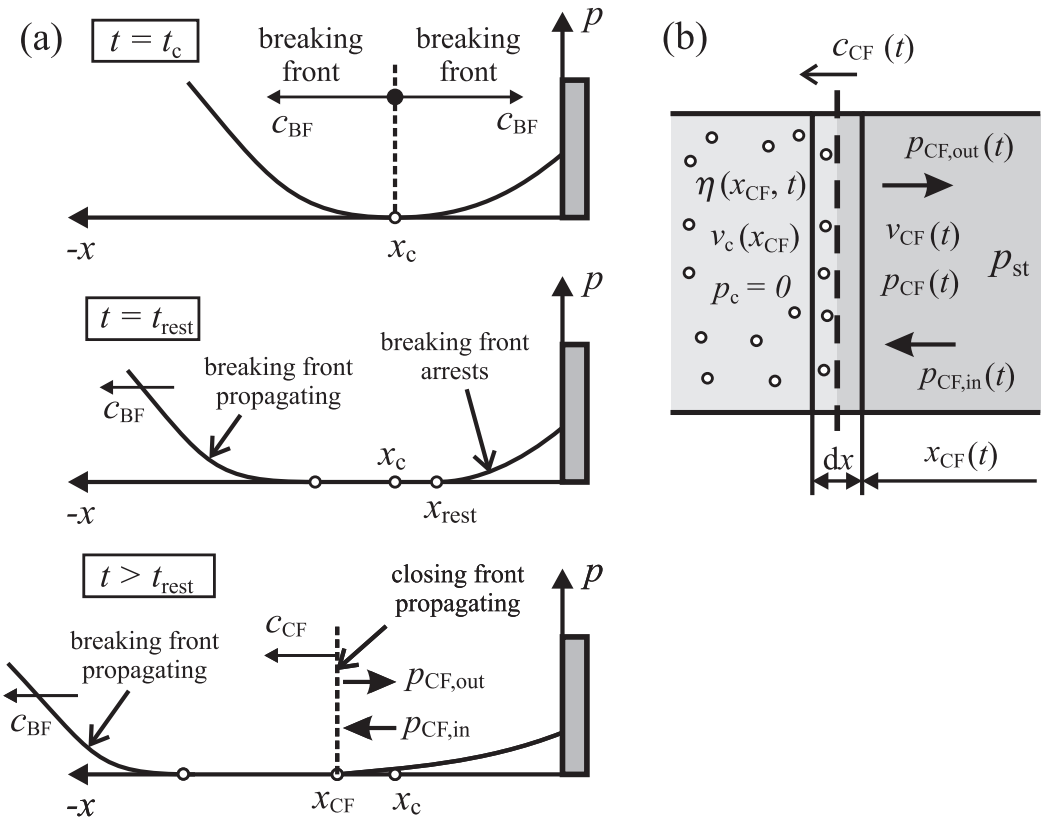



Fig. 3.2: (a) Schematic illustration of the phenomena of initial cavitation, emergence and propagation of BFs, development of a CF. (b) Detail of the fluid conditions at a propagating CF.

The analysis below will make use of the findings of Kennard [3], who provided criteria for the propagation (and arrest) of breaking fronts and closing fronts in terms of the pressure and velocity fields in the cavitated and uncavitated fluid adjacent to such fronts. We shall treat both breaking and closing fronts as reflective interfaces, with the objective of determining the

pressure and velocity field in the fluid adjacent to the plate's front face, thereby determining interface pressure, plate velocity and transmitted impulse during Stage II.

**a) Solution scheme and governing equations**

We proceed to describe the calculation steps required to determine the Stage II response for problems 1 and 2.

*(i) Calculation of location and time of first cavitation*

In order to determine the location and time of first cavitation, the pressure fields (3.18) or (3.26) (for problems 1 or 2, respectively) are set to zero, giving an implicit relation between position and time

$$p(x,t)=0 \tag{3.30}$$

or $\bar{p}(\bar{x},\bar{t})=0$, in non-dimensional form. Equation (3.30) has infinite solution pairs $(x,t)$, describing a curve in $x-t$ space. The point where this curve attains the minimum value of $t$ gives the position and time at first cavitation $(x_c,t_c)$, which can be extracted via a numerical algorithm. In the particular case of an unsupported plate ('Taylor' model) it is found that $x_c=0$ and $t_c$ is given by (3.10).

*(ii) Propagation and arrest of the breaking front*

The conditions for propagation of a breaking front in the water subsequent to the onset of cavitation are given by Kennard [3] as

$$
\begin{aligned}
&p\big|_{x=x_{BF}} = 0 \;;\quad \left.\frac{\partial v_w}{\partial x}\right|_{x=x_{BF}} > 0 \;;\quad \left|\left.\frac{\partial p}{\partial x}\right|_{x=x_{BF}}\right| < \rho_w c_w \left.\frac{\partial v_w}{\partial x}\right|_{x=x_{BF}} \;; \\
&\left.\frac{\partial p}{\partial x}\right|_{x=x_{BF}} \geq 0 \;\left(\text{propagation in the } +x \text{ direction}\right) \;\text{ OR} \\
&\left.\frac{\partial p}{\partial x}\right|_{x=x_{BF}} \leq 0 \;\left(\text{propagation in the } -x \text{ direction}\right)
\end{aligned}
\tag{3.31}
$$

where $x_{BF}$ denotes the current position of the breaking front and velocity gradients $\partial v_w / \partial x$ are evaluated in the uncavitated region ahead of the breaking front. For the problems under investigation, these conditions are always met at any time $t \geq t_c$, for the breaking front travelling in the negative *x*-direction, i.e. away from the fluid-structure interface. This front will therefore propagate indefinitely in the negative *x*-direction at a velocity in excess of the speed of sound in water, and will never affect motion of the plate. In contrast, for a breaking front travelling in the positive *x*-direction, the conditions (3.31) are met at $t = t_c$ but may not hold indefinitely. Consequently, propagation of this front may terminate after some time $t_{rest} > t_c$ at a position $x_{rest}$.

In order to evaluate $x_{rest}$ and $t_{rest}$, we observe that the breaking front travelling in the positive *x*-direction moves supersonically. Therefore, the pressure and velocity fields ahead of this breaking front are not affected by its propagation and can be computed from the expressions found for the Stage I response of the plate (see Section 3.2.2). Note that for both problems 1 and 2, the Stage I expressions for the plate velocity $v(t)$ are valid for $t \leq t_{rest} - x_{rest} / c_w$; in contrast, Stage I pressure and particle velocity fields are only valid for $t \leq t_c$.

The current position of the breaking front $x_{bf}$ and the arrest point $x_{rest}$ are found by evaluating numerically the conditions (3.31) along the curve (3.30). A time increment $\Delta t$ is chosen (typically around $10^{-8}$ s) and the time $t > t_c$ is discretised. At discrete points in time

$t_{bf,i} = t_c + i\,\Delta t \ \ (i = 0,1..)$, eq. (3.30) is employed to evaluate the corresponding position of the breaking front, $x_{bf,i}$. At each pair $\left(x_{bf,i}, t_{bf,i}\right)$ the conditions (3.31) are evaluated; $x_{rest}$ and $t_{rest}$ represent the first point on the curve (3.30) at which at least one of the conditions (3.31) fails. The trajectory of the breaking front moving in the positive *x*-direction is defined by the pairs $\left(x_{bf,i}, t_{bf,i}\right)$, with $t_{bf,i} < t_{rest}$; this trajectory represents a portion of the implicit curve given in eq. (3.30).

*(iii) Propagation of a closing front*

Once the breaking front travelling in the positive *x*-direction has arrested, a closing front can emerge and propagate in the opposite direction. The analysis of this phenomenon is facilitated if the pressure field in the uncavitated water in contact with the plate's front face is written as superposition of wave trains approaching the cavitated region (denoted by $p_{CF,in}$) and travelling away from the boundary with the cavitated region (denoted by $p_{CF,out}$), as sketched in Fig. 3.2 (b). It follows that pressure and particle velocity at the cavitation boundary, evaluated in the uncavitated fluid, $p_{CF}$ and $v_{CF} = v_w\left(x_{CF}, t\right)$, are given by

$$\begin{aligned} p_{CF} &= p_{CF,in} + p_{CF,out} + p_{st} = \rho_w c_w v_{CF,in} - \rho_w c_w v_{CF,out} + p_{st} \ , \\ v_{CF} &= v_{CF,in} + v_{CF,out} = \frac{p_{CF,in} - p_{CF,out}}{\rho_w c_w} \end{aligned} \tag{3.32}$$

where $v_{CF,in}$ and $v_{CF,out}$ are particle velocities associated with the wave trains $p_{CF,in}$ and $p_{CF,out}$, respectively.

The conditions for propagation of a closing front are given by Kennard [3] as

$$2p_{CF,in} > \rho_w c_w v_c \ ; \quad \eta(x,t) = \int_{t_{bf}(x)}^{t} \frac{\partial v_c}{\partial x}\, d\tau > 0 \tag{3.33}$$

where $v_c$ represents the particle velocity of the cavitated water, evaluated at a position just ahead of the closing front. Since both the pressure and the pressure gradient within the cavitation zone vanish, the velocity profile $v_c = v_c(x)$ in the cavitated water remains independent of time, as long as the cavitation conditions persist. The velocity profile $v_c(x)$ is obtained by evaluating numerically the particle velocity $v_w(x,t)$ in the uncavitated water immediately before arrival of the breaking front, namely

$$v_c\left(x_{bf,i}\right) = v_w\left(x_{bf,i}, t_{bf,i}\right). \tag{3.34}$$

The quantity $\eta(x,t)$ defined in eq. (3.33) represents a measure of the strain in the cavitated water. The integral in eq. (3.33) is computed by integrating numerically in time the velocity gradient in the cavitated water $\partial v_c / \partial x$, from time $t_{bf}(x)$ to the current time $t$; $t_{bf}(x)$ denotes the time at which the breaking front reaches particles at a general position $x$. Note that the pairs $\left(x_{bf,i}, t_{bf,i}\right)$ and the function $t_{b,i}\left(x_{b,i}\right)$ are known from the analysis of propagation of the breaking front described above.

Analysis of the propagation of a closing front in previously cavitated water has been performed by Kennard and it is used here to determine the trajectory of the closing front and the pressure and velocity behind this front. With reference to Fig. 3.2 (b), consider motion of a closing front through a layer of cavitated water d$x$; momentum conservation provides

$$p_{CF} = (1-\eta)\rho_w c_{CF}\left(v_{CF} - v_c\right) \tag{3.35}$$

where $c_{CF} = \mathrm{d}x_{CF}/\mathrm{d}t$ denotes the velocity of the closing front and $x_{CF}(t)$ is its current position. Note that the coordinate system for the closing front analysis (see Fig. 3.2 b) is chosen such that the positive $x$-direction is taken towards the cavitated region. It has been shown that a closing front always propagates with velocity less than the speed of sound [3].

Consequently, the pressure and velocity fields in the uncavitated water between the closing front and the fluid-structure interface are affected by the motion of the closing front. A change of thickness occurs within the layer d$x$ due to passage of the closing front; continuity gives

$$\rho_w c_w^2 \left(v_{CF} - v_c\right) = \left[\rho_w c_w^2 \eta + p_{CF}\left(1-\eta\right)\right] c_{CF}. \tag{3.36}$$

Equations (3.32), (3.35) and (3.36) can be re-written as

$$\begin{aligned} &c_{CF} = \frac{c_w \lambda}{\lambda + \left(c_w - \lambda\right)\eta}, \quad p_{CF} = \frac{\left(1-\eta\right)\rho_w c_w \lambda^2}{2\lambda + \left(c_w - 2\lambda\right)\eta}, \\ &v_{CF} - v_c = \lambda \frac{\lambda + \left(c_w - \lambda\right)\eta}{2\lambda + \left(c_w - 2\lambda\right)\eta}, \; p_{CF,out} = p_{CF} - p_{CF,in} - p_{st}, \end{aligned} \tag{3.37}$$

with the auxiliary quantity $\lambda$ given by $\lambda = \left(2p_{CF,in} + p_{st}\right)/\left(\rho_w c_w\right) - v_c$ .

The sequence of events associated with propagation and arrest of a breaking front and subsequent propagation of a closing front is described below:

$t = t_{rest}$: The closing front pressure $p_{CF}$ is given by the Stage I expressions. The incoming and outgoing pressure wave trains $p_{CF,in}$ and $p_{CF,out}$ can be written as

$$\begin{aligned} p_{CF,in} &= p_{I,out} = p_0 e^{-\left(t + x/c_w\right)/\theta} - \rho_w c_w v\left(t + x/c_w\right), \\ p_{CF,out} &= p_{I.in} = p_0 e^{-\left(t - x/c_w\right)/\theta} \end{aligned} \tag{3.38}$$

where $p_{I,out}$ and $p_{I,in}$ are the Stage I pressure wave trains travelling away from and towards the fluid-structure interface, respectively. $p_{I,out}$ comprises the reflected and rarefaction waves, while $p_{I,in}$ represents the incident pressure wave. The conditions (3.33) are satisfied at this instant and therefore a closing front will start propagating.

$t_{rest} < t < t_{rest} - x_{rest}/c_w$: In this phase of the response the incoming wave train $p_{CF,in}$ is still given by eq. (3.38). In contrast, the wave train $p_{CF,out}$ is radiated from the closing front and

travels towards the structural interface without reaching this interface. The time $t > t_{rest}$ is discretised and at $t_{cf,j} = t_{rest} + j\,\Delta t \;\; (j = 0,1..)$, the quantities $p_{CF,in}$ (eq. (3.38)), $\eta\left(x_{CF}, t_{cf,j}\right)$ and $v_c\left(x_{CF}\right)$ are evaluated, conditions (3.33) are checked, and eqs. (3.37) are solved for $p_{CF,out}$ and $c_{CF}$. The current position of the closing front $x_{CF}$ is updated, and the values of $p_{CF,out}\left(t_{cf,j}\right)$ are used to generate a wave train $p_{II,in}$ that will impinge on the plate at time $t_{cf,j} - x_{CF}\left(t_{cf,j}\right)/c_w$.

$t = t_{rest} - x_{rest}/c_w$: At this instant the wave train $p_{CF,out}$ (calculated by eq. (3.37)) emanating from the closing front reaches the plate, invalidating the Stage I expressions for the plate velocity.

$t > t_{rest} - x_{rest}/c_w$: In this phase of the response, the wave train $p_{CF,out}$ emitted by the moving closing front interacts with the fluid-structure interface. $p_{CF,in}$ is still given by eq. (3.38) and the analysis of the closing front propagation is similar to that outlined above for $t_{rest} < t < t_{rest} - x_{rest}/c_w$. In order to compute the wave train $p_{II,out}$ created by the fluid-structure interface and the Stage II plate velocity expression, the equation of motion of the plate is solved by numerical time integration; the current acceleration for Problem 1 and Problem 2 is calculated as

$$\ddot{u}\left(t_{cf,j}\right) = \left[2p_{II,in} - \rho_w c_w \dot{u}\left(t_{cf,j}\right) - k\,u\left(t_{cf,j}\right)\right]/m \tag{3.39}$$

and

$$\ddot{u}\left(t_{cf,j}\right) = \left[2p_{II,in} - 2\rho_w c_w \dot{u}\left(t_{cf,j}\right) - k\,u\left(t_{cf,j}\right)\right]/m \tag{3.40}$$

respectively, where $p_{II,in}$ coincides with the wave train $p_{CF,out}$ emanating from the closing front. The current acceleration is used to update the plate velocity, namely $\dot{u}\left(t_{cf,j+1}\right) = \Delta t\, \ddot{u}\left(t_{cf,j}\right)$.

$t >> t_{rest} - x_{rest} / c_w$: Due to the fact that the closing front velocity is subsonic [3], the pressure wave train $p_{II,out}$ (moving at the speed of sound $c_w$) will reach the closing front as time elapses. In general, this will result in an interaction of $p_{II,out}$ with the closing front and originate a wave train $p_{CF,out}$ travelling towards (and finally impinging on) the fluid-structure interface. This phenomenon is modelled by the same technique described above.

We note in passing that the problem of a non-negligible cavitation pressure, $p_c \neq 0$, can be dealt with by the present analysis by simply considering a fictitious initial static pressure

$$p'_{st} = p_{st} - p_c . \tag{3.41}$$

**b) Regimes of behaviour**

(i) *Problem 1*:

In this section we proceed to analyse the structural response for Problem 1 described above. We begin by noting that the phenomenon of cavitation may not necessarily occur for this problem. If the water is initially at a sufficiently high static pressure $p_{st}$, or if the mass of the plate and/or the stiffness of the supporting spring attain sufficiently high values, the absolute pressure in the fluid may not reach zero during the blast loading event. The presence of cavitation affects the plate response and therefore both Stage I and Stage II analyses presented

above need to be performed in this case. In contrast, in the absence of cavitation the Stage I analysis is sufficient to predict the plate response.

Three regimes of behaviour can be identified: we refer to *regime 1* in the absence of cavitation. If, in contrast, cavitation occurs, two scenarios are possible: the breaking front travelling towards the structure arrests at $x_{rest} < 0$, without reaching the fluid-structure interface (*regime 2*) or it reaches the fluid-structure interface (*regime 3*).

The regime charts in Fig. 3.3 can be used to determine the active regime of behaviour for a given set of non-dimensional parameters $\psi$, $\kappa$ and $\overline{p}_{st}$. The curves in Fig. 3.3 (a) denote the transitions between different regimes for the case of zero static pressure ($\overline{p}_{st} = 0$) while Fig. 3.3 (b) illustrates the regime transitions for $\overline{p}_{st} = 0.6$. We note that an increase in $\overline{p}_{st}$ causes *regime 1* to dominate; *regime 3* response is active (for $\overline{p}_{st} = 0.6$) only at very large values of $\psi$ (this is not shown in Fig. 3.3 b). It can be shown numerically that if $\overline{p}_{st}$ exceeds 0.82, cavitation is prevented for any choice of $\psi$ and $\kappa$.

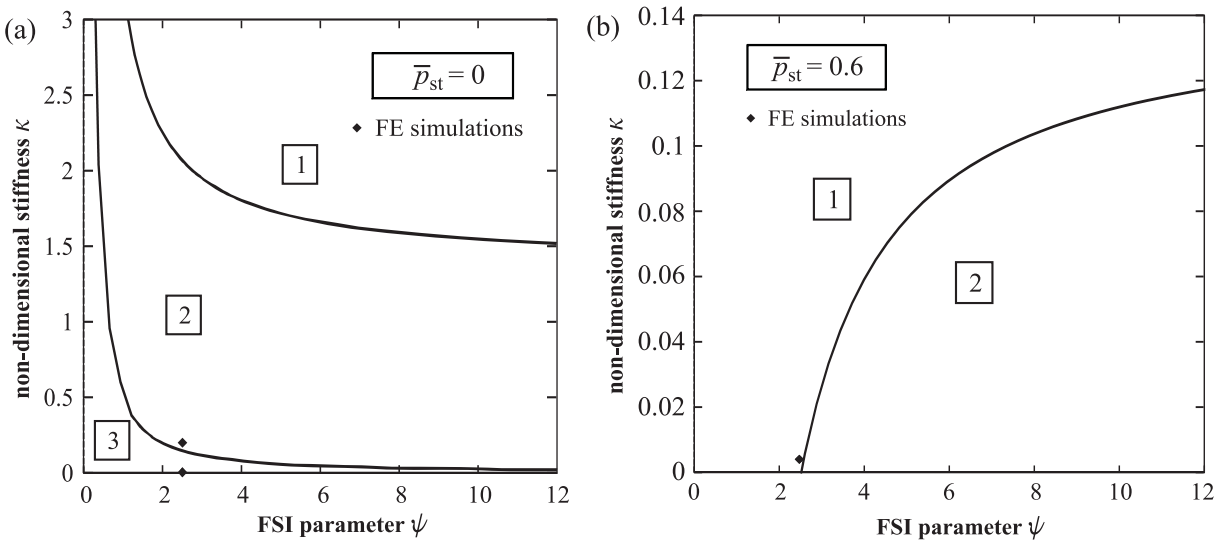



Fig. 3.3: Non-dimensional regime charts for Problem 1. The curves show the transitions between different regimes for two different values of non-dimensional static pressure: (a) $\overline{p}_{st} = 0$ and (b) $\overline{p}_{st} = 0.6$.

(ii) *Problem 2*:

We now analyse the structural response for Problem 2. As described above, in this problem a plate is in contact with water on both sides and is supported by a linear spring. Loading by the incident wave results in plate motion, which generates a pressure wave propagating in the fluid in contact with the plate's back face (eq. (3.21)). Initially, the motion of the plate in the positive *x*-direction results in an over-pressure in the fluid adjacent to the back face, of amount $\rho_w c_w v(t)$. The presence of the supporting spring can result in the plate inverting its motion, and the absolute back interface pressure $p_{st} + \rho_w c_w v(t)$ vanishing, giving rise to cavitation.

It can be shown that cavitation in the fluid at the back of the plate always occurs at the plate interface, at time $t_c'$ ($\overline{t}_c' = t_c'/\theta$ in non-dimensional terms). Subsequently, a breaking front emerges from the plate's back face and propagates in the positive *x*-direction. In principle, the cavitated region at the back interface may collapse if the plate inverts again its direction of motion and moves in the positive *x*-direction at sufficiently high velocity. This is accounted for in the models presented herein; however, for typical values of $\psi$, $\kappa$ and $\overline{p}_{st}$, collapse of the cavitation zone at the back interface occurs after a relatively long time ($\overline{t} > 10$) and has only a minor effect on the plate's response. Similar to Problem 1, we note that cavitation on either side of the plate may be prevented for Problem 2 if the water is initially at a sufficiently high static pressure $p_{st}$.

Different regimes of behaviour can be identified for Problem 2, as described below:

- *regime 1*, $\bar{p}_{st} \geq \bar{p}_{st,c}$: no cavitation occurs in the fluid on either side of the plate, if the initially applied static pressure exceeds a critical value $\bar{p}_{st,c}$, which is a function of $\psi$ and $\kappa$.
- *regime 2*, $t_c' \leq t_c$: cavitation at the back face occurs before cavitation in the fluid in front of the plate.
- *regime 3*, $t_c < t_c' < \left(t_{rest} - x_{rest} / c_w\right)$: cavitation occurs at the back face after it has originated in the fluid in front of the plate but before the Stage II response of the plate has begun.
- *regime 4*, $t_c' \geq \left(t_c - x_c / c_w\right)$: cavitation at the back face occurs after the beginning of the Stage II response of the plate.

The charts in Fig. 3.4 can be used to determine the active regime of behaviour for a given set of non-dimensional parameters $\psi$, $\kappa$ and $\bar{p}_{st}$. The curves in Fig. 3.4 (a) denote the transitions between regimes for the case of zero static pressure ($\bar{p}_{st} = 0$) while Fig. 3.4 (b) illustrates the regime transitions for $\bar{p}_{st} = 0.07$. Upon increasing the static pressure, *regime 1* occupies a larger region in the regime chart. The critical static pressure to suppress cavitation $\bar{p}_{st,c}$ is in general a function of $\psi$ and $\kappa$. However, it can be shown numerically that when $\bar{p}_{st} \to 0.14$, *regime 1* becomes the active regime for all values of $\psi$ and $\kappa$.

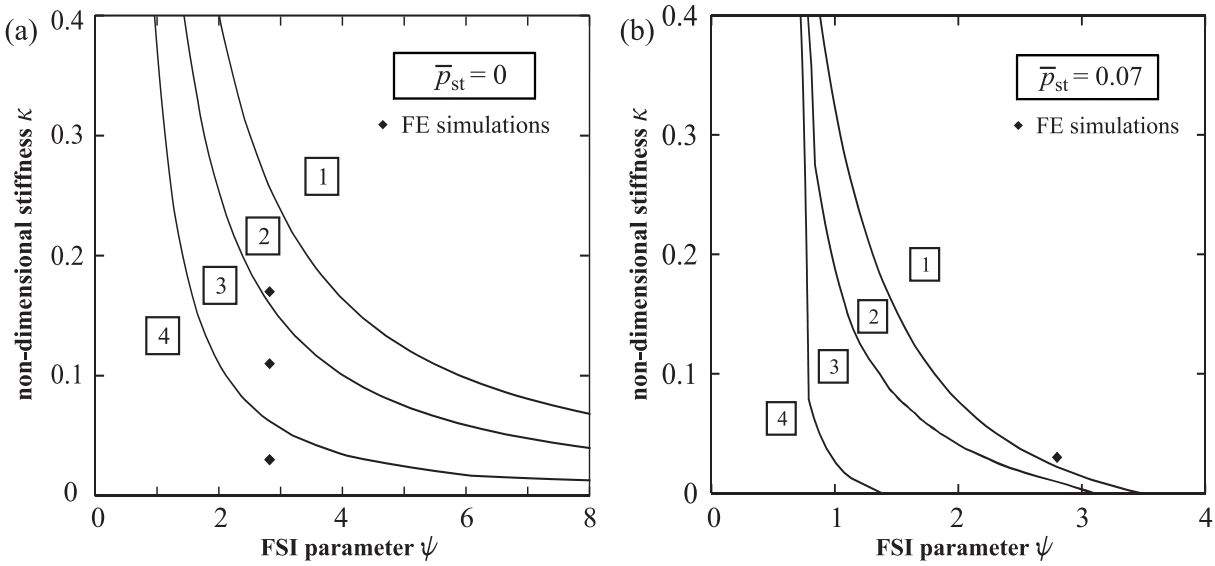



Fig. 3.4: Non-dimensional regime charts for Problem 2. The curves show the transitions between different regimes for two different values of non-dimensional static pressure: (a) $\overline{p}_{st} = 0$ and (b) $\overline{p}_{st} = 0.07$.

## 3.3 Finite Element Calculations

One-dimensional, dynamic FE simulations were performed in ABAQUS/Explicit [49] in order to validate the analytical models described in Section 3.2. The problem geometry is sketched in Fig. 3.5 for the case of Problem 2: the structure is modelled as a rigid plate supported by a linear spring (Type 'SpringA' in ABAQUS) of constant stiffness *k*. The plate, of unit area, is tied to two columns of water (of unit width) at the front and back face. For Problem 1, the plate is tied to a water column only at the front face.

For the constitutive response of water, a linear relation between the fluid pressure and the volumetric strain was employed, in accordance to eq. (3.29), with vanishing shear modulus. Such relationship was modelled in ABAQUS by using a Mie-Gruneisen equation of state with a linear Hugoniot relation [49] which can be written as

$$p = \frac{\rho_0 c_0^2 \varepsilon_V}{(1 - s\varepsilon_V)}\left(1 - \frac{\Gamma_0 \varepsilon_V}{2}\right) + \Gamma_0 \rho_0 E_m \tag{3.42}$$

where $\Gamma_0$ is a material constant, $E_m$ denotes the internal energy per unit mass, $s$ defines the linear Hugoniot relation between shock velocity $v_s$ and particle velocity $v_w$, $v_s = c_0 + s v_w$, and $\rho_0 c_0^2$ represents the bulk viscosity at small nominal strains, $K_0$. To implement the desired constitutive relation (eq. (3.29)) in the FE model, the parameters $E_m$, $\Gamma_0$ and $s$ were set to zero while density and wave speed were taken as $\rho_0 = \rho_w = 1000\,\text{kgm}^{-3}$ and $c_0 = c_w = 1498\,\text{ms}^{-1}$, respectively, giving a bulk modulus of $K_0 = K_w = 2.244\,\text{GPa}$. Note that the choice $s = 0$ corresponds to the case where $v_s = c_w$ (see equation above). Neglecting the vapour pressure of water ( $p_v = 2.3\,\text{kPa}$ at 20°C), cavitation was modelled by introducing a pressure cut-off at a tensile failure of zero, $p_c = 0$, according to eq. (3.29).

As suggested by other authors [29], the presence of a default artificial bulk viscosity in ABAQUS/Explicit can lead to significant artificial energy dissipation. Preliminary simulations were conducted to examine the sensitivity of the predicted pressure fields to the bulk viscosity coefficients and it was concluded that coefficients equal to 20% of the default values were sufficiently low not to affect the predictions and sufficiently high to eliminate numerical pressure ringing effects.

The transverse displacement of the rigid plate and of the fluid elements was constrained, as indicated in Fig. 3.5. An initial hydrostatic stress field of $\sigma_H = -p_{st}$ was imposed on all fluid elements. For Problem 2, an equal amount of pressure was applied at the ends of fluid columns not in contact with the plate (see Fig. 3.5). For the case of Problem 1, with the plate in contact with a single water column, a traction $-p_{st}$ was applied at the free end of the front water column and at the back face of the plate in order to guarantee equilibrium of the fluid-structure system prior to loading by the blast wave. In order to simulate loading by the incoming shock wave, a pressure boundary condition was imposed at the free end of the front

fluid column. This wave had an exponentially decaying shape with peak pressure $p_0$ and decay constant $\theta$. The water columns were chosen to be sufficiently long to avoid pressure waves reflected at the free ends reaching the structure before the end of the fluid-structure interaction phase.

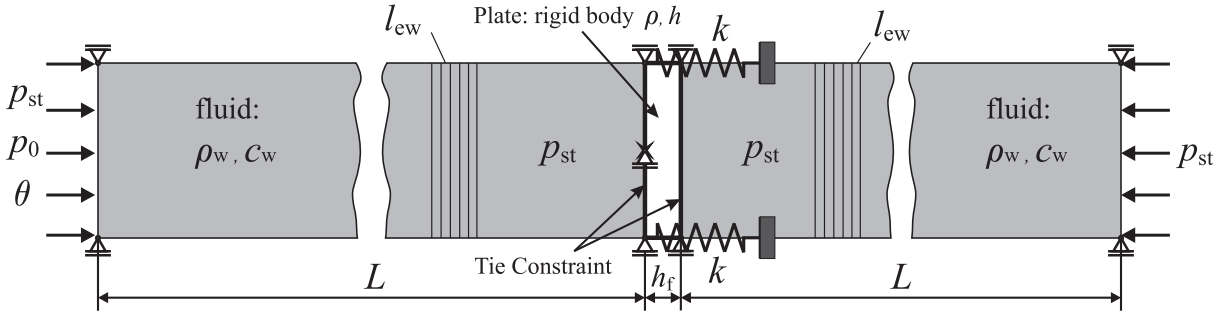



Fig. 3.5: Schematic of the Abaqus/Explicit FE model used to investigate the 1D water-backed plate response (Problem 2). FE simulations for Problem 1 follow a similar scheme, with the fluid column attached to the plate's back face absent.

Four-noded, plane quadrilateral elements with reduced integration (type CPE4R in ABAQUS) were used to discretise the water. In order to adequately capture the discontinous change in pressure at the shock front of the incident wave, the element size $l_{ew}$ needs to be chosen sufficiently small. To aid the choice of an appropriate mesh size, FE simulations were performed with different values of $l_{ew}$ (0.1 mm / 0.2 mm / 0.5 mm / 1 mm / 2 mm / 4 mm) using the model illustrated in Fig. 3.5, measuring for each discretisation rise time $t_r^{FE}$ and peak pressure $p_0^{FE}$ of the incident schock wave (at a distance of 5 mm from the fluid-structure interface before the impact). Results obtained from these measurements are shown in Fig. 3.6 as functions of the mesh size. It can be seen that the normalised rise time $\overline{t}_r^{FE} = t_r^{FE} / \theta$ approaches zero when $l_{ew} \to 0$, see Fig. 3.6 (a), while the normalised peak pressure $\overline{p}_0^{FE} = p_0^{FE} / p_0$ converges to unity for $l_{ew} \to 0$, see Fig. 3.6 (b). A mesh size $l_{ew} = 0.1\,\text{mm}$

appears to capture the shock front with good accuracy, and therefore, the size of the fluid elements was set to 0.1 mm in the direction of wave propagation, while one single element was chosen to discretise the fluid column along the width.

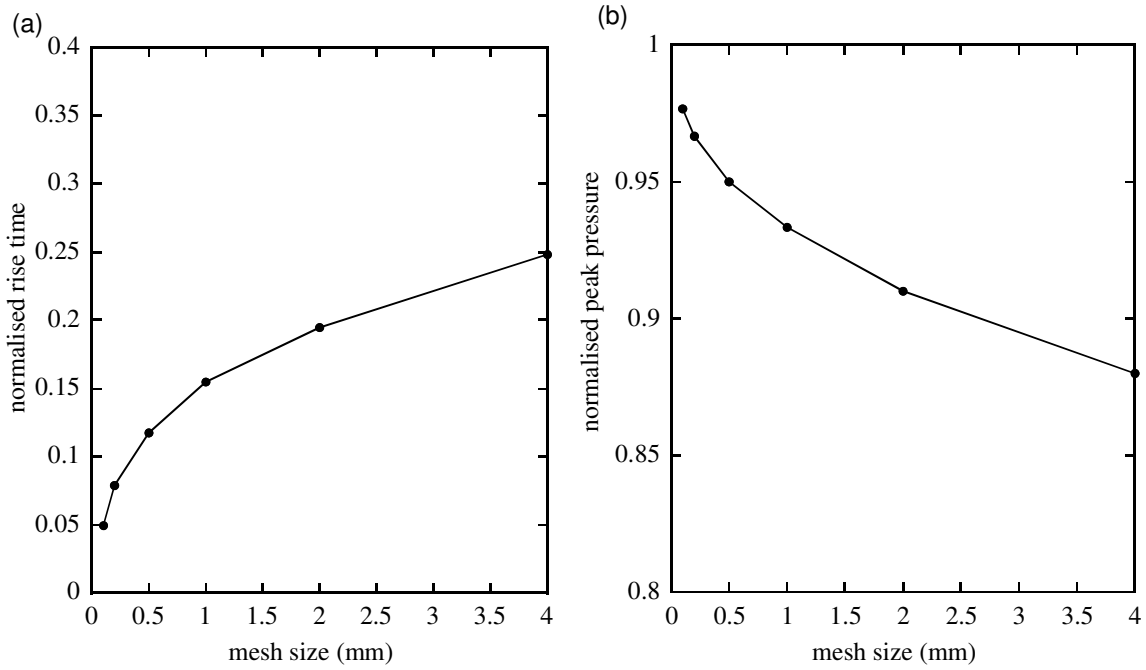



Fig. 3.6: Normalised rise time $\overline{t}_r^{FE} = t_r^{FE} / \theta$ (a) and peak pressure $\overline{p}_0^{FE} = p_0^{FE} / p_0$ (b) of the incident shock wave as functions of the mesh size used in the FE calculations.

## 3.4 Comparison of analytical and FE predictions

In this section we compare analytical and FE predictions for interface pressure and plate velocity histories, as well as for the motion of breaking and closing fronts, in order to assess the accuracy of the analytical models. We shall examine both problems 1 and 2, and explore all the regimes of behaviour identified above.

### 3.4.1 Problem 1: closing front and breaking front propagation

Analytical and FE predictions of the non-dimensional position and time of first cavitation, as well as of the motion of breaking fronts (BFs) and closing fronts (CFs) following first cavitation are presented in Fig. 3.7 for Problem 1. The curves in these charts denote analytical predictions of BF and CF trajectories. The minimum (in time $\bar{t}$) on these curves represents the position and time of the onset of cavitation, $(\bar{x}_c, \bar{t}_c)$. Two branches originate from this point, corresponding to propagation of two breaking fronts travelling away from (left of $\bar{x}_c$) and towards (right of $\bar{x}_c$) the fluid-structure interface. The breaking front travelling away from the structure propagates indefinitely with a velocity in excess of the speed of sound but approaching $c_w$ as time elapses (corresponding to a slope of -1 for the curves in Fig. 3.7). In contrast, the breaking front travelling towards the structure initially moves supersonically and subsequently arrests at a position $\bar{x}_{rest}$ and time $\bar{t}_{rest}$, inverting its direction of motion and becoming a closing front. This closing front moves away from the structure, at a velocity always below $c_w$ but approaching this value as time elapses.

The chart in Fig. 3.7 (a) refers to the case of a fluid at initially vanishing static pressure, $\bar{p}_{st} = 0$, and illustrates the effect of structural stiffness on the details of the cavitation process, for a plate of given mass (corresponding to $\psi = 2.5$). For an unsupported plate ($\kappa = 0$, Taylor problem [4]), cavitation initiates at the fluid-structure interface and gives rise to a breaking front travelling away from the interface, while a closing front does not propagate, as expected. Increasing the structural stiffness results in the point of first cavitation being located within the fluid region rather than at the interface and in the appearance of a breaking front travelling towards the structure and subsequently inverting its motion, becoming a closing front.

The effect of the initial pressure in the fluid $\overline{p}_{st}$, for selected values of non-dimensional plate mass ($\psi = 2.5$) and stiffness ($\kappa = 0.004$) is illustrated in Fig. 3.7 (b). Increasing the initially applied static pressure results in increased values of $|\overline{x}_{rest}|$; the point of first cavitation moves away from the interface and the velocity of the closing front increases. As $\overline{p}_{st}$ approaches the critical value of $\overline{p}_{st,c} = 0.59$ (for the parameters chosen here), $|\overline{x}_{rest}| \to \infty$ indicating that cavitation does not occur.

The FE and analytical predictions in Fig. 3.7 are in excellent agreement. This correlation gives us confidence in the accuracy of the analytical models developed in this chapter. We proceed to explore the Problem 1 response in more detail in the following sections using both the analytical and FE models.

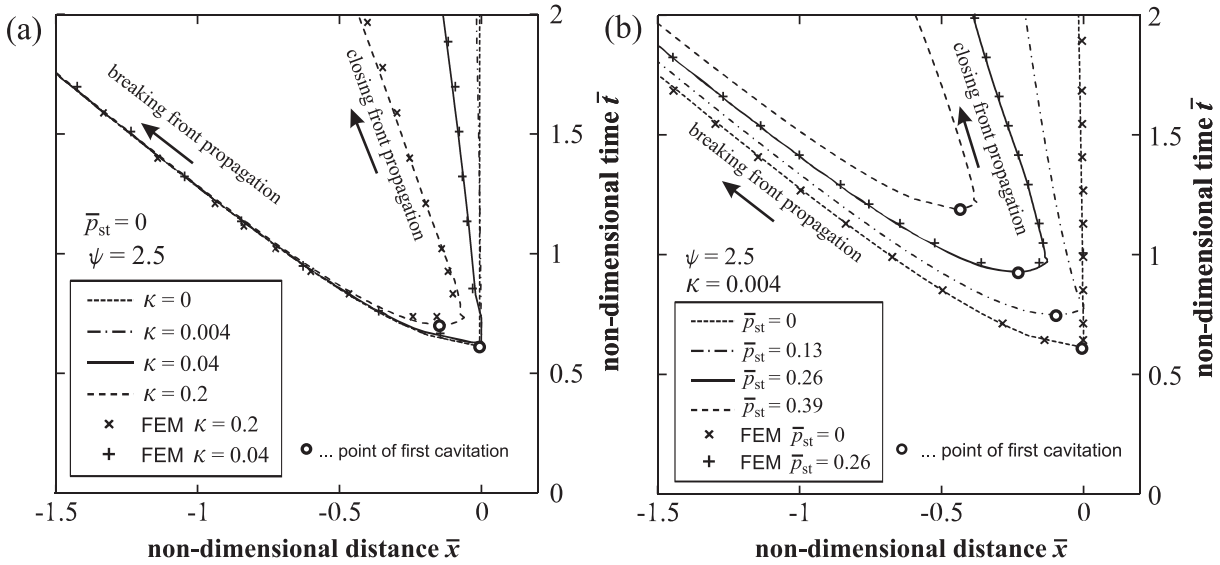



Fig. 3.7: Non-dimensional time versus position charts illustrating, for Problem 1, emergence of cavitation in the fluid attached to the plate's front face and subsequent propagation of breaking fronts and closing fronts: (a) effect of non-dimensional stiffness and (b) effect of the initial static pressure.

### 3.4.2 Problem 1: pressure and velocity histories

Three FE simulations were conducted and the mass per unit area of the plate *m*, the decay constant of the incident shock wave $\theta$, the stiffness of the supporting spring $k$ and the static pressure $p_{st}$ were chosen to give three different sets of non-dimensional parameters $\psi = \rho_w c_w \theta / m$, $\kappa = km/(\rho_w^2 c_w^2)$ and $\bar{p}_{st} = p_{st} / p_0$, corresponding to regimes 1, 2 and 3 presented in Section 3.2.3 (b). The chosen sets of parameters are indicated on the regime chart presented in Fig. 3.3.

In Fig. 3.8 (a) we show non-dimensional interface pressure and plate velocity histories for $\psi = 2.5$, $\kappa = 0.004$ and $\bar{p}_{st} = 0.6$ corresponding to *regime 1*. According to the regime chart in Fig. 3.3 (b), the selected non-dimensional parameters result in a point within *regime 1* located close to the transition curve to *regime 2*. No fluid cavitation is expected in this case, and FE simulations confirm this. The analytically predicted pressure and velocity histories are in excellent agreement with those extracted from FE simulations.

Time histories of non-dimensional interface pressure and plate velocity for $\psi = 2.5$, $\kappa = 0.2$ and $\bar{p}_{st} = 0$ are presented in Fig. 3.8 (b). According to the regime map in Fig. 3.3 (a), this choice of non-dimensional parameters result in a *regime 2* response. In this case the analytical model predicts that the relatively high stiffness of the supporting spring will cause the breaking front to arrest before it reaches the interface, and to invert its motion as a closing front (see Fig. 3.7 a). Even in this regime, the analytical and FE predictions match. Both types of predictions show that the water cavitates at $\bar{x}_c < 0$ and the interface pressure drops to a small value at time $\bar{t}_I$ (corresponding to the end of Stage I). Subsequently, this pressure increases again, due to wave reflection at the propagating closing front, imparting additional impulse to the plate. As time elapses, the pressure drops to zero and the water cavitates at the

interface; loading of the plate ceases and the structure oscillates around the equilibrium position.

The pressure and velocity histories in Fig. 3.8 (c) represent a case with $\bar{p}_{st} = 0$, $\psi = 2.5$ and relatively low spring stiffness, $\kappa = 0.004$. This set of non-dimensional parameters gives a point in the regime chart clearly located within *regime 3* (see Fig. 3.3 a). The analytical model predicts that a breaking front will reach the structure and reflects as a closing front, initially travelling slowly away from the interface (Fig. 3.7 a). Excellent agreement between FE and analytical predictions is achieved for this regime, both qualitatively and quantitatively. Both FE calculations and analytical model predict the interface pressure to vanish when the breaking front reaches the interface (at time $\bar{t}_I = \bar{t}_{rest}$) and, correspondingly, the plate velocity attains its maximum value. Subsequently, the interface pressure slowly increases due to collapse of the cavitated region by propagation of a closing front and the plate slowly decelerates.

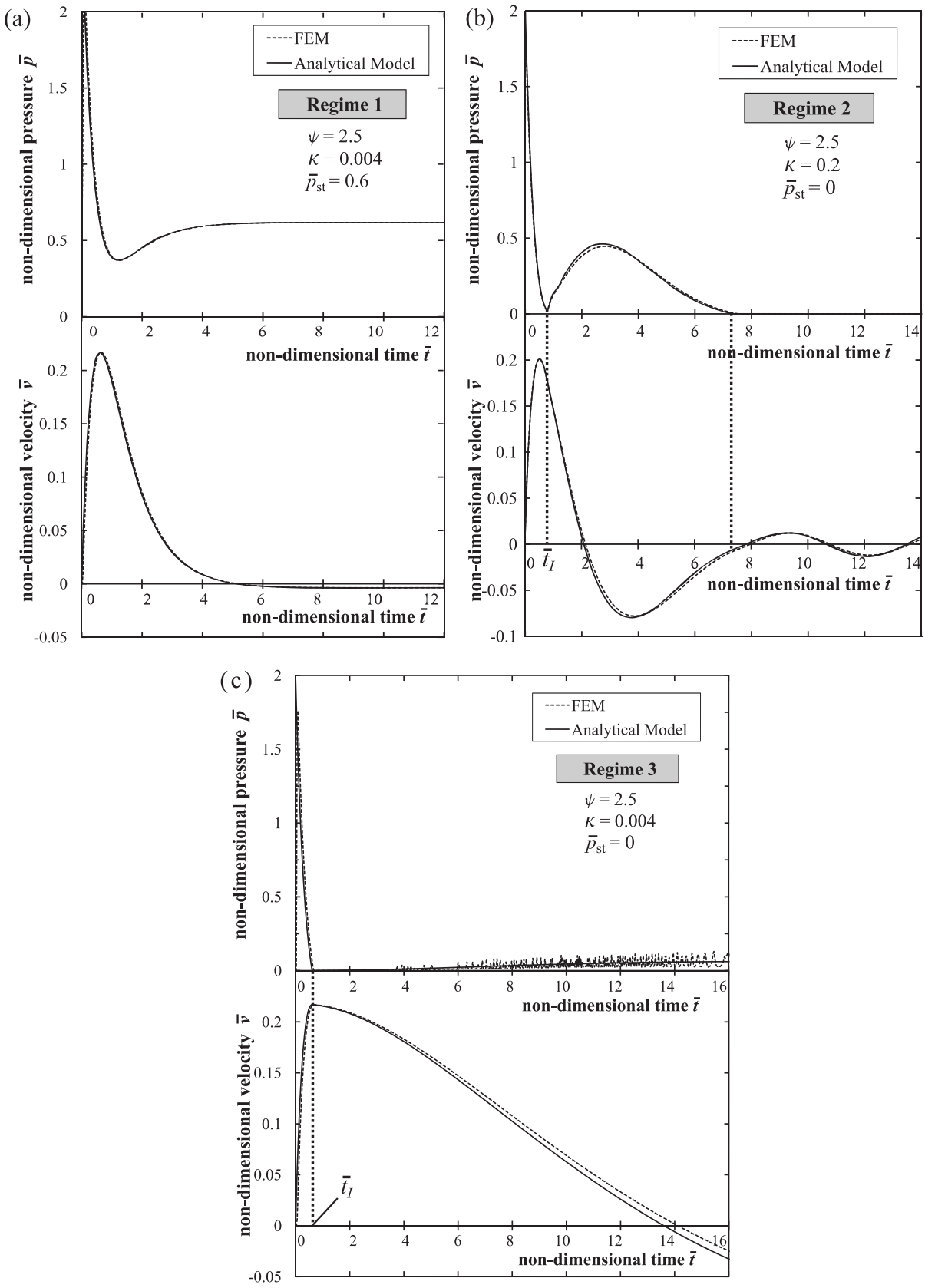



Fig. 3.8: Analytical and FE predictions of non-dimensional front face pressure and plate velocity time histories for Problem 1: (a) *regime* 1, (b) *regime* 2 and (c) *regime* 3.

### 3.4.3 Problem 2: closing front and breaking front propagation

The charts in Fig. 3.9 present a comparison between analytical and FE predictions of the onset of cavitation as well as of the propagation of breaking and closing fronts for Problem 2 (water-backed plate). In Fig. 3.9 (a) the effect of structural stiffness on the evolution of the cavitated region is illustrated for the case $\bar{p}_{st} = 0$ and $\psi = 2.8$. For any choice of $\kappa$, cavitation initiates at a finite distance from the structure (recall that for Problem 1, cavitation occurs at the fluid-structure interface for $\kappa = \bar{p}_{st} = 0$), and the effect of increasing $\kappa$ is similar to that observed for Problem 1. Similarly, Fig. 3.9 (b) reports the effect of an increasing static pressure: again, this results in increased values of $|\bar{x}_{rest}|$ as well as in a faster propagation of the closing front. The predictions from FE simulations in Fig. 3.9 (a) and Fig. 3.9 (b) show a perfect agreement with the analytical model.

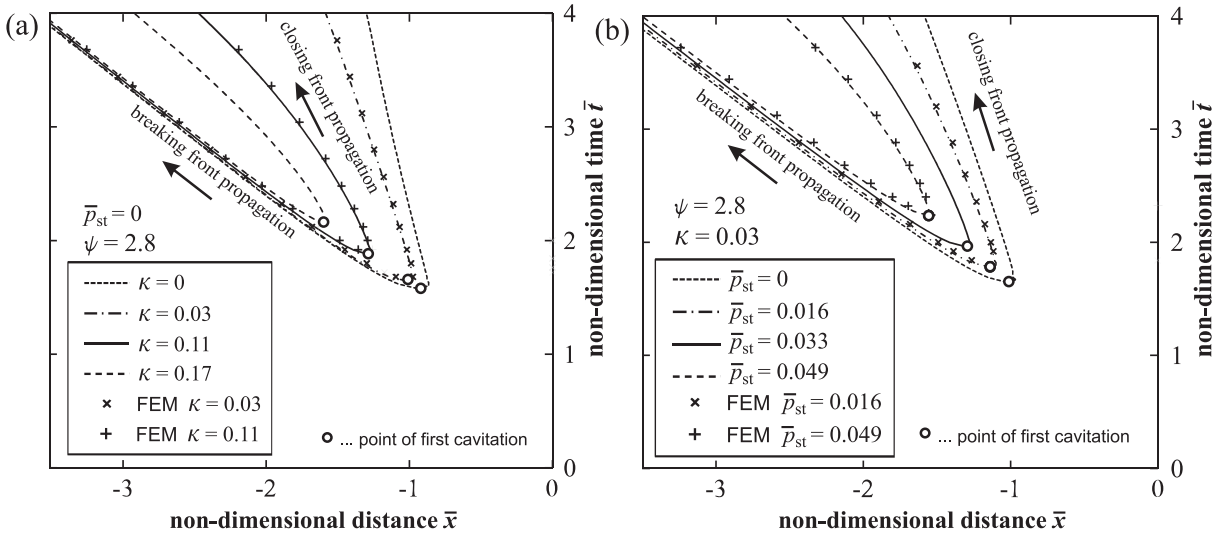



Fig. 3.9: Non-dimensional time versus position charts illustrating, for Problem 2, emergence of cavitation in the fluid attached to the plate's front face and subsequent propagation of breaking fronts and closing fronts: (a) effect of non-dimensional stiffness and (b) effect of the initially applied pressure.

### 3.4.4 Problem 2: pressure and velocity histories

Four FE simulations were conducted for Problem 2. Parameters *m*, $\theta$, *k* and $p_{st}$ were chosen to give four different sets of parameters $\psi$, $\kappa$ and $\bar{p}_{st}$ corresponding to the four different regimes described in Section 3.2.3 (b).

In Fig. 3.10 (a) the interface pressure (at both the front and back interfaces) and plate velocity histories are presented for the case $\psi = 2.8$, $\kappa$=0.004 and $\bar{p}_{st} = 0.07$. The highlighted point in the regime map for this choice of non-dimensional parameters (see Fig. 3.4 b) indicates a *regime 1* response. No fluid cavitation is expected in this case at the front or at the back of the plate. FE simulations are in excellent agreement with analytical predictions. In this case, Stage I analysis is sufficient to predict the response of the system.

Interface pressure and velocity histories for $\psi = 2.8$, $\kappa$=0.17 and $\bar{p}_{st} = 0$ are illustrated in Fig. 3.10 (b). This set of non-dimensional parameters results in a *regime 2* response of the plate, as the corresponding point in the regime chart indicates (Fig. 3.4 a). The analytical model predicts that cavitation occurs initially in the water in contact with the plate's back face. Finite element simulations confirm this and their predictions are again in excellent agreement with the analytical calculations. Both analytical and FE predictions show that the water attached to the back face cavitates at a time $\bar{t}_c' < \bar{t}_c$, corresponding to the plate inverting its direction of motion (as expected for $\bar{p}_{st} = 0$, see eq. (3.21)). For $\bar{t}_c' < \bar{t}_c$, the back interface pressure vanishes and a zone of cavitated water spreads from the plate's back face into the positive *x*-direction. At $\bar{t} > \bar{t}_c$ the front water cavitates and for $\bar{t} > \bar{t}_I = [\, t_{rest} - x_{rest} / c_w \,] / \theta$ the motion of the plate is affected by this phenomenon.

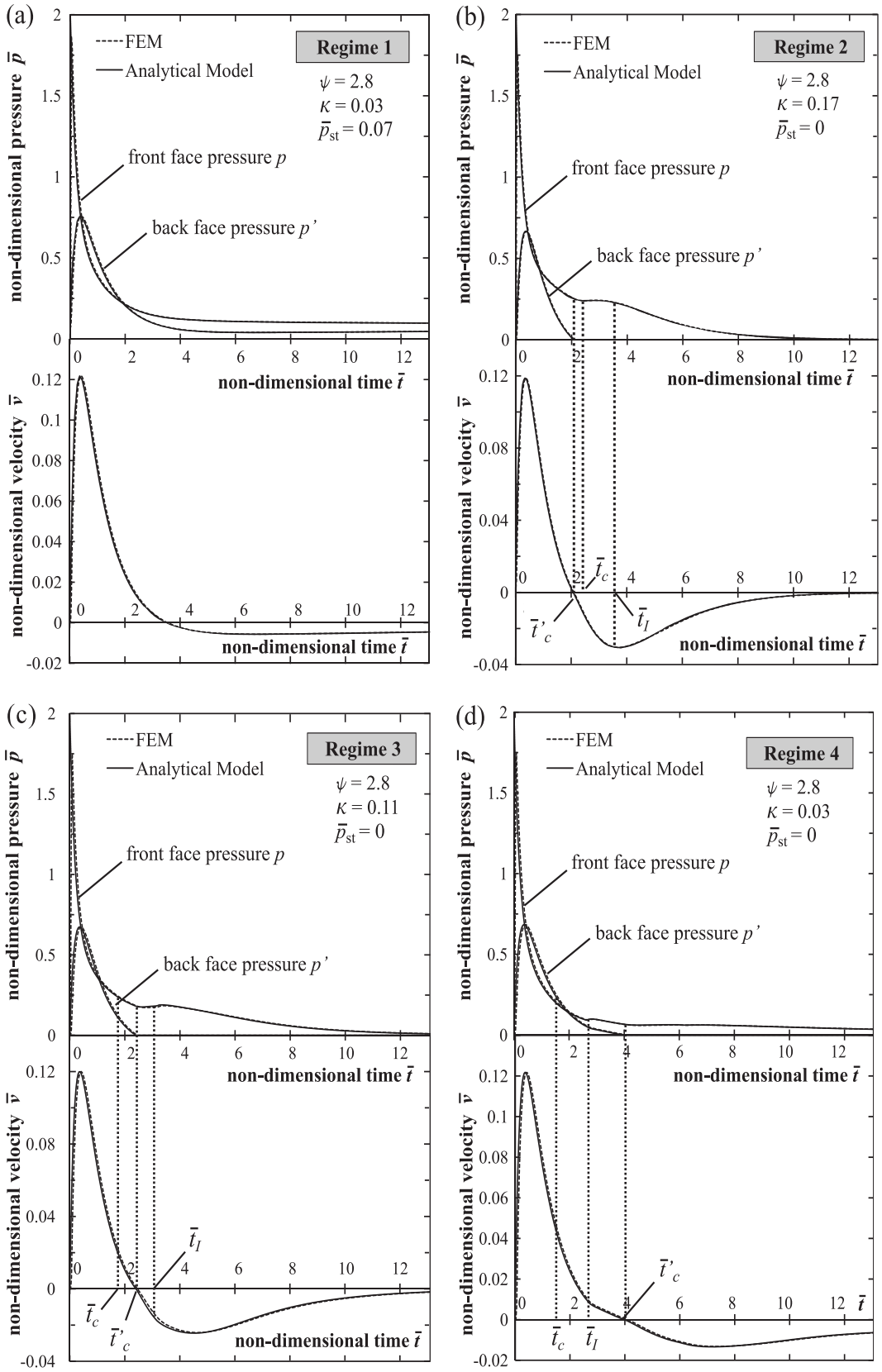



Fig. 3.10: Analytical and FE predictions of the non-dimensional front face pressure, back face pressure and plate velocity histories for Problem 2: (a) *regime* 1, (b) *regime* 2, (c) *regime* 3 and (d) *regime* 4.

The case $\psi = 2.8$, $\kappa$=0.11 and $\bar{p}_{st} = 0$ corresponds to a *regime 3* response according to the regime map in Fig. 3.4 (a) and the predicted interface pressures and plate velocity histories for this particular choice of parameters are presented in Fig. 3.10 (c). Analytical calculations and FE predictions coincide. The sequence of events predicted by FE simulations matches the analytical predictions: cavitation occurs initially in the water in front of the plate at time $\bar{t}_c$. Before the effects of this event begin to influence the plate's motion (at time $\bar{t}_I$), cavitation takes place at the plate's back face. The corresponding pressure histories are very similar to those observed for *regime 2*.

By further reducing the non-dimensional stiffness to $\kappa = 0.03$ ($\psi = 2.8, \bar{p}_{st} = 0$), *regime 4* becomes the active regime of behaviour (Fig. 3.4 a). The curves in Fig. 3.10 (d) indicate that, in this regime, first cavitation occurs in the front of the plate at time $\bar{t}_c$; the plate experiences this event at a time $\bar{t}_I > \bar{t}_c$, before cavitation sets in at the plate's back face at time $\bar{t}_c' > \bar{t}_I$; the pressure histories are similar to those observed for *regimes* 2 and 3.

## 3.5 Sensitivity of the response to $\kappa$, $\psi$ and $\bar{p}_{st}$

Having established the accuracy of the analytical predictions, the analytical models are now used to determine the sensitivity of the plate response to the non-dimensional parameters $\psi$ and $\bar{p}_{st}$, for both problems 1 and 2. The maximum value of the non-dimensional impulse transmitted to the plate's front interface $\bar{I}_t$, defined as

$$\bar{I}_t = \max_{0 \le t < \infty} \left[ (1/I_0) \int_0^t (p - p_{st}) \mathrm{d}\tau \right] \tag{3.43}$$

as well as the non-dimensional peak plate velocity $\bar{v}_{\max}$, can be used to quantify the plate's response to blast loading. Both FE and analytical predictions show that the plate attains its

peak velocity in Stage I, i.e., prior to occurrence of cavitation in the fluid; it follows that the value of $\overline{v}_{\max}$ can be obtained from eqs. (3.17) and (3.25) for problems 1 and 2, respectively. In contrast, no simple analytical expressions can be derived for the transmitted impulse, as calculation of $\overline{I}_t$ involves, in general, both Stage I and Stage II analyses.

The definition of $\overline{I}_t$ in eq. (3.43) merits some comment. The interface pressure versus time histories presented above show that in some cases the overpressure loading on the plate's front face ceases after a relatively short time, on the order of $10\theta$ or less (this can be seen, for example, in Fig. 3.8 a, Fig. 3.8 b, Fig. 3.10 b, Fig. 3.10 c). In other cases (see Fig. 3.8 c, Fig. 3.10 a, Fig. 3.10 d), after an initial peak and subsequent decay, the pressure increases again slowly (due to the plate inverting its direction of motion) and finally drops to zero after a time that can be on the order of $10^3\theta$, for very small values of the stiffness $\kappa$. Definition (3.43) accounts for both the impulse delivered to the plate 'quickly' (within a time of the order of $10\theta$) and the impulse delivered to the plate 'slowly' (within a time $>10\theta$). However, from the structural design perspective, it would be valuable to separate the two contributions. We shall therefore compute both the 'total impulse' $\overline{I}_t$, as defined in eq. (3.43), and a 'partial impulse' defined as

$$\overline{I}_p = \max_{0\le t\le t_{\max}} \left[ (1/I_0)\int_0^t (p - p_{st})\mathrm{d}\tau \right] \tag{3.44}$$

where $t_{\max}$ denotes the time at which the plate attains its maximum displacement; this partial impulse quantifies the amount of impulse that is delivered to the structure 'quickly'.

The sensitivity of $\overline{I}_t$ to $\kappa$, $\psi$ and $\overline{p}_{st}$ is illustrated in Fig. 3.11 for Problem 1.

In Fig. 3.11 (a), both $\overline{I}_t$ and $\overline{I}_p$ are plotted as a function of the non-dimensional stiffness $\kappa$, for $\psi = 2.5$ and three different values of $\overline{p}_{st}$. Predictions from the analytical model indicate that $\overline{I}_t$ increases with increasing $\kappa$ (for $\kappa < 0.02$), approaching unity as $\kappa$ tends to infinity (the case of a fixed rigid plate). It is interesting to note that a range of $\kappa$ exists for which $\overline{I}_t > 1$; oscillations of the plate can result in a transmitted impulse in excess of $I_0$. The effect of an increase in the non-dimensional static pressure is to reduce $\overline{I}_p$ for any choice of $\kappa$. It can be deduced from Fig. 3.3 that, for the range of $\kappa$, $\psi$ and $\overline{p}_{st}$ shown in Fig. 3.11 (a), the response is *regime 3* for $\overline{p}_{st} = 0$ and $\overline{p}_{st} = 0.01$; for $\overline{p}_{st} = 0.1$ the response switches from *regime 3* to *regime 2* when $\kappa > 0.05$.

The sensitivity of the transmitted impulse (Problem 1) to the non-dimensional parameters $\psi$ and $\overline{p}_{st}$ is illustrated in Fig. 3.11 (b) for the case $\kappa = 0.01$. With this choice of a relatively high stiffness, the total transmitted impulse $\overline{I}_t$ approaches the value of 1 with increasing $\psi$ (i.e., with decreasing mass); a range of $\psi$ exists for which $\overline{I}_t > 1$; this is due to the plate, supported by the spring, inverting its motion and causing collapse of the cavitated region, and in turn, acquiring additional impulse. The effect of increasing the applied static pressure is again to reduce $\overline{I}_p$ for any choice of $\psi$. The dominant regime of response is again *regime 3* for the range shown, with the exception of the case ($\overline{p}_{st} = 0.1, \psi > 4.5$) which corresponds to a *regime 2* response.

In Fig. 3.12 the sensitivity of the transmitted impulse to $\kappa$, $\psi$ and $\overline{p}_{st}$ is presented for a water-backed plate (Problem 2). In particular, Fig. 3.12 (a) presents the variation of $\overline{I}_t$ and $\overline{I}_p$

as a function of $\kappa$, for $\psi = 2.8$ and three selected values of $\overline{p}_{st}$. The total transmitted impulse increases rapidly for low values of $\kappa$ and attains the value of 1. The partial transmitted impulse $\overline{I}_p$ is weakly sensitive to the stiffness $\kappa$; $\overline{I}_p$ decreases as the initial static pressure is increased. It can be deduced from Fig. 3.4 that the active regime of response switches from regimes 4 to 3, 2 and 1 as $\kappa$ is progressively increased from 0 to 0.1.

Finally, Fig. 3.12 (b) illustrates the effect of the mass of a water-backed plate, quantified by $\psi$, on the transmitted impulse, for the case $\kappa = 0$ (note that for $\kappa = 0$, $\overline{I}_t$ and $\overline{I}_p$ coincide). The figure shows that $\overline{I}_t$ decreases with $\psi$ increasing or, equivalently, with the mass *m* decreasing; an increase in the static pressure leads to a reduction in $\overline{I}_t$ for any choice of $\psi$. The corresponding regime chart given in Fig. 3.4 indicates that *regime 4* is active for the cases $\overline{p}_{st} = 0$ and $\overline{p}_{st} = 0.02$ (in the range displayed in the figure); for $\overline{p}_{st} = 0.04$ the response switches from regimes 4 to 3, 2 and 1 as $\psi$ is progressively increased; at high values of $\psi$, corresponding to a *regime 1* response, the transmitted impulse approaches the theoretical value $\overline{I}_t = 0.5$ (this result can be obtained by integration of eq. (3.26)).

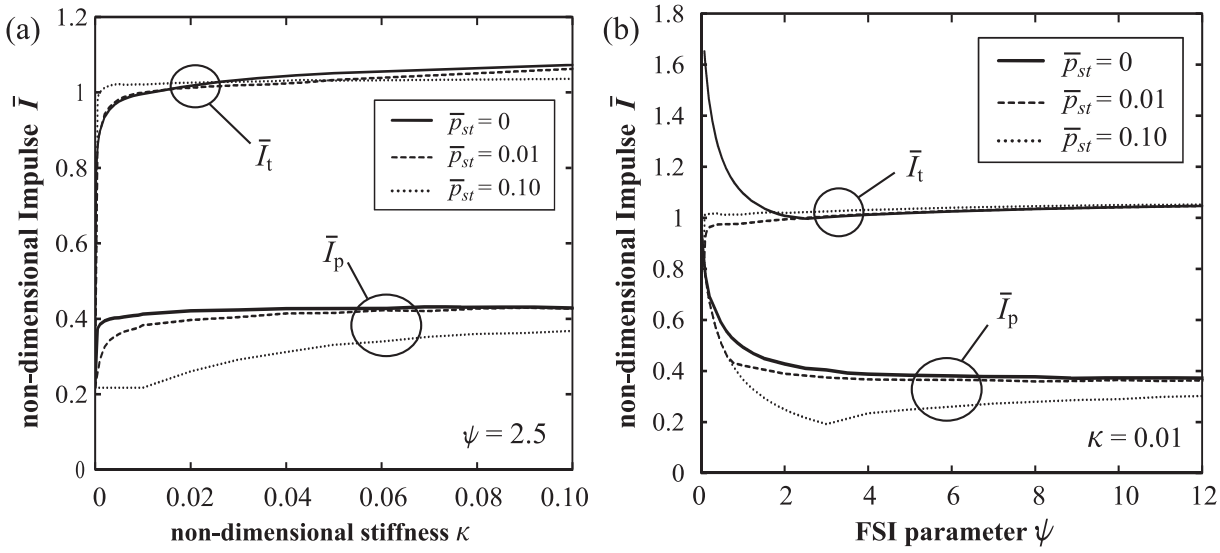



Fig. 3.11: (a) Problem 1: Partial and total non-dimensional impulse imparted to the front face as a function of non-dimensional stiffness $\kappa$ for selected values of $\bar{p}_{st}$. (b) Problem 1: Partial and total non-dimensional impulse imparted to the front face as a function of the non-dimensional parameter $\psi$ for selected values of $\bar{p}_{st}$.

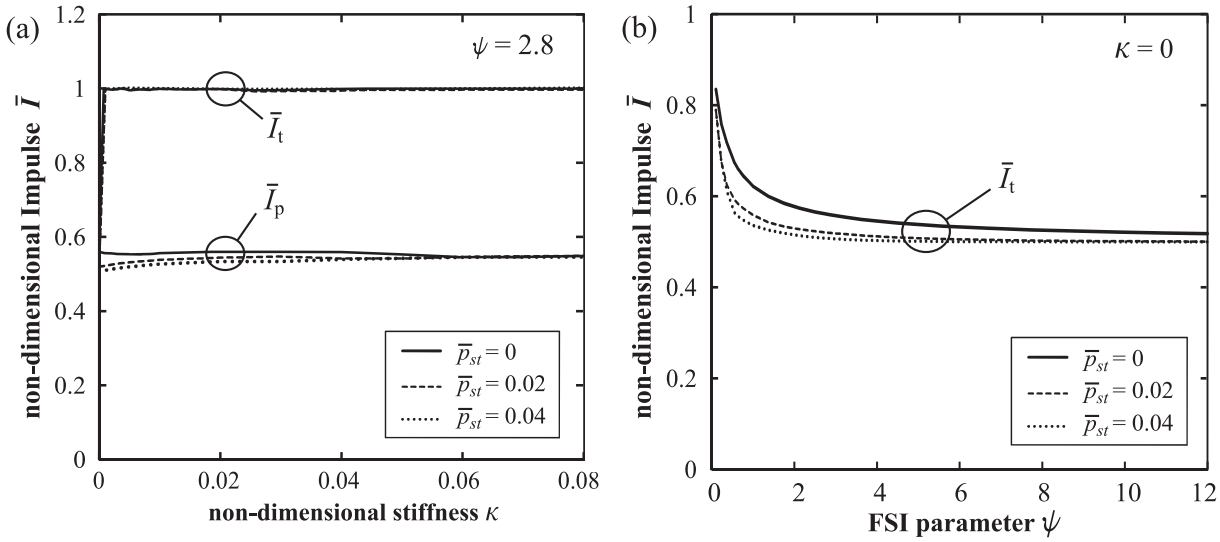



Fig. 3.12: (a) Problem 2: Partial and total non-dimensional impulse imparted to the front face as a function of non-dimensional stiffness $\kappa$ for selected values of $\bar{p}_{st}$. (b) Problem 2: Total non-dimensional impulse applied to the front face as a function of the non-dimensional parameter $\psi$ for selected values of $\bar{p}_{st}$. $\bar{I}_t = \bar{I}_p$ in this case.

## 3.6 Conclusions

The 1D response of a spring-supported, rigid plate to underwater blast has been investigated, for a plate in contact with water on one or both sides. Analytical models have been derived to predict plate velocity and interface pressure histories; such models account explicitly for cavitation phenomena in the fluid, including propagation and arrest of breaking fronts and closing fronts, as well as for the effect of an initially applied static fluid pressure on the system response.

Regimes of behaviour were identified for both problems under investigation, and non-dimensional regime maps were constructed. The system response was found to depend only on three non-dimensional parameters $\kappa$, $\psi$ and $\overline{p}_{st}$, representing the stiffness of the supporting spring, the mass of the plate and the initially applied static pressure in the fluid. The analytical models were validated by comparing their predictions with those obtained from detailed explicit 1D FE simulations; the two types of predictions were found in excellent agreement.

The study indicates that the FSI phenomena associated with loading of structures by underwater shock-waves substantially affect the structural response and need to be modelled in detail. The approximate models used in previous studies for sandwich constructions (based on the assumption of impulsive loading [22] or water layer attached to structural interface [27, 28]) are not able to predict accurately the structural response and can only be used for a limited range of problems.

The sensitivity of the underwater blast response of a rigid, spring-supported plate to structural mass and spring stiffness was investigated. It has been a long-accepted paradigm that a reduction in structural mass (hence an increase of $\psi$) leads to a reduction in the imparted impulse; in this study we have demonstated that a decrease in the plate's mass can increase

the severity of structural loading (hence the imparted impulse) for particular choices of spring stiffness and static pressure (see Fig. 3.11b). On the other hand, an increase of the spring stiffness always results in an increase in the imparted impulse. For some choices of non-dimensional stiffness, mass and initially applied pressure, the impulse applied on the plate can exceed the reference value $I_0 = 2p_0\theta$, owing to elastic spring-back of the system.

The application of a hydrostatic pressure in the fluid prior to blast loading affects substantially cavitation phenomena; specifically, the point of first cavitation in the front water column is found at increasing distance from the structure and collapse process of the cavitated zone is faster, as the static pressure is increased. This results in a reduction of the impulse imparted to the plate for an increase in initial static pressure. For both problems investigated herein, a sufficient level of initially applied pressure results in suppression of cavitation in the fluid; simple analytical expressions for the transmitted impulse can be derived in this particular case. The effect of a non-vanishing fluid cavitation pressure can be determined by our analysis considering a fictitious static pressure given by eq. (3.41).

The design of structures loaded by underwater blast is often done by neglecting FSI phenomena and assuming either impulsive loading of the structure (by an impulse $I_0$) or loading by a traction versus time history (whose time integral equals $I_0$). The present study shows that these apparently 'conservative' simplifications can lead to high inaccuracy in the predicted structural response: such simplifications are not necessarily conservative (see Fig. 3.11) and in some cases, they may be too conservative (see Fig. 3.11b and Fig. 3.12b). The non-dimensional charts in Fig. 3.11 and Fig. 3.12 can provide the designer with more accurate estimates of the impulse imparted to a structure when dynamic FE solutions are not available.

The analytical models also provide a clear physical picture of the cavitation process and how this influences the detailed response of the structure to a blast event. In the process, they provide guidance and insight into the design and selection of structural components for blast resistant structures.

However, the results offered in this chapter are limited to predicting the response of structures subject to a non-contact explosion in water, where the loading pressure pulse can be well-approximated by a planar, exponentially decaying shock wave travelling at approximately sonic speed. In close proximity to the point of detonation, the propagation speed as well as the peak pressure associated with the generated shock can be dramatically higher, necessitating a more advanced description of the loading phase.

Moreover, the extent to which the proposed 1D calculations can represent the response of real structures requires further study. Beam and plate bending are 2D or 3D phenomena, and when beams or plates are loaded dynamically their local stiffness is in general a function of time. More detailed 2D and 3D calculations are therefore needed to predict the response of real-life structures to explosions in water. This will be investigated in Chapters 8 and 9, for the case of circular clamped plates subject to underwater blast.

# Chapter 4

# The Response of Rigid Plates to Blast in Deep Water: Fluid-structure interaction Experiments

## 4.1 Introduction

The response of structures to underwater blast is difficult to observe at laboratory scale and for this reason experimental studies have appeared only in the last decade. The existing experimental techniques are capable of reproducing, at a laboratory scale, the dynamic response of submerged structures to underwater blast; on the other hand, none of them allows measuring the effects of an initially applied hydrostatic pressure in the fluid, which is fundamental in order to design structural components loaded by blast waves in deep water. In addition, while growth and collapse of cavitation bubbles in proximity of solid surfaces has been observed by several authors (Benjamin & Ellis [45], Lauterborn & Bolle [46], Tomita & Kodama [47]) in order to explore cavitation-induced erosion, no studies so far report direct observation of the propagation of cavitation fronts subsequent to structural loading by underwater shock waves.

In this study we shall fill these gaps in the literature by developing an apparatus able to generate planar, exponentially decaying shock waves in initially pressurised water; we shall use this apparatus to study the response of both air-backed and water-backed unsupported rigid specimens and its sensitivity to initial static pressure and structural mass. In doing so we shall also provide experimental evidence supporting the theoretical findings of Kennard [3]; this will be achieved by observing the structural response as well as the ensuing cavitation processes by means of high speed photography. The experimental results will also be used to validate the predictions of the theoretical models presented in Chapter 3.

## 4.2 Problem definition

The two 1D problems under investigation are sketched in Fig. 4.1 and briefly described below.

(i) *Loading of an air-backed rigid plate:* an unsupported rigid plate of mass per unit area *m* is in contact on one side (front face) with water at initially uniform hydrostatic pressure $p_{st}$ and on the opposite side (back face) with air at the same pressure $p_{st}$ in order to ensure initial equilibrium prior to dynamic loading by an exponentially decaying, planar blast wave impinging on the front face at $t=0$ (Fig. 4.1a). The problem is equivalent to that of a rigid plate supported by a perfectly plastic foundation with compressive yield stress equal to $p_{st}$ .

(ii) *Loading of a water-backed rigid plate:* a rigid plate of mass per unit area m is initially in contact with water at uniform hydrostatic pressure $p_{st}$ on both sides. The plate is loaded by an exponentially decaying blast wave on one side (Fig. 4.1 b).

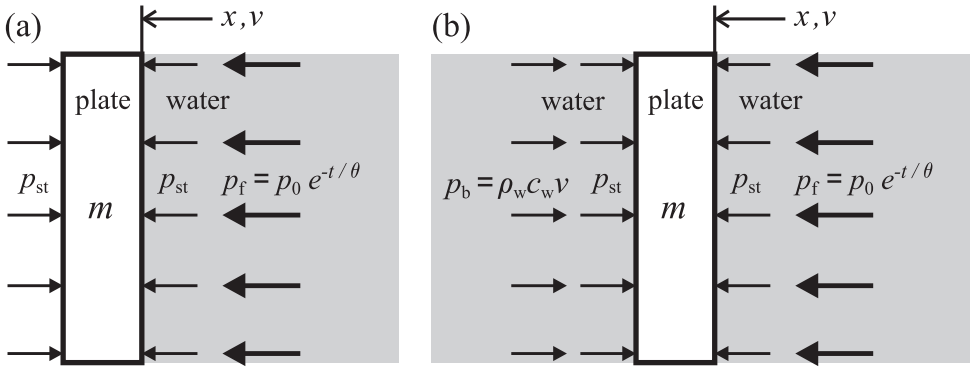



Fig. 4.1: Free body diagram of rigid plates for the two problems under investigation: (a) air-backed plate and (b) water-backed plate. Plates are loaded by exponentially decaying pressure waves in initially pressurised water.

## 4.3 Experimental apparatus

### 4.3.1 Transparent shock tube and instrumentation

The experimental technique developed in this chapter is an extension of that established by Deshpande et al. [36]; this technique is modified here in order to permit initial pressurization of the water and to allow direct observation of cavitation. The apparatus, sketched in Fig. 4.2, consists of a transparent shock tube of inner diameter $d = 27\,\text{mm}$ and length $L = 2\,\text{m}$. The tube was machined from a cast acrylic rod of density $\rho = 1190\,\text{kgm}^{-3}$, Young's modulus $E = 3.3\,\text{GPa}$ and tensile strength of approximately 80 MPa; honing of the bore provided a glossy finish to ensure clear observation of fluid and plate by high-speed photography. The wall thickness of the tube was chosen to guarantee no failure or plastic deformation upon loading by an internal pressure of 20 MPa, while the length was chosen to ensure sufficient time of observation of specimens placed inside the tube, prior to secondary loading due to reflections of pressure waves at the tube's ends. The same tube was used in two different configurations to explore the response of air-backed and water-backed plates, as described below.

*Air-backed configuration:* cylindrical monolithic specimens were machined from stainless steel rods, fitted with two O-rings and inserted in the shock tube at a short distance from its distal end, as illustrated in Fig. 4.2 (a). The shock tube was then filled, in a vertical position, with filtered tap water and closed at the opposite end (front end) by a sliding nylon piston fitted with O-rings; the front piston included a bleed valve to evacuate air bubbles trapped in the water column prior to the experiments. The front end of the tube was provided with an anvil to avoid the front piston from being ejected when the water was pressurised.

In order to mimic the idealised problem sketched in Fig. 4.1 (a), it is necessary to apply a constant, uniform pressure $p_{st}$ at the specimen's back face and to pressurise the water column to the same hydrostatic pressure $p_{st}$. This was achieved by placing a foam cylinder in contact with the specimen's back face and compressing this cylinder by quasi-static application of a force $F$ (measured via a resistive load cell) immediately before the experiment; the force was increased until the desired pressure $p_{st}$ was reached and an initial plastic strain of around 5% was induced in the foam cylinder. During the dynamic experiment, specimen motion induces additional plastic strain in the foam cylinder; however the plastic collapse of the foam occurs at constant stress during the plateau response of this compressible solid; the length of the foam cylinder was chosen to obtain a strain below the densification strain $\varepsilon_D$, thereby guaranteeing a constant back pressure $p_{st}$. Different Rohacell foams were employed to manufacture the foam cylinders and the cylinder's cross-section was varied in order to adjust $p_{st}$. For experiments with air at atmospheric condition (i.e. approximately $p_{st} = 0.1\text{MPa}$) the supporting foam cylinder was not employed.

Note that if the plate is in contact with air on the back face, motion of the specimen induces an increase in back pressure proportional to the velocity of the plate; this velocity was small in our tests ($< 15$ ms$^{-1}$) and therefore such pressure increase was negligible compared to the initial pressure $p_{st}$ and to the dynamic pressure induced by the blast wave. Compression of the foam during the dynamic experiments occurred at strain rates on the order of $10\text{s}^{-1}$; the Rohacell foams employed in this study possess negligible strain rate sensitivity in the range $\dot{\varepsilon} = 10^{-3} \div 10^{3}\ \text{s}^{-1}$ (Arezoo et al. [18]) and we therefore assume that the foam's yield stress can be treated as a constant.

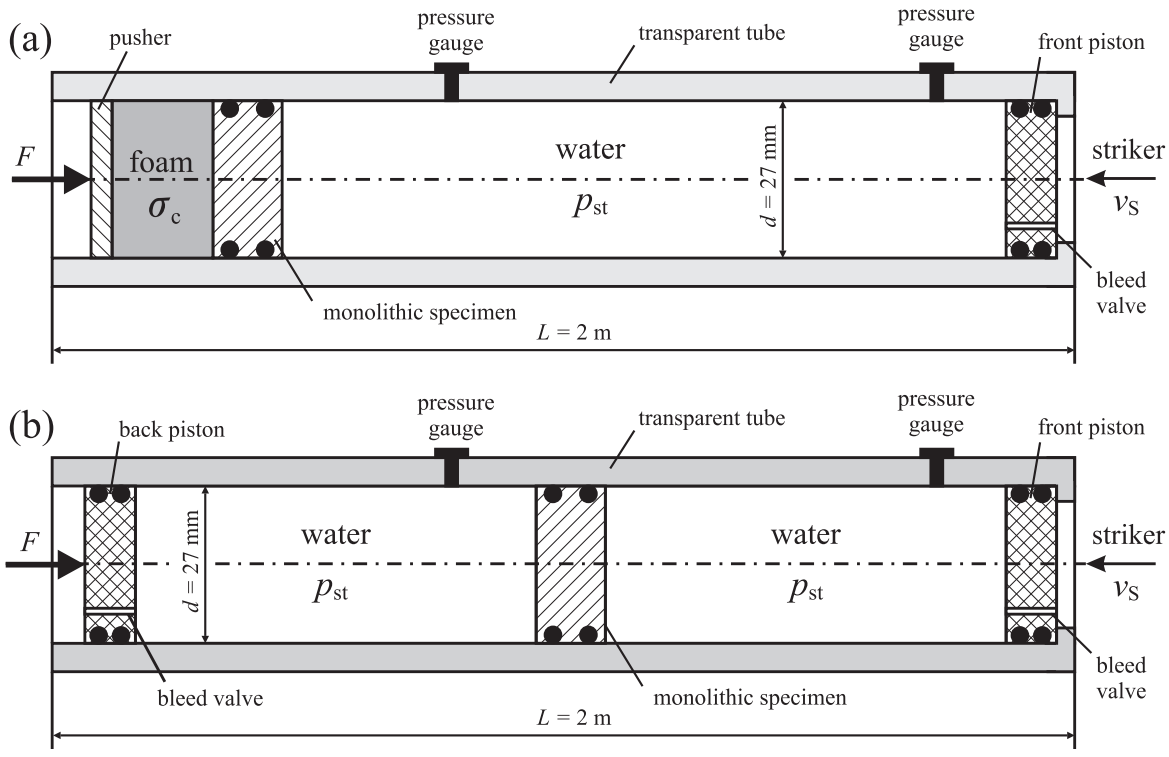



Fig. 4.2: Sketch of the apparatus employed in this study to explore the response of (a) air-backed unsupported rigid plates and (b) water-backed unsupported rigid plates.

*Water-backed configuration:* in order to reproduce the problem sketched in Fig. 4.1 (b), the steel specimen was placed at the centre of the shock tube, separating the bore into two sections. Both front and back sections were filled with filtered tap water and both tube ends were closed with sliding nylon pistons as described above. To induce a hydrostatic pressure $p_{st}$ in the water the sliding piston at the distal end of the tube was loaded with a compressive force $F$ until the desired pressure was attained. Such force was not applied in experiments with $p_{st} = 0.1\text{MPa}$.

A Phantom 'Vision Research' (V7.1) high-speed camera was used to observe the motion of the specimen and the details of water cavitation. The pressure in the water columns was measured using piezoelectric pressure transducers manufactured by PCB Piezoelectronics Inc. (of type 113B23) and mounted flush to the inner surface of the tube; one of such transducers was placed at a distance of 120 mm from the front end of the tube in order to record the incident pressure versus time history. A second transducer was placed at a distance of 120 mm from the centre of the tube (on the distal side) in order to measure pressure waves emanating from the specimen's back face during the dynamic experiments. Hoop resistance strain gauges were adhered to the external surface of the tube in order to provide triggering signals and additional readings of the fluid pressure transient, as well as to measure the speed of wave propagation in the tube.

Photographs of the laboratory setup for an experiment in water-backed configuration are illustrated in Fig. 4.3, showing the apparatus from two different viewing angles.

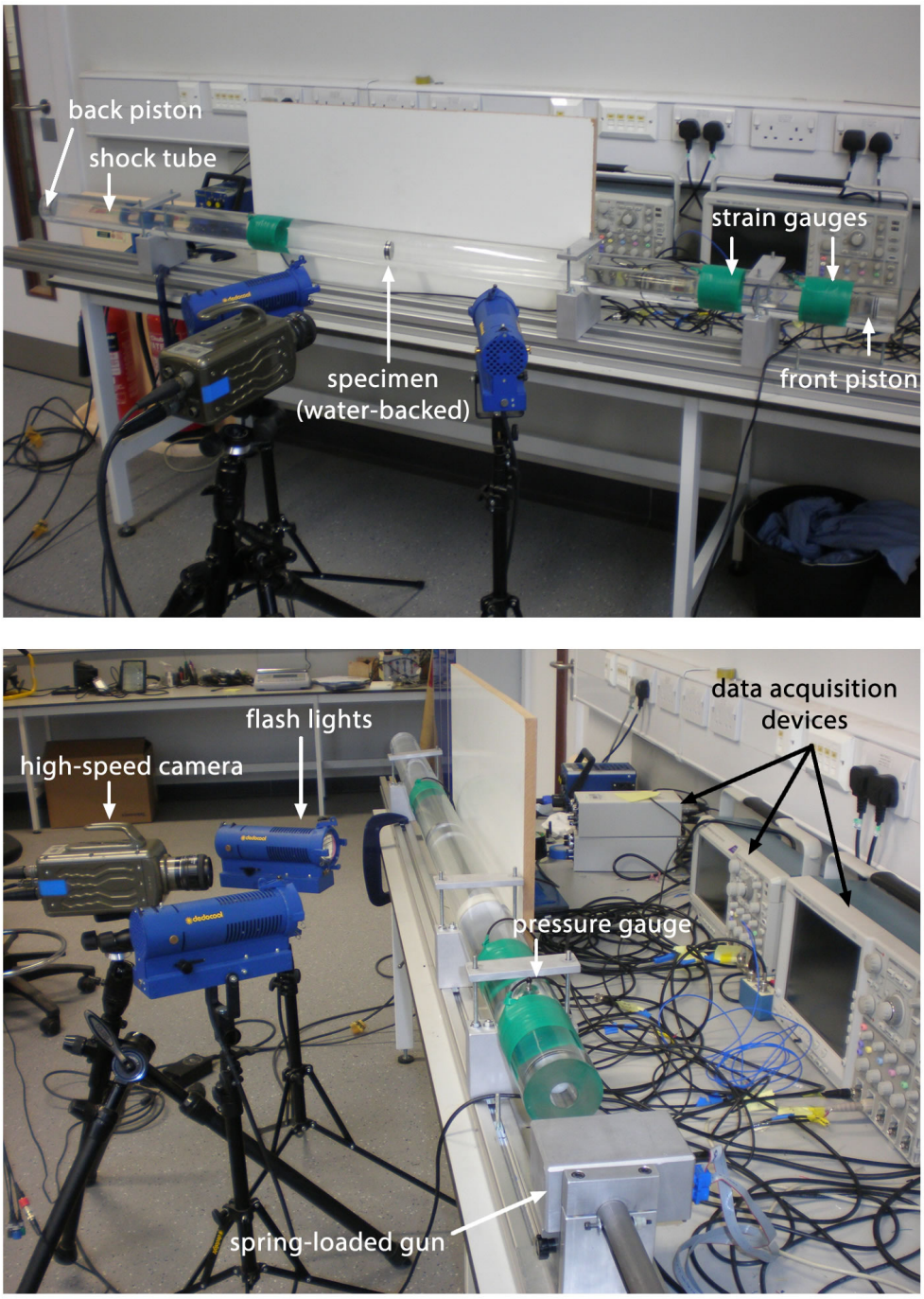



Fig. 4.3: Photographs of the laboratory setup for the case of an experiment in water-backed configuration.

### 4.3.2 Generation of the shock wave

When a blast event takes place in deep water at initial pressure $p_{st}$, an exponentially decaying pressure wave is generated [5, 6]. At sufficient distance from the detonation point, the pressure versus time history associated with the passage of the pressure wave at a point in the fluid can be written as

$$p(t) = p_{st} + p_0 e^{-t/\theta} \tag{4.1}$$

where the peak overpressure $p_0$ and the decay time $\theta$ depend upon the mass and type of explosive material as well as on the distance from the point of detonation.

The above pressure history (eq. (4.1)) was generated by impacting the nylon piston placed at the front end of the shock tube with a compound projectile made from a combination of stainless steel and a compressible foam; projectiles were fired using a spring-loaded gun. The reasons for using a compound striker, rather than a simpler steel cylinder as in Deshpande et al. [36] are explained below.

Prior to the loading phase, the nylon piston at the front end of the shock tube, of mass $M_P$, is subject to a static pressure $p_{st}$, whose action is equilibrated by the reaction force exerted by the anvil placed at the tube's end (Fig. 4.4 a); such anvil imposes a unilateral constraint to motion of the nylon piston in the negative *x*-direction. Now consider the inelastic impact of a cylindrical steel striker of mass $M_S$ and velocity $v_S$ on the nylon piston; treating both piston and striker as rigid bodies and employing the acoustic approximation for the response of water, dynamic equilibrium of the combined striker-piston system can be written as

$$m_{S,P}\dot{v} = -p_{st} - \rho_w c_w v \tag{4.2}$$

where $m_{S,P}$ is the total mass of the striker-piston system divided by the cross section of the piston $A_P$, $m_{S,P} = (M_S + M_P)/A_P$, $v$ is the system velocity, $\rho_w$ and $c_w$ are the density and the speed of sound of water, respectively. The initial velocity of the striker-piston system is dictated by conservation of linear momentum and given by

$$v_0 = \frac{M_S v_S}{M_S + M_P} . \tag{4.3}$$

Equation (4.2) can be solved with the initial condition $v(t=0) = v_0$, giving the interface pressure $p(x=0,t) = p_{st} + \rho_w c_w v(t)$ as

$$p(x=0,t) = (p_{st} + p_0) e^{-t/\theta} \tag{4.4}$$

where the peak pressure $p_0$ and the decay time $\theta$ are given by

$$p_0 = \rho_w c_w v_0 \quad , \quad \theta = \frac{m_{S,P}}{\rho_w c_w} . \tag{4.5}$$

It follows from eq. (4.4) that impact of the nylon piston by a rigid projectile generates a pressure pulse whose amplitude decays exponentially to zero, rather than to a finite value $p_{st}$ as desired and prescribed by eq. (4.1). This is due to the fact that, subsequent to the impact, the nylon piston loses contact with the supporting anvil (Fig. 4.4 a) and sends into the water column a pressure wave of magnitude $-p_{st}$. To avoid this problem, it is necessary to apply an additional constant pressure $p_{st}$ to the dry face of the piston during the impact event.

In order to overcome this problem, we employ the compound striker sketched in Fig. 4.4 (b), comprising of steel skins and a polymeric foam cylinder, which allows generation of the desired pressure pulse (eq. (4.1)) in the water column. A cylindrical steel projectile is placed in series with a foam cylinder, followed by a foam crusher. Impact of the steel projectile

generates an exponentially decaying pressure pulse in the water while the plastic collapse of the foam exerts the necessary constant force on the piston; the function of the 'foam crusher' is to provide sufficient kinetic energy to drive the plastic collapse of the foam. The geometry of this compound striker induces a delay between the application of the exponentially decaying pressure pulse and that of the constant pressure associated with the plastic collapse of the foam. However, such delay is on the order of nanoseconds, therefore negligible compared to the decay time of the exponential pulse (in this study it was typically $\theta \approx 0.12\,\text{ms}$ ).

An alternative striker capable of generating the pressure pulses given by (eq. (4.1)) was also developed in this study. In this second striker a steel projectile is coupled to a hollow foam cylinder, free to slide along the steel projectile; such cylinder is backed by a hollow metallic striker ('foam crusher'). This compound projectile is accelerated in such a way that the steel projectile and the hollow foam cylinder make contact with the piston simultaneously; the plastic collapse of the foam exerts the necessary constant force on the piston, while impact of the steel projectile generates an exponentially decaying pressure pulse in water. The first striker (Fig. 4.4 b) was used in this study due to its relative simplicity.

Rohacell foams of different densities were employed to construct the compound strikers sketched in Fig. 4.4 (b) and their cross-section $A_F$ was chosen to guarantee a contact pressure at the foam-piston interface equal to the desired $p_{st}$, i.e. $A_F = A_P\left(p_{st}/\sigma_c\right)$, where $\sigma_c$ is the plastic collapse stress of the foam employed. In first approximation such collapse stress relates to the quasi-static yield stress of the foam $\sigma_Y$ and to the impact velocity $v_S$ as $\sigma_c = \sigma_Y + \rho_F v_S^{\,2}/\varepsilon_D$ (Deshpande & Fleck [27]). In the present study impact velocities were

low ($v_S < 20\,\mathrm{ms}^{-1}$) and $\sigma_c \approx \sigma_Y$. The quasi-static collapse strength of the different foams used was taken from Arezoo et al. [17] and the strain rate sensitivity of the foam was neglected, as reported by Arezoo et al. [18].

For the case of experiments at atmospheric pressure, i.e. $p_{st} = 0.1\mathrm{MPa}$, the loading pulse was generated in the water column by simply impacting the nylon piston by a cylindrical steel projectile, as used in Deshpande et al. [36].

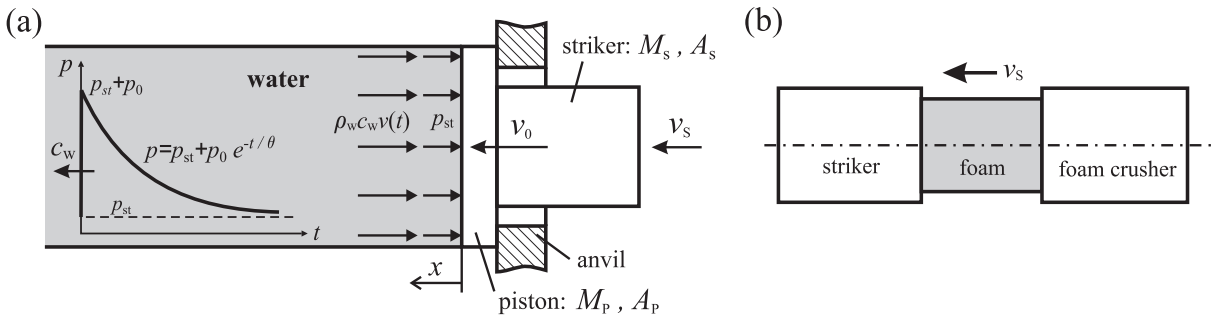



Fig. 4.4: Impact of the striker on a piston in contact with pressurised water (a); sketch of the compound steel-foam striker employed in this study (b).

Examples of the pressure waves generated in the water column are plotted in Fig. 4.5; dynamic pressure histories measured by the piezoelectric transducer placed at the left-hand side of the nylon piston are compared with the desired pulse (eq. (4.1)). Pressure histories generated by firing steel strikers of different mass at similar velocities are shown in Fig. 4.5 (a), for the case $p_{st} = 0.1\mathrm{MPa}$; the pressure decays exponentially to 0.1 MPa, as expected, and the decay time can be precisely adjusted by using strikers of different mass. Measurements (and corresponding predictions) for $p_{st} >> 0.1$ MPa are reported in Fig. 4.5 (b); in this case loading was induced by impact of a compound striker, as sketched in Fig. 4.4 (b). The generated pressure pulses have initial amplitudes of $p_{st} + p_0$ and decay exponentially to the initial pressure $p_{st}$, as required. Although measured peak pressures are slightly lower

than theoretical predictions but the agreement between experiments and predictions is satisfactory.

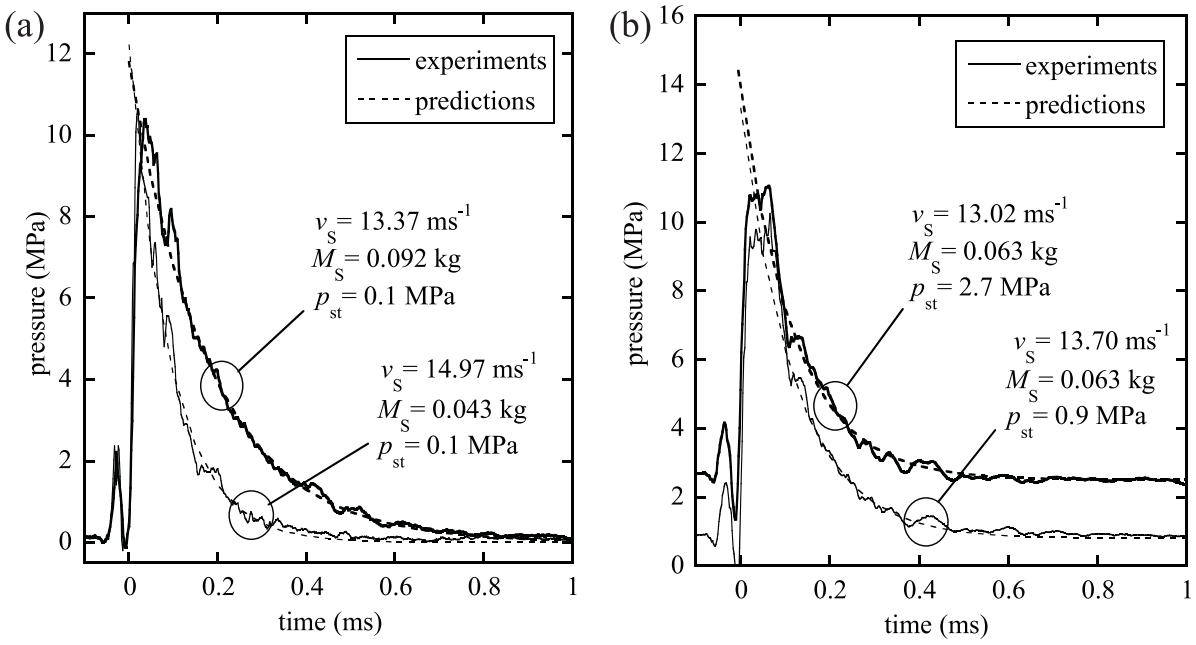



Fig. 4.5: Comparison between theoretical predictions and experimental measurements of the incident pressure versus time histories in water at (a) atmospheric pressure and (b) higher initial static pressure.

### 4.3.3 Propagation of shock waves in the compliant tube

The exponentially decaying pressure wave radiated by the nylon piston travels in the water column towards the specimen. The speed at which waves propagate in the tube depends on the density, geometry and stiffness of the acrylic tube employed. For the case of a rigid tube, waves propagate at the sonic speed of water ($c_w \approx 1498\,\mathrm{ms}^{-1}$); in contrast, if the tube undergoes significant hoop deformation and consequent change in diameter due to the passage of the pressure wave, pressure pulses propagate at lower speeds than the speed of sound in water; in addition, the pressure pulses progressively attenuate and distort as they propagate along the tube (Korteweg [50]).

Due to the relatively low Young's modulus of the acrylic tube ($E = 3.3\text{GPa}$), the wave speed in the tube was expected to be lower than the speed of sound in water; measurements of the wave speed, deduced from the pressure readings of the two transducers fitted on the tube (at relative distance of 1 m, Fig. 4.2), confirmed this. Measurements provided $c_w = 1000\,\text{ms}^{-1}$, significantly lower than sonic speed in water and in agreement with the predictions of Korteweg [50]; the observed amplitude attenuation of the pressure pulses after 1 m was approximately 5%, and the initial rise time of the pressure pulse was also observed to increase by around 5%; the decay time of the exponential pulse also increased by approximately 15%. Note that the mechanical coupling between the tube and the water column, by reducing the speed at which waves propagate, affects the calculation of the peak pressure $p_0$ and decay time $\theta$ of the generated pressure wave (eq. (4.5)). For this reason all calculations in this study were performed by using the measured wave speed $c_w = 1000\,\text{ms}^{-1}$.

## 4.4 Results and discussion

We proceed to present observations and results obtained with the apparatus described above. First we describe the response of fluid to shock loading of ridid plates, with emphasis on the phenomenon of cavitation; then, we examine the structural response and deduce the impulse imparted to these by the underwater shock.

### 4.4.1 Response of fluid

High-speed photography was employed to measure the position and time at which cavitation in water first occurs and the subsequent propagation of breaking fronts and closing fronts. We present photographic sequences from four selected experiments; experiments 1 and 2 are

performed in air-backed configuration while tests 4 and 5 are conducted with a water-backed arrangement, as described in Section 4.2.

Details of the masses of strikers and specimens, as well as impact velocities and corresponding characteristic of the loading pulses in each experiment are reported in Table 4.1. We include in this table the calculated FSI parameter $\psi = \rho_w c_w \theta / m$ (Taylor [4]) which is a non-dimensional measure of the mass, for a given loading pulse. The values of $\psi$ were chosen to match those associated to typical blast events on large-scale structures.

Table 4.1: Details of selected experiments performed in this study.

| test | configuration | $p_{st}$ (MPa) | $p_0$ (MPa) | $\theta$ (ms) | $\psi$ | $\bar{p}_{st,c}$ | $M$ (kg) | $M_s$ (kg) | $v_s$ ($ms^{-1}$) |
|---|---|---|---|---|---|---|---|---|---|
| 1 | air-backed | 0.1 | 14.9 | 0.12 | 1.13 | 0.467 | 0.061 | 0.063 | 16.3 |
| 2 | air-backed | 2.7 | 11.9 | 0.12 | 1.13 | 0.467 | 0.061 | 0.063 | 13.0 |
| 3 | air-backed | 0.9 | 12.5 | 0.12 | 1.13 | 0.467 | 0.061 | 0.063 | 13.7 |
| 4 | water-backed | 0.1 | 15.1 | 0.096 | 0.91 | 0.128 | 0.061 | 0.049 | 16.9 |
| 5 | water-backed | 1.1 | 13.1 | 0.096 | 0.91 | 0.128 | 0.061 | 0.049 | 14.7 |
| 6 | water-backed | 2.1 | 12.4 | 0.12 | 1.13 | 0.121 | 0.061 | 0.063 | 13.6 |
| 7 | air-backed | 0.1 | 14.7 | 0.12 | 1.94 | 0.557 | 0.036 | 0.063 | 13.6 |

(i) *Air-backed specimens.*

Experiment 1 was conducted in air-backed configuration ($p_{st} = 0.1\text{MPa}$, $\psi = 1.13$, $p_0 = 14.9\text{MPa}$) and the high-speed photographs obtained from this experiment are presented in Fig. 4.6; frame (a) shows the air-backed specimen in contact with water at the instant when the pressure wave, travelling from right to left, reaches the specimen ($t = 0$). In Fig. 4.6 (b) we observe that soon after the specimen has been set in motion, bubbles form in the water; initially these appear very close to the fluid-specimen interface but subsequently, they also form on the walls of the transparent tube. This indicates that cavitation initiates near the

specimen's wet face and subsequently extends towards the right into the fluid column by propagation of a breaking front (BF), as predicted theoretically by Kennard [3]. In Fig. 4.6 (c) we note that while the specimen accelerates further, the BF propagates towards the blast event and the bubbles have increased in size, as a result of the increased strain in the liquid. As time elapses (Fig. 4.6 d) the specimen decelerates due to air resistance; it can be predicted theoretically that a closing front (CF) must emerge from the fluid-structure interface and propagate towards the blast event, forcing collapse of the bubbles and leaving uncavitated water behind, as observed in the test. This CF continues to propagate and after a sufficiently long time the cavitated region completely disappears, as shown in Fig. 4.6 (e).

The high-speed photographs in Fig. 4.7 refer to experiment 2, which was conducted in air-backed configuration with $\psi = 1.13$, $p_{st} = 2.7\,\text{MPa}$ and $p_0 = 11.9\,\text{MPa}$, in order to explore the effect of an increased hydrostatic pressure in the water. Note that the specimen is now supported on the left-hand side by a Rohacell foam cylinder of diameter $d_F = 25\,\text{mm}$ and collapse strength $\sigma_c = 2.6\,\text{MPa}$.

The photograph in Fig. 4.7 (a) illustrates the configuration of the specimen at the instant when the incident pressure wave reaches the fluid-structure interface. For $p_{st} >> 0.1$ MPa the theoretical models presented in Chapter 3 predict onset of cavitation at a finite distance from the fluid-structure interface, rather than very close to this interface and Fig. 4.7 (b) shows that this is the case; cavitation initiates at a distance of approximately 45 mm from the specimen's wet face, and two breaking fronts emerge and propagate in two opposite directions at speeds in excess of the speed of sound, as predicted by Kennard [3], creating an extending pool of cavitated water. In Fig. 4.7 (c) we observe that the breaking front travelling towards the specimen arrests before reaching the fluid-structure interface and inverts its motion, becoming

a closing front and the strain in the cavitated water increases. In Fig. 4.7 (d) the closing front continues propagating and forcing collapse of the cavitation bubbles, and the cavitation zone completely disappears from the field of observation in Fig. 4.7 (e). The size of the bubbles (and hence the strain in the cavitated water) is significantly lower in this experiment, compared to experiment 1; this is due to the reduced displacement of the specimen, consequent to the higher initial pressure $p_{st}$ applied on the left-hand side.

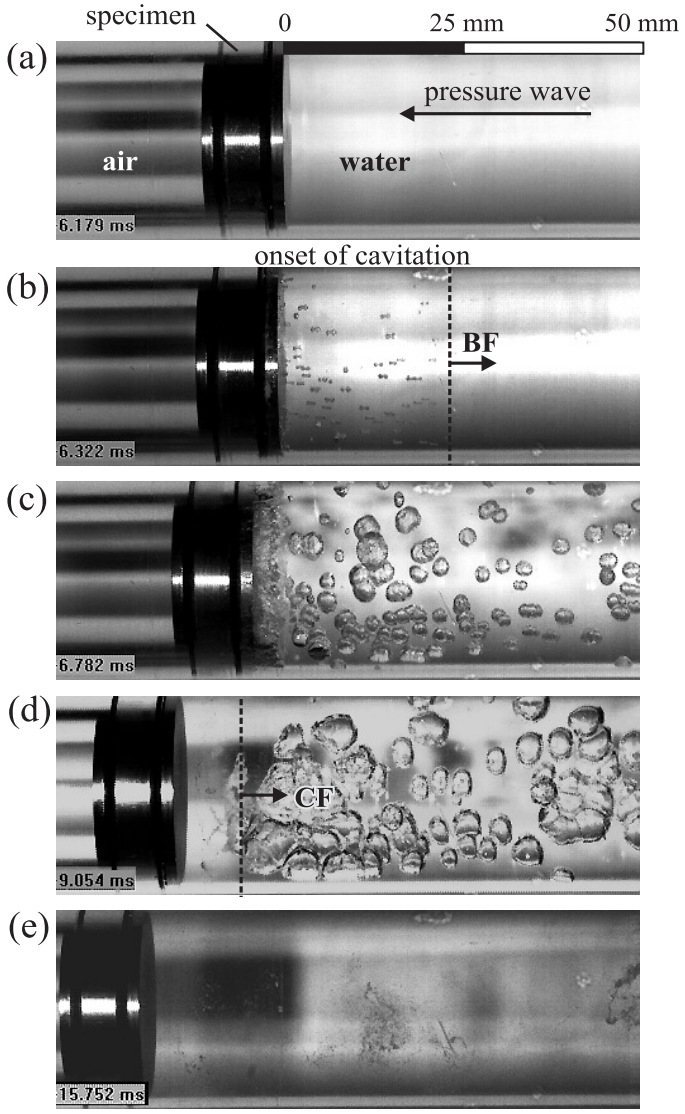



Fig. 4.6: High-speed photographs for experiment 1 ( $p_{st} = 0.1\,\text{MPa}$ , $\psi = 1.13$ , $p_0 = 14.9\,\text{MPa}$ ): (a) shock wave reaches the specimen; (b) onset of cavitation and propagation of a breaking front (BF); (c) further propagation of the BF and increase of strain in the liquid; (d) emergence of a closing front (CF) at the fluid-structure interface; (e) complete collapse of the cavitation zone.

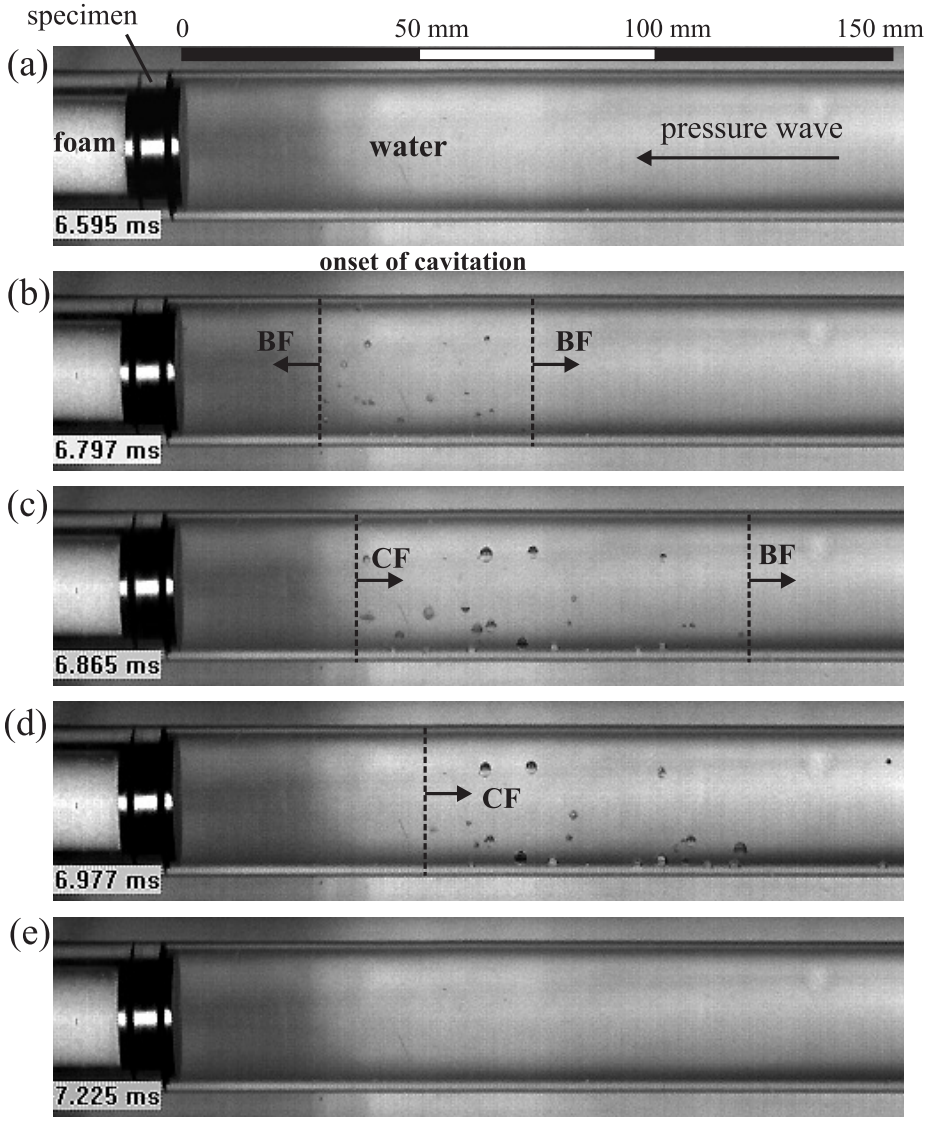



Fig. 4.7: High-speed photographs for experiment 2 ( $p_{st} = 2.7\,\text{MPa}$ , $\psi = 1.13$ , $p_0 = 11.9\,\text{MPa}$ ): (a) shock wave reaches the specimen; (b) onset of cavitation and propagation of two breaking fronts (BF); (c) propagation of one of the BFs and emergence of a closing front (CF); (d) further propagation of the CF; (e) complete collapse of the cavitation zone.

We now proceed to a quantitative comparison of the measurements conducted in this study with the predictions of the analytical models derived in Chapter 3, with focus on the cavitation processes in the water and for the case of air-backed specimens. A convenient way to perform this comparison is to plot the measured and predicted trajectories of breaking fronts and closing fronts as shown in Fig. 4.8 (a). High-speed photographs such as those

shown in Fig. 4.6 and Fig. 4.7 were used to measure the distance of the cavitation boundaries from the fluid-structure interface, as a function of time. The position of the breaking and closing fronts are determined from the horizontal coordinate of the edge of the first bubble visible in high-speed photographs. The limited temporal and spatial resolution of the high-speed camera used in the experiments introduced finite errors in the measurements of time and distance (on the order of the inter-frame time, $28\,\mu s$, and pixel size, $500\,\mu m$; this uncertainty in measurements is graphically indicated by a grey ellipse in Fig. 4.8 a). However, it is clear from Fig. 4.8 (a) that the theoretical predictions are in good agreement with the measurements.

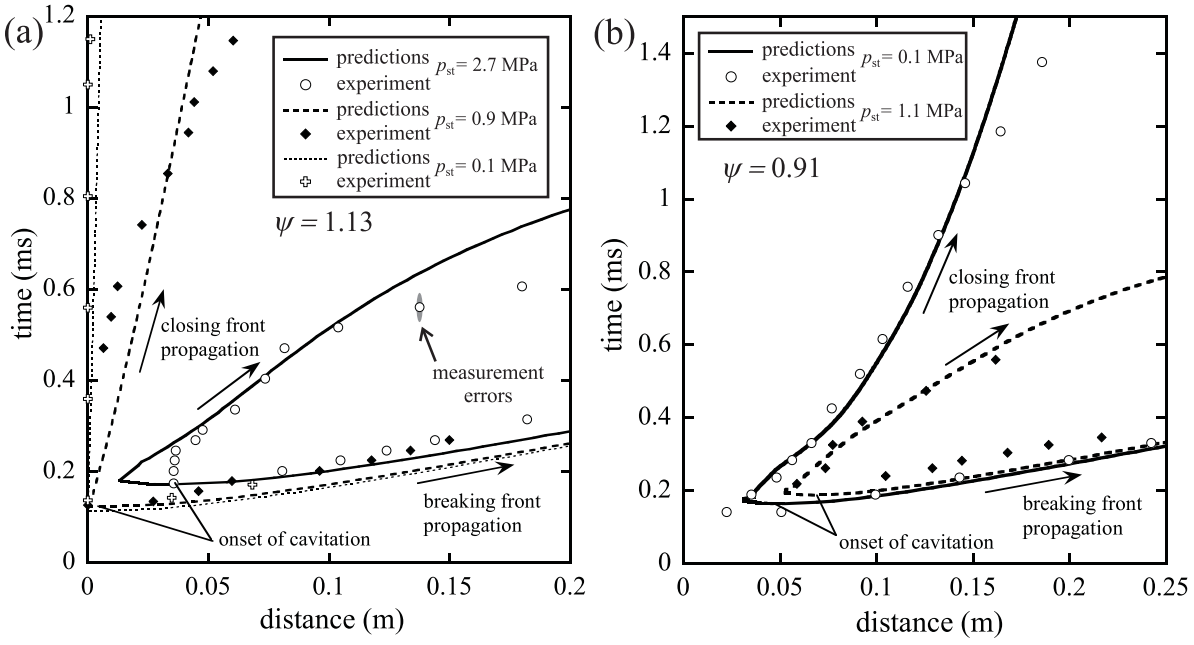



Fig. 4.8: (a) Measurements and analytical predictions of closing front and breaking front trajectories in a time versus distance chart for experiments 1 ($p_{st} = 0.1\text{MPa}$), experiment 2 ($p_{st} = 2.7\,\text{MPa}$) and experiment 3 ($p_{st} = 0.9\,\text{MPa}$), all of which conducted in air-backed configuration with $\psi = 1.13$. (b) Similar information for experiment 4 ($p_{st} = 0.1\text{MPa}$) and experiment 5 ($p_{st} = 1.1\text{MPa}$) both of which performed in water-backed configuration with $\psi = 0.91$.

The onset of cavitation and the trajectories of breaking fronts and closing fronts are presented in Fig. 4.8 (a) for experiments conducted in air-backed configuration at different initial static pressures by holding $\psi$ fixed, $\psi = 1.13$. For the case of experiment 1 ($p_{st} = 0.1\text{MPa}$) both measurements and predictions give onset of cavitation very close to the interface ($x = 0.5\text{mm}$) and propagation of BFs and a CF. Measurements and predictions for experiment 3 ($p_{st} = 0.9\text{MPa}$; the high-speed photographs associated with this test are not presented for the sake of brevity) indicate that cavitation initiates near the interface ($x = 6\text{mm}$) and is followed by propagation of two BFs; one of these subsequently inverts its direction of motion, hence becoming a CF. For the case of experiment 2, conducted at a higher initial static pressure ($p_{st} = 2.7\text{MPa}$), the onset of cavitation occurs at a much greater distance from the fluid-structure interface ($x$ = 45 mm, see also Fig. 4.7), in line with theoretical predictions; such predictions also capture accurately the velocity of the propagating cavitation fronts; in particular, the velocity of the closing front increases with increased initial pressure.

(ii) *Water-backed specimens.*

High-speed photographs for experiment 4 are presented in Fig. 4.9. In frame (a), the incident shock wave reaches the water-backed specimen, in contact with water at $p_{st} = 0.1\text{MPa}$ on both sides. The ensuing response of the fluid is similar to that observed for experiment 2 and presented in Fig. 4.7. In Fig. 4.9 (b) cavitation occurs at a distance $x = 23\text{mm}$ from the specimen and gives rise to propagation of two BFs in two opposite directions. The BF travelling away from the interface continues advancing further into the water column while the other BF arrests before reaching the specimen and inverts its motion becoming a CF, propagating away from the specimen and causing collapse of the bubbles in the cavitation

zone (Fig. 4.9 c). Cavitation occurs in the water column in contact with the specimen's back face (Fig. 4.9 d), in line with the findings of the analytical models presented in Chapter 3.

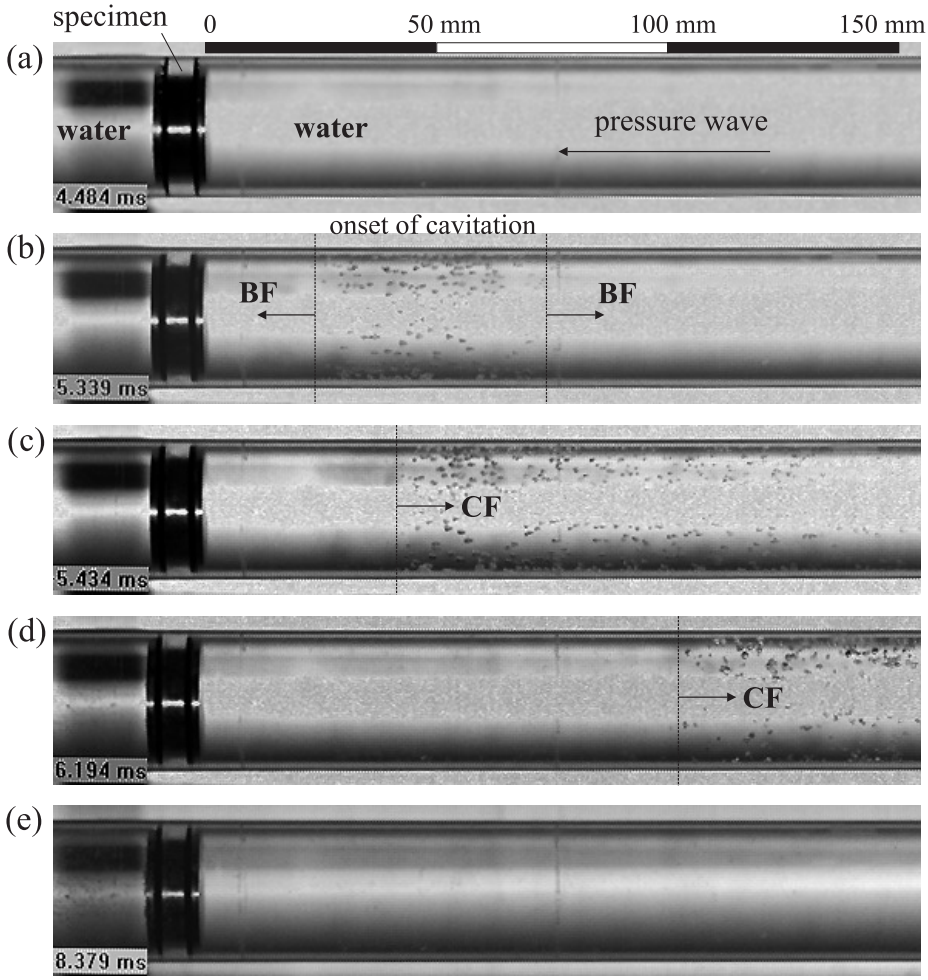



Fig. 4.9: High-speed photographs for experiment 4 ($p_{st} = 0.1\text{MPa}$, $\psi = 0.91$, $p_0 = 15.1\text{MPa}$): (a) shock wave reaches the specimen; (b) onset of cavitation and propagation of two breaking fronts (BF); (c) propagation of one of the BFs and emergence of a closing front (CF); (d) further propagation of the CF and cavitation at the specimen's back face; (e) complete collapse of the cavitation zone.

Experiment 5 was conducted in the same conditions as experiment 4 but with a higher initial hydrostatic pressure in the water, $p_{st} = 1.1\text{MPa}$. The fluid and specimen responses are presented in the high-speed photographs of Fig. 4.10. The sequence of events is similar to that observed in experiment 4; however, in this test the onset of cavitation occurs at increased distance from the fluid-structure interface ($x = 59\text{mm}$); in addition, the strain in water is

remarkably lower than in experiment 4, due to the reduced displacement of the specimen. Such observations are again in agreement with the predictions of Chapter 3.

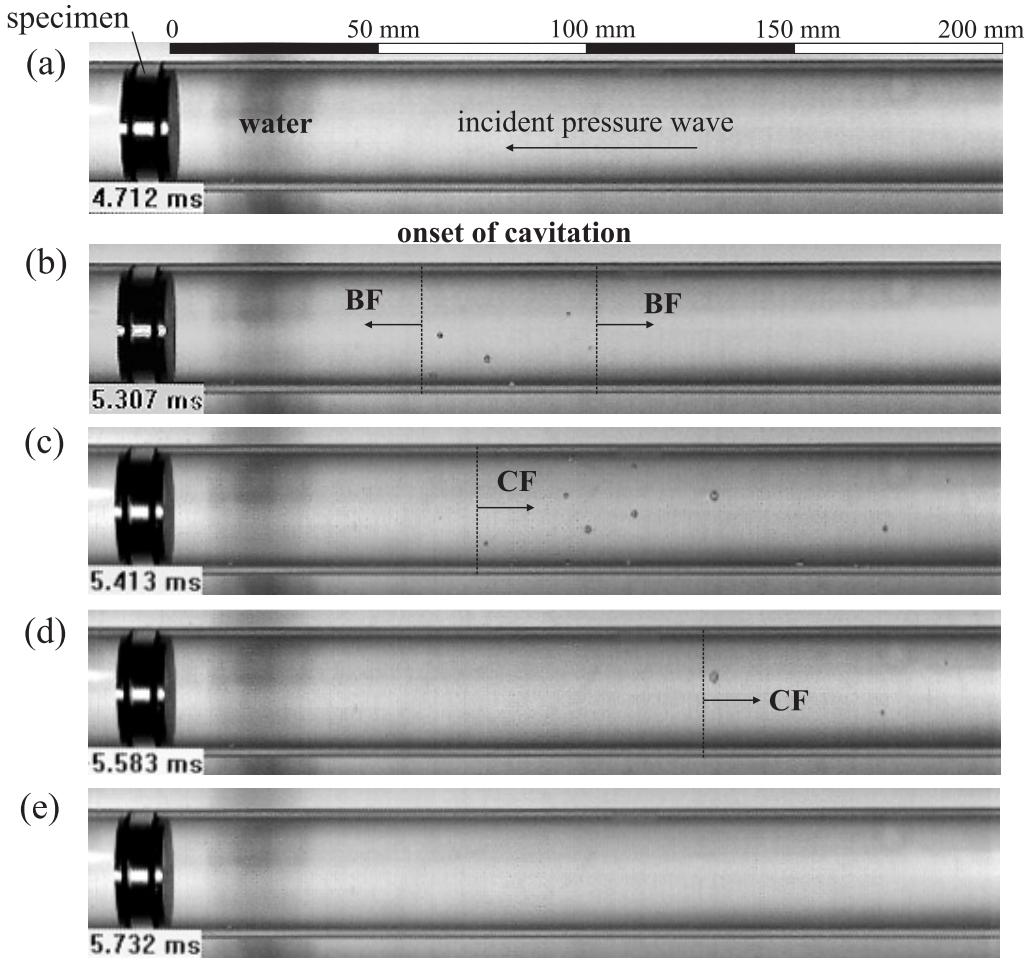



Fig. 4.10: High-speed photographs for experiment 5 ( $p_{st} = 1.1\,\text{MPa}$ , $\psi = 0.91$, $p_0 = 13.1\text{MPa}$ ): (a) shock wave reaches the specimen; (b) onset of cavitation and propagation of two breaking fronts (BF); (c) emergence of a closing front (CF); (d) further propagation of the CF; (e) complete collapse of the cavitation zone.

The trajectories of BFs and CFs measured in experiments 4 and 5 ( $p_{st} = 0.1\text{MPa}$ and $p_{st} = 1.1\text{MPa}$, respectively) are compared in Fig. 4.8 (b) with the theoretical predictions (Chapter 3). Excellent agreement between observations and analytical predictions is found. The theretical models also predicted that in the case of water-backed specimens a limit value

$\overline{p}_{st,c} = p_{st,c} / p_0$ exists beyond which cavitation in water is completely suppressed; this critical value is only a function of the parameter $\psi = \rho_w c_w \theta / m$ for the experiments reported here and is included in Table 4.1. In order to verify this prediction, an additional test was conducted at $\psi = 1.13$, $p_0 = 12.4\,\text{MPa}$ and $p_{st} = 2.1\,\text{MPa}$, giving $p_{st} / p_0 = 0.169 > \overline{p}_{st,c} = 0.121$ (experiment 6 in Table 4.1). The high-speed photographs for this test are omitted for the sake of brevity; however, no cavitation was observed in the experiment, in line with theoretical predictions.

(iii) *Volumetric strain field in the water.*

High-speed photographs have also been used to estimate the volumetric strain field in water. Such measurements are presented in Fig. 4.11 together with analytical predictions performed with the models of Chapter 3, for experiment 7 in Table 4.1 ($\psi = 1.94$, $p_{st} = 0.1\,\text{MPa}$, $p_0 = 14.7\,\text{MPa}$). The insert of Fig. 4.11 shows three high-speed photographs recorded in this experiment at three specific times. Each of the photographs was subdivided in three regions as indicated by the numbers 1, 2 and 3 in the figure (each of equal volume $V_w$). The diameters of all bubbles in each of the regions were measured and the volume of bubbles $V_c$ in each region was calculated by assuming that the observed bubbles can be idealised as hemispheres with centre on the internal surface of the tube, consistent with the notion that nucleation of cavitation bubbles occurs at this surface, driven by surface roughness; this is also consistent with observations by other authors (Benjamin & Ellis [45]). This allowed calculating the average true volumetric strain in water as

$$\eta = \ln\left(1 + V_c / V_w\right) \tag{4.6}$$

upon neglecting the small elastic contribution to this volumetric strain.

The chart in Fig. 4.11 presents the fluid strain measurements as a function of distance from the fluid-structure interface, together with predictions obtained from the analytical models of Chapter 3. Measurements are about 15% lower than the analytical predictions, however, they exhibit a similar trend; such discrepancy can be justified by the fact that not all bubbles emerging in the cavitated water can be seen in the high-speed photographs, since (i) some of these bubbles are hidden behind other bubbles and (ii) some bubbles are too small to be observed.

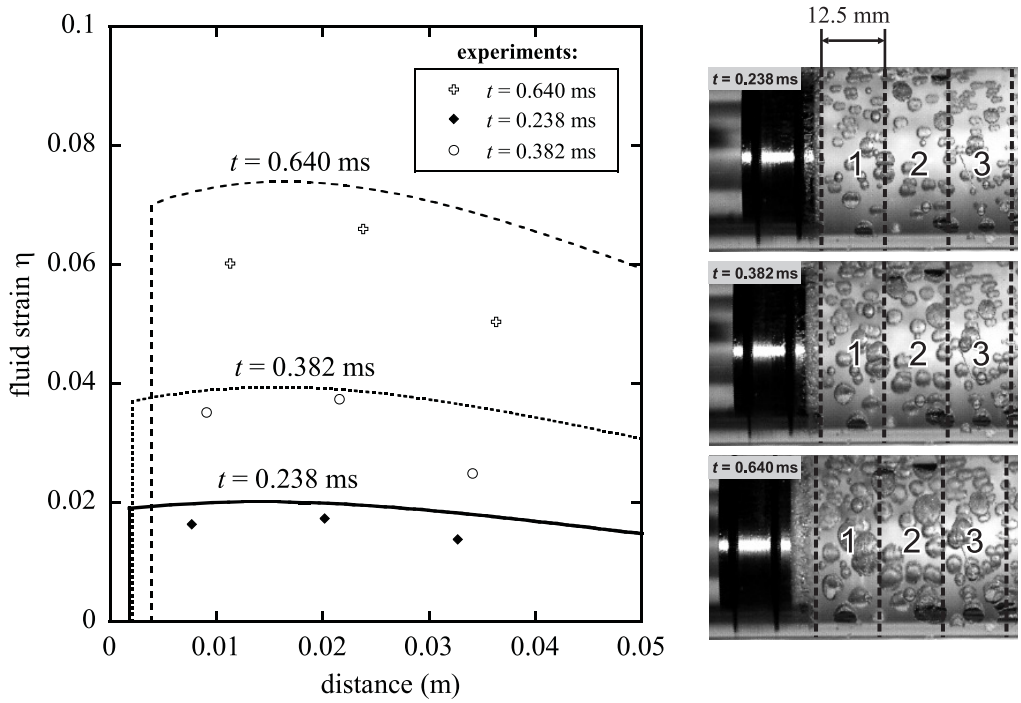



Fig. 4.11: Volumetric strain field in the water adjacent to the air-backed specimen in experiment 7 ($\psi = 1.94$, $p_{st} = 0.1\text{MPa}$, $p_0 = 14.7\,\text{MPa}$) measured at three specific instants corresponding to the high-speed photographs; the continuous lines represent analytical predictions obtained with the models presented in Chapter 3.

### 4.4.2 Response of the specimen

(i) *Air-backed plates.*

High-speed photographs allowed measuring the displacement versus time histories of the steel specimens consequent to blast loading. The intensity of the load imparted to an air-backed specimen, as quantified by the specific impulse (impulse per unit area) imparted to the specimen's front face, $I_f(t)$, can be deduced my measuring its velocity histories. Upon neglecting friction between O-rings and tube wall (frictional forces were measured to be <10 N), conservation of linear momentum dictates

$$I_f(t) = \int_0^t \left[ p_f(\tau) - p_{st} \right] \mathrm{d}\tau = mv(t) \tag{4.7}$$

where $p_f(t)$ is the time history of the pressure applied on the specimen's front face. The velocity histories $v(t)$ were extracted from the high-speed photographs. Note that eq. (4.7) is valid for any choice of $p_{st}$.

Measurements of non-dimensional time histories $\bar{I}_f(t) = I_f(t)/(2p_0\theta)$ are presented in Fig. 4.12 (a) for experiments 1 and 2 (Table 4.1), together with the predictions of the analytical models detailed in Chapter 3. These models predict a greater impulse than measured, with the difference being on the order of 15%; this can be justified by recalling that while analytical models assume a perfectly sharp incident shock wave, a finite rise time of such wave was observed in the experiments, together with a 5% attenuation of the incident peak pressure and an increase in decay time, due to propagation in the compliant shock tube. However, the agreement between measurements and predictions is more than satisfactory. Both analytical predictions and experiments show that an increase in static pressure results in lower displacement (displacement of the specimen is proportional to the area under the

$\bar{I}_f(t)$ curves); on the other hand, the peak value of $\bar{I}_f(t)$ is independent of the initial hydrostatic pressure $p_{st}$.

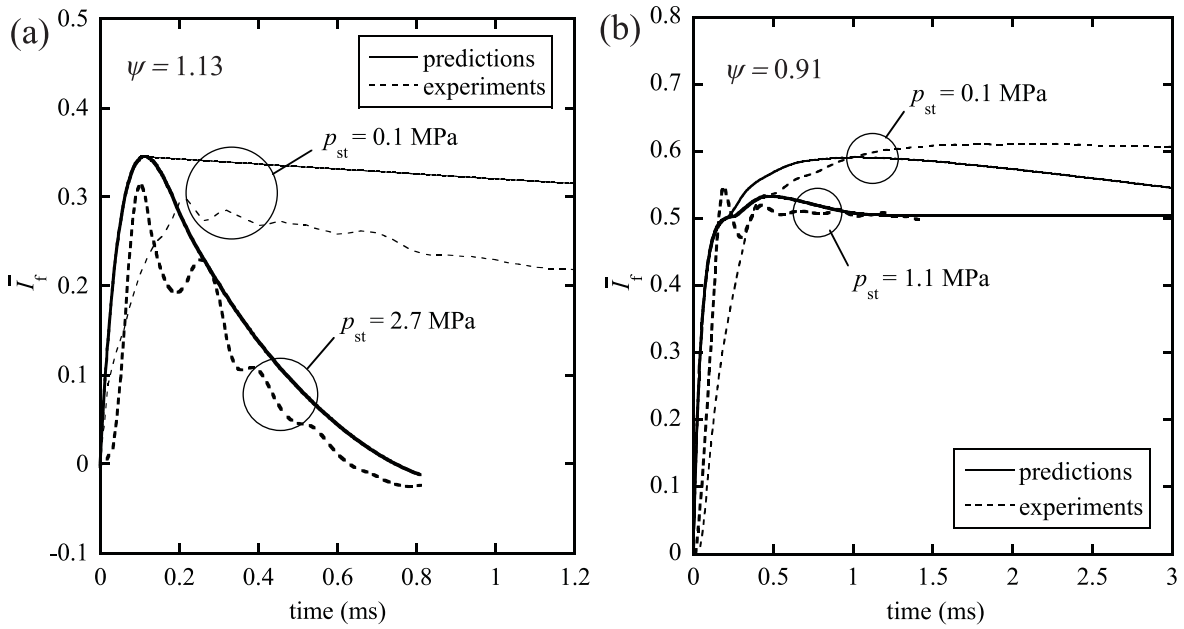



Fig. 4.12: (a) Time histories of the non-dimensional impulse $\bar{I}_f = I_f/(2p_0\theta)$ for experiment 1 ($p_{st} = 0.1\text{MPa}$) and experiment 2 ($p_{st} = 2.7\,\text{MPa}$) conducted in air-backed configuration with $\psi = 1.13$; analytical predictions are included. (b) Similar information for experiment 4 ($p_{st} = 0.1\text{MPa}$) and experiment 5 ($p_{st} = 1.1\text{MPa}$) conducted in water-backed specimen configuration with $\psi = 0.91$; analytical predictions are compared to measurements.

(ii) *Water-backed plates.*

When a water-backed specimen is set in motion by the incident shock wave, a pressure wave is radiated into the water column in contact with the specimen's back face. Given the low specimen velocity observed in our experiments, the acoustic approximation can be employed and the pressure at the specimen's back face can be written as

$$p_b(t) = p_{st} + \rho_w c_w v(t). \tag{4.8}$$

(measurements of the pressure history at the specimen back face combined with high-speed photography allowed validation of eq. (4.8)). Now write conservation of linear momentum for

the specimen to obtain the specific impulse applied to the front face as a function of the specimen's velocity history

$$\begin{aligned} & mv(t) = \int_0^t \left[ p_f(\tau) - p_b(\tau) \right] d\tau = I_f(t) - \rho_w c_w \int_0^t v(\tau) d\tau \Rightarrow \\ & \Rightarrow I_f(t) = mv(t) + \rho_w c_w \int_0^t v(\tau) d\tau \end{aligned} \tag{4.9}$$

Equation (4.9) was employed in order to plot the non-dimensional specific impulse applied to the front face $\overline{I}_f(t)$ in experiments 4 and 5 (see Table 4.1), as shown in Fig. 4.12 (b). This figure includes predictions computed with the analytical models described in Chapter 3, which are in good agreement with the measurements. Contrary to what observed for air-backed plates, both measurements and predictions suggest that the maximum value of $\overline{I}_f(t)$ can be decreased by increasing the static pressure $\overline{p}_{st}$.

### 4.4.3 Sensitivity of impulse to mass and initial static pressure

The peak value $\overline{I}_{f,\max} = \max\left[ \overline{I}_f(t) \right]$ can be considered as a measure of the severity of the structural loading induced by an underwater blast event on a rigid plate. A large series of experiments was performed in this study in order to measure the sensitivity of $\overline{I}_{f,\max}$ to (i) the specimen mass, quantified by the non-dimensional fluid-structure interaction parameter $\psi = \rho_w c_w \theta / m$ and to (ii) the initial hydrostatic pressure, expressed in non-dimensional terms by $\overline{p}_{st} = p_{st} / p_0$. In the following, the measured sensitivity is compared to that predicted by the analytical models of Chapter 3, for both air-backed and water-backed specimens.

The dependence of $\overline{I}_{f,\max}$ upon $\psi$ is presented in Fig. 4.13 (a) for a hydrostatic pressure of $p_{st} = 0.1\text{MPa}$ and both air-backed and water-backed plates. Different values of $\psi$ were

obtained in the experiments by varying either the areal mass of the specimen $m$ or the combined areal mass of the striker and piston $m_{S,P}$ (thereby varying the decay time $\theta$, eq.(4.5)). For both problems the maximum impulse $\overline{I}_{f,\max}$ decreases by increasing $\psi$, and experiments are in excellent agreement with theoretical predictions.

Water-backed plates are subject to higher blast impulses than air-backed plates of equal mass and the reduction in applied impulse with decreasing plate mass is less pronounced if the structure is in contact with water on both sides. The experimental scatter is higher in tests on water-backed plates due to the small displacements of these plates, leading to less accurate measurements of $v(t)$.

We now examine the sensitivity of $\overline{I}_{f,\max}$ to $\overline{p}_{st}$, for two selected values of $\psi$ and for both air-backed and water-backed rigid plates. In Fig. 4.13 (b), measurements and predictions by the analytical models of Chapter 3 are shown and are found in good agreement. As discussed above and shown in Fig. 4.12 (a), both experiments and theoretical models show that $\overline{I}_{f,\max}$ is insensitive to the initial static pressure for the case of air-backed plates and a reduction in applied impulse of more than 50% is achieved if the parameter $\psi$ is increased from 1.13 to 4.25, in line with what shown in Fig. 4.13 (b).

In contrast, the impulse imparted on water-backed plates is only mildly sensitive to $\psi$ and $\overline{I}_{f,\max}$, gradually decreases as $\overline{p}_{st}$ increases, stabilising at $\overline{I}_{f,\max} = 0.5$ for non-dimensional static pressures $\overline{p}_{st}$ beyond a critical value $\overline{p}_{st,c}(\psi)$. This was predicted by Schiffer et al. [51], who showed that when $\overline{p}_{st} \geq \overline{p}_{st,c}(\psi)$ cavitation in the fluid is completely suppressed

and $\bar{I}_{f,\max} = 0.5$ irrespective of $\psi$. It is clear from what has been shown above that the theoretical predictions of Chapter 3 are accurate.

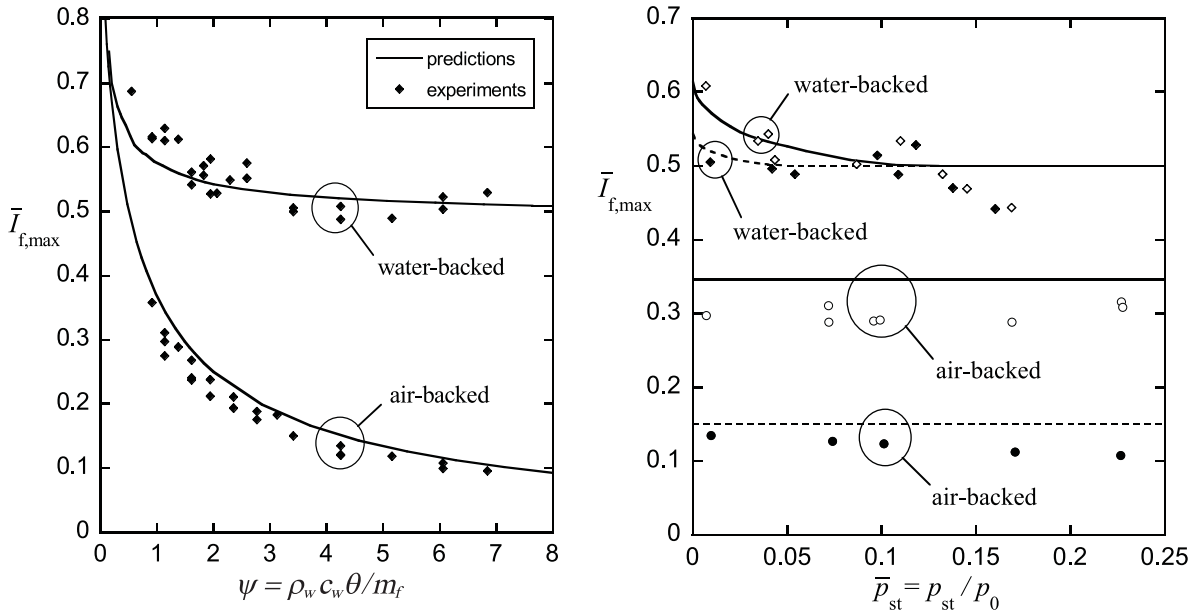



Fig. 4.13: (a) Maximum non-dimensional impulse $\bar{I}_{f,\max}$ as a function of $\psi$ for experiments performed with both air-backed and water-backed plates at $p_{st} = 0.1\text{MPa}$; analytical predictions are included for comparison. (b) $\bar{I}_{f,\max}$ as a function of the non-dimensional static pressure $\bar{p}_{st}$, for experiments performed on both air-backed and water-backed plates; two different choices of $\psi$ are considered and measurements are compared with analytical predictions.

## 4.5 Conclusions

We have presented a novel experimental technique to produce controlled blast loading in liquids subject to an initial hydrostatic pressure, in order to mimic, at a laboratory scale, structural loading consequent to explosions in deep water. This technique has been employed to investigate the response to exponentially decaying underwater shock waves of both air-backed and water-backed unsupported rigid plates, and to measure the effects of the initial hydrostatic pressure on the cavitation process in the water and on the response of the plates.

The apparatus developed in this chapter allowed visualising for the first time the nucleation and propagation of cavitation fronts initiated by FSI in a blast event and their interaction with the loaded structure; it also allowed measuring the strain field in cavitated water regions consequent to FSI, providing experimental evidence for the theoretical predictions of Kennard [3]. Experimental results were compared to the predictions of the theoretical models developed in Chapter 3 and we concluded that these models are accurate and capable of capturing all details of the response of both fluid and structure to underwater blast in deep water.

The main conclusions from this study are the following:

- for both air-backed and water-backed rigid plates loaded by exponentially decaying blast waves, an increase in initial hydrostatic pressure causes first cavitation in the fluid to occur at increasing distance from the fluid-structure interface; breaking fronts emerge from the point of first cavitation and propagate at supersonic speeds. The breaking front travelling towards the structure can arrest and invert its direction of motion, hence becoming a closing front and moving at subsonic speed.
- for given incident blast wave and initial static pressure, air-backed plates are imparted less impulse than water-backed plates; the impulse imparted to air-backed plates can be greatly reduced by reducing the mass of the plate, while a smaller reduction in imparted impulse is observed by reducing the mass of water-backed plates.
- the peak impulse imparted to air-backed plates is insensitive to the initial hydrostatic pressure while that imparted to water-backed plates decreases with increasing static pressure.

The experimental technique presented in this chapter is suitable to investigate the blast response of different types of structures, in which both deformation and FSI are two-

dimensional or three-dimensional in nature; it can also be employed to examine the performance of blast-mitigators, such as sandwich plates or multi-walled structural systems and to study their effect on FSI. We shall examine these problems in the following chapters.

# Chapter 5

# The One-dimensional Response of Sandwich Plates to Blast in Deep and Shallow Water

## 5.1 Introduction

Sandwich panels are potential candidates for the construction of naval hulls because they are low in weight, high in stiffness and capable of absorbing kinetic energy via mechanical deformation processes in the core. Underwater blast loading of sandwich plates has been recently examined by several authors [22, 23, 29, 52]. They concluded that sandwich plates can outperform monolithic structures of equal mass in terms of blast resistance. Some authors [25, 26, 28] have investigated this topic in more detail and developed design maps to aid the selection of blast resistant and light-weight sandwich designs. However, some important engineering questions concerning underwater blast loading of sandwich panels still remain unanswered. For example, only very little is known about the performance of water-backed sandwich plates in a blast event, particularly in deep water environment, where the hydrostatic fluid pressure can remarkably affect FSI as well as structural loading histories.

In this chapter, the 1D response of air-backed and water-backed sandwich plates to blast loading in deep and shallow water is examined. The sandwich plates under investigation are

composed of metallic face sheets and low-density foam cores (polymeric or metallic). Underwater blast experiments will be performed by using the transparent shock tube apparatus presented in Chapter 4 and the evolution of the cavitation process as well as face sheet motion and core compression will be observed by means of high-speed photography. A combination of dynamic pressure measurements and analysis of high-speed photographs will be employed to deduce the impulse imparted to the sandwich specimens in order to quantify the severity of structural loading and hence the blast performance of the specimens. Finite element simulations will be performed in accordance to the experiments and their predictions will be compared with the measurements.

## 5.2 Specimen design and manufacture

In this study five different types of sandwich specimens are considered and their core properties and dimensions are given in Table 5.1. The sandwich cores were machined to diameter $d_c$ and thickness $c$ from either closed-cell aluminium foam (Alporas) or polymer foam (Rohacell) and were bonded to the face sheets using epoxy adhesive (*Scotch Weld*). The Alporas foam employed herein had a density $\rho_c = 110\,\mathrm{kgm^{-2}}$ and pore size $d_p = 3.5\,\mathrm{mm}$. Rohacell foams are closed-cell foams made from polymetacrylimide (PMI) and are available in a range of densities. In this study, three different core densities are considered, $\rho_c = 51\,\mathrm{kgm^{-2}}$, $\rho_c = 71\,\mathrm{kgm^{-2}}$ and $\rho_c = 110\,\mathrm{kgm^{-2}}$ (pore sizes are listed in Table 5.1).

All specimens had aluminium face sheets machined to diameter $d_f = 27\,\mathrm{mm}$ and thickness $h_f = 8\,\mathrm{mm}$; two circular grooves were included in each face sheet and fitted with O-rings to allow sealing of the water columns, as illustrated in Fig. 5.2 (b). For experiments conducted in air-backed configuration, blank back face sheets of thickness $h_b = 7.8\,\mathrm{mm}$ were used to

reduce frictional forces; masses of the face sheets varied between 11.4 g and 11.8 g, thus $M_f = M_b = 11.6\,\mathrm{g}$ for simplicity.

Table 5.1: Properties and dimensions of the sandwich foam cores considered in this study

| | foam material | foam density $\rho_c$ (kgm$^{-3}$) | foam pore size $d_p$ (mm) | core diameter $d_c$ (mm) | core width $c$ (mm) | compressive strength $\sigma_c$ (MPa) | densification strain $\varepsilon_D$ | Young's modulus $E_c$ (MPa) |
|---|---|---|---|---|---|---|---|---|
| 1 | Alporas | 215 | 3.50 | 26 | 10 | 2.00 | 0.56 | 600 |
| 2 | Alporas | 215 | 3.50 | 23 | 14 | 0.85 | 0.65 | 300 |
| 3 | Rohacell | 51 | 0.38 | 20 | 35 | 0.44 | 0.89 | 35 |
| 4 | Rohacell | 71 | 0.96 | 25.5 | 30 | 1.10 | 0.86 | 100 |
| 5 | Rohacell | 110 | 0.93 | 25.5 | 20 | 2.80 | 0.85 | 160 |

Each type of specimen was loaded in compression across the face sheets in a screw-driven testing machine (*Zwick Z250*) at a strain rate of $10^{-4}\,\mathrm{s}^{-1}$, in order to determine their quasi-static compressive response. The through thickness compressive force was gauged with a load cell (maximum load 150 kN) and a laser extensometer was used to measure the core strain.

The chart in Fig. 5.1 (a) shows the quasi-static stress-strain response of specimens 1 and 2 (see Table 5.1), both of which with cores made from Alporas foam. Specimen 2 ($d_c = 23\,\mathrm{mm}$, $c = 14\,\mathrm{mm}$) attained a flat stress plateau at $\sigma_c = 0.85\,\mathrm{MPa}$ and started to harden at a compressive strain $\varepsilon = 0.4$ until full densification was reached at $\varepsilon_D = 0.65$, arbitrarily defined as the point on the curve where $\sigma(\varepsilon_D) = 10\sigma_c$. In contrast, for specimen 1 ($d_c = 26\,\mathrm{mm}$, $c = 10\,\mathrm{mm}$) a decreased densification strain of $\varepsilon_D = 0.56$ was measured and the plateau stress increased out of proportion to $\sigma_c = 2\,\mathrm{MPa}$. This can be justified by size effects in the compressive response of foam materials when the foam's thickness is on the order of its pore size, as reported in Chen & Fleck [53].

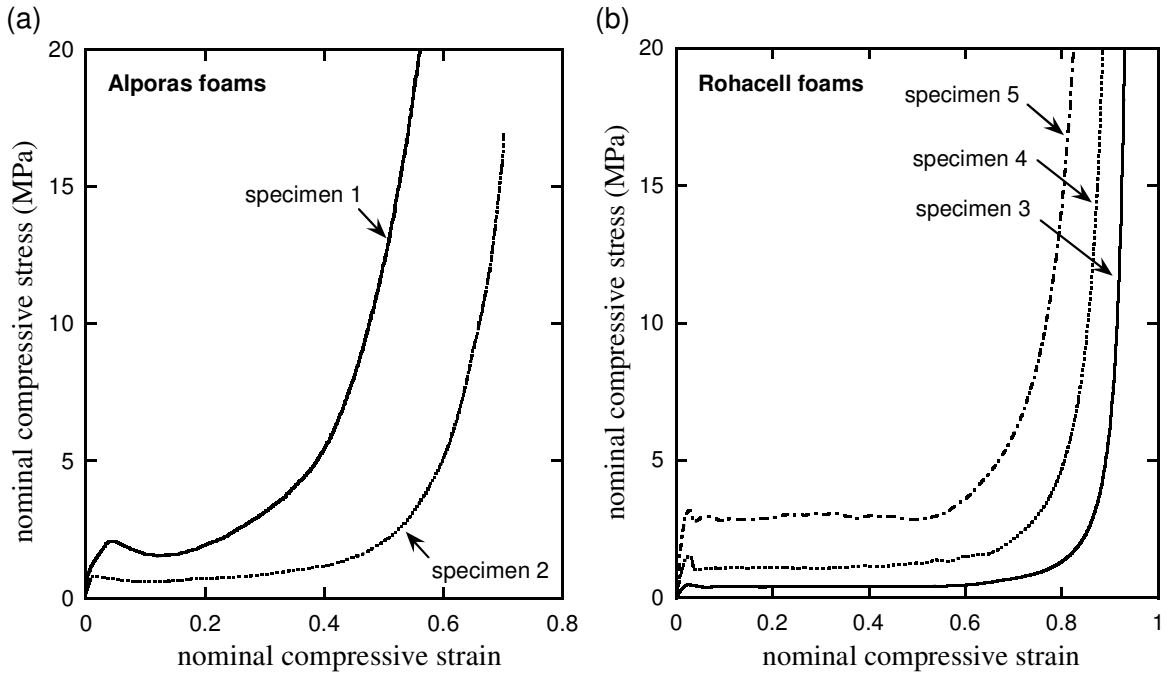



Fig. 5.1: Measurements of the nominal compressive stress versus strain response obtained from quasi-static compression tests with (a) specimens 1 and 2 (Alporas) and (b) specimens 3-5 (Rohacell).

Similar information is shown in Fig. 5.1 (b) for Rohacell foam cored sandwich plates (specimens 3, 4 and 5 listed in Table 5.1). Upon yielding, the stress-strain curves of all specimens exhibit a slight drop but quickly approach the level of the plateau stress. In all cases shown in this figure, strain hardening commences at $\varepsilon \approx 0.6$. It can be seen that foams of higher densities reach higher levels of compressive strength, $\sigma_c$, and show a minor decrease in densification strain $\varepsilon_D$ compared to the foams of lower densities.

Numerical values of $\sigma_c$, $\varepsilon_D$ and $E_c$ (compressive Young's modulus) were deduced from the measurements and are included in Table 5.1 for each type of specimen. It merits comment that in all compression tests the transverse plastic strain $\varepsilon_{22}^p$ was negligible compared to the longitudinal plastic strain $\varepsilon_{11}^p$ and thus the plastic Poisson's ratio $\nu_p = -\varepsilon_{22}^p / \varepsilon_{11}^p$ can be taken as zero.

## 5.3 Experimental technique

The shock tube apparatus presented in Chapter 4 was employed to perform underwater blast experiments on sandwich specimens and a sketch of the laboratory setting is shown in Fig. 5.2 (a) for an experiment conducted in water-backed configuration. The apparatus consists of a water shock tube made from a transparent material and allows observation of structural motion and cavitation processes in the fluid by means of high-speed photography. Experiments were conducted with two different specimen configurations, as described below.

(i) *Water-backed configuration.*

As shown in Fig. 5.2 (b), the specimen was located in the centre of the shock tube, separating the bore hole into two sections. Both front and back sections were filled with filtered tap water and the tube ends were capped with sealing nylon pistons; bleed valves were included in the pistons to evacuate air-bubbles trapped in the water columns prior to the dynamic experiment. A hydrostatic pressure field is induced in the water by loading the sliding back piston with a compressive force $F$ ; such force was applied by using a screw-driven loading fixture fitted with a resistive load cell to measure the inital hydrostatic pressure induced in the fluid. For experiments with water at atmospheric pressure, such force was not applied.

(ii) *Air-backed configuration.*

Specimens were located in the shock tube approximately 200 mm from the distal end. The tube was then filled with filtered tap water and closed by a nylon piston at the opposite end.

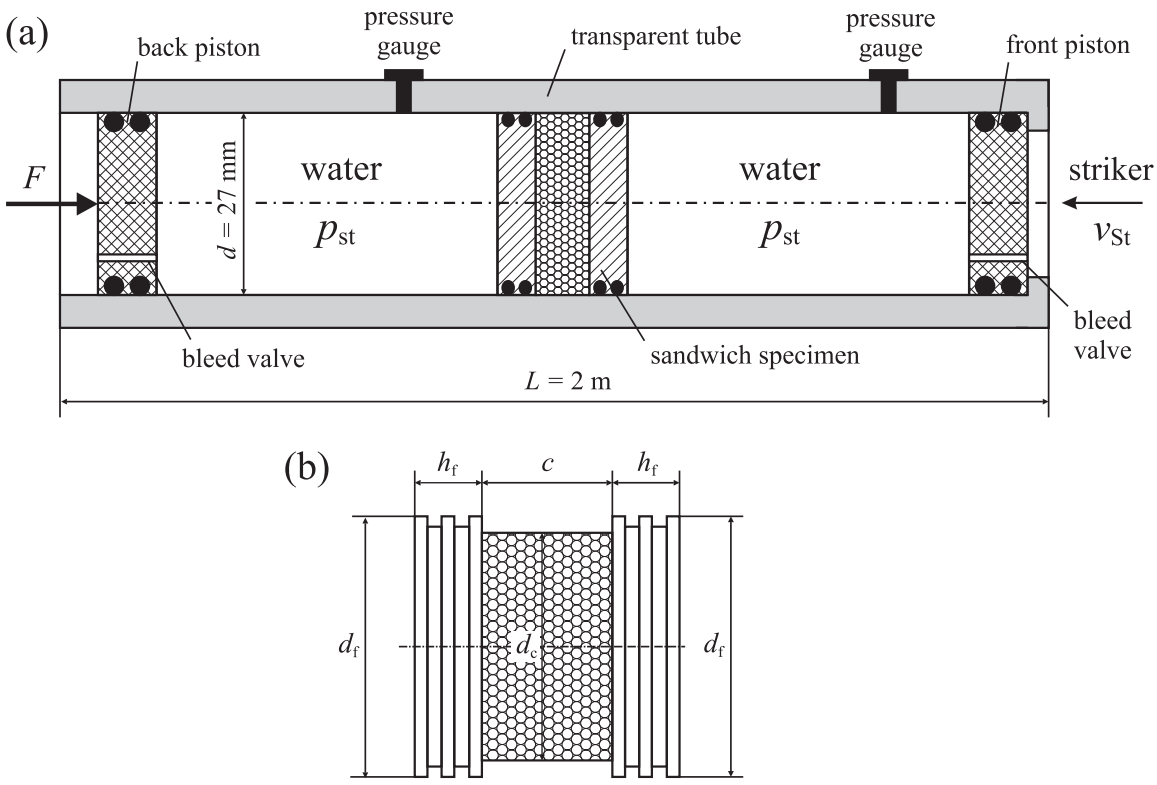



Fig. 5.2: (a) Schematic of the laboratory setup used for performing underwater shock experiments on a water-backed sandwich specimen and (b) details of the specimen geometry.

Exponentially decaying pressure shock waves were generated in the tube by firing a compound striker (consisting of a foam cylinder encased betwen two metallic skins) at one of the pistons; this technique has been used and described in Chapter 4. For the case of experiments at atmospheric pressure, i.e. $p_{st} = 0.1\text{MPa}$, pressure waves were generated by impacting the nylon piston with a monolithic steel projectile, as described by Deshpande et al. [36]. The pressure pulses in the shock tube were measured using piezoelectric pressure gauges (*PCB Piezoelectronics Inc.)* located at a distance approximately 120 mm from the front piston (see Fig. 5.2 a). A second transducer of same type was placed at a distance of 120 mm from the centre of the tube (on the distal side) in order to measure pressure waves radiated from the specimen's back face sheet during the dynamic experiments. The speed of pressure wave

propagation in the compliant shock tube was measured to be $c_w = 1053\,\mathrm{ms}^{-1}$ which is significantly lower than the speed of sound in open water due to tube bulging effects [50].

A 'Vision Research (V7.1)' high-speed phantom camera with a set of 'CORDIN' flash lights was used to observe face sheet motion, core compression as well as cavitation processes in the water.

## 5.4 Finite element models

Dynamic FE simulations were performed in ABAQUS/Explicit [49] in order to validate the observations and measurements obtained from the underwater shock experiments. A schematic of the problem geometry is shown in Fig. 5.3 for a sandwich plate in contact with water on both face sheets. The water columns were chosen sufficiently long to guarantee that the FSI phase finished before pressure wave reflections at the free ends of the fluid columns could reach the structure.

Four-noded, plane, quadrilateral elements with reduced integration (type CPE4R in ABAQUS) were used to discretise the fluid columns and the structure and 'Tie constraints' were used to connect the nodes at each interface. FE models for air-backed sandwich plates follow a similar scheme with the back fluid column absent.

The constitutive response of water was modelled using a Mie-Gruneisen equation of state with a linear Hugoniot relation, such to give a linear-elastic relationship between fluid pressure and compressive volumetric strain (see Section 3.3). Assuming that the vapour pressure of water is negligible, cavitation was modelled by setting tensile failure in ABAQUS to zero [49], i.e. assuming a cavitation pressure $p_c = 0$. Density and speed of sound in water were taken as $\rho_w = 1000\,\mathrm{kgm}^{-3}$ and $c_w = 1053\,\mathrm{ms}^{-1}$, respectively, and the shear modulus was

assumed to be zero. For the water columns the element size in the direction of wave propagation was set to 0.1 mm, while one single element was used to discretise the water columns along the width. Note that the effect of the mesh size on peak pressure and rise time of the incident shock wave has been examined in Section 3.3 and is reported in Fig. 3.6.

The aluminium face sheets were modelled as linear elastic solids with density $\rho_f = 2700\,\mathrm{kgm}^{-3}$, Young's modulus $E_f = 69\,\mathrm{GPa}$ and Poisson's ratio $\nu_f = 0$; an element size of 0.3 mm was used along the through-thickness direction of the face sheets.

The constitutive description of the foam materials are as follows. The elastic response was taken as isotropic with density $\rho_c$, Young's modulus $E_c$, Poisson's ratio $\nu_c = 0$ and yield strain $\varepsilon_{cY}$. Numerical values for $\rho_c$, $E_c$ and $\varepsilon_{cY}$ are listed in Table 5.1. The plastic behaviour was modelled using the 'crushable foam' plasticity model with isotropic hardening, originally developed by Deshpande & Fleck [54] and available in ABAQUS [49]. Upon assuming normality of plastic flow to the yield surface, the yield ratio $k_Y = \sigma_c^0 / p_c^0$ (with $\sigma_c^0$ the initial yield stress in uniaxial compression and $p_c^0$ the yield stress in hydrostatic compression) can be written in terms of the plastic Poisson's ratio $\nu_p$

$$k_Y = \sqrt{3\left(1-2\nu_p\right)}. \tag{5.1}$$

For the foam materials considered herein $\nu_p = 0$, thus $k_Y = \sqrt{3}$ (eq. (5.1)). Note that the strain hardening curves were specified according to the stress-strain curves obtained from the quasi-static compression tests (see Fig. 5.1).

The strain rate dependency of the foams is modelled as follows. Dynamic experiments on Rohacell and Alporas foams (Arezoo et al. [18], Dannemann & Lankford [55]) revealed that the dependence of the yield stress upon the strain rate can be neglected. However, when a foam material is subjected to intense shock loading, the compressive dynamic response entails

propagation of a plastic shock wave leading to additional energy dissipation in the core. As proposed by Radford et al. [56], we introduce linear strain rate dependency in the constitutive model by employing an overstress visco-plastic model

$$\dot{\varepsilon}^{pl} = \left( \frac{\hat{\sigma}_c - \sigma_c}{\beta} \right) \tag{5.2}$$

where $\hat{\sigma}_c$ is the yield stress at nonzero strain rate and $\beta$ is the viscosity to satisfy energy conservation

$$\beta = \frac{l_s \rho_c \Delta v}{\varepsilon_D} \tag{5.3}$$

with $l_s$ the width of the plastic shock wave, $\rho_c$ and $\varepsilon_D$ density and densification strain of the foam material, respectively, and $\Delta v$ the velocity jump across the plastic shock. The shock width $l_s$ is assumed to be on the order of the foam's pore size (Table 5.1) and the velocity jump $\Delta v$ is taken as the maximum front face velocity $v_{f,\max}$. Experimental measurements (see Section 5.5.2) revealed that $v_{f,\max}$ can be approximated by the velocity imparted to a free-standing rigid plate, $v_{f,0}$, of mass equal to the sandwich. According to Taylor [4], such velocity can be expressed as

$$v_{f,0} = \frac{2 p_0 \theta \psi_f^{\psi_f/(1-\psi_f)}}{m_f} \tag{5.4}$$

where $\psi_f$ is a non-dimensional parameter related to the areal mass of the front face sheet $m_f$ and is defined as

$$\psi_f = \frac{\rho_w c_w \theta}{m_f}. \tag{5.5}$$

In order to implement this constitutive relationship in the FE model, a Cowper-Symonds overstress power law [49]

$$\dot{\varepsilon}^{pl} = Y\left(\frac{\bar{\sigma}_c}{\sigma_c} - 1\right)^{\lambda} \tag{5.6}$$

was used. Upon setting $\lambda = 1$ in eq. (5.6) and combining eqs. (5.6) and (5.2), the multiplier $Y$ can be written as

$$Y = \frac{\sigma_c}{\beta}. \tag{5.7}$$

To ensure accurate resolution of the stress and strain gradients across the plastic shock wave, an element size of $l_s/12$ was chosen to discretise the foam core in through-thickness direction.

The transverse displacements of all nodes were constrained to zero (see Fig. 5.3) and the presence of initial hydrostatic pressure was modelled by inducing initial stress fields in the fluid columns, $\sigma_{\mathrm{x}} = \sigma_{\mathrm{y}} = \sigma_z = -p_{st}$, as well as in the core and face sheets, $\sigma_{\mathrm{x}} = -p_{st}$. In order to equilibrate the fluid-structure system prior to shock loading, a constant traction $p_{st}$ was applied on fluid-columns, face sheets and sandwich core.

The incident shock wave was generated by imposing a pressure boundary condition $p(t) = p_0 \mathrm{e}^{-t/\theta}$ at the free end of the front water column. Peak pressure $p_0$ and decay time $\theta$ were chosen in accordance to the measurements performed in the experiments (Table 5.2).

To reduce artificial energy dissipation associated to large volumetric straining in ABAQUS, the bulk viscosity in the core was set to zero and reduced to 20% of the default values in the water columns and face sheets.

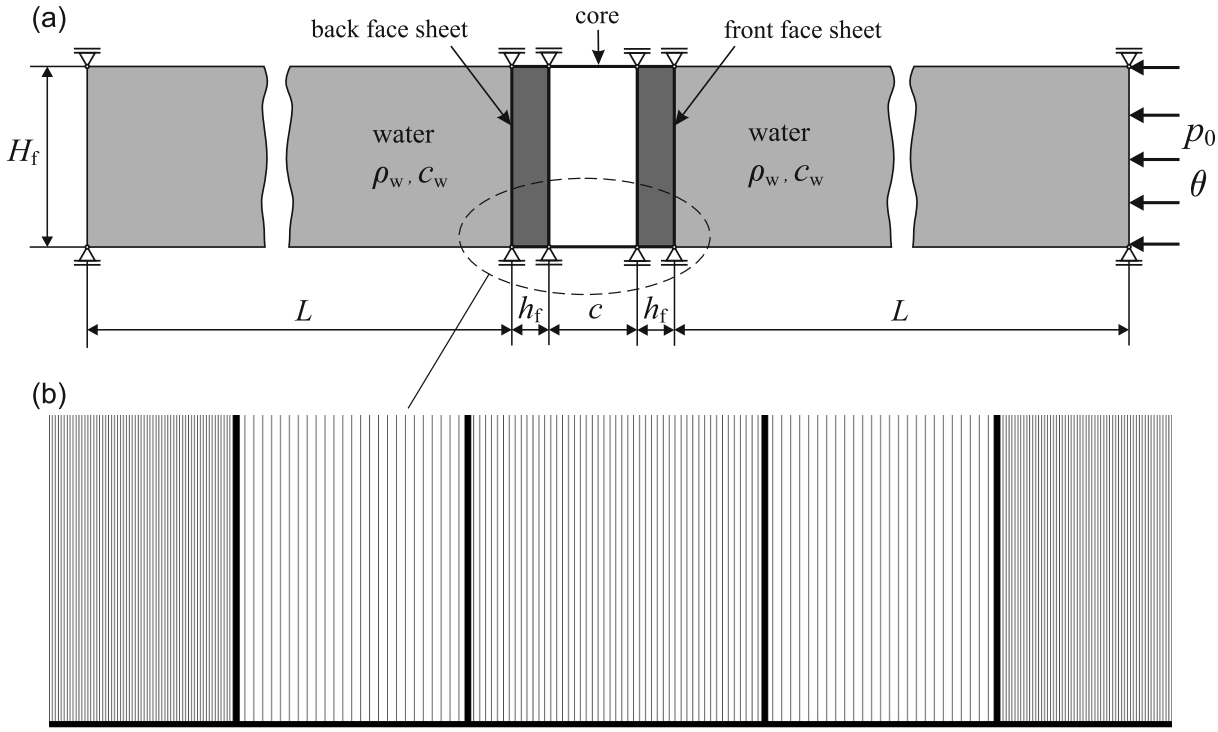



Fig. 5.3: (a) Schematic of the FE model used to simulate the 1D response of a water-backed sandwich plate subjected to loading by a shock wave at the front face sheet with initially unpressurised fluid-columns. The FE models for air-backed sandwich plates follow a similar scheme, with the fluid column attached to the plate's back face sheet absent. (b) Detail of the mesh used for a simulation performed for a water-backed experiment with specimen 1 (Alporas foam core, see Table 5.1).

## 5.5 Results

### 5.5.1 Fluid response

In this section we present high-speed photographic sequences obtained from selected experiments and describe the cavitation phenomena taking place in the fluid consequent to blast loading. Then we employ the high-speed photographs to measure trajectories of closing fronts (CFs) and breaking fronts (BFs) and we compare these measurements with predictions obtained from detailed FE simulations.

Details of geometric and physical properties of the cores employed, total masses of specimens, characteristics of the generated pressure pulses as well as the initial hydrostatic

pressure used in each experiment are listed in Table 5.2. In addition, we include in this table numerical values for the normalised crush strength $\bar{\sigma}_c = \sigma_c / p_0$, the normalised static pressure $\bar{p}^*_{st} = p_{st}/\sigma_c$ as well as the FSI parameter [4]

$$\psi = \frac{\rho_w c_w \theta}{m} \tag{5.8}$$

related to the areal mass of the total sandwich, $m = 2m_f + m_c$. Note that the values of $\psi$ were chosen to correlate with those associated to underwater blast loading of real-size naval structures.

Table 5.2: Details of selected experiments performed in this study

| test | specimen arrangement | core material | $d_c$ (mm) | $p_{st}$ (MPa) | $p_0$ (MPa) | $\theta$ (ms) | $M$ (g) | $\psi$ | $\sigma_c/p_0$ | $p_{st}/\sigma_c$ |
|---|---|---|---|---|---|---|---|---|---|---|
| 1 | water-backed | Alporas | 26 | 0.1 | 11.4 | 0.145 | 25.4 | 3.5 | 0.175 | 0.05 |
| 2 | water-backed | Rohacell 71 | 25.5 | 0.1 | 11.4 | 0.145 | 24.5 | 3.6 | 0.096 | 0.09 |
| 3 | air-backed | Alporas | 26 | 0.1 | 8.1 | 0.11 | 25.6 | 2.6 | 0.25 | 0.05 |
| 4 | air-backed | Rohacell 71 | 25.5 | 0.1 | 11.1 | 0.145 | 24.4 | 2.8 | 0.1 | 0.09 |
| 5 | water-backed | Alporas | 26 | 1.05 | 8.8 | 0.12 | 25.8 | 2.6 | 0.23 | 0.53 |
| 6 | water-backed | Rohacell 71 | 25.5 | 0.72 | 9.2 | 0.12 | 24.3 | 2.8 | 0.12 | 0.66 |

**(i) Water-backed sandwich plates.**

In Fig. 5.4 (a) we present a sequence of high-speed photographs obtained from experiment 1 which was performed on a water-backed sandwich specimen with an Alporas foam core (*specimen 1*, $\sigma_c = 2\,\text{MPa}$). The experiment was conducted with $p_0 = 11.4\,\text{MPa}$ and $\theta = 0.145\,\text{ms}$ without pressurisation of the water columns prior to shock loading, thus $p_{st} = 0.1\,\text{MPa}$. In frame 1 of Fig. 5.4 (a), the incident shock wave, travelling from the right to the left, reaches the specimen's front face. Subsequently, the front face sheet is set in motion and bubbles emerge in the water column at a finite distance from the fluid-structure interface, as shown in frame 2 (Fig. 5.4 a), and two BFs start propagating into opposite directions with

supersonic speed, rapidly opening a pool of cavitated water. Note that these observations are consistent with the theoretical findings of Kennard [3]. The BF travelling away from the specimen continues propagating and leaves the field of observation while the breaking front approaching the sandwich specimen reaches the fluid-structure interface. The resistance offered by the sandwich core forces the front face sheet to decelerate; consequently, the cavitation front contiguous to the specimen inverts its direction of motion and becomes a CF [3], forcing collapse of the cavitation bubbles and leaving uncavitated water behind, as illustrated in frame 3 (Fig. 5.4 a ). We also note that the bubbles increase in size as time elapses owing to increased strain in the cavitated fluid induced by the displacement of the front face sheet. The CF continues propagating and leaves the field of observation, as shown in the last frame of Fig. 5.4 (a).

Experiment 2 ( $p_0 = 11.4\,\text{MPa}$ , $\theta = 0.145\,\text{ms}$ , $p_{st} = 0.1\text{MPa}$ ) was performed on a water-backed sandwich specimen comprising a Rohacell foam core $\sigma_c = 1.1\text{MPa}$ (*specimen 4*, $\sigma_c = 1.1\text{MPa}$ ). High-speed photographs recorded in this experiment are illustrated in Fig. 5.4 (b) for four selected instants. Frame 1 shows the specimen and the fluid columns at the instant when the incident shock wave reaches the front face sheet. The impact of this wave on the sandwich specimen results in rapid acceleration of the front face sheet. Subsequently, cavitation bubbles emerge in the water very close to the fluid-structure interface and this cavitation zone expands by propagation of two supersonic BFs, as seen in frame 2 (Fig. 5.4 b). It merits comment that the BF travelling away from the plate could not be captured in this photographic sequence owing to the limited temporal resolution of the high-speed camera used in this experiment. However, it can be observed that the BF approaching the structure reaches the fluid-structure interface, subsequently inverts its direction of motion and becomes

a CF immediately thereafter due to front face sheet deceleration induced by plastic core compression (see frame 3). While the core is further compressed, the CF continues propagating and leaves the field of observation, as seen in frame 4. Now compare Fig. 5.4 (a) and Fig. 5.4 (b): frame 3 shows that the core compression $\varepsilon_c$ is significantly larger in Fig. 5.4 (b), owing to the relatively low compressive strength of the sandwich specimen used in this experiment, $\sigma_c = 1.1\text{MPa}$; the increase in $\varepsilon_c$ also increases the fluid strain in the cavitated water which is proportional to the size of the cavitation bubbles.

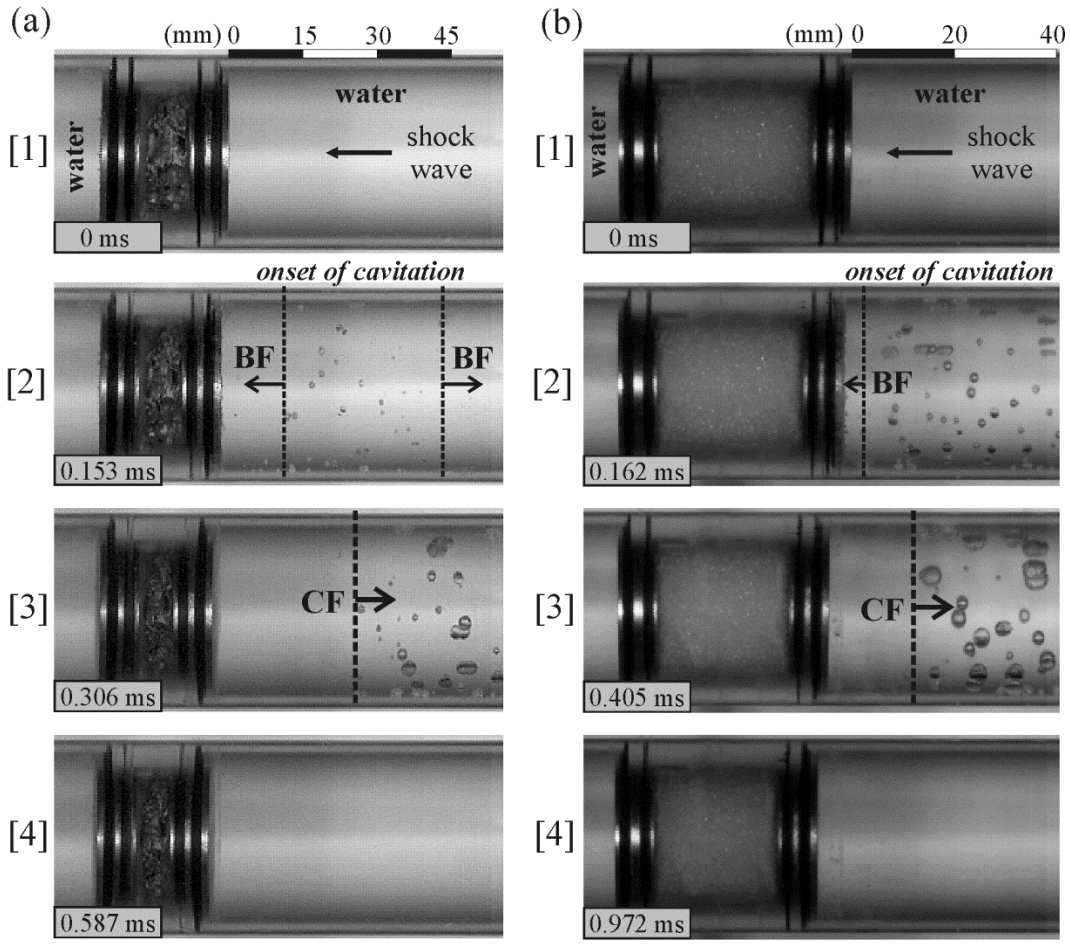



Fig. 5.4: (a) High-speed photographic sequence for experiment 1 (Alporas foam): (1) shock wave reaches the water-backed sandwich specimen; (2) onset of cavitation and propagation of two breaking fronts (BF); (3) emergence of a closing front (CF); (4) complete collapse of the cavitated region; (b) similar information for experiment 2 (Rohacell foam).

High-speed photographs, such as presented in Fig. 5.4, allow measuring trajectories of BFs and CFs. We now proceed to present such measurements together with predictions obtained from detailed FE simulations. To perform this comparison it is instructive to plot the measured and predicted cavitation front trajectories in a distance versus time chart, as shown in Fig. 5.5 for experiments 1 and 2. Recall that the corresponding high-speed photographs are shown in Fig. 5.4 (a) and (b), respectively. In the experiments, the positions of the cavitation fronts were determined by measuring the distance between the fluid-structure interface and the edge of the first bubble visible in the cavitated region. Note that the CF and BF velocities, denoted as $c_{CF}$ and $c_{BF}$ , respectively, are inversely proportional to the slopes of the trajectories plotted in Fig. 5.5. The limited spatial and temporal resolution of the high-speed camera used in these experiments (interframe time $\Delta t_i = 27\,\mu\text{s}$ and pixel size $\Delta x_i = 300\,\mu\text{m}$) introduced finite errors in the time and distance measurements; this uncertainty is indicated by the grey ellipse in Fig. 5.5. However, it can be seen that the experimental measurements are captured with good accuracy. For both experiments 1 and 2 the measured and predicted trajectories show that the points of first cavitation are located at a finite distance from the fluid-structure interface, as indicated in Fig. 5.5 by $x_{c,1}$ and $x_{c,2}$, respectively. Moreover, $x_{c,1} > x_{c,1}$ and $c_{CF,1} > c_{CF,2}$.

In addition, we include in Fig. 5.5 analytical predictions of cavitation front trajectories for the case of a water-backed rigid plate of mass equal to the total sandwich ($M = 24.5\,\text{g}$) subject to loading by a shock wave of $p_0 = 11.1\text{MPa}$ and $\theta = 0.145\,\text{ms}$; these predictions were performed using the 1D FSI models developed in Chapter 3. Now compare the rigid plate and sandwich trajectories: the effect of sandwich construction is to substantially decrease the distance of first cavitation ($x_{c,1} \ll x_{c,r}$, $x_{c,2} \ll x_{c,r}$) and such discrepancy in FSI also affects

structural loading as well as the impulse imparted to the structure. This will be examined in Section 5.6.3.

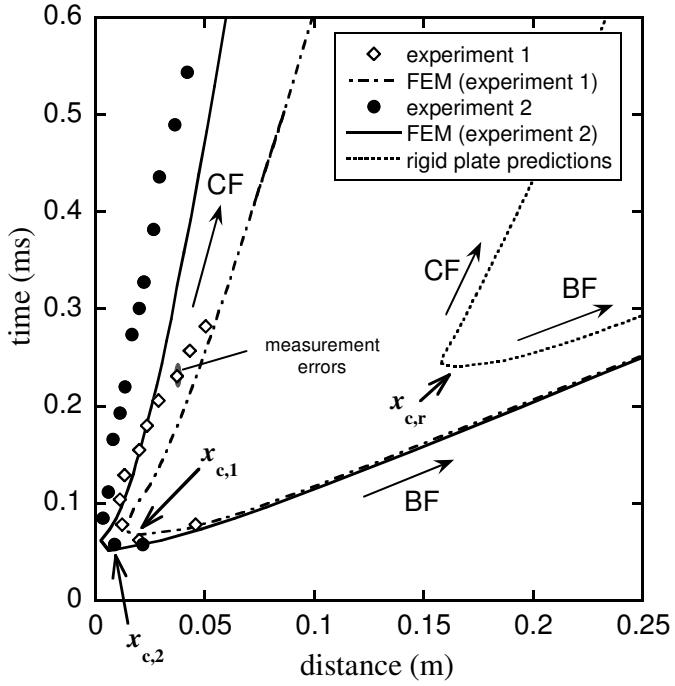



Fig. 5.5: Measurements and FE predictions of closing front (CF) and breaking front (BF) trajectories plotted in a time versus distance chart for experiments 1 and 2, both conducted in water-backed configuration; analytical predictions for a rigid plate of mass equal to the total sandwich ($M = 24.5\,\mathrm{g}$, $p_0 = 11.4\,\mathrm{MPa}$, $p_{st} = 0.1\,\mathrm{MPa}$, $\theta = 0.145\,\mathrm{ms}$) are included for comparison.

**(ii) Air-backed sandwich plates.**

In Fig. 5.6 (a) we present high-speed photographs recorded in experiment 3 performed on an air-backed sandwich plate with an Alporas foam core $\sigma_c = 1.1\mathrm{MPa}$ (*specimen 1*, $\sigma_c = 1.1\mathrm{MPa}$) with $p_{st} = 0.1\mathrm{MPa}$. In frame 1, the generated shock wave ($p_0 = 8.1\mathrm{MPa}$, $\theta = 0.11\mathrm{ms}$) reaches the front face of the specimen. The ensuing cavitation process is similar to what observed in the water-backed experiment (see Fig. 5.4 a) : cavitation initiates at a finite distance from the front face sheet and a cavitation zone spreads by propagation of two BFs. Contrary to the water-backed experiment, the breaking front approaching the structure

inverts its motion before reaching the front face sheet, as shown in frame 2, and becomes a closing front, propagating away from the structure into the cavitated region, with relatively low speed, as seen in frames 3 and 4.

Similar information is shown in Fig. 5.6 (b) for experiment 4 ( $p_{st} = 0.1\text{MPa}$ , $p_0 = 11.4\text{MPa}$ , $\theta = 0.145\text{ms}$ ) performed on an air-backed sandwich specimen comprising a Rohacell foam core (*specimen 4,* $\sigma_c = 1.1\text{MPa}$ ). It can be seen that the sequence of cavitation phenomena is similar to what observed in experiment 3 and described above. However, the cavitation process is located at decreased distance from the fluid-structure interface, which can be attributed to the reduced compressive strength ( $\sigma_c = 1.1\text{MPa}$ ) of the specimen used in experiment 4.

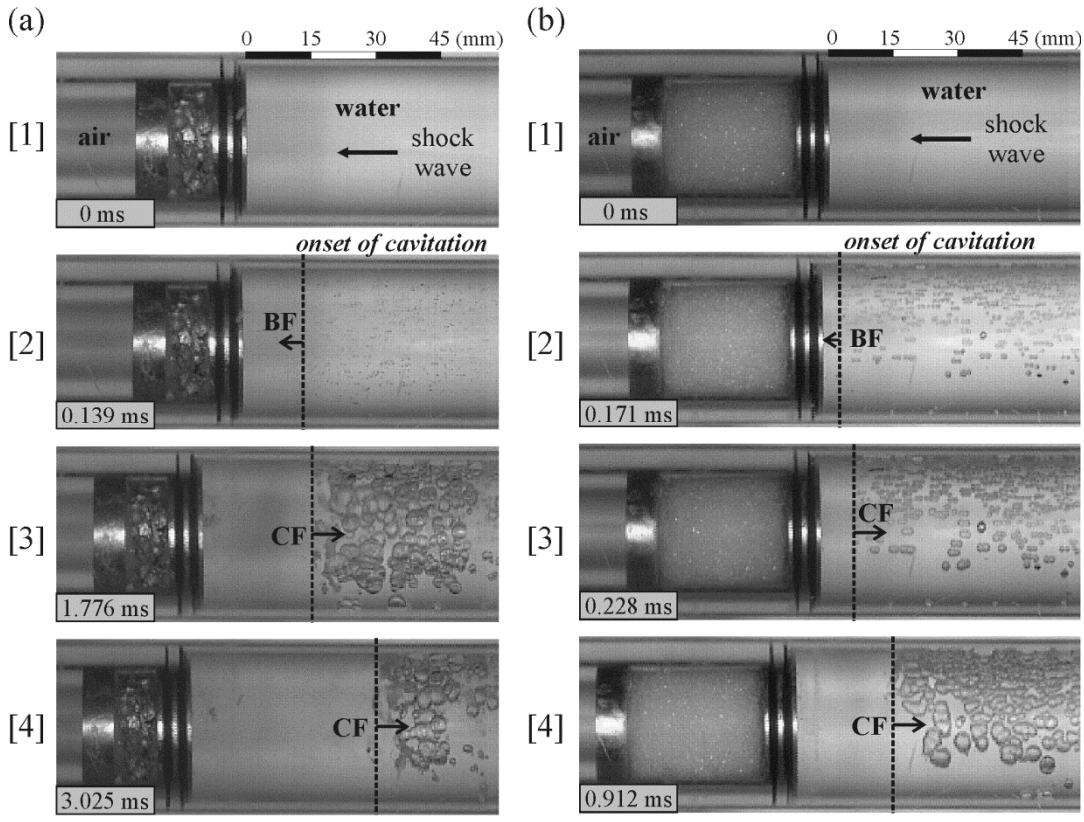



Fig. 5.6: (a) High-speed photographic sequence for experiment 3 (Alporas foam): (1) shock wave reaches the air-backed sandwich specimen; (2) onset of cavitation and propagation of a breaking front (BF); (3) emergence of a closing front (CF); (4) further propagation of the closing front (CF); (b) similar information for experiment 4 (Rohacell foam).

Measurements and FE predictions of CF and BF trajectories for experiments 3 and 4 are plotted in Fig. 5.7. The measurements show that the cavitation zone did not reach the fluid-structure interface in both experiments, and the FE predictions confirm this. Moreover, the closing fronts propagated in the experiments at approximately constant speed, $c_{CF,3}$ and $c_{CF,4}$, respectively. Although the FE models predict much larger velocities $c_{CF,3}$ and $c_{CF,4}$ at the points where the BFs invert their direction of motion, the predicted CFs nearly arrest at $x \approx 0.04\,\text{m}$ and subsequently approach the measured trajectories.

In addition, we include in this figure CF and BF trajectories obtained from analytical predictions (see Chapter 3) performed for an air-backed rigid plate of mass equal to the total sandwich ($M = 24.4\,\text{g}$, $p_{st} = 0.1\text{MPa}$, $p_0 = 11.1\text{MPa}$, $\theta = 0.145\,\text{ms}$). Now compare the rigid plate and sandwich predictions: the effect of sandwich construction is to locate the point of first cavitation at increased distance from the fluid-structure interface, i.e. $x_{c,3} > x_{c,r}$ and $x_{c,4} > x_{c,r}$, in line with previous theoretical studies [27-29]. The effect of this phenomenon on the impulse imparted to the structure will be investigated in Section 5.6.1

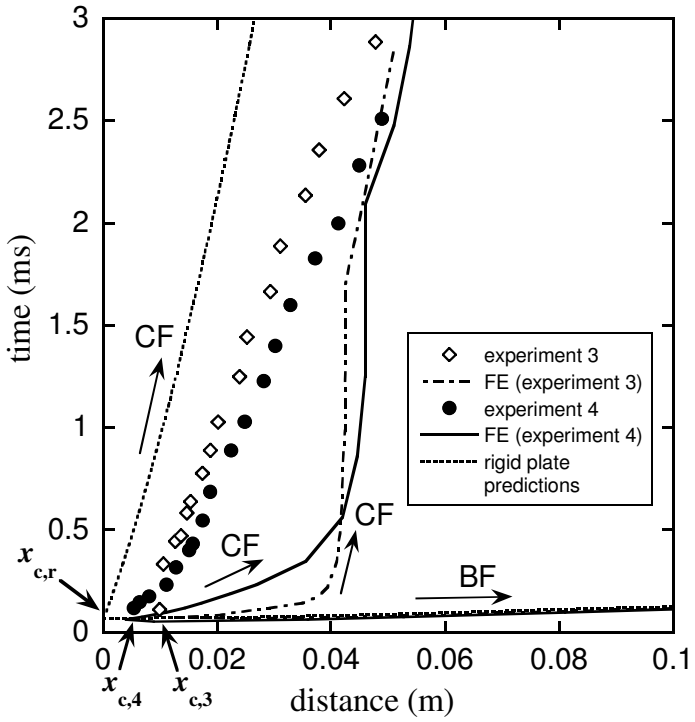



Fig. 5.7: Measurements and FE predictions of closing front (CF) and breaking front (BF) trajectories plotted in a time versus distance chart for experiments 3 and 4, both performed in air-backed configuration; analytical predictions for a monolithic plate of mass equal to the total sandwich ( $M = 24.4\,\mathrm{g}$ , $p_{st} = 0.1\,\mathrm{MPa}$ , $p_0 = 11.1\,\mathrm{MPa}$ , $\theta = 0.145\,\mathrm{ms}$ ) are included for comparison.

### *(iii) Effect of core strength on the point of first cavitation*

In this section we examine the sensitivity of the location of first cavitation $x_c$ to the normalised collapse strength of the sandwich, $\bar{\sigma}_c = \sigma_c / p_0$ , for a set of experiments performed in both air-backed and water-backed configuration.

In Fig. 5.8, the measurements of $x_c$ are plotted against $\bar{\sigma}_c$ together with analytical predictions performed with the formulas presented in Liang et al. [29], which were originally derived for air-backed sandwich plates. It is seen that the predictions are found in good agreement with the measurements, indicating that the specimen's arrangement, i.e. water-backed or air-backed, does not notably affect the location of first cavitation.

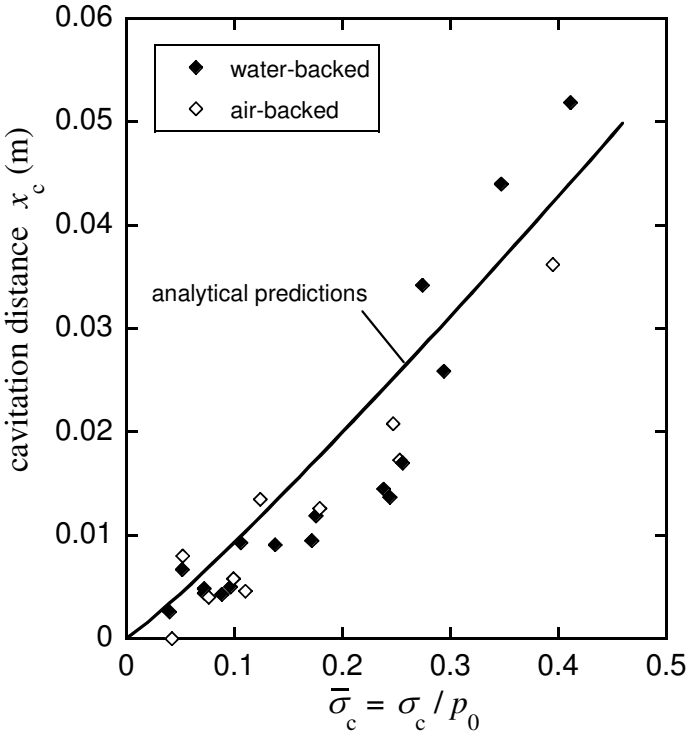



Fig. 5.8: Measurements of the point of first cavitation (cavitation distance) plotted against the normalised core strength $\overline{\sigma}_c$ for experiments conducted with specimens 1-5 in both air-backed and water-backed configurations; analytical predictions (Liang et al. [29]) are included for comparison.

### 5.5.2 Structural response

We now proceed to examine the structural response observed in the experiments with a focus on face sheet motion and core compression and we compare the measurements with predictions obtained from FE simulations.

**(i)** ***Water-backed sandwich plates.***

In Fig. 5.9 (a) we present velocity versus time traces of front and back face sheets, $v_f(t)$ and $v_b(t)$, respectively, measured for experiment 1 (see Table 5.2); the corresponding displacement histories, $u_f(t)$ and $u_b(t)$, respectively, are presented in Fig. 5.9 (b). The time histories of face sheet displacements and velocities were extracted from the high-speed

photographs (see Fig. 5.4 a) and smoothed by employing a Savitzky-Golay filter. In addition, FE predictions of $v_f(t)$, $v_b(t)$, $u_f(t)$ and $u_b(t)$ performed in accordance to this experiment are included in Fig. 5.9 (a) and (b), respectively. It can be seen from this figure that the front face sheet rapidly attains a peak velocity $v_{f,\max}$ and subsequently decelerates due to the support offered by the sandwich core.

Let us now assume that the core material is compressed at constant uniaxial stress $\sigma_c$ under the combined compressive load of incident pressure wave and static overpressure $p_{st} - p_{\text{atm}}$; then dynamic equilibrium for the back face sheet ($m_b = m_f$) dictates

$$m_b \dot{v}_b(t) = (\sigma_c - p_{st} + p_{\text{atm}}) - \rho_w c_w v_b(t) \tag{5.9}$$

Equation (5.9) can be solved for $v_b(t)$ upon imposing the initial condition $v_b(t=0) = 0$; the solution is

$$v_b(t) = \frac{\sigma_c - p_{st} + p_{\text{atm}}}{\rho_w c_w}\left(1 - e^{-\frac{t}{t_b}}\right). \tag{5.10}$$

where $t_b = m_b / (\rho_w c_w)$ is the characteristic time associated to the exponential rise of $v_b(t)$. According to eq. (5.10), the velocity of the back face sheet reaches a final value (after $t \approx 4t_b$) of

$$v_F = \lim_{t\to\infty}(v_b) = \frac{\sigma_c - p_{st} + p_{\text{atm}}}{\rho_w c_w} = v_P \tag{5.11}$$

For experiment 1 we had $\sigma_c = 2\,\text{MPa}$, $p_{st} = p_{\text{atm}} = 0.1\,\text{MPa}$, $\rho_w = 1000\,\text{kgm}^{-3}$ and $c_w = 1053\,\text{ms}^{-1}$ and thus the final velocity follows from eq. (5.11) as $v_F = 1.9\,\text{ms}^{-1}$ and is found in good agreement with the corresponding measurements of $v_b(t)$, as seen in Fig. 5.9 (a). At $t_{com} = 0.5\,\text{ms}$, front and back face sheet attain a common velocity and plastic core

compression ceases, thus $\Delta c_F = u_f(t_{com}) - u_b(t_{com}) = 2.2$ mm the final core compression. The measured time histories $v_f(t)$, $v_b(t)$, $u_f(t)$ and $u_b(t)$ presented in Fig. 5.9 for experiment 1 are adequately predicted by the FE simulation.

Experiment 5 (see Table 5.2) was conducted on the same type of sandwich (*specimen 1*) but with the hydrostatic pressure in the fluid increased to $p_{st} = 1.05\,\text{MPa}$ prior to shock loading with $p_0 = 8.8\,\text{MPa}$ and $\theta = 0.12\,\text{ms}$; time histories $v_f(t)$, $v_b(t)$, $u_f(t)$ and $u_b(t)$ measured for this experiment are included in Fig. 5.9 (a) and (b), respectively. In this test, the sandwich core was compressed by an overpressure of magnitude $p_{st} - p_{atm} = 0.95\,\text{MPa}$ prior to shock loading, hence the reduced final velocity $v_F = 1.0\,\text{ms}^{-1}$ (calculated from eq.(5.11)) which is also reflected in the measurements of $v_b(t)$ shown in Fig. 5.9 (a). In addition, Fig. 5.9 (b) shows that when the static pressure is increased to $p_{st} = 1.05\,\text{MPa}$ (as in experiment 5), the final core compression decreased to $\Delta c_F = 1.75\,\text{mm}$ and both front and back face sheet invert motion after reaching their respective peak displacements.

In Fig. 5.10, we provide similar information for experiments 2 and 6 performed with $p_{st} = 0.1\,\text{MPa}$ and $p_{st} = 0.72\,\text{MPa}$, respectively, with Rohacell foam cored specimens (*specimen 4*) in contact with water on both face sheets. Similar to what shown in Fig. 5.9, $v_f(t)$ quickly attains a peak value and rapidly decreases thereafter, while $v_b(t)$ reaches a plateau. Both $v_f(t)$ and $v_b(t)$ first equalise at $t = 0.001\,\text{s}$ but subsequently start to oscillate, owing to the low elastic stiffness of the polymer foam core, $E_c = 100\,\text{MPa}$. As time elapses, $v_f(t)$ and $v_b(t)$ decay to zero and plastic core compression reaches a final value

$\Delta c_F = 5.4\,\text{mm}$ at $t = 0.002\,\text{s}$. We also include in Fig. 5.10, FE predictions of $v_f(t)$, $v_b(t)$, $u_f(t)$ and $u_b(t)$ computed in accordance to experiment 2 ($p_{st} = 0.1\,\text{MPa}$), which are found to be in good correlation with the corresponding measurements.

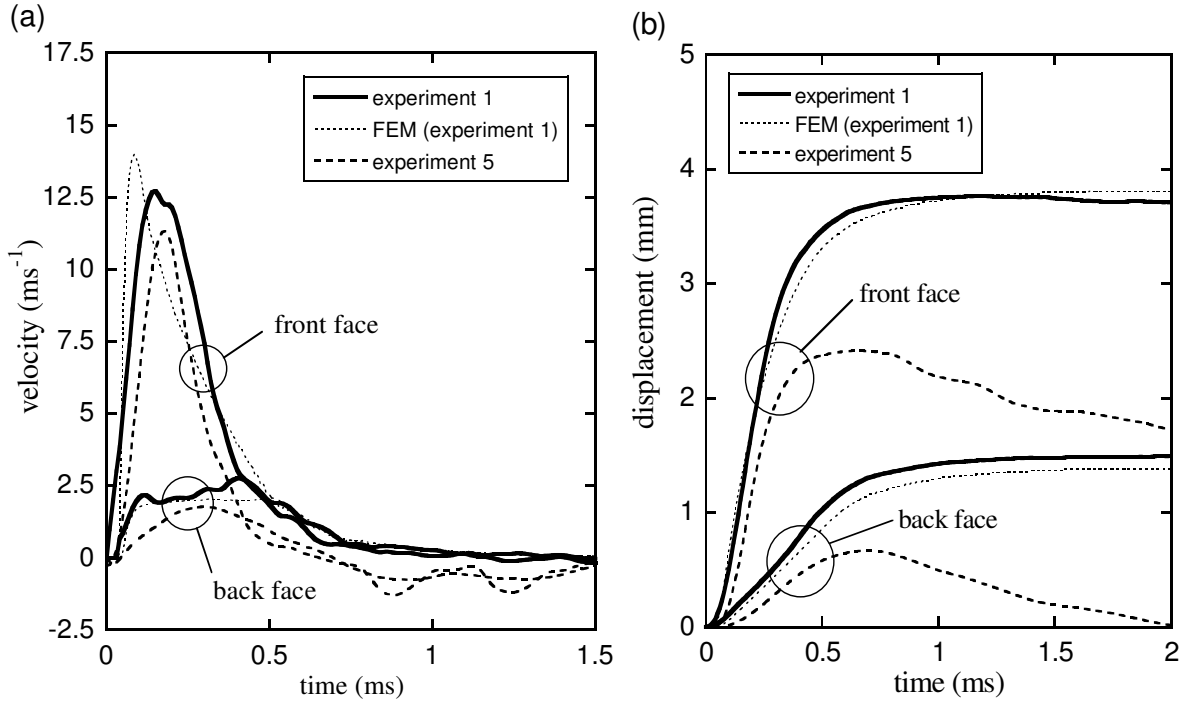



Fig. 5.9: (a) Measured time histories of front and back face velocities for experiment 1 ($p_{st} = 0.1\,\text{MPa}$, $p_0 = 11.4\,\text{MPa}$, $\theta = 0.145\,\text{ms}$) and experiment 5 ($p_{st} = 1.05\,\text{MPa}$, $p_0 = 8.8\,\text{MPa}$, $\theta = 0.12\,\text{ms}$) both performed on specimen 1 (Alporas foam) in water-backed configuration; (b) displacement versus time histories for the same experiments; FE predictions for experiment 1are included in both figures.

Furthermore, the results presented in Fig. 5.10 confirm the findings drawn from Fig. 5.9: an increase in static pressure ($p_{st} = 0.72\,\text{MPa}$ in experiment 6) prior to shock loading leads to a decrease in $v_b(t)$ during the core compression phase (Fig. 5.10 a), to a reduction in $\Delta c_F$ and to reverse motion of the sandwich specimen (Fig. 5.10 b).

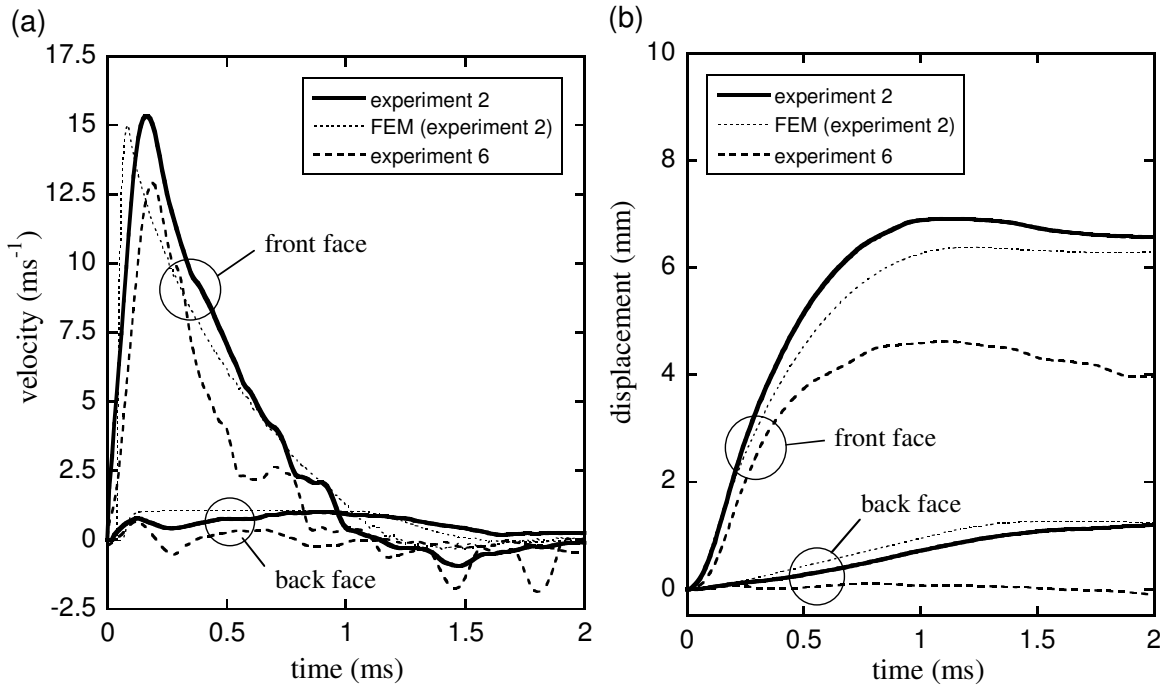



Fig. 5.10: (a) Measured time histories of front and back face velocities for experiment 2 ( $p_{st} = 0.1\text{MPa}$, $p_0 = 11.4\text{MPa}$, $\theta = 0.145\text{ms}$ ) and experiment 6 ( $p_{st} = 0.72\text{MPa}$, $p_0 = 9.2\text{MPa}$, $\theta = 0.12\text{ms}$ ) both conducted with specimen 4 (Rohacell foam) in water-backed configuration; (b) displacement versus time histories for the same experiments; FE predictions for experiment 2 are included in both figures.

**(ii)** ***Air-backed sandwich plates.***

In Fig. 5.11 (a) we present FE predictions and measurements of $v_f(t)$ and $v_b(t)$ for experiment 3 (see Table 5.2) performed on an air-backed specimen with Alporas foam core (*specimen 1*). The corresponding time histories $u_f(t)$ and $u_b(t)$ are shown in Fig. 5.11 (b) and high-speed photographs for this experiment are illustrated in Fig. 5.6 (a). Upon the impact of the shock wave on the specimen, both face sheets are set in motion, almost simultaneously, and rapidly reach their respective peak values (see Fig. 5.11 a), approximately at the time of the onset of cavitation (see Fig. 5.6 a). The occurrence of cavitation causes the pressure at the fluid-structure interface to drop to a very low level, leading to deceleration of both face sheets, as a consequence of air-resistance and friction between O-rings and tube wall. Note

that the pressure drop at the wet face of the specimen leads to elastic unloading of the sandwich core and this gives rise to oscillations of the face sheets. Such oscillations are more pronounced in the FE predictions due to the lack of damping in the numerical models (e.g. friction between O-rings and tube). The measurements of $u_f(t)$ and $u_b(t)$ plotted in Fig. 5.11 (b) show that plastic core deformation was negligible in this experiment and the FE predictions confirm this.

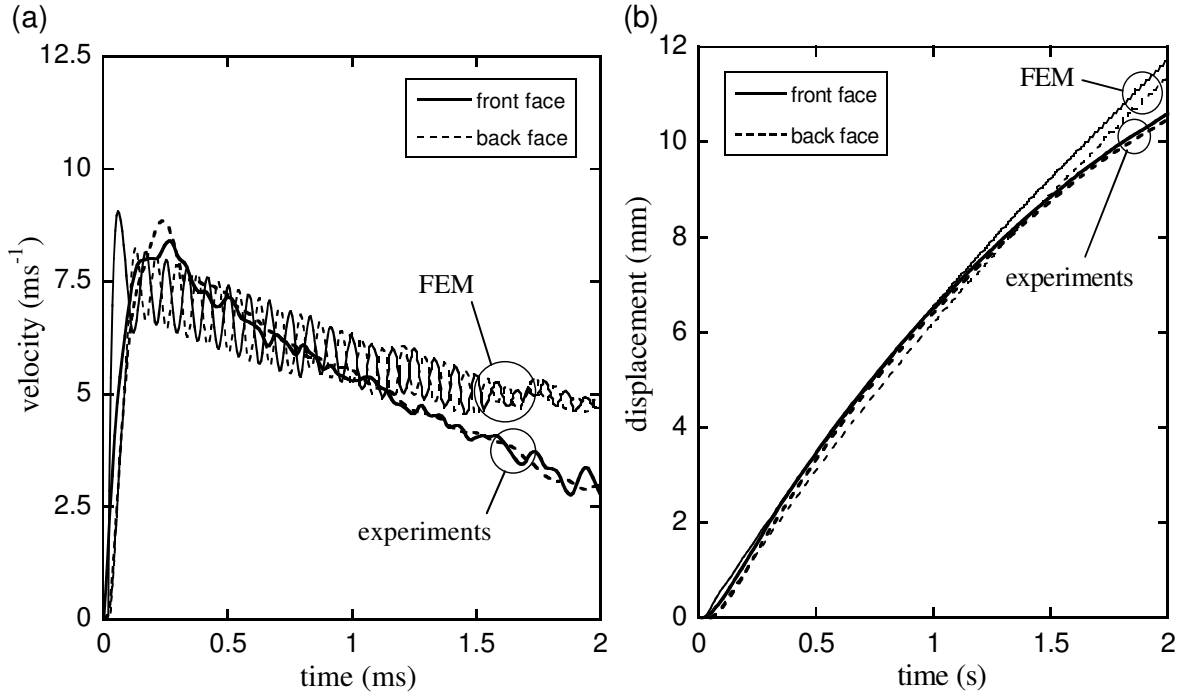



Fig. 5.11: (a) Measurements and FE predictions of front and back face velocities as functions of time for experiment 3 ( $p_{st} = 0.1\text{MPa}$ , $p_0 = 8.1\text{MPa}$ , $\theta = 0.11\text{ms}$ ) performed on *specimen 1* (Alporas foam) in air-backed configuration; (b) displacement versus time histories for the same experiment.

## 5.6 Discussion

The severity of structural loading consequent to underwater blast can be quantified by the maximum impulse $I_{f,\max} = \max\left[I_f(t)\right]$ (per unit area) applied on the wet surface of the

structure. In addition, the permanent core compression $\varepsilon_c = \Delta c_F / c$ quantifies to what extent the sandwich effect is maintained after blast loading.

In the following, we employ measurements and FE predictions of $I_{f,\max}$ and $\varepsilon_c$ to assess the blast resistance of sandwich plates in contact with water on one or both sides.

### 5.6.1 Comparison of $I_{f,max}$ and $\varepsilon_c$ between air-backed and water-backed sandwich plates

First, consider the 1D problem of a sandwich plate in contact with water on the front face sheet and subjected to loading by an arbitrary pressure history $p_f(t)$ on the wet face. Assume that the mass of the core is negligible in comparison to the face sheets (sandwich cores only contributed 4%-6% to the mass of the total sandwich specimens). Then conservation of linear momentum dictates

$$I_f(t) = \int_0^t \left[ p_f(\tau) - p_{st} \right] \mathrm{d}\tau = m_f v_f(t) + m_b v_b(t). \tag{5.12}$$

The velocity histories $v_f(t)$ and $v_b(t)$, such as shown in Fig. 5.11, are deduced from the high-speed photographs and the impulse $I_f(t)$ imparted to the air-backed plate immediately follows from eq. (5.12).

If the sandwich plate is in contact with water on both face sheets, a pressure wave $p_b(t)$ is radiated into the water column from the specimen's back face; then, conservation of linear momentum provides

$$\begin{aligned} & m_f v_f(t) + m_b v_b(t) = \int_0^t \left[ p_f(\tau) - p_{st} - p_b(\tau) \right] d\tau = I_f(t) - \int_0^t p_b(\tau) d\tau \Rightarrow \\ & \Rightarrow I_f(t) = m_f v_f(t) + m_b v_b(t) + \int_0^t p_b(\tau)\, d\tau \,. \end{aligned} \tag{5.13}$$

The time histories $p_b(t)$ are measured using a piezoelectric pressure gauge fitted on the tube (see Fig. 5.2) while the time histories $v_f(t)$ and $v_b(t)$ are obtained from high-speed photographs. Equation (5.13) can then be used to evaluate the impulse $I_f(t)$ imparted to the front face sheet of a water-backed sandwich plate.

Note that friction between the O-rings and the tube wall is neglected in eqs. (5.12) and (5.13) (frictional forces were measured to be < 15 N).

In Fig. 5.12 the measured core crush $\varepsilon_c = \Delta c_F / c$ is plotted against the shock intensity $I_0 = 2p_0\theta$ for a set of experiments performed at atmospheric pressure with shock waves of peak pressures and decay times in the range of $p_0 = 10.5 - 11.5\,\text{MPa}$ and $\theta = 0.12 - 0.2\,\text{ms}$, respectively, without pressuring the fluid columns prior to shock loading, i.e. $p_{st} = 0.1\,\text{MPa}$. Two different core materials are considered, Alporas metal foam (*specimen 1*) and Rohacell polymer foam (*specimen 4*); masses of the sandwich specimens only varied between $M = 24.2 - 25.7\,\text{g}$, hence $M = 25\,\text{g}$ for simplicity. Finite element simulations were performed in accordance to these experiments and their predictions are included in Fig. 5.12. It can be seen from the measurements that the core crush of a sandwich plate is remarkably higher when the plate is in contact with water at both face sheets and this is also reflected in the FE results. Moreover, both predictions and measurements show that Alporas foam cored specimens exhibit larger values of $\varepsilon_c$ than those comprising Rohacell foam.

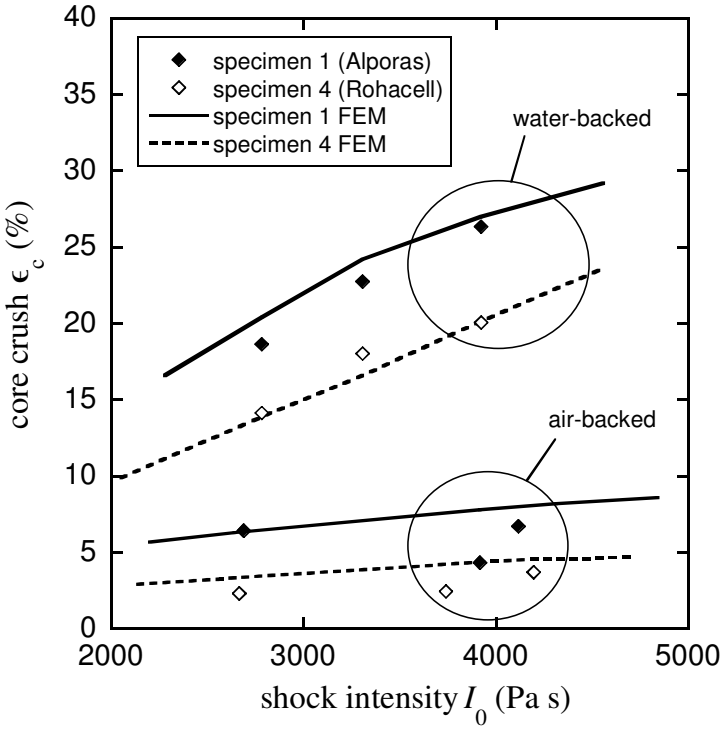



Fig. 5.12: Sensitivity of core crush $\varepsilon_c$ to shock intensity $I_0 = 2p_0\theta$ measured for experiments performed on specimen 1 (Alporas foam) and specimen 2 (Rohacell foam), both of which tested in air-backed and water-backed configuration; FE predictions are included for comparison.

Measurements and FE predictions of the normalised peak impulse $\bar{I}_{f,\max} = I_{f,\max}/(2p_0\theta)$ are presented in Fig. 5.13 as functions of the parameter $\psi$ (eq.(5.8)) for the same set of experiments; analytical predictions for rigid plates of mass equal to the total sandwich specimens ($M = 25\,\text{g}$) are included in Fig. 5.13 for both air-backed and water-backed loading cases (computed with the 1D FSI models presented in Chapter 3). It can be seen that the measured and predicted impulse $\bar{I}_{f,\max}$ associated to blast loading of water-backed sandwich plates is approximately 30% lower than the corresponding rigid plate predictions; such reductions in $\bar{I}_{f,\max}$ are more pronounced for experiments conducted with Rohacell foam cored specimens owing to the low values of normalised core strength $\bar{\sigma}_c = \sigma_c/p_0$ in these

tests (Rohacell foam $\sigma_c / p_0 \approx 0.097$, Alporas foam $\sigma_c / p_0 \approx 0.175$). In Section 5.6.3, we shall explore the effect of $\bar{\sigma}_c$ on the impulse $\bar{I}_{f,\max}$ in more detail.

In contrast, for sandwich plates in air-backed configuration the measurements and FE predictions of $\bar{I}_{f,\max}$ included in Fig. 5.13 show reductions of only 10% compared to the predictions for rigid plates of equal mass (lower dotted curve). (recall Fig. 5.12), which produces an overall structural response similar to that of a rigid plate.

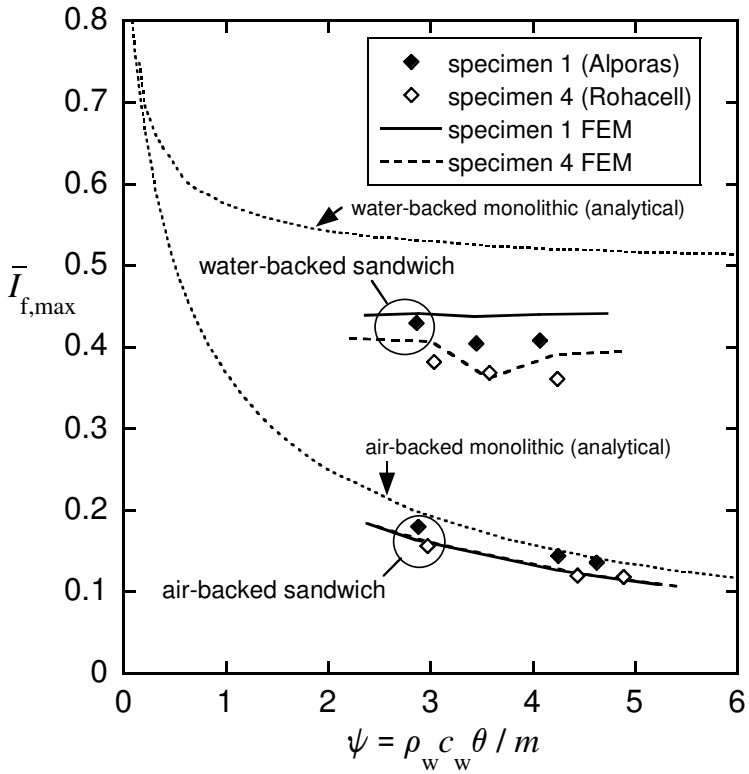



Fig. 5.13: Experimental measurements and FE predictions of the non-dimensional impulse $\bar{I}_{f,\max}$ as functions of the parameter $\psi$ for experiments performed on *specimen 1* (Alporas foam) and *specimen 4* (Rohacell foam) in both air-backed and water-backed configuration; analytical predictions for monolithic plates of mass equal to the total sandwich (dotted curves) are included for comparison.

### 5.6.2 Effect of initial hydrostatic fluid pressure on $I_{f,max}$ and $\varepsilon_c$

Additional FSI experiments were performed on water-backed sandwich plates, in order to explore the sensitivity of $\bar{I}_{f,\max}$ and $\varepsilon_c$ on the initially applied static pressure in the fluid; in these tests, specimens were loaded by exponentially decaying shock waves ($\theta = 0.12\,\text{ms}$, $p_0 = 8.8 - 9.2\,\text{MPa}$) generated in initially pressurised fluid columns, i.e. $p_{st} \gg 0.1\,\text{MPa}$. Two different types of specimens were considered, *specimen 1* (Alporas foam) and *specimen 4* (Rohacell foam), and their masses varied between $M = 24.1 - 25.8\,\text{g}$, hence $M \approx 25\,\text{g}$ and $\psi = \rho_w c_w \theta / m \approx 2.9$ for simplicity.

The impulse $\bar{I}_{f,\max}$ deduced from the obtained measurements (eq. (5.13)) is plotted in Fig. 5.14 (a) as a function of the normalised static pressure $\bar{p}^*_{st} = p_{st}/\sigma_c$, together with the corresponding FE results. The impulse measurements show that $\bar{I}_{f,\max}$ is drastically reduced when $\bar{p}^*_{st}$ is increased and the FE predictions confirm this scenario; in particular, impulse reductions of 70% are reported for $\bar{p}^*_{st} \to 1$.

The corresponding measurements and FE predictions of the normalised core crush $\bar{\varepsilon}_c = \varepsilon_c/\varepsilon_D$ are plotted in Fig. 5.14 (b) as functions of $\bar{p}^*_{st}$. It is seen from the measurements that the effect of elevated static pressure $\bar{p}^*_{st}$ is to increase $\bar{\varepsilon}_c$ and this trend is more pronounced for *specimen 1*. The FE results capture the core crush $\bar{\varepsilon}_c$ induced in the Alporas foam cored specimens (*specimen 1*) with adequate accuracy, but under-predict the $\bar{\varepsilon}_c$ measurements for the tests performed with *specimen 2* by 10% - 30%.

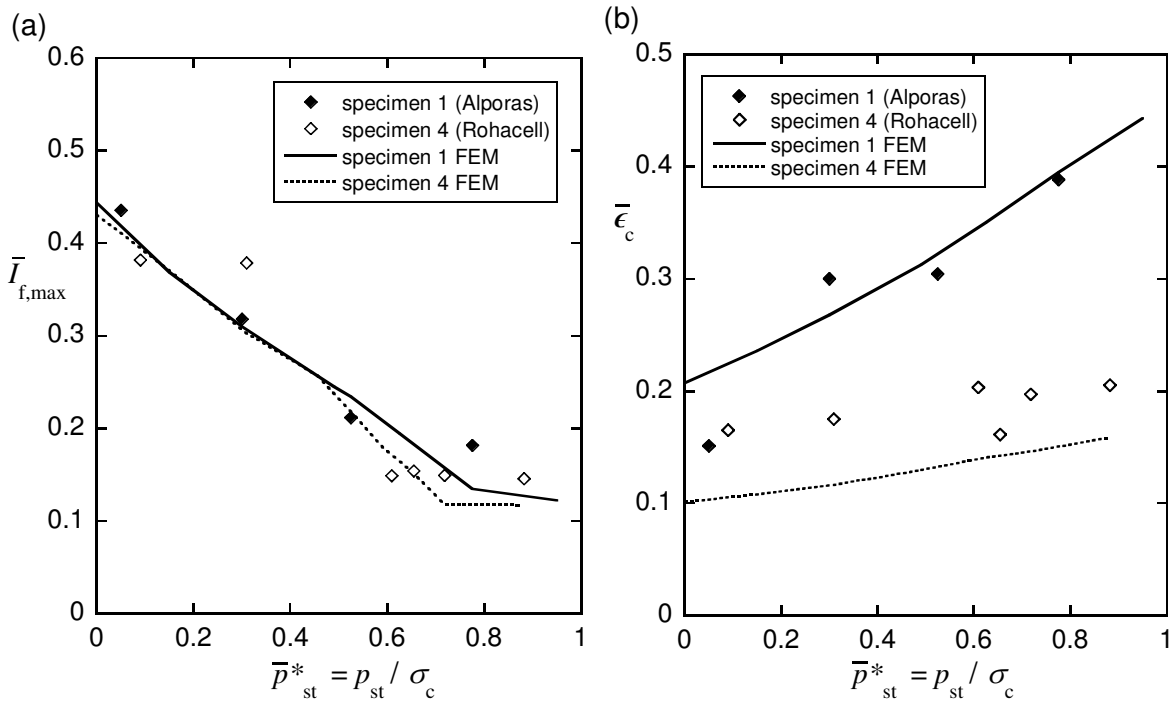



Fig. 5.14: (a) Sensitivity of the non-dimensional impulse $\bar{I}_{f,\max}$ to the normalised static pressure $\bar{p}^*_{st} = p_{st} / p_0$ measured for experiments performed in water-backed configuration on specimen 1 (Alporas foam) and specimen 2 (Rohacell foam) with pressure waves of $p_0 = 8.8 - 9.2\,\text{MPa}$ and $\theta = 0.12\,\text{ms}$ ($\psi \approx 2.9$ in all experiments); FE predictions are included for comparison; (b) measurements and FE predictions of the core crush $\bar{\varepsilon}_c = \varepsilon_c / \varepsilon_D$ as functions of $\bar{p}^*_{st}$ for the same set of experiments.

### 5.6.3 Effect of normalised core strength $\bar{\sigma}_c$ on applied impulse $\bar{I}_{f,\max}$ and core crush $\varepsilon_c$

Previous studies [27, 38] have shown that the impulse imparted to an air-backed sandwich plate consequent to blast loading lies, in general, between that applied on a rigid plate of mass equal to the total sandwich, $\bar{I}_{TOT}$ (upper bound), and to the front face sheet alone, $\bar{I}_{FF}$ (lower bound). They also noted that the effect of $\bar{\sigma}_c = \sigma_c / p_0$ is to govern the impulse imparted to the sandwich, $\bar{I}_{f,\max}$: for large values of $\bar{\sigma}_c$, $\bar{I}_{f,\max} \to \bar{I}_{TOT}$, while $\bar{I}_{f,\max} \to \bar{I}_{FF}$ for sufficiently small values of $\bar{\sigma}_c$.

In this section we present similar information for underwater blast loading on water-backed sandwich plates. In the process, a series of experiments was performed on sandwich specimens with both face sheets in contact with water at atmospheric pressure, i.e. $p_{st} = 0.1\text{MPa}$, and $\bar{\sigma}_c$ was adjusted by varying the peak pressure of the blast wave ($p_0 = 6.1-11.8\,\text{MPa}$) as well as the core strength of the sandwich plate ($\sigma_c = 0.44-2.8\,\text{MPa}$) via selection of different core geometric and physical properties (see Table 5.1); masses of the total sandwiches and the face sheets ranged between $M = 26.0-27\,\text{g}$ and $M_f = 12.1-13\,\text{g}$, respectively, thus $M \approx 26.5\,\text{g}$ and $M_f \approx 12.5\,\text{g}$ for simplicity. Note that the Young's modulus of Alporas foam cores is much larger than that of Rohacell foams (Table 5.1). In order to explore the influence of $E_c$ on the blast response of sandwich plates, it is instructive to plot the experimental results for Rohacell and Alporas foam cored specimens in separate graphs, as in Fig. 5.15 and Fig. 5.16, respectively.

Measurements of $\bar{I}_{f,\max}$ obtained from the experiments performed on Rohacell foam cored sandwich plates (*specimens* 3, 4 and 5) are plotted against the normalised core strength $\bar{\sigma}_c = \sigma_c / p_0$ in Fig. 5.15 (a) together with corresponding FE predictions. Experimental results are indicated by circles, triangles and diamonds while the dotted, dashed and solid curves respresent the corresponding FE predictions. Note that the measurements only cover a limited range of $\bar{\sigma}_c$ due to limitations in the maximal allowable internal pressure of the shock tube. Moreover, we include in Fig. 5.15 (a) analytical predictions of the imparted impulse associated with blast loading on water-backed rigid plates of mass equal to the total sandwich ($M = 26.5\,\text{g}$, $\psi = 2.73$), $\bar{I}_{TOT}$, and to the front face sheet alone ($M_f = 12.5\,\text{g}$, $\psi_f = 5.8$), $\bar{I}_{FF}$.

The small difference between the rigid plate predictions $\bar{I}_{TOT}$ and $\bar{I}_{FF}$ can be explained by recalling Fig. 5.13: the impulse imparted to a water-backed rigid plate in a blast event converges to a limit value of 0.5 when $\psi \to \infty$, while for air-backed rigid plates, $\bar{I}_{f,\max} \to 0$ when $\psi \to \infty$. Therefore impulse reductions consequent to light-weight construction are less pronounced when a rigid plate is in contact with water on both sides.

The measurements presented in Fig. 5.15 (a) show that $\bar{I}_{f,\max}$ is steadily increased by increasing $\bar{\sigma}_c$, with all values of $\bar{I}_{f,\max}$ lower than the predictions $\bar{I}_{TOT}$. The current literature on underwater blast loading of sandwich plates supports the conclusion that $\bar{I}_{FF}$ and $\bar{I}_{TOT}$ are lower and upper bounds for the impulse imparted to air-backed sandwich plates [27, 38], respectively. However, for water-backed sandwich plates, the impulse measurements presented in Fig. 5.15 (a) suggest a change of paradigm, as all values of $\bar{I}_{f,\max}$ lie below $\bar{I}_{FF}$. This can be explained that the sandwich cores considered here offer a ‚softer' support to the front face sheet compared to that provided by a water column (in case of a rigid water-backed plate), thus increasing acceleration as well as total displacement of the structure and affecting the cavitation process, recall Fig. 5.5.

The FE results included in Fig. 5.15 (a) are found in good agreement with the measurements. Similar trends emerge for all specimens considered here: upon increasing $p_0$, i.e. decreasing $\bar{\sigma}_c = \sigma_c / p_0$, the impulse $\bar{I}_{f,\max}$ is gradually reduced until a minimum is reached. The location of this minimum on the $\bar{\sigma}_c$- axis depends on the compressive strength of the foam core employed. When $\bar{\sigma}_c$ is decreased beyond this minimum, strain hardening effects come into play, effectively increasing $\sigma_c$ of the sandwich core and thus increasing $\bar{I}_{f,\max}$.

The corresponding measurements and FE predictions of the normalised core crush $\bar{\varepsilon}_c = \varepsilon_c / \varepsilon_D$ are shown in Fig. 5.15 (b) as functions of $\bar{\sigma}_c$. For each type of specimen, the effect of increasing $\bar{\sigma}_c$ is to reduce $\bar{\varepsilon}_c$. We also observe that the core strength of the sandwich $\sigma_c$ governs the value of the parameter $\bar{\sigma}_c$ at which full densification occurs, i.e. $\bar{\varepsilon}_c \to 1$. Again, good agreement is achieved between measurements and FE predictions.

Now compare Fig. 5.15 (a) and (b): when $\bar{\sigma}_c$ is sufficiently large, the sandwich effect becomes negligible, $\bar{\varepsilon}_c \to 0$, and the impulse $\bar{I}_{f,\max}$ can exceed the rigid plate predictions $\bar{I}_{TOT}$. This can be justified by the fact that the core response is purely elastic in this regime and the ensuing elastic spring-back can affect FSI, leading to an increase in impulse imparted to the sandwich, qualitatively consistent with the conclusions of Chapter 3.

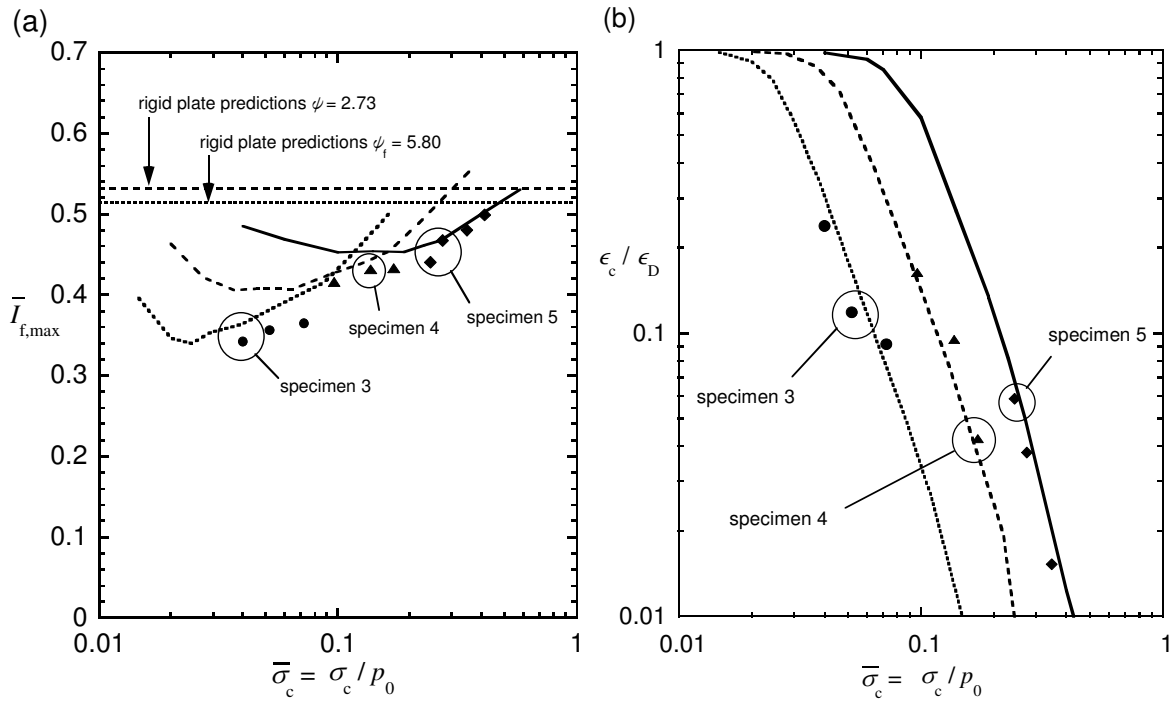



Fig. 5.15: Measurements and FE predictions of (a) the non-dimensional impulse $\bar{I}_{f,\max}$ and (b) core crush $\bar{\varepsilon}_c = \varepsilon_c / \varepsilon_D$ as functions of the normalised core strength $\bar{\sigma}_c = \sigma_c / p_0$ for Rohacell foam-cored sandwich plates (*specimens* 3, 4 and 5) in contact with water at atmospheric pressure ( $p_{st} = 0.1\text{MPa}$ ) and loaded by shock waves of decay time $\theta = 0.12\,\text{ms}$.

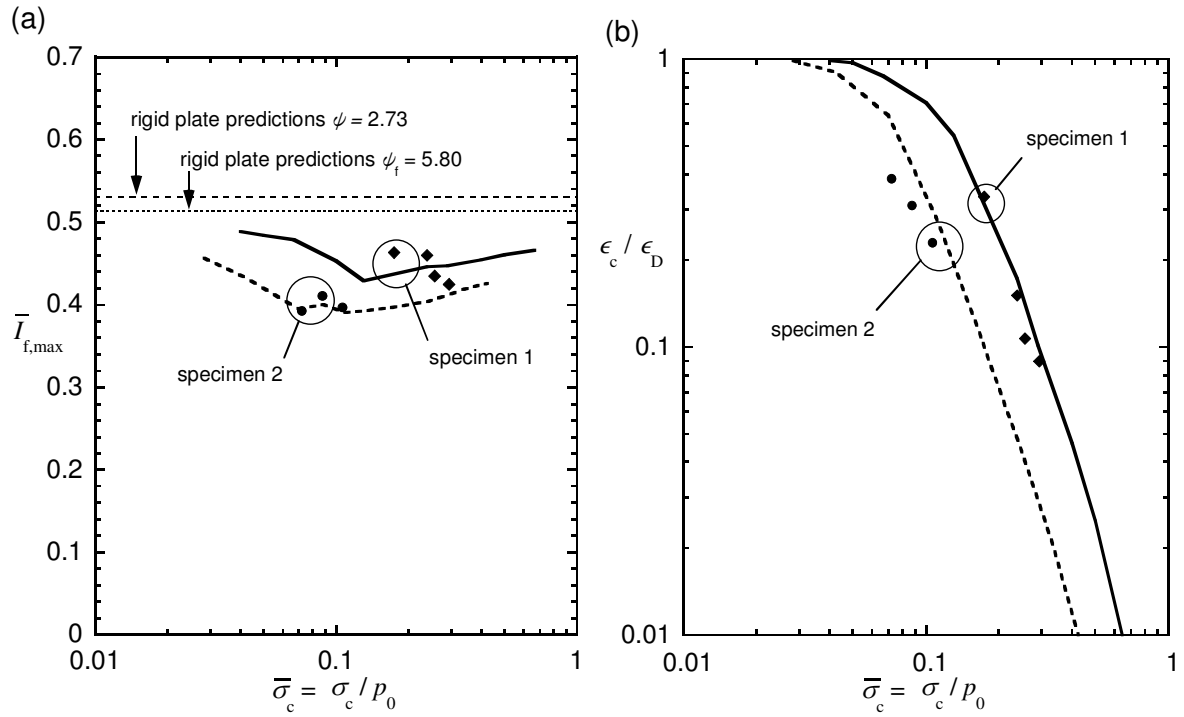



Fig. 5.16: Measurements and FE predictions of (a) the non-dimensional impulse $\overline{I}_{f,\max}$ and (b) core crush $\overline{\varepsilon}_c = \varepsilon_c / \varepsilon_D$ as functions of the normalised core strength $\overline{\sigma}_c = \sigma_c / p_0$ for Alporas foam-cored sandwich plates (*specimens* 1 and 2) in contact with water at atmospheric pressure ( $p_{st} = 0.1\text{MPa}$ ) on both sides and loaded by shock waves of decay time $\theta = 0.12\text{ms}$.

In Fig. 5.16 we present similar information for experiments performed on Alporas foam-cored sandwich plates (*specimens* 1 and 2); the diamonds and circles indicate experimental results for *specimens* 1 and 2, respectively, while the solid and dashed curves represent the corresponding FE results. Both the measurements and the FE predictions are found in good agreement. It is worth mentioning that the impulse $\overline{I}_{f,\max}$ remains well below both thresholds $\overline{I}_{TOT}$ and $\overline{I}_{FF}$, as indicated by the horizontal lines in Fig. 5.16 (a), even for large values of $\overline{\sigma}_c$. Now compare the $\overline{\varepsilon}_c$ versus $\overline{\sigma}_c$ response between Rohacell (Fig. 5.15 b) and Alporas foam cored specimens (Fig. 5.16 b): the range of $\overline{\sigma}_c$ for which $0.01 \le \overline{\varepsilon}_c \le 1$ is extended if Alporas foam cores are employed. This can be addressed to the relatively large elastic stiffness $E_c$ of the Alporas foam: less blast energy is needed to trigger plastic deformation in the core and

therefore shock loading with small pressure amplitudes $p_0$ (i.e. large $\bar{\sigma}_c$) can produce sufficient $\bar{\varepsilon}_c$ to activate the sandwich effect, thus reducing $\bar{I}_{f,\max}$, recall Fig. 5.15 (a).

## 5.7 Conclusions

In this study the response of air-backed and water-backed sandwich plates subject to blast loading in initially pressurised water has been investigated. Underwater blast experiments were performed on sandwich specimens comprising of metallic face sheets and low-density foam cores (metallic and polymeric) by using the experimental method detailed in Chapter 4. Face sheet motion, core compression and cavitation processes were observed using high-speed photography and the impulse imparted to the structure was deduced by analysing dynamic fluid pressure measurements as well as high-speed photographs. The experimental results of permanent core compression, imparted impulse and cavitation front trajectories were adequately captured by the corresponding dynamic FE simulations and allowed drawing the following conclusions:

- The cavitation process associated to underwater blast loading of water-backed and air-backed sandwich plates initiates at a finite distance $x_c$ from the fluid-structure interface and becomes visible in form of rapidly growing cavitation bubbles. Subsequently, the cavitation zone collapsed by propagation of a closing front. The distance $x_c$ was found to be governed by the ratio of core strength to peak pressure of the incident wave, in line with the findings of previous theoretical studies.
- Both air-backed and water-backed sandwich plates outperform rigid plates of equal mass in terms of the impulse imparted to the structure in a blast event. For a given incident

wave and core collapse strength, the permanent core compression of water-backed sandwich plates is higher than that of air-backed sandwiches and thus impulse reductions are more pronounced when sandwich plates are loaded in water-backed configuration.

- For the case of blast loading of water-backed sandwich plates, the impulse imparted to a rigid plate of mass equal to the front face sheet cannot be taken as a lower bound for the impulse imparted to a sandwich structure.
- For water-backed sandwich plates of given core strength, appropriate adjustment of the peak pressure of the incident blast wave can minimise the imparted impulse and the impulse reductions achieved at this minimum depend on the compressive collapse strength of the sandwich.
- The impulse imparted to water-backed sandwich plates can be drastically reduced by increasing the initial hydrostatic pressure in the surrounding fluid; impulse reductions of $\approx 70\%$ (in relation to the unpressurised loading case) can be achieved when the initially applied fluid pressure was on the order of the foam core's collapse strength.

The experiments presented in this study give valuable insight into the main phenomena of shock wave induced cavitation and how these affect the dynamic response of sandwich plates. However, to improve the current understanding of FSI in underwater blast loading of sandwich constructions, rigorous 1D analytical models are needed, which account for all the details of the cavitation process in the fluid, without the need of simplifying assumptions. This is left as a topic for a future study.

# Chapter 6

# The One-dimensional Response of Double-walled Structures Subject to Underwater Blast

## 6.1 Introduction

Hulls of underwater vehicles typically consist of an inner pressure hull encapsulated in an outer shell [48], with the gap between both structures flooded with water when the vessel submerses. Double-hull construction complicates the prediction of structural loading histories produced in a blast event, as cavitation processes can occur in the water gap subsequent to blast loading. The effects of such phenomena on the overall structural response of the hull are still unexplored in the current literature and need to undergo a thorough study.

In this study, we investigate the 1D response to underwater blast loading of double-walled hulls, comprising of a monolithic inner pressure hull and an outer skin, with a water gap separating both structures. Underwater blast experiments will be performed on representative double-walled structural systems by using the shock tube apparatus presented in Chapter 4 and the benefits of sandwich construction in double-walled hull designs will be interrogated. Structural motion, sandwich core compression and cavitation processes consequent to blast loading will be observed by using high-speed photography. Dynamic pressure measurements

will serve to deduce the impulse imparted to the specimens and its sensitivity to the width of the water gap. In addition, detailed FE simulations will be performed in accordance to the experiments and the obtained predictons will be validated against the experimental evidence.

## 6.2 Problem definition

In this study, the response of double-hulls subject to underwater blast is examined. Two different design concepts are considered and described below.

**a) Monolithic double-hull.**

The schematic in Fig. 6.1 (a) is an illustration of the problem geometry of a monolithic double-hull consisting of two monolithic plates separated by a water gap of width $D$. We define as 'outer skin' the plate in contact with water on both sides while the underlying inner structure is termed as 'inner hull' and is in contact with water on the front face only. The outer skin (mass per unit area $m_F$) is loaded on the outer surface by an exponentially decaying shock wave of peak pressure $p_0$ and decay time $\theta$. Subsequently, pressure waves transmitted into the water gap impinge on the inner hull (mass per unit area $m_B$).

**b) Sandwich double-hull.**

The problem geometry for a sandwich double-hull is sketched in Fig. 6.1 (b). It comprises of a monolithic inner hull (areal mass $m_B$) and an outer skin in sandwich construction (areal mass $m_F$), with a water gap (width $D$) located between both structures; the loading case is taken as described above for monolithic double-hulls.

For each of the above design concepts, two different boundary conditions are considered:

(i) *Stationary inner hull:* the outer skin is free to move in direction of wave propagation while the motion of the inner hull is constraint to zero, representing the case of a double-hull with $m_B \to \infty$.

(ii) *Unsupported inner hull:* both outer skin and inner hull are unsupported and $m_B \approx m_F$.

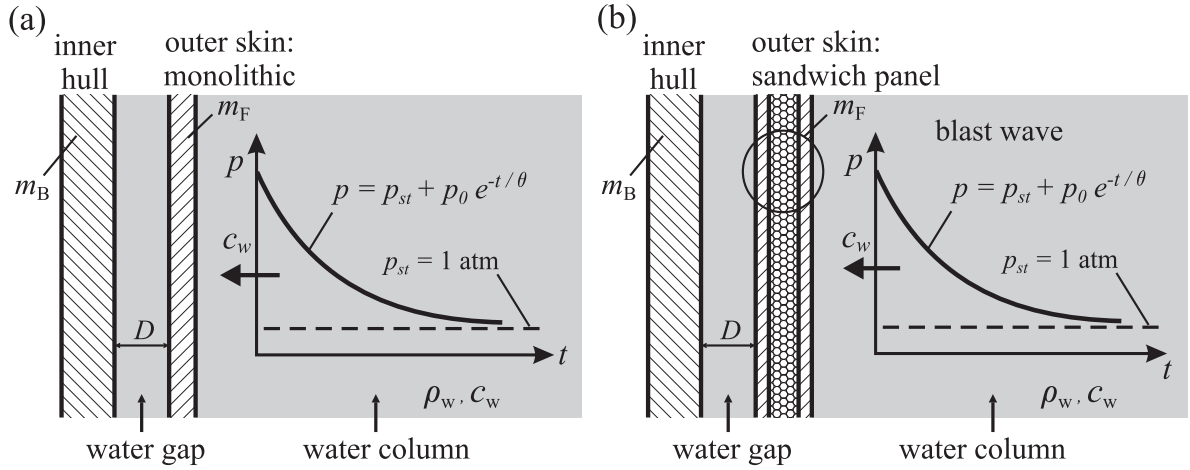



Fig. 6.1: Sketches of problem geometry and loading case of (a) monolithic double-hulls and (b) sandwich double-hulls.

## 6.3 Fluid-structure interaction experiments

### 6.3.1 Laboratory setup

In this study, FSI experiments were performed using the transparent shock tube apparatus presented in Chapter 4. A sketch of the laboratory setup is shown in Fig. 6.2 (a), for an experiment on a monolithic double-hull with a stationary inner hull specimen. The apparatus allows observing specimen motion as well cavitation processes in the water by means of high-speed photography.

The outer skin specimen was inserted into the shock tube, approximately 200 mm from the distal end, and two water columns were located in the tube on both sides of the specimen. The tube was sealed at the front end with a nylon piston and at the distal end with the inner hull specimen; bleed valves were included in front piston and inner hull specimen to evacuate air-bubbles trapped in the water columns prior to the dynamic experiment. The time histories of the interface pressure applied on the wet face of the inner hull was measured by using a piezoelectric pressure gauge of type 113B23 SN 21266 (PCB Piezoelectronics Inc.) centrally mounted on the inner hull specimen (flush with the specimen front face). As shown in Fig. 6.2 (a), motion of the inner hull specimen was constrained in one direction by locating a metallic distance bush between the specimen and an anvil. In the other direction, the position of the specimen was locked by mounting a stud between specimen and anvil. For experiments conducted with free-standing inner hull specimens, the distance bush and the stud were not used.

Exponentially decaying pressure waves were generated in the tube by firing a round steel striker of diameter $d_S = 18.5\,\text{mm}$ at the front piston; details on this technique can be found in Deshpande et al. [36]. The pressure pulses generated in the shock tube were measured with a piezoelectric pressure gauge of type 113B23 SN 21266 (PCB Piezoelectronics Inc.) at a distance approximately 120 mm behind the front piston (see Fig.2a). The speed of pressure wave propagation in the shock tube was measured as $c_w = 1053\,\text{ms}^{-1}$.

A 'Vision Research (V7.1)' high-speed phantom camera was used to observe specimen motion as well as cavitation phenomena in the water columns.

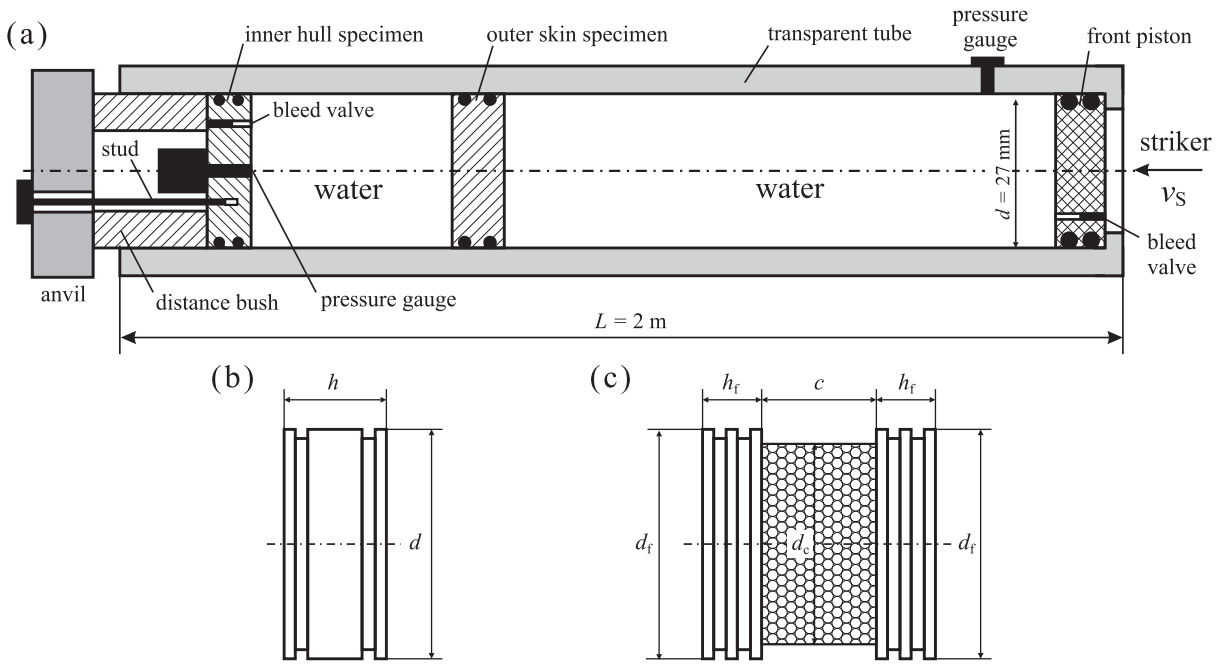



Fig. 6.2: (a) Schematic of the experimental apparatus used to perform underwater blast experiments on a structural system representative of a monolithic double-hull with motion of the inner hull constraint to zero. Experiments on free-standing inner hulls are performed with anvil and distance bush absent. (b) Specimen geometry of outer skin specimen in monolithic design and (c) in sandwich construction.

### 6.3.2 Specimen design and manufacture

(a) *Outer skin specimens.*

The specimen geometry of monolithic outer skin specimens is sketched in Fig. 6.2 (b). Round specimens were machined from either aluminium or stainless steel to diameter $d = 27\,\text{mm}$; two circular grooves were included for fitting O-rings on the specimens to allow sealing of the water columns. The areal mass of the stainless steel and aluminium specimens was measured as $43.0\,\text{kgm}^{-2}$ and $74.8\,\text{kgm}^{-2}$, respectively.

The geometry of a typical sandwich specimen used to reproduce the response of a sandwich double-hull is sketched in Fig. 6.2 (c); it comprises of a crushable foam core encased between metallic face sheets, each of thickness $h_f$ and areal mass $m_f$. The sandwich cores were machined from polymer foam (Rohacell) to diameter $d_c$ and thickness $c$. Rohacell foams are

closed cell foams made from polymetacrylimide (PMI) and are available in a range of densities. In this study, three different core densities are considered, $\rho_c = 71\,\mathrm{kgm^{-2}}$, $\rho_c = 110\,\mathrm{kgm^{-2}}$ and $\rho_c = 200\,\mathrm{kgm^{-2}}$. Details on material properties, thickness and diameter of the cores considered herein are listed in Table 6.1. Note that the mechanical properties were taken from the results of the quasi-static compression tests presented in Section 5.2.

The face sheets were machined from aluminium to diameter $d_f = 27\,\mathrm{mm}$ and thickness $h_f = 8\,\mathrm{mm}$, fitted with two O-rings and bonded to the sandwich core using epoxy adhesive ('Scotch Weld'); the total masses of the obtained sandwich specimens varied between $m_F = 41.9 - 42.7\,\mathrm{kgm^{-2}}$.

Table 6.1: Core properties and dimensions of the sandwich specimens considered in this study.

| | **foam material** | **foam density** $\rho_c$ **(kgm$^{-3}$)** | **foam pore size** $d_p$ **(mm)** | **core diameter** $d_c$ **(mm)** | **core width** $c$ **(mm)** | **compressive strength** $\sigma_c$ **(MPa)** | **densification strain** $\varepsilon_D$ | **Young's modulus** $E_c$ **(MPa)** |
|---|---|---|---|---|---|---|---|---|
| 1 | Rohacell | 71 | 0.96 | 25.5 | 30 | 1.1 | 0.86 | 100 |
| 2 | Rohacell | 110 | 0.93 | 25.5 | 20 | 2.8 | 0.85 | 160 |
| 3 | Rohacell | 200 | 0.64 | 26.0 | 15 | 6.5 | 0.83 | 250 |

(b) *Inner hull specimens:*

In all experiments performed in this study, monolithic inner hull specimens were used and their geometry was similar to that sketched in Fig. 6.2 (b) but with a central mounting port included for mounting the pressure sensor. In addition, they were machined with a bleed valve (out of centre) to evacuate air-bubbles trapped in the water gap. The total areal mass of pressure gauge and specimen was measured as $m_B = 80.2\,\mathrm{kgm^{-2}}$.

### 6.3.3 Outline of the experimental study

The impulse imparted to the inner hull, $I_B$, as well as the core crush of the outer skin specimen, $\varepsilon_c^{pl}$, are measured in the experiments to assess the shock resistance of double-walled hulls subject to underwater blast. The objective of this study is to examine, for both monolithic and sandwich designs (see Fig. 6.1), the sensitivity of the performance metrics $I_B$ and $\varepsilon_c^{pl}$ to the width of the water gap, in order to determine the effect of sandwich construction on the blast performance of submerged double-walled structures. To achieve this, the following test series were performed:

(i) *Stationary inner hull* ($m_B \to \infty$).

In test series 1, experiments were performed with rigidly supported inner hull specimens and outer skin specimens made from either monolithic or sandwich plates; the outer skin mass $m_F$ as well as the decay time $\theta$ were held fixed, while the gap width $D$ was varied.

Test series 2 was carried out to explore the effect of sandwich core strength $\sigma_c$ on the performance metrics $I_B$ and $\varepsilon_c$. In these experiments, three different types of sandwich specimens were considered, as listed in Table 6.1, and the water gap width $D$, areal mass of the sandwich $m_F$ as well as the decay time of the loading pressure pulse $\theta$ were held fixed.

Details of specimen geometries and masses, widths of the water gaps as well as the characteristics of the generated pressure pulses used in the experiments for series 1 and 2 are summarised in Table 6.2. Moreover, we include in Table 6.2 numerical values of the fluid-structure interaction parameter [4]

$$\psi_F = \frac{\rho_w c_w \theta}{m_F} \tag{6.1}$$

related to the areal mass $m_F$ of the outer skin specimen ($m_F = 2m_f + m_c$ for sandwich plates). Note that the values of $\psi_F$ were chosen to match those of typical blast loading on full-scale structures.

Table 6.2: List of experiments conducted with rigid, stationary inner hull specimens, reporting masses of the outer skin specimens, widths of water gaps as well as the characteristics of the loading pressure pulses.

| **test series** | **test no.** | **outer skin specimen** | $p_0$ **(MPa)** | $\theta$ **(ms)** | $m_F$ **(kgm$^{-2}$)** | $\psi_F$ | $D$ **(mm)** |
|---|---|---|---|---|---|---|---|
| 1 | 1 | monolithic | 12.5 | 0.14 | 43.0 | 3.4 | 30 |
| 1 | 2 | monolithic | 12.0 | 0.14 | 43.0 | 3.4 | 80 |
| 1&2 | 3 | monolithic | 11.6 | 0.14 | 43.0 | 3.4 | 120 |
| 1 | 4 | monolithic | 11.6 | 0.14 | 43.0 | 3.4 | 160 |
| 1 | 5 | Rohacell 110 | 11.5 | 0.14 | 42.3 | 3.4 | 30 |
| 1 | 6 | Rohacell 110 | 11.5 | 0.14 | 41.9 | 3.5 | 80 |
| 1&2 | 7 | Rohacell 110 | 11.6 | 0.14 | 42.3 | 3.4 | 120 |
| 1 | 8 | Rohacell 110 | 11.7 | 0.14 | 42.7 | 3.4 | 160 |
| 2 | 9 | Rohacell 71 | 12.0 | 0.14 | 42.7 | 3.4 | 120 |
| 2 | 10 | Rohacell 200 | 11.6 | 0.14 | 42.5 | 3.4 | 120 |

(ii) *Unsupported inner hull* ($m_B \approx m_F$).

In test series 3, experiments were performed with unsupported inner hull specimens and outer skin specimens made from either monolithic or sandwich plates; the decay time of the pressure pulse $\theta$ as well as the masses of the outer skin and inner hull, $m_F$ and $m_B$, respectively, were held fixed, while the gap width $D$ was varied, with $m_F / m_B = 0.5$ the mass ratio between outer skin and inner hull specimens.

In addition, test series 4 was performed in order to explore, for the case of a monolithic double-hull, the effect of an increased mass ratio $m_F / m_B = 3.2$ on the impulse imparted to the inner hull, $I_B$.

In Table 6.3 we summarise details on masses of outer skin and inner hull specimens, distance between the specimens and the characteristics of the generated pressure pulses in each experiment performed for test series 3 and 4, with $\psi_B = \rho_w c_w \theta / m_B$ the FSI parameter related to the mass of the inner hull, $m_B$.

Table 6.3: List of experiments conducted with rigid, unsupported inner hull specimens, reporting masses of the specimens, withs of water gaps as well as the characteristics of the loading pressure pulses.

| test series | test no. | outer skin specimen | $p_0$ (MPa) | $\theta$ (ms) | $m_F$ (kgm$^{-2}$) | $m_B$ (kgm$^{-2}$) | $\psi_F$ | $\psi_B$ | $D$ (mm) |
|---|---|---|---|---|---|---|---|---|---|
| 3 | 11 | Monolithic | 11.2 | 0.14 | 43.0 | 80.2 | 3.4 | 1.8 | 30 |
| 3 | 12 | Monolithic | 12.0 | 0.14 | 43.0 | 80.2 | 3.4 | 1.8 | 60 |
| 3 | 13 | Monolithic | 12.0 | 0.14 | 43.0 | 80.2 | 3.4 | 1.8 | 80 |
| 3 | 14 | Monolithic | 11.5 | 0.14 | 43.0 | 80.2 | 3.4 | 1.8 | 120 |
| 3 | 15 | Rohacell 71 | 11.5 | 0.14 | 42.4 | 80.2 | 3.4 | 1.8 | 30 |
| 3 | 16 | Rohacell 71 | 11.5 | 0.14 | 42.5 | 80.2 | 3.4 | 1.8 | 60 |
| 3 | 17 | Rohacell 71 | 11.4 | 0.14 | 42.7 | 80.2 | 3.4 | 1.8 | 90 |
| 3 | 18 | Rohacell 71 | 11.6 | 0.14 | 42.4 | 80.2 | 3.4 | 1.8 | 120 |
| 4 | 19 | Monolithic | 11.8 | 0.14 | 74.8 | 22.9 | 1.9 | 6.3 | 30 |
| 4 | 20 | Monolithic | 11.6 | 0.14 | 74.8 | 22.9 | 1.9 | 6.3 | 60 |
| 4 | 21 | Monolithic | 11.2 | 0.14 | 74.8 | 22.9 | 1.9 | 6.3 | 95 |
| 4 | 22 | Monolithic | 11.4 | 0.14 | 74.8 | 22.9 | 1.9 | 6.3 | 120 |

## 6.4 Finite element models

One-dimensional FE simulations were performed in ABAQUS/Explicit [49] in order to validate the results obtained with the shock tube apparatus. FE simulations also provide insight into the loading histories applied on the outer skin in a blast event which could not be measured with the experimental technique employed here. The FE model used to simulate blast loading of sandwich double-hulls is sketched in Fig. 6.3. It consists of a front water column, a water gap, a rigid inner hull plate and a sandwich plate representing the outer skin, all of which of unit width and height $H_f$. The sandwich plate comprises a foam core of

thickness $c$, encased between two face sheets, each of thickness $h_f$. The fluid columns, the face sheets and the sandwich core were tied at their interfaces and discretised by using four-noded, plane quadrilateral elements with reduced integration (type CPE4R in ABAQUS/Explicit). The FE models for monolithic double-hulls followed a similar scheme with sandwich core and back face sheet absent.

To model fluid behaviour in ABAQUS/Explicit a simple hydrodynamic model was used which introduces a linear-elastic relationship between fluid pressure and volumetric strain. To achieve this, a Mie-Gruneisen equation of state with a linear Hugoniot relation [49] was employed with fluid density and wave speed set to $\rho_w = 1000\,\mathrm{kgm^{-3}}$ and $c_w = 1053\,\mathrm{ms^{-1}}$, respectively (see Section 3.3 for further details). The shear modulus of water was taken as zero and, to model the cavitation phenomena in water, tensile pressure cut-off was set to 0.1 MPa in ABAQUS [49], in line with measurements of the pressure in cavitated water obtained from the shock tube experiments. The element size of the fluid mesh was set to 0.1 mm in direction of wave propagation, while one single element was used along the height of the water columns, $H_f$. Note that the effect of the mesh size on peak pressure and rise time of the incident shock wave has been examined in Section 3.3 and is reported in Fig. 3.6.

The aluminium face sheets were modelled as linear elastic solids with density $\rho_f = 2700\,\mathrm{kgm^{-3}}$, Young's modulus $E_f = 69\,\mathrm{GPa}$ and Poisson's ratio $\nu_f = 0$; to discretise the face sheets, an element size of 0.3 mm was used along the through-thickness direction.

For the foam materials the constitutive model described in Section 5.4 was employed and the material properties of the foams used in the sandwich cores are listed in Fig. 6.1.

The boundary conditions were taken as follows. As shown in Fig. 6.3, the transverse displacements of all nodes were constrained to zero. For simulations performed to mimic the

response of a double-hull with $m_B \to \infty$, longitudinal motion of the inner hull plate was also constrained to zero.

Underwater blast loading was performed by imposing an exponentially decaying pressure boundary condition (peak pressure $p_0$, decay time $\theta$) at the free end of the front water column (see Fig. 6.3). The length of this water column $L$ was sufficient to guarantee that the dynamic response of the structure had finished before pressure waves reflected at the free end of the front water column could impinge on the outer skin plate.

The presence of bulk viscosity in ABAQUS/Explicit [49] can lead to significant artificial energy dissipation due to the large volumetric compression of the foam core. To minimise such effects, the bulk viscosity was set to zero for the core elements and reduced to 20% of the default values for the fluid columns and the face sheets.

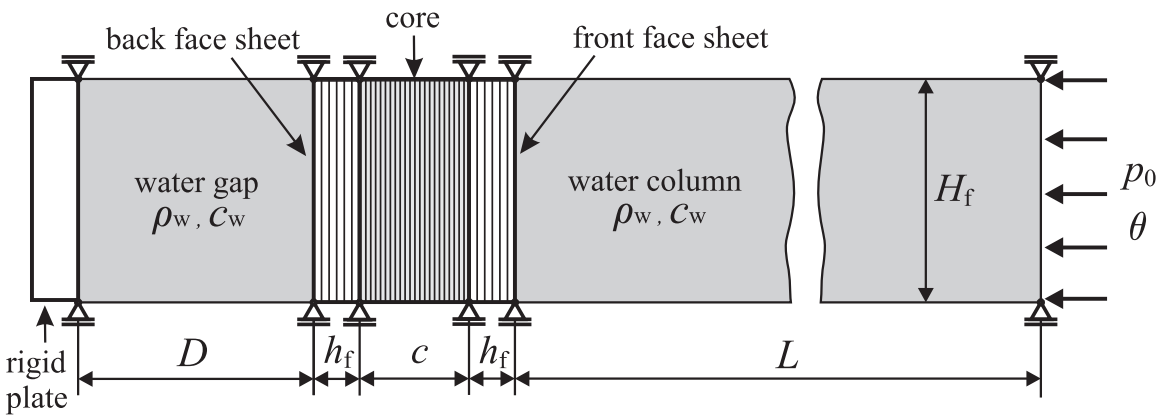



Fig. 6.3: Schematic of the FE model used to simulate the 1D response of a sandwich double-hull. The FE models for monolithic double-hulls follow a similar scheme, but with the core and the back face sheet absent.

## 6.5 Results and discussion

We proceed to present observations and results obtained from the performed experiments. First, we present high-speed photographs recorded in selected experiments and describe the

observed cavitation phenomena. Second, we examine the response of the specimens by analysing measurements and FE predictions of core crush and impulse imparted to the structures. Finally, the experimental and numerical results are used to explore the sensitivity of impulse and core crush to the width of the water gap.

### 6.5.1 Fluid response

(i) *Stationary inner hull* ($m_B \to \infty$).

In Fig. 6.4, we present a sequence of high-speed photographs recorded in experiment 3 (Table 6.2), which was performed to reproduce blast loading of monolithic double-hulls with $m_B \to \infty$; motion of the inner hull specimen was fully constrained to zero and the gap width was adjusted to $D = 120\,\text{mm}$.

In Fig. 6.4 (a), the incident wave ($p_0 = 11.6\,\text{MPa}$, $\theta = 0.14\,\text{ms}$), travelling from the right to the left, reaches the front face of the outer skin specimen. Subsequently, this specimen accelerates (see Fig. 6.4 b) and a compressive wave emanates from its back face, travelling in the water gap towards the inner hull and impinging on its wet face. Subsequently, this wave is fully reflected[†] at this stationary interface and the reflected wave reaches the back face of the outer skin at a later time ($t \approx 2D/c_w$), affecting its response and promoting reverse motion of the specimen. After multiple pressure wave reflections in the water between both specimens, the outer skin specimen moves back to its initial position, as illustrated in Fig. 6.4 (c). From the high-speed photographs presented in Fig. 6.4 it is obvious that cavitation did not occur within the field of observation.

[†] The large discrepancy in acoustic impedance between the water and the steel specimen justifies the notion of full wave reflection at this interface.

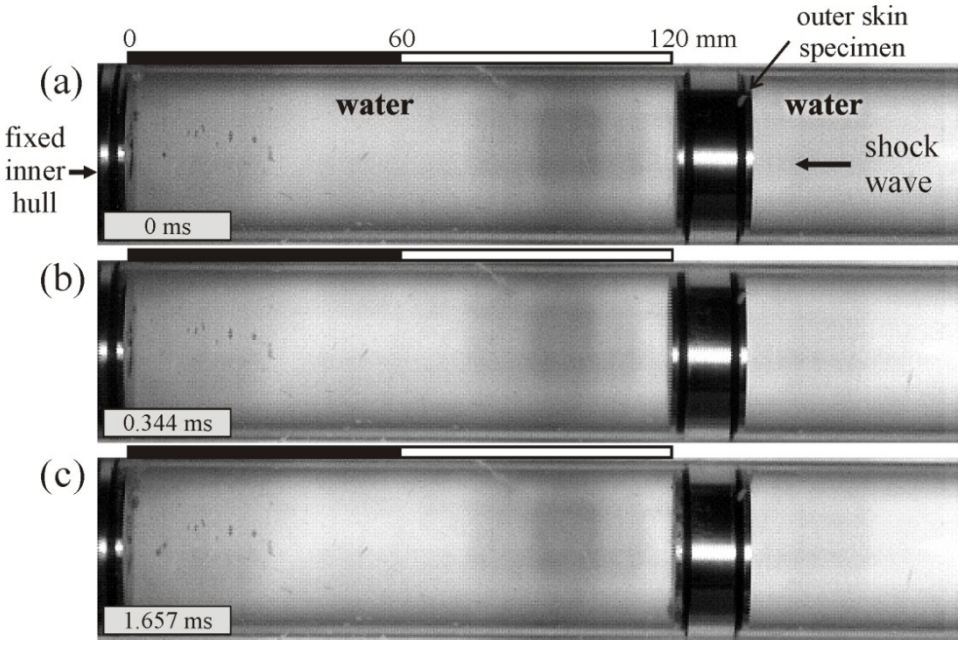



Fig. 6.4: Sequence of high-speed photographs for experiment 3 showing the response of a monolithic double-hull with a stationary inner hull specimen consequent to underwater shock loading ( $p_0 = 11.6\,\text{MPa}$ , $\theta = 0.14\,\text{ms}$ , areal mass of the outer skin was $m_F = 43.0\,\text{kgm}^{-2}$ ).

Experiment 7 (Table 6.2) was conducted under similar conditions but with the monolithic outer skin specimen replaced by a sandwich plate of equal mass in order to mimic the response of a sandwich double-hull; high-speed photographs obtained from this experiment are shown in Fig. 6.5 for four selected instants.

In Fig. 6.5 (a) the shock wave reaches the sandwich specimen. Soon after the front face sheet has started moving, bubbles emerge in the front water column very close to the fluid-structure interface, as shown in Fig. 6.5 (b). Theoretical models [3] predict that two breaking fronts (BF) emerge at the point of first cavitation, propagating in opposite directions and opening a pool of cavitated water, as observed in the experiment (see Fig. 6.5 b). The BF approaching the sandwich plate reaches the fluid-structure interface while the opposite BF continues propagating away from the structure. Subsequently, the front face sheet decelerates owing to the support offered by the foam core. As a consequence, the cavitation front contiguous to the

fluid-structure interface starts propagating away from the structure, becoming a closing front (CF) and forcing collapse of cavitation bubbles (see Fig. 6.5 c). As time elapses the bubbles increase in size due to the increased strain induced in the cavitated fluid by displacement of the front face sheet. Propagation of the closing front persists and, after sufficient time has elapsed, the cavitated region has entirely collapsed in the field of observation, as observed in Fig. 6.5 (d).

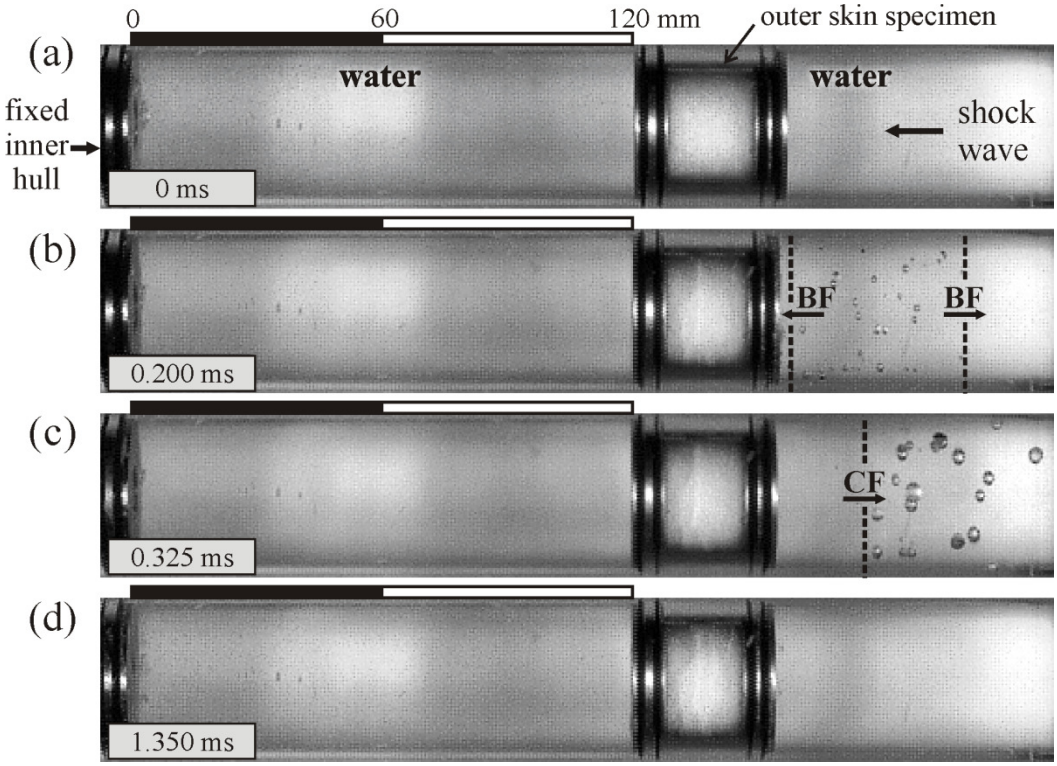



Fig. 6.5: Sequence of high-speed photographs for experiment 7 showing the response of a sandwich double-hull with a rigid, stationary inner hull specimen consequent to underwater shock loading ( $p_0 = 11.6\,\text{MPa}$ , $\theta = 0.14\,\text{ms}$ , areal mass of the outer skin was $m_F = 42.3\,\text{kgm}^{-2}$ ).

(ii) *Unsupported inner hull* ( $m_B \approx m_F$ ).

In experiment 12 (Table 6.3), the 1D response of monolithic double-hulls with $m_B \approx m_F$ was reproduced by locating two monolithic plates in the shock tube, separated by a water gap of width $D = 60\,\text{mm}$ ; the inner hull specimen was unsupported (i.e. free to move in the shock

tube) and the mass ratio of outer skin and inner hull specimen was chosen to be $m_F/m_B = 0.5$ (the areal mass of the outer skin specimen was $m_F = 43.0\,\mathrm{kgm^{-2}}$). A sequence of high-speed photographs recorded in this experiment is shown in Fig. 6.6. In frame (a) the incident shock wave ( $p_0 = 12.0\,\mathrm{MPa}$ , $\theta = 0.14\,\mathrm{ms}$ ) reaches the outer skin specimen. The ensuing motion of this specimen results in a pressure wave radiated from its back face, passing through the water gap and impinging on the wet surface of the inner hull specimen. Subsequently, this specimen is set in motion and a zone of cavitated water spreads from the fluid-structure interface into the water gap by propagation of a BF, as seen in Fig. 6.6 (b). Upon arrival of this BF at the back face of the outer skin specimen, the pressure at this interface vanishes and this leads to a rapid increase in plate velocity because the front face of this specimen is subject to loading by the incident shock wave. Consequently, a tensile rarefaction wave is radiated from the front interface and travelling into the fluid, giving rise to cavitation in the front water, as illustrated in Fig. 6.6 (c). As time elapses, both specimens slowly decelerate due to a combination of air resistance and frictional forces. Consequently, closing fronts (CF) emerge from the front interfaces of each specimen, almost simultaneously, propagating into the cavitated water and forcing collapse of the cavitation bubbles which have drastically increased in size as a result of increased strain in the cavitated fluid, see Fig. 6.6 (d). Both CFs continue propagating and after a sufficiently long time, the cavitation zone in the front water column has contracted beyond the field of observation, while a gap of cavitated water forms at the back interface of the outer skin plate which slowly collapses by propagation of the CF (see Fig. 6.6 e).

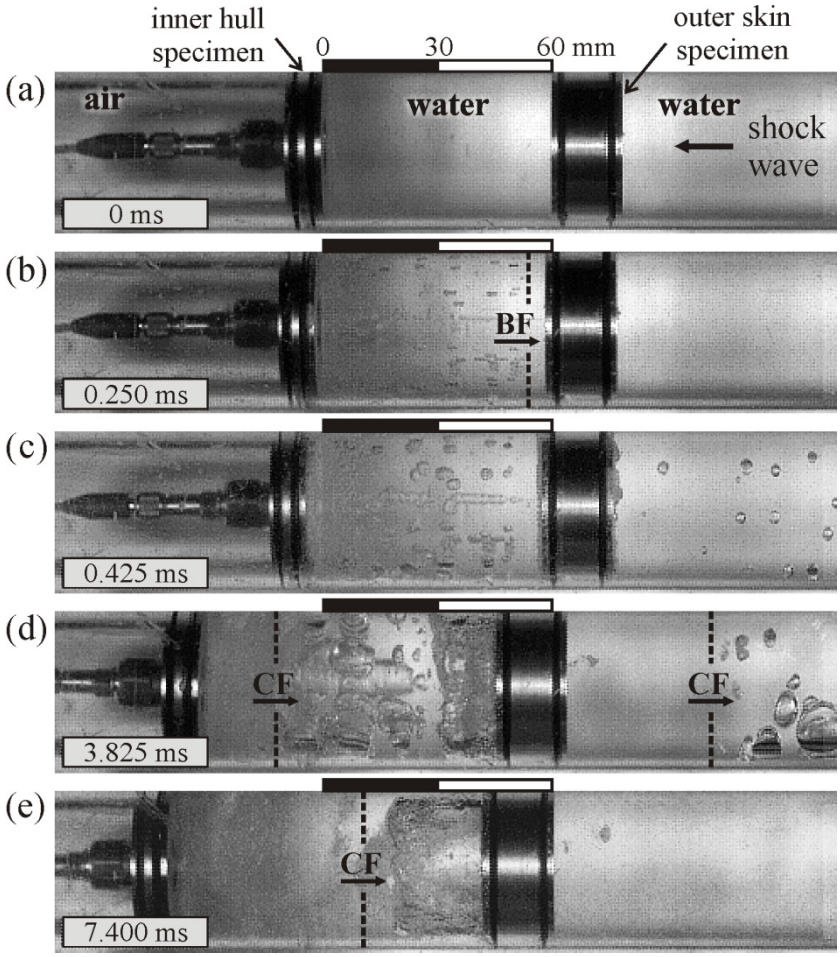



Fig. 6.6: Sequence of high-speed photographs for experiment 12 showing the response of a monolithic double-hull with an unsupported inner hull specimen consequent to underwater shock loading ( $p_0 = 12.0\,\mathrm{MPa}$ , $\theta = 0.14\,\mathrm{ms}$ , $m_F = 43.0\,\mathrm{kgm^{-2}}$ , $m_F / m_B = 0.5$ ).

Experiment 16 (Table 6.3), was conducted under similar conditions as experiment 12 but with the monolithic outer skin specimen replaced by a sandwich of approximately equal mass ( $m_F = 42.5\,\mathrm{kgm^{-2}}$ ); high-speed photographs obtained from this experiment are illustrated in Fig. 6.7 for four selected frames. Upon the impact of the incident pressure wave ( $p_0 = 11.5\,\mathrm{MPa}$ , $\theta = 0.14\,\mathrm{ms}$ ) on the sandwich plate (see Fig. 6.7 a), the front face sheet rapidly acquires a sufficiently high velocity to trigger cavitation in the water very close to the front face sheet, which expands by two BFs propagating into opposite directions (see Fig. 6.7 b). As indicated in Fig. 6.7 (b), the BF approaching the structure reaches the fluid-

structure interface, inverts its direction of motion and becomes a CF, propagating away from the interface and forcing the cavitation zone to contract, as seen in Fig. 6.7 (c). The acceleration of the monolithic inner hull specimen is not sufficient to initiate a BF in the water gap. However, while the cavitated region in the front water entirely collapses in the field of observation, a gap of cavitated water forms at the interface between the sandwich specimen and the water gap due to reverse motion of the back face sheet (see Fig. 6.7 d).

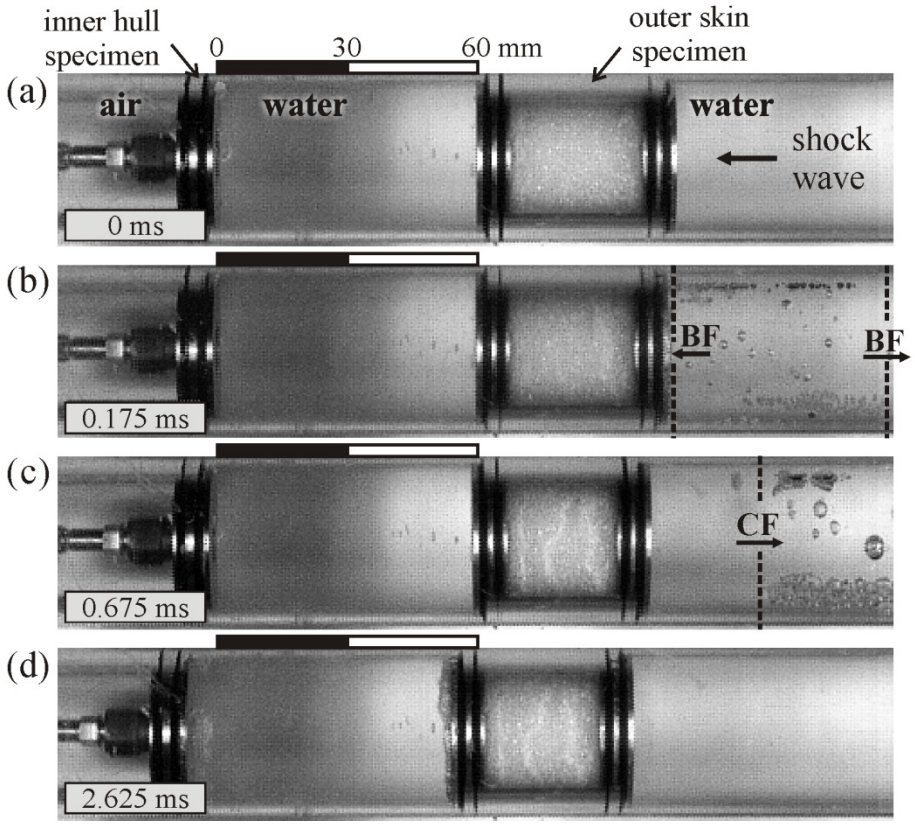



Fig. 6.7: Sequence of high-speed photographs for experiment 16 showing the response of a sandwich double-hull with an unsupported inner hull specimen consequent to underwater shock loading ( $p_0 = 11.5\,\text{MPa}$ , $\theta = 0.14\,\text{ms}$ , $m_F = 42.5\,\text{kgm}^{-2}$ , $m_F / m_B = 0.5$ ).

### 6.5.2 Structural response

Having described the main phenomena of the cavitation process observed in the experiments, we now proceed to analyse the response of outer skin and inner hull specimens. The intensity

of structural loading consequent to blast loading can be quantified by the specific impulse (impulse per unit area) imparted to the structure. Upon neglecting frictional forces between O-rings and tube wall, the impulse applied on the wet face of the inner hull specimen is given by

$$I_B(t) = \int_0^t p_B^f(\tau)\,\mathrm{d}\tau = m_B v_B(t) \tag{6.2}$$

where $p_B^f(\tau)$ denotes the time history of the dynamic pressure applied on the front face of the inner hull. In the experiments, $p_B^f(\tau)$ was measured using the pressure transducer mounted on the inner hull specimen and the impulse $I_B$ was obtained from eq. (6.2).

Now write linear momentum conservation for a monolithic outer skin plate,

$$I_F(t) = m_F v_F(t) + \int_0^t p_F^b(\tau)\,\mathrm{d}\tau\,, \tag{6.3}$$

with $p_F^b(\tau)$ the pressure history applied dynamically on the back face of the outer skin. Note that the experimental apparatus employed in this study does not allow measuring $p_F^b(\tau)$ and therefore the impulse $I_F(t)$ cannot be deduced from measurements.

In the following we present the time histories of the non-dimensional impulse $\bar{I}_B(t) = I_B(t)/(2p_0\theta)$ deduced from selected experiments by employing eq. (6.2) and we compare the experimental results with those obtained from corresponding FE simulations. In addition, FE results of the non-dimensional impulse $\bar{I}_F(t) = I_F(t)/(2p_0\theta)$ are provided to give insight into structural loading of the outer skin in a blast event.

(i) *Stationary inner hull* ($m_B \to \infty$).

Test series 2 (Table 6.2) was performed to investigate, for the case of rigidly supported inner hull specimens (thus, mimicking the 1D response of double-hulls with $m_B \to \infty$), the effect of core strength on structural loading, by holding the water gap width fixed, $D = 120\,\mathrm{mm}$.

Measurements of $\bar{I}_B(t) = I_B(t)/(2p_0\theta)$ obtained from these experiments are presented in Fig. 6.8 (a), together with the corresponding FE predictions. Both FE results and measurements show that when a monolithic outer skin specimen was used, the peak impulse imparted to the inner hull, $\bar{I}_{\mathrm{B,max}} = \max_{t\to\infty}\left[\bar{I}_{\mathrm{B}}(t)\right]$, exceeded $\bar{I}_0 = 1$, which represents the impulse applied on a rigid stationary plate consequent to loading by an exponentially decaying shock wave. In contrast, the impulse $\bar{I}_{\mathrm{B,max}}$ is remarkably reduced if sandwich construction is employed. The effect of sandwich core strength $\sigma_c$ is to govern $\bar{I}_{\mathrm{B,max}}$: cores of lower density $\rho_c$ and thus of lower collapse strength $\sigma_c$ result in larger impulse reductions. In particular, Fig. 6.8 (a) shows that the impulse $\bar{I}_{\mathrm{B,max}}$ was reduced by 60% when the sandwich core was made from the Rohacell 71 foam (in comparison to a monolithic plate of equal mass).

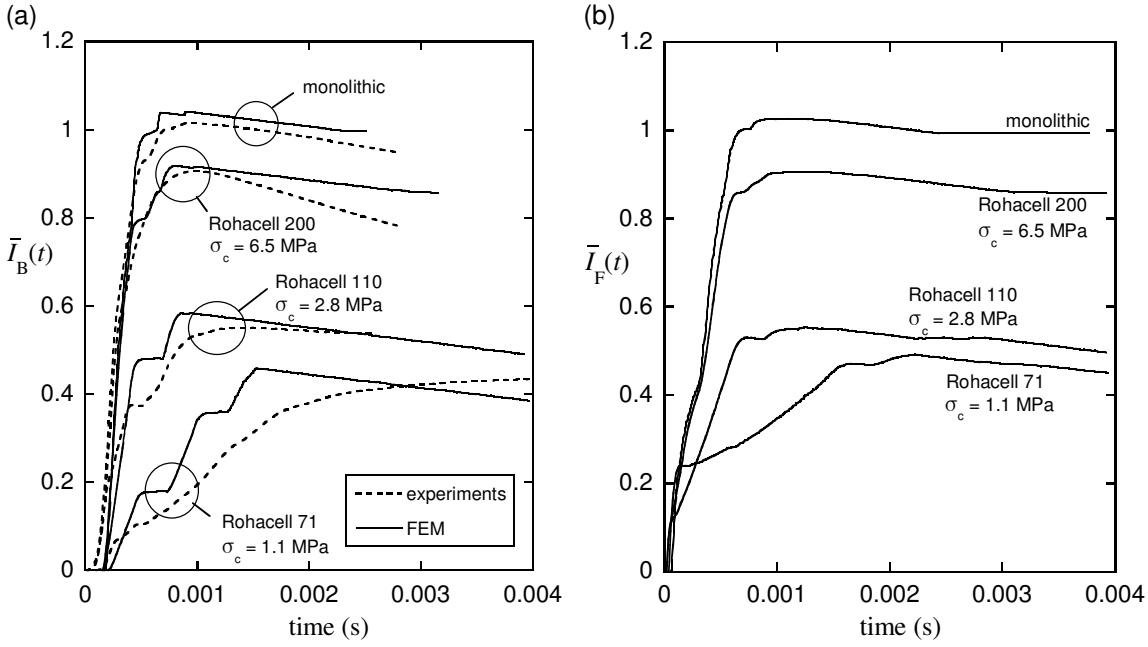



Fig. 6.8: Test series 2, stationary inner hull ($\psi_F = 3.4$, $D = 120\,\mathrm{mm}$): (a) Measurements and FE predictions of the non-dimensional impulse applied on the inner hull $\bar{I}_B(t)$ as functions of time; results obtained with both monolithic and sandwich double-hulls are included. (b) FE predictions of the non-dimensional impulse imparted to the outer skin $\bar{I}_F(t)$ for the same set of experiments.

The corresponding FE predictions of the normalised impulse $\overline{I}_F(t) = I_F(t)/(2p_0\theta)$ are plotted in Fig. 6.8 (b). It can be seen that the time histories $\overline{I}_F(t)$ follow similar trends as the corresponding $\overline{I}_B(t)$ histories. Moreover, $\overline{I}_{\mathrm{F,max}} \approx \overline{I}_{\mathrm{B,max}}$.

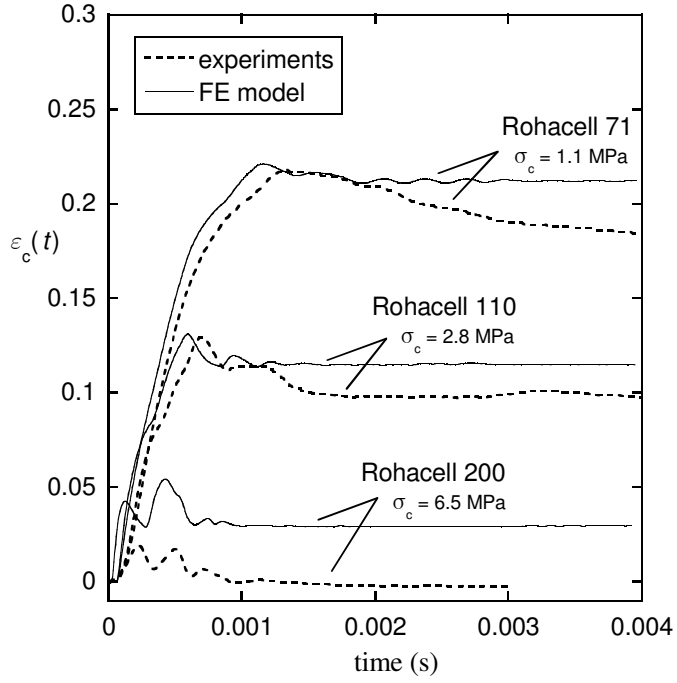



Fig. 6.9: Measurements and FE predictions of the compressive core strain $\varepsilon_c(t)$ as functions of time for for test series 2 ($\psi_F = 3.4$, $D = 120\,\mathrm{mm}$); sandwich plates with different types of core are compared.

In Fig. 6.9 we present measurements and FE predictions of the compressive core strain $\varepsilon_c(t) = \Delta c(t)/c$ as functions of time for the same test series. Time histories of core compression $\Delta c(t)$ were extracted from the high-speed photographs, such as illustrated in Fig. 6.5. All types of core considered here show similar trends: $\varepsilon_c(t)$ quickly reaches a peak value after which the core strain modestly decreases owing to elastic spring-back. Now compare Figs. 9a and 10: weak sandwich cores, such as Rohacell 71 cores, achieve the largest

reductions in impulse $\bar{I}_{\mathrm{B,max}}$, but at the expense of increased permanent core compression. However, the degree of core crush is relatively low in the experiments reported here and the FE predictions confirm this.

(ii) *Unsupported inner hull* ($m_B \approx m_F$).

In Fig. 6.10 (a), we report time histories of $\bar{I}_B(t)$ measured for experiment 12 (Table 6.3) performed to mimic the 1D blast response of a monolithic double-hull with $m_B \approx m_F$ (unsupported inner hull specimen), together with FE predictions of $\bar{I}_F(t)$ and $\bar{I}_B(t)$. Selected high-speed photographs recorded in this experiment are shown in Fig. 6.6. The upper horizontal line in Fig. 6.10 (a) represents predictions of the impulse applied on the outer skin for the case of infinite gap width, $D \to \infty$, while the lower horizontal line denotes predictions of the impulse imparted to the inner hull alone, i.e. with the outer skin structure absent, thus representing a case for which $m_F \to 0$. Note that the latter predictions were performed by using the analytical models presented in Chapter 3.

Upon the impact of the shock wave on the outer skin, $\bar{I}_F(t)$ rises rapidly until the water cavitates on both sides of the outer skin specimen, recall Fig. 6.6 (c); subsequently, loading ceases and $\bar{I}_F(t)$ slowly decreases, with the peak value $\bar{I}_{\mathrm{F,max}}$ well below the rigid plate predictions, $D \to \infty$. Pressure waves emanated from the back face of the outer skin impinge on the inner hull at a later time, hence the time shift between $\bar{I}_B(t)$ and $\bar{I}_F(t)$. Inner hull motion gives rise to cavitation in the water gap (Fig. 6.6 b) and this event terminates the loading phase of the inner hull due to vanishing pressure in the cavitated fluid and the imparted impulse attains a peak value $\bar{I}_{\mathrm{B,max}}$. Measurements and FE predictions of $\bar{I}_B(t)$ are

found in excellent agreement and show that the peak impulse $\overline{I}_{\mathrm{B,max}}$ slightly exceeds the predictions $m_F \to 0$. This can be explained by recalling that the inner hull is loaded by a pressure wave radiated from the back face of the outer skin. Such wave has significant rise time owing to the inertia of the outer skin and this can lead to delayed onset of cavitation and to prolonged structural loading of the inner hull.

Similar information is shown in Fig. 6.10 (b) for experiment 16 (Table 6.3). This test was similar to experiment 12 (see Fig. 6.10 a) but with the monolithic outer skin specimen replaced by a sandwich plate of equal mass. In this case, the outer skin perceives a sharp rise in $\overline{I}_F(t)$ consequent to the impact of the incident wave. Subsequently, the water cavitates very close to the front face sheet (recall Fig. 7b), which causes a bend in the $\overline{I}_F(t)$ curve. In the ensuing response, the impulse continues to rise at a relatively high rate due to the rapid collapse of the cavitated zone by propagation of a CF (see Fig. 6.7 c). Note that these observations are qualitatively consistent with the findings of previous studies on blast loading of sandwich plates [29]. Such cavitation process did not occur in the water gap (Fig. 6.7) and the impulse $\overline{I}_B(t)$ increases stepwise due to pressure waves travelling in the water gap. Now compare the peak values $\overline{I}_{\mathrm{F,max}}$ and $\overline{I}_{\mathrm{B,max}}$ between Fig. 6.10 (a) and Fig. 6.10 (b): sandwich construction leads to significant reductions of both $\overline{I}_{\mathrm{F,max}}$ and $\overline{I}_{\mathrm{B,max}}$ compared to monolithic designs of equal mass. Again, good correlation was achieved between FE predictions and measurements.

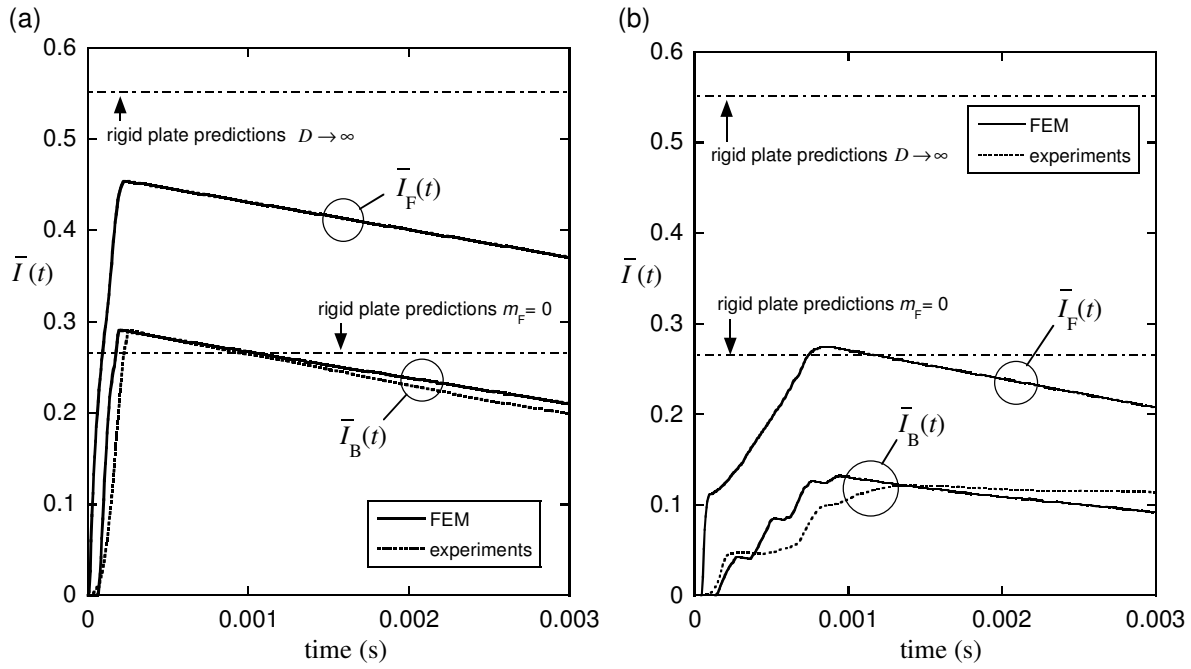



Fig. 6.10: Measurements and FE predictions of the impulse imparted to outer skin and inner hull specimens, $\bar{I}_F(t)$ and $\bar{I}_B(t)$, respectively, as functions of time for experiments conducted with unsupported inner hull specimens ($D = 60\,\text{mm}$, $\psi_F = 3.4$, $\psi_B = 1.8$): (a) monolithic double-hull (experiment 12); (b) sandwich double-hull (experiment 16); $\psi_F = 3.4$, $\psi_B = 1.8$ and $D = 60\,\text{mm}$ in both experiments.

### 6.5.3 Sensitivity of applied impulse and core crush to the gap width

The peak impulse $\bar{I}_{\max} = \max_{0 \le t < \infty} \left[ \bar{I}(t) \right]$ imparted to a structure in a blast event can be taken to quantify the severity of structural loading. For sandwich plates, the permanent core compression $\varepsilon_c^{pl} = \lim_{t \to \infty} \left[ \varepsilon_c(t) \right]$ determines to what extent the sandwich effect is maintained after blast loading.

We now proceed to examine the sensitivities of the performance metrics $\bar{I}_{\text{F,max}}$, $\bar{I}_{\text{B,max}}$ and $\varepsilon_c^{pl}$ to the width of the water gap for both stationary and unsupported inner hulls.

(i) *Stationary inner hull* ($m_B \to \infty$).

In Fig. 6.11 (a), the measurements of $\bar{I}_{\mathrm{B,max}}$ obtained from test series 1 (Table 6.2) are plotted against the gap width $D$; we include in Fig. 6.11 (a) the corresponding FE predictions of $\bar{I}_{\mathrm{F,max}}$ and $\bar{I}_{\mathrm{B,max}}$. For the tests performed with monolithic double-hulls, the impulse $\bar{I}_{\mathrm{B,max}}$ is approximately equal to the reference impulse $\bar{I}_0 = 1$ and increases modestly by increasing $D$. It can be seen from Fig. 6.11 (a) that sandwich construction mitigates the severity of structural loading dramatically: we report reductions in $\bar{I}_{\mathrm{B,max}}$ of approximately 40% as well as a slight increase of $\bar{I}_{\mathrm{B,max}}$ when $D$ is increased. Moreover, the FE predictions show that the discrepancies between $\bar{I}_{\mathrm{F,max}}$ and $\bar{I}_{\mathrm{B,max}}$ are insignificant. While measurements and FE predictions of $\bar{I}_{\mathrm{B,max}}$ are found in good correlation for the sandwich experiments reported in Fig. 6.11 (a), the FE results over-predict the $\bar{I}_{\mathrm{B,max}}$ measurements for the monolithic cases. Such discrepancy can be justified by small displacements of the inner hull specimen caused by imperfections in the constraints enforced on the specimen in the experiments; such displacements are less pronounced for the sandwich cases due to mitigated loading of the inner hull.

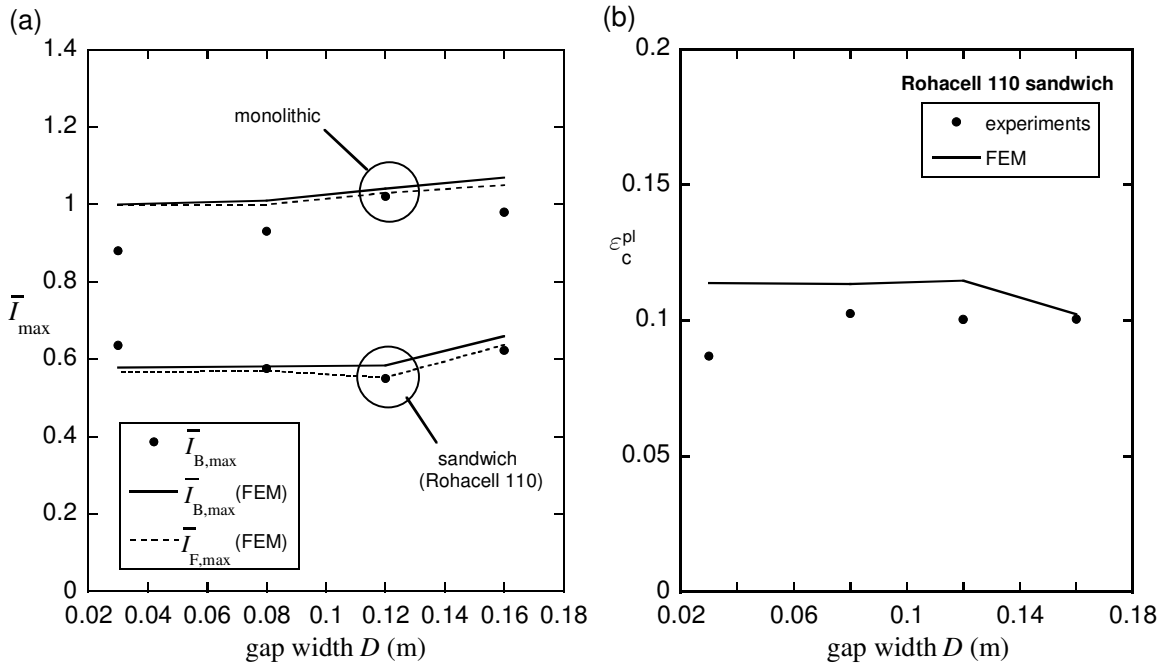



Fig. 6.11: Test series 1, stationary inner hull ($\psi_F = 3.4$): (a) effect of the water gap width $D$ on the maximum non-dimensional impulse imparted to the outer skin and inner hull, $\bar{I}_{\mathrm{F,max}}$ and $\bar{I}_{\mathrm{B,max}}$, respectively; measurements are indicated by full circles and the solid and dashed curves represent FE predictions. (b) Measurements and FE predictions of the core crush $\varepsilon_c^{pl}$ as functions of the water gap width $D$.

The measured variation of $\varepsilon_c^{pl}$ with gap width $D$ is shown in Fig. 6.11 (b) for the same series of experiments and compared with dynamic FE results. Both measurements and FE predictions show that $\varepsilon_c^{pl}$ is only mildly sensitive to $D$ and this is consistent with the impulse measurements shown in Fig. 6.11 (a). It is interesting to note that a core crush of $\varepsilon_c^{pl} \approx 0.1$ is sufficient to reduce the impulse by 40% in relation to a monolithic plate of equal mass.

(ii) *Unsupported inner hull* ($m_B \approx m_F$).

In Fig. 6.12 we present $\bar{I}_{\mathrm{B,max}}$ measurements obtained from the experiments performed within test series 3 (Table 6.3), all of which conducted with unsupported inner hull specimens and with $m_F / m_B = 0.5$ the mass ratio between outer skin and inner hull.

The chart in Fig. 6.12 (a) shows the sensitivity of $\bar{I}_{\mathrm{B,max}}$ to the width of the water gap $D$ for experiments with monolithic double-hulls. In addition, we include in Fig. 6.12 (a) the corresponding FE predictions of $\bar{I}_{\mathrm{B,max}}$ and $\bar{I}_{\mathrm{F,max}}$ as well as analytical rigid plate predictions for the cases $D \to \infty$ and $m_F = 0$, respectively, computed with the analytical models of Chapter 3. Upon increasing $D$, a modest increase in $\bar{I}_{\mathrm{F,max}}$ is observed; for $D \to \infty$ the outer skin response resembles that of a water-backed free-standing plate and, thereby, $\bar{I}_{\mathrm{F,max}}$ approaches the rigid plate predictions $D \to \infty$. The dependence of $\bar{I}_{\mathrm{B,max}}$ on the gap width $D$ is only marginal, with the values of $\bar{I}_{\mathrm{B,max}}$ approximately equal to the predictions $m_F = 0$. The measurements of $\bar{I}_{\mathrm{B,max}}$ are adequately predicted by the FE simulations.

In test series 3, experiments were also performed with sandwich (outer skin) specimens and the measurements of $\bar{I}_{\mathrm{B,max}}$ obtained from these tests are presented in Fig. 6.12 (b), together with FE predictions of $\bar{I}_{\mathrm{B,max}}$ and $\bar{I}_{\mathrm{F,max}}$. It can be seen from this figure that, upon increasing the width of the water gap $D$, the impulse $\bar{I}_{\mathrm{F,max}}$ increases while the values of $\bar{I}_{\mathrm{B,max}}$ slightly drop. The predictions and measurements of $\bar{I}_{\mathrm{B,max}}$ and $\bar{I}_{\mathrm{F,max}}$ are significantly lower than those shown in Fig. 6.12 (a) for the monolithic designs. Note that the core crush $\varepsilon_c^{pl}$ measured in these experiments was less than 15%.

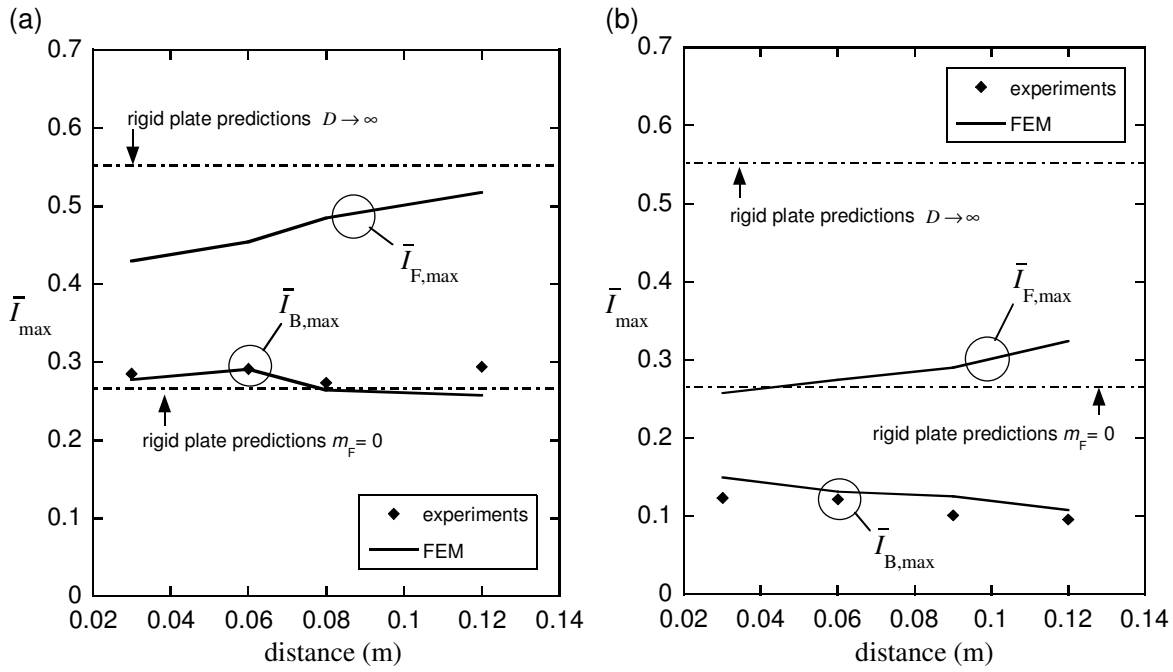



Fig. 6.12: Test series 3, unsupported inner hull ($m_F/m_B = 0.5$, $\psi_F = 3.4$, $\psi_B = 1.8$): (a) Measurements and FE predictions of $\bar{I}_{\mathrm{F,max}}$ and $\bar{I}_{\mathrm{B,max}}$ as functions of the water gap width $D$ for monolithic double-hulls; (b) similar information for the experiments performed with sandwich-double hulls.

In order to probe the effect of mass ratio $m_F/m_B$ on the impulse applied on the plates of a monolithic double-hull, additional experiments were conducted with $m_F/m_B = 3.3$ (test series 4, Table 6.3) and with the inner hull specimen free to move in the shock tube.

The measurements of $\bar{I}_{\mathrm{B,max}}$ obtained from these experiments are presented in Fig. 6.13 as functions of the gap width $D$; in addition, we include in this figure FE predictions of $\bar{I}_{\mathrm{B,max}}$ and $\bar{I}_{\mathrm{F,max}}$ as well as rigid plate predictions for the cases $D \to \infty$ and $m_F = 0$. Now compare Fig. 6.12 (a) and Fig. 6.13: increasing the mass ratio $m_F/m_B$ from 0.5 to 3.3 has only marginal effects on the predictions $D \to \infty$ (associated to the response of a water-backed rigid plate of mass $m_F$), while those for $m_F = 0$ (corresponding to blast loading of an air-backed rigid plate of mass $m_B$) are significantly reduced. This can be rationalised by recalling

that the impulse imparted to a water-backed rigid plate in a blast event is less sensitive to variations in mass compared to air-backed rigid plates, recall Fig. 4.13. The measurements and FE predictions of $\bar{I}_{\mathrm{B,max}}$ and $\bar{I}_{\mathrm{F,max}}$ also reflect this trend and are found in good correlation.

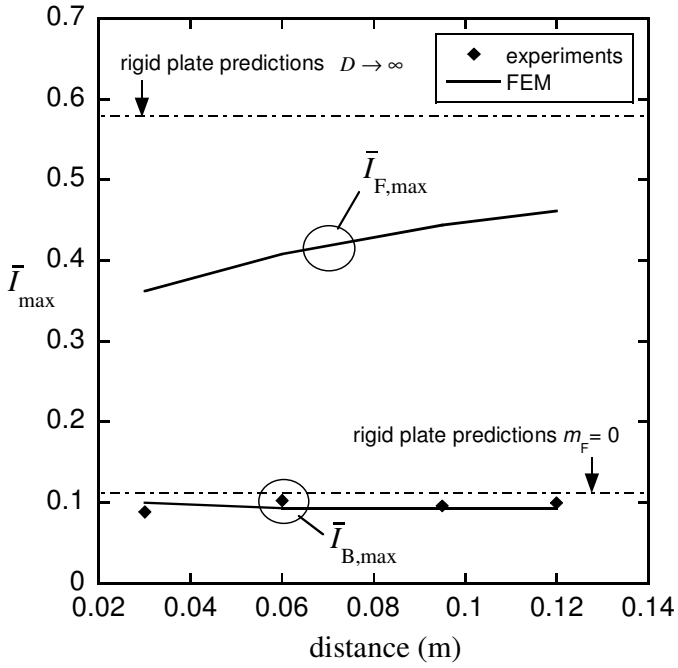



Fig. 6.13: Test series 4, unsupported inner hull ($m_F/m_B = 3.4$, $\psi_F = 1.9$, $\psi_B = 6.3$): (a) Measurements and FE predictions of $\bar{I}_{\mathrm{F,max}}$ and $\bar{I}_{\mathrm{B,max}}$ as functions of the water gap width $D$ for the case of monolithic double-hulls.

## 6.6 Conclusions

In this chapter we have investigated the 1D response to underwater blast loading of double-walled hulls comprising of a monolithic inner pressure hull, an outer shell and a water gap located between both structures.

Laboratory scale underwater shock experiments were performed on representative structural systems by using the shock tube apparatus presented in Chapter 4. High-speed photography was employed to observe structural motion as well as the ensuing cavitation phenomena

initiated by FSI. Dynamic fluid pressure measurements and high-speed photographs were employed to evaluate the permanent sandwich core compression as well as the impulse imparted to the inner hull consequent to blast loading. The obtained results of impulse and core crush were found in good agreement with the predictions obtained from detailed FE simulations and the main findings of this study are the following:

- For monolithic double hulls with rigid, stationary inner hulls (or, equivalently, with $m_B \to \infty$), cavitation does not occur in the water located between inner hull and outer skin and the peak impulse applied on the inner hull is approximately equal to that applied on a stationary rigid plate ($\bar{I}_0 = 1$) by an exponentially decaying shock wave. In contrast, when the outer skin is made from a sandwich plate, cavitation processes initiate in the water very close to the front face sheet of the outer skin. Such cavitation phenomena can substantially mitigate the severity of structural loading: for the types of core considered herein, the impulse imparted to the inner hull dropped by 60% in relation to that imparted to a monolithic double-hull with the mass of the outer skin equal to the total sandwich.

- For monolithic double-hulls with unsupported rigid inner hulls and with $m_B \approx m_F$, cavitation initiates in the water gap and continues to evolve in the front water column. The cavitation phenomena triggered by the motion of the inner hull lead to a reduction in impulse imparted to this structure (in relation to the impulse applied on a stationary inner hull in the same blast event). Further reductions in impulse can be achieved by (i) increasing the mass ratio between outer skin and inner hull or (ii) by employing the sandwich construction for the outer skin.

- The loading histories applied on outer skin and inner hull in a blast event are only scarcely sensitive to variations in the width of the water gap for all boundary conditions and problem geometries considered here.

The experimental results give valuable visual insight into the cavitation process and provide practical guidelines for the design of double-walled hulls resistant to underwater blast. However, the effect of initial static pressure on the response of both fluid and structure has not been addressed in this study and is left as a topic for a future study.

# Chapter 7

# Analytical Models for the Response of Elastic Circular Plates to Underwater Blast

## 7.1 Introduction

In the previous chapters, the 1D response of structures subject to blast loading in deep and shallow water was studied. Calculations based on theoretical models (Chapter 3) have shown that the ensuing cavitation process encompasses propagation of breaking fronts and closing fronts and their temporal and spatial evolution significantly affects structural loading. Experimental evidence for these theoretical findings was produced by simulating underwater blast loading of monolithic plates (Chapter 4), sandwich plates (Chapter 5) and double-walled structural systems (Chapter 6) in a transparent shock tube and observing structural motion as well as cavitation phenomena by means of high-speed photography.

Although experimental studies and theoretical models for 1D FSI problems provide great insight into the underlying physics, it still remains unclear how the discovered FSI phenomena affect the response of real-life structures, such as plates, beams or shells, in which both dynamic deformation and FSI are two-dimensional or three-dimensional in nature.

In this chapter we shall start answering this question by deriving an original analytical model capable to predict the dynamic deflection of elastic plates subject to loading by exponentially decaying shock waves in water or in a similar inviscid fluid. Such models are based on plate theory and take into account transverse shear deformations, stretching forces due to large deflections as well as the orthotropic material behaviour of fibre-reinforced composite plates; moreover, they also include, for the first time, the effects of flexural wave propagation on the response of fluid and structure. Phenomena arising from fluid-structure interaction subsequent to first cavitation will be taken as one-dimensional and the effects of cavitation will be included by employing the 1D theory developed in Chapter 3. The accuracy of the analytical models will be probed by comparing their predictions with those obtained from fully coupled 3D FE simulations. Finally, we shall use the validated analytical FSI models to construct design maps in order to determine the optimal designs which maximise the resistance to underwater blast.

## 7.2 Analytical models

In this section, we present analytical models for the dynamic response to underwater blast loading of clamped circular elastic plates with orthotropic or isotropic material properties. First, we derive the governing equations for the case of pressure pulse loading and impulsive loading with the effects of FSI neglected. These equations are, to the best of the author's knowledge, original and have not been derived elsewhere in the current literature. Then, we specialise these equations to the case of underwater blast loading and we present a procedure that takes into account the effects of FSI subsequent to first cavitation.

### 7.2.1 Pressure pulse loading

Consider a circular plate of thickness $h$ and radius $R$ with mass per unit area $\mu$, as sketched in Fig. 7.1. The plate is fully clamped at its boundary and made from an orthotropic (transversely isotropic) solid material, see Appendix B. The surface of the plate is loaded by an arbitrary pressure versus time history, $p_f(r,t)$, which is assumed to be uniformly distributed over the circular plate in direction of the circumferential coordinate $\varphi$.

Now assume that the initial dynamic response is governed by propagation of a flexural wave propagating in radial direction towards the centre of the plate, at velocity $\dot{\zeta}$, spanning the annular portion $(R-\zeta) \le r \le R$, as sketched in Fig. 7.1 (b). Accordingly, we separate the overall response in two phases and define as 'Phase 1' the response ranging from $t = 0$ to the instant when the flexural wave reaches the plate's centre point, $t_1$, i.e. $\zeta(t_1) = R$, while we denote as 'Phase 2' the response subsequent to $t_1$.

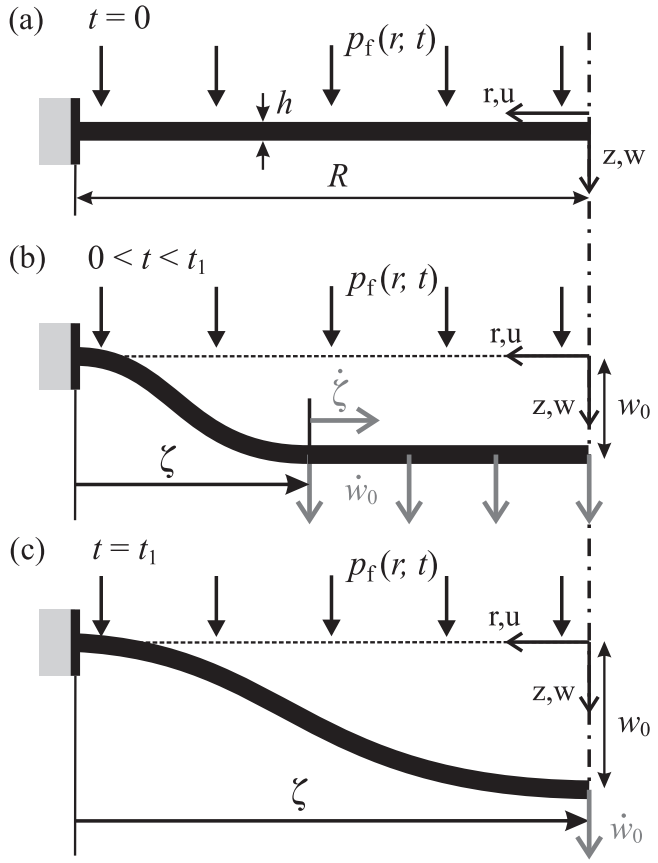



Fig. 7.1: Dynamic plate deformation consequent to pressure pulse loading: (a) initial configuration; (b) propagation of a flexural wave with the wave front located at $\zeta$; (c) the wave front reaches the plate's centre point and Phase 1 response terminates.

**a) Phase 1: wave propagation phase** $(0 \le t \le t_1)$**.**

In this section we proceed to derive the governing equations for calculating plate deflection $w(r,t)$ and flexural wave position $\zeta(t)$ during Phase 1 (Fig. 7.1 b).

Transverse loading of solid plates produces a response governed by a combination of bending and shear deformation. Deflection of the middle surface, $w(r,t)$, can be written as the summation of the deflection due to bending $w_B(r,t)$ and transverse shearing $w_S(r,t)$. The bending deformation profile for $(R-\zeta) \le r \le R$ is assumed to be described by

$$w_B(r,t) = w_{B0}(t)\left[3\left(\frac{R-r}{\zeta}\right)^2 - 2\left(\frac{R-r}{\zeta}\right)^3\right] \tag{7.1}$$

where $w_{B0}(t)$ is the bending deflection at the plate's centre point.

Let us now assume that the shear deformation $\gamma_{rz}$ is largest at the plate's periphery and decreases linearly in the negative *r*-direction, vanishing at the position of the wave front, $r = R - \zeta$. For the sake of simplicity, we assume that both shear wave and flexural wave propagate with equal velocity, $\dot{\zeta}$; thus the shear deformation profile for $(R-\zeta) \le r \le R$ can be written as

$$\gamma_{rz}(r,t) = \gamma_{rz0}(t)\left(1 - \frac{R-r}{\zeta}\right) \tag{7.2}$$

where $\gamma_{rz0}(t)$ denotes the shear angle at the clamped boundary, $r = R$. The resulting displacement profile $w_S(t)$ is obtained by integrating eq. (7.2) with respect to the coordinate *r* and employing the boundary conditions $w_{S0}(r = R) = 0$ and $w_S(r = R - \zeta) = w_{S0}$; the solution is

$$w_S(r,t) = w_{S0}(t)\left[2\left(\frac{R-r}{\zeta}\right) - \left(\frac{R-r}{\zeta}\right)^2\right]. \tag{7.3}$$

The deformed shape of the plate is then obtained by superposition of eq. (7.1) and eq. (7.3),

$$w(r,t) = w_{B0}(t)\left[3\left(\frac{R-r}{\zeta}\right)^2 - 2\left(\frac{R-r}{\zeta}\right)^3\right] + w_{S0}(t)\left[2\left(\frac{R-r}{\zeta}\right) - \left(\frac{R-r}{\zeta}\right)^2\right], \tag{7.4}$$

and the velocity profile follows from differentiating eq. (7.4) with respect to time as

$$\begin{aligned}\dot{w}(r,t) = {} & \dot{w}_{B0}\left[3\left(\frac{R-r}{\zeta}\right)^2 - 2\left(\frac{R-r}{\zeta}\right)^3\right] - \frac{w_{B0}\dot{\zeta}}{\zeta}\left[6\left(\frac{R-r}{\zeta}\right)^2 - 6\left(\frac{R-r}{\zeta}\right)^3\right] + \\ & + \dot{w}_{S0}\left[2\left(\frac{R-r}{\zeta}\right) - \left(\frac{R-r}{\zeta}\right)^2\right] - \frac{w_{S0}\dot{\zeta}}{\zeta}\left[2\left(\frac{R-r}{\zeta}\right) - 2\left(\frac{R-r}{\zeta}\right)^2\right].\end{aligned} \tag{7.5}$$

In order to write the governing equations more concisely, it is instructive to introduce two loading functions defined as

$$P_F\left(r_1, r_2, t\right) = 2\pi \int_{r_1}^{r_2} p_f\left(r, t\right) r dr \tag{7.6}$$

and

$$P_M\left(r_1, r_2, t\right) = \hat{\varphi} \int_{r_1}^{r_2} p_f\left(r, t\right)\left(R - r\right) r dr. \tag{7.7}$$

respectively, where $p_f\left(r,t\right)$ denotes the interface pressure with $r_1$ and $r_2$ the upper and lower boundary of the loaded area on the *r*-coordinate, respectively.

Let us assume that the circular plate is made from a laminate comprising $n$ layers of transversely isotropic composite materials stacked at arbitrary orientations (see Appendix B). For this class of materials it is convenient to write the relationship between in-plane forces $N_i$ (per unit width) and the corresponding in-plane strains $\varepsilon_i$ in Matrix form

$$\left(N_r \quad N_t \quad N_{rt}\right)^{\mathrm{T}} = \mathbf{A} \cdot \left(\varepsilon_r \quad \varepsilon_t \quad \gamma_{rt}\right)^{\mathrm{T}} \tag{7.8}$$

where $\mathbf{A}$ denotes the stiffness matrix of the laminate in the reference system $\left(r, \varphi, z\right)$, rotated by the angle $\varphi_k$ relative to the material coordinates $\left(1,2,3\right)_k$ of the *k*-th lamina $\left(k = 1,2,\ldots,n\right)$; the elements of the laminate's stiffness matrix, $A_{ij}$, can be deduced from the relative rotation $\varphi_k$, stiffness matrix $\mathbf{Q}_k$ (in material coordinates) and the thickness $h_k$ of each lamina by using appropriate transformations.

Likewise, for the bending and twisting moments $M_i$ (per unit width) we write

$$\left(M_r \quad M_t \quad M_{rt}\right)^{\mathrm{T}} = \mathbf{D} \cdot \left(\kappa_r \quad \kappa_t \quad \kappa_{rt}\right)^{\mathrm{T}} \tag{7.9}$$

with $\mathbf{D}$ the bending stiffness matrix of the laminate and $\kappa_i$ the bending and twisting curvatures; note that $D_{ij} = D_{ij}\left(\varphi_k, h_k, \mathbf{Q}_k\right)$ with $\left(k = 1,2,\ldots,n\right)$, as described above.

In a first approximation, dynamic plate deformation is taken as axisymmetric; also assume that the radial and tangential displacements are small compared to the transverse components, i.e. $|u| \ll |w|$, $|v| \ll |w|$. Consequently, the in-plane strains, bending curvatures and transverse shear deformations can be written as

$$\varepsilon_r = \frac{1}{2}\left(\frac{w_{B0} + w_{S0}}{\zeta}\right)^2 \; ; \; \varepsilon_t = \frac{u}{r} \approx 0 \; ; \; \gamma_{rt} = 0 \; ; \tag{7.10}$$

$$\kappa_r = -\frac{\partial^2 w_B}{\partial r^2} \; ; \; \kappa_t = -\frac{1}{r}\frac{\partial w_B}{\partial r} - \frac{1}{r^2}\frac{\partial w^2{}_B}{\partial \varphi^2} = -\frac{1}{r}\frac{\partial w_B}{\partial r} \; ; \; \kappa_{rt} = \frac{1}{r^2}\frac{\partial w_B}{\partial \varphi} - \frac{1}{r}\frac{\partial w_B}{\partial r \partial \varphi} = 0 ; \tag{7.11}$$

$$\gamma_{rz} = \frac{\partial w_S}{\partial r}; \; \gamma_{tz} = \frac{1}{r}\frac{\partial w_S}{\partial \varphi} = 0 \; ; \tag{7.12}$$

respectively. Note that $\varepsilon_r$ (eq. (7.10)) is a Taylor approximation of the in-plain strain induced in the plate in radial direction (due to stretching of its middle surface) by assuming a straight line for the deflection profile within the boundaries $r = R$ and $r = R - \zeta$. Upon combining eqs. (7.8), (7.9), (7.10) and (7.11), the in-plane forces, and bending moments can be written as

$$N_r = \frac{A_{11}}{2}\left(\frac{w_{B0} + w_{S0}}{\zeta}\right)^2 \; ; \; N_t = \frac{A_{12}}{2}\left(\frac{w_{B0} + w_{S0}}{\zeta}\right)^2 \tag{7.13}$$

and

$$M_r = -D_{11}\frac{\partial^2 w_B}{\partial r^2} - D_{12}\frac{1}{r}\frac{\partial w_B}{\partial r} \; ; \; M_t = -D_{21}\frac{\partial^2 w_B}{\partial r^2} - D_{22}\frac{1}{r}\frac{\partial w_B}{\partial r} \tag{7.14}$$

respectively. The transverse shear force $Q_{rz}$ is taken as uniform over the plate width and can be related to the shear deformation profile (eq. (7.2)) via

$$Q_{rz} = G_{rz} h \gamma_{rz} = \frac{2G_{rz} h\left(r - R + \zeta\right)}{\zeta^2} w_{S0}\left(t\right) \tag{7.15}$$

where $G_{rz}$ is the transverse shear modulus in the reference system $(r,\varphi,z)$ and can be calculated from the transverse shear moduli $(G_{13},G_{23})_k$ of each laminate and their rotation $\varphi_k$ relative to the laminate's reference system; $(k=1,2,\ldots,n)$.

Upon employing the loading function $P_F(r_1,r_2,t)$ defined in eq. (7.6), as well as deflection and velocity profiles given in eqs. (7.4) and (7.5), respectively, linear momentum conservation in *z*-direction (see Fig. 7.2 a) dictates

$$\int_0^t P_F(r_1,r_2,t)\,dt = 2\pi\int_0^{R-\zeta}\mu\dot{w}_0(t)\,r dr + 2\pi\int_{R-\zeta}^{R}\mu\dot{w}(r,t)\,r dr + R\int_0^t\int_0^{2\pi} Q_{rz}\big|_{r=R}\,d\varphi dt - \\ -R\int_0^t\int_0^{2\pi} N_r\big|_{r=R}\,\gamma_{rz}\big|_{r=R}\,d\varphi dt\ . \tag{7.16}$$

In the central portion of the plate, $0<r<(R-\zeta)$, both rotatory inertia and shear deformations vanish. At position $r=R-\zeta$, it is assumed that a jump in radial bending moment $M_r$ occurs across the wave front owing to the unsteadiness of plate curvature $\kappa_r$ at this point. Moreover, the shear deformations are zero at $r=R-\zeta$ (see eq.(7.2)) and thus the transverse shear force $Q_{rz}$ vanishes. Then, transverse equilibrium for $0<r<(R-\zeta)$ yields

$$\pi(R-\zeta)^2\,\mu\ddot{w}_0(t) = P_F(0,R-\zeta,t). \tag{7.17}$$

Now consider the circular plate sector of angle $\hat{\varphi}$ (arbitrarily chosen), as illustrated in Fig. 7.2 (b). Within $0<r<(R-\zeta)$ bending and shear deformations vanish; however, stretching forces are induced within this portion justified by the fact that tensile waves propagate much faster than shear and bending waves. Assuming that radial accelerations $\ddot{u}(t)$ are small compared to the induced in-plane forces, equilibrium in *r*-direction within $0<r<(R-\zeta)$ provides

$$\tilde{N}_r\big|_{R-\zeta}(R-\zeta)\hat{\varphi} = \int_0^{R-\zeta} \tilde{N}_t \hat{\varphi} dr. \tag{7.18}$$

Upon employing eqs. (7.7) and (7.18), conservation of angular momentum can be written as

$$\begin{aligned}\int_0^t P_M(r_1, r_2, t)dt = &\int_0^{R-\zeta} \mu \dot{w}_0(t)(R-r)rdr\,\hat{\varphi} + \int_{R-\zeta}^{R} \mu \dot{w}(r,t)(R-r)rdr\,\hat{\varphi} - \\ -\int_0^t \tilde{M}_r\big|_R R\hat{\varphi}dt + &\int_0^t \int_{R-\zeta}^{R} \tilde{M}_t \hat{\varphi} drdt + \int_0^t \int_{R-\zeta}^{R} \tilde{N}_t \hat{\varphi} w drdt + \int_0^t \tilde{N}_r\big|_{R-\zeta}(R-\zeta)\hat{\varphi}w_0 dt\end{aligned} \tag{7.19}$$

where $\tilde{N}_r$, $\tilde{N}_t$, $\tilde{M}_r$ and $\tilde{M}_t$ represent average values of in-plane forces (eq. (7.13)) and bending moments (eq. (7.14)) and are defined as

$$\begin{aligned}\tilde{N}_r &= \frac{1}{\hat{\varphi}}\int_0^{\hat{\varphi}} N_r(\varphi)d\hat{\varphi} \;\; ; \;\; \tilde{N}_t = \frac{1}{\hat{\varphi}}\int_0^{\hat{\varphi}} N_t(\varphi)d\hat{\varphi} \\ \tilde{M}_r &= \frac{1}{\hat{\varphi}}\int_0^{\hat{\varphi}} M_r(\varphi)d\hat{\varphi} \;\; ; \;\; \tilde{M}_t = \frac{1}{\hat{\varphi}}\int_0^{\hat{\varphi}} M_t(\varphi)d\hat{\varphi}.\end{aligned} \tag{7.20}$$

Combining eqs. (7.1), (7.3), (7.13), (7.14), (7.20) and evaluating the remaining integrals yields

$$\begin{aligned}\tilde{M}_r &= -\left(\frac{3D_{11}}{8} + \frac{D_{12}}{4} + \frac{3D_{22}}{8} + \frac{D_{66}}{2}\right)\frac{\partial^2 w_B}{\partial r^2} - \left(\frac{D_{11}}{8} + \frac{3D_{12}}{4} + \frac{D_{22}}{8} - \frac{D_{66}}{2}\right)\frac{1}{r}\frac{\partial w_B}{\partial r}; \\ \tilde{M}_t &= -\left(\frac{D_{11}}{8} + \frac{3D_{12}}{4} + \frac{D_{22}}{8} - \frac{D_{66}}{2}\right)\frac{\partial^2 w_B}{\partial r^2} - \left(\frac{3D_{11}}{8} + \frac{D_{12}}{4} + \frac{3D_{22}}{8} + \frac{D_{66}}{2}\right)\frac{1}{r}\frac{\partial w_B}{\partial r}.\end{aligned} \tag{7.21}$$

and

$$\begin{aligned}\tilde{N}_r &= \left(\frac{3A_{11}}{16} + \frac{A_{12}}{8} + \frac{3A_{22}}{16} + \frac{A_{66}}{4}\right)\left(\frac{w_{B0} + w_{S0}}{\zeta}\right)^2; \\ \tilde{N}_t &= \left(\frac{A_{11}}{16} + \frac{3A_{12}}{8} + \frac{A_{22}}{16} - \frac{A_{66}}{4}\right)\left(\frac{w_{B0} + w_{S0}}{\zeta}\right)^2.\end{aligned} \tag{7.22}$$

Substituting eqs. (7.4), (7.5), (7.15) and (7.22) into the equation of linear momentum conservation (7.16), evaluating the remaining integrals with respect to the coordinate $r$ and differentiating with respect to time $t$ gives

$$P_F\left(r_1,r_2,t\right)=\frac{\pi\mu}{30}\Big[\dot{\zeta}^2\left(18w_{B0}+10w_{S0}\right)-\zeta^2\left(21\ddot{w}_{B0}+25\ddot{w}_{S0}\right)+20R\dot{\zeta}\dot{w}_{S0}-R\ddot{\zeta}\left(30w_{B0}+20\ddot{w}_{S0}\right)+$$
$$+R\zeta\left(30\ddot{w}_{B0}+40\ddot{w}_{S0}\right)-\dot{\zeta}\zeta\left(24\dot{w}_{B0}+40\dot{w}_{S0}\right)+\ddot{\zeta}\zeta\left(18w_{B0}+10w_{S0}\right)\Big]-\pi\mu\left(R-\zeta\right)\Big[2\dot{\zeta}\left(\dot{w}_{B0}+\dot{w}_{S0}\right)+$$
$$+\left(\zeta-R\right)\left(\ddot{w}_{B0}+\ddot{w}_{S0}\right)\Big]+\frac{2\pi\left(G_{13}+G_{23}\right)hRw_{S0}}{\zeta}+\frac{4\pi Rw_{S0}\left(w_{B0}+w_{S0}\right)^2}{\zeta^3}\left(\frac{3A_{11}}{16}+\frac{A_{12}}{8}+\frac{3A_{22}}{16}+\frac{A_{66}}{4}\right). \tag{7.23}$$

Upon combining eqs. (7.4), (7.5), (7.19), (7.21) and (7.22) with the angular momentum conservation equation (7.19), evaluating the space integrals and differentiating with respect to time $t$, we obtain

$$P_M\left(r_1,r_2,t\right)=\frac{\mu}{6}\hat{\varphi}\left(R-\zeta\right)\Big[\left(R^2-2\zeta^2+R\zeta\right)\left(\ddot{w}_{B0}+\ddot{w}_{S0}\right)-6\dot{\zeta}\zeta\left(\dot{w}_{B0}+\dot{w}_{S0}\right)\Big]-\frac{\mu}{60}\hat{\varphi}\Big[\zeta^3\left(16\ddot{w}_{B0}+\right.$$
$$+18\ddot{w}_{S0}\left.\right)+\dot{\zeta}\zeta\left(36\dot{w}_{B0}+48\dot{w}_{S0}\right)-\left(\ddot{\zeta}\zeta^2+2\dot{\zeta}^2\zeta\right)\left(12w_{B0}+6w_{S0}\right)+\left(R\dot{\zeta}^2+R\ddot{\zeta}\zeta\right)\left(18w_{B0}+10w_{S0}\right)-$$
$$-R\zeta^2\left(21\ddot{w}_{B0}+25\ddot{w}_{S0}\right)-R\dot{\zeta}\zeta\left(24\dot{w}_{B0}+40\dot{w}_{S0}\right)\Big]+\frac{3w_{B0}\hat{\varphi}}{\zeta^3}\left(\frac{3D_{11}}{8}+\frac{D_{12}}{4}+\frac{3D_{22}}{8}+\frac{D_{66}}{2}\right)\times$$
$$\times\left[2R^2\ln\left(\frac{R-\zeta}{R}\right)-\zeta^2+2R\zeta\left(1+\ln\left(\frac{R}{R-\zeta}\right)\right)\right]+\frac{6Rw_{B0}\hat{\varphi}}{\zeta^2}\left(\frac{D_{11}}{8}+\frac{3D_{12}}{4}+\frac{D_{22}}{8}-\frac{D_{66}}{2}\right)+$$
$$\frac{\left(w_{B0}+w_{S0}\right)^3\left(R-\zeta\right)\hat{\varphi}}{\zeta^2}\left(\frac{3A_{11}}{16}+\frac{A_{12}}{8}+\frac{3A_{22}}{16}+\frac{A_{66}}{4}\right)+\frac{\hat{\varphi}\left(3w_{B0}+4w_{S0}\right)\left(w_{B0}+w_{S0}\right)^2}{12\zeta}\times$$
$$\times\left(\frac{A_{11}}{8}+\frac{3A_{12}}{4}+\frac{A_{22}}{8}-\frac{A_{66}}{2}\right). \tag{7.24}$$

The derived differential equations (7.17), (7.23) and (7.24) represent the equations of motion for $\zeta\left(t\right)$, $w_{B0}\left(t\right)$ and $w_{S0}\left(t\right)$ and can be solved numerically by imposing the initial conditions

$$\zeta\left(t=0\right)=0\ ;\ \dot{\zeta}\left(t=0\right)=0\ ;\ w_{S0}\left(t=0\right)=0\ ;$$
$$\dot{w}_{S0}\left(t=0\right)=0\ ;\ w_{B0}\left(t=0\right)=0\ ;\ \dot{w}_{B0}\left(t=0\right)=0 \tag{7.25}$$

for arbitrary loading functions $P_F\left(r_1,r_r,t\right)$ and $P_M\left(r_1,r_r,t\right)$ which can be calculated from eqs. (7.6) and (7.7) , by integrating the pressure history $p_f\left(r,t\right)$ over the loaded area of the plate.

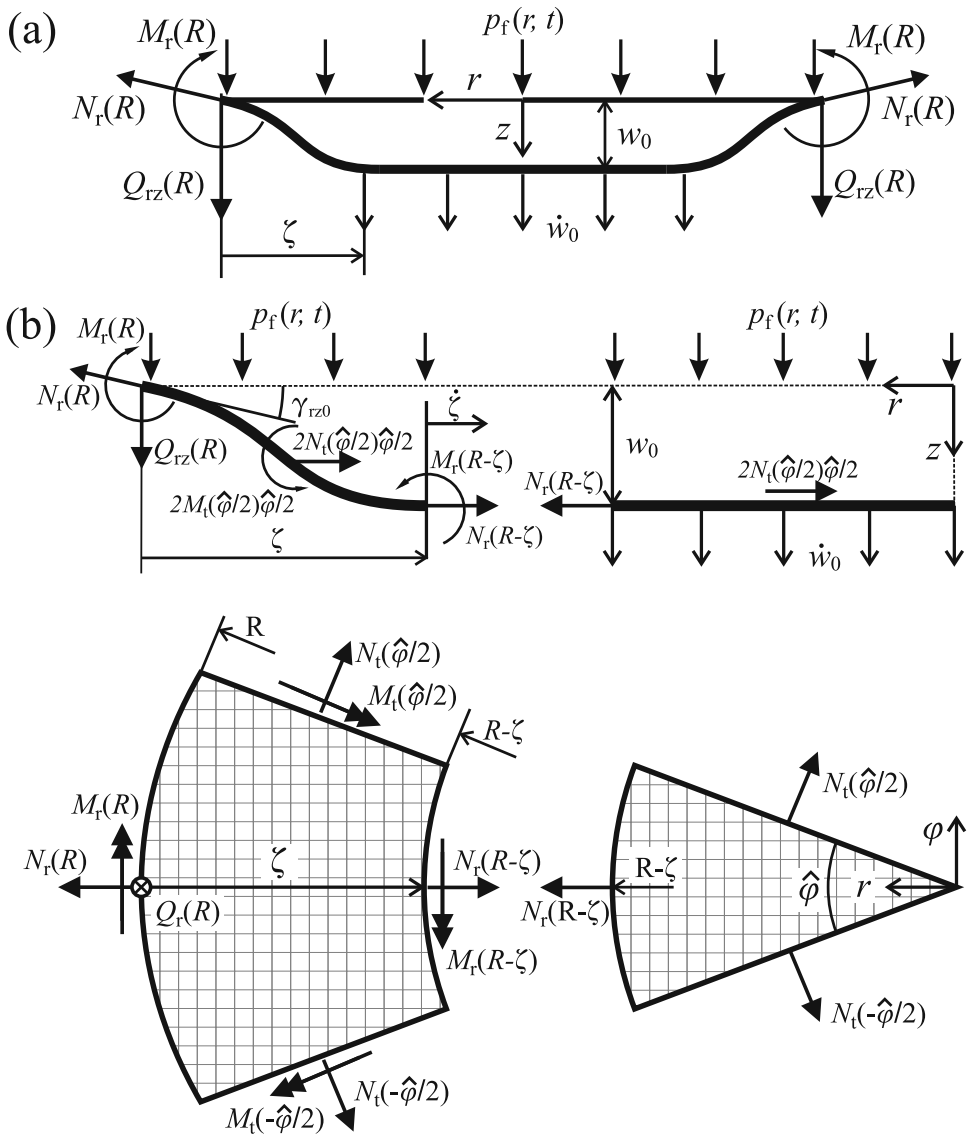



Fig. 7.2: Free body diagrams of the circular plate in deformed configuration: (a) section through the whole structure; (b) circular sector.

Note that for specific types of blast loading (e.g. underwater blast on large and thin structures, air-blast on stiff structures), structural loading can be taken as impulsive by imparting the plate an initial velocity

$$v_0 = \frac{I}{\mu} \tag{7.26}$$

in accordance to the blast impulse $I$ delivered to the structure. For the impulsive loading case both $P_F$ (eq. (7.6)) and $P_M$ (eq. (7.7)) vanish and solutions of $\zeta(t)$, $w_{B0}(t)$ and $w_{S0}(t)$

can be obtained via numerical integration of eqs. (7.17), (7.23) and (7.24) by using the initial conditions

$$\begin{aligned} &\zeta(0)=0\ ;\ \dot{\zeta}(0)=0\ ;\ w_{S0}(0)=0\ ; \\ &\dot{w}_{S0}(0)=0\ ;\ w_{B0}(0)=0\ ;\ \dot{w}_{B0}(0)=v_0\,. \end{aligned} \tag{7.27}$$

Phase 1 terminates at the instant when the flexural wave reaches the centre point, $\zeta(t_1)=R$, as shown in Fig. 7.1 (c).

**b) Phase 2: retardation phase** ($t>t_1$)**.**

We now proceed to derive the governing equations for the ensuing Phase 2 response. Now assume that flexural wave propagation phenomena become negligible for $t>t_1$ and that plate motion retards such that the deflection profile can be approximated by

$$w(r,t)=w_{B0}(t)\left[3\left(1-\frac{r}{R}\right)^2-2\left(1-\frac{r}{R}\right)^3\right]+w_{S0}(t)\left[2\left(1-\frac{r}{R}\right)-\left(1-\frac{r}{R}\right)^2\right]. \tag{7.28}$$

Note that eq. (7.28) was found by setting $\zeta=R=\text{const}$ in eq. (7.4). The velocity profile follows from differentiating eq. (7.28) with respect to time,

$$\dot{w}(r,t)=\dot{w}_{B0}\left[3\left(1-\frac{r}{R}\right)^2-2\left(1-\frac{r}{R}\right)^3\right]+\dot{w}_{S0}\left[2\left(1-\frac{r}{R}\right)-\left(1-\frac{r}{R}\right)^2\right]. \tag{7.29}$$

With the help of eqs. (7.28) and (7.29), the equations of motion (7.23) and (7.24) can be re-written as

$$P_F(r_1,r_2,t)=\frac{\pi\mu R^2}{10}\left(3\ddot{w}_{B0}+5\ddot{w}_{S0}\right)+4\pi Ghw_{S0}+\frac{4\pi w_{S0}\left(w_{B0}+w_{S0}\right)^2}{R^2}\left(\frac{3A_{11}}{16}+\frac{A_{12}}{8}+\frac{3A_{22}}{16}+\frac{A_{66}}{4}\right) \tag{7.30}$$

and

$$P_M\left(r_1,r_2,t\right)=\frac{\mu}{60}R^3\left(5\ddot{w}_{B0}+7\ddot{w}_{S0}\right)+\frac{9w_{B0}}{R}\left(\frac{3D_{11}}{8}+\frac{D_{12}}{4}+\frac{3D_{22}}{8}+\frac{D_{66}}{2}\right)+$$
$$+\frac{\left(3w_{B0}+4w_{S0}\right)\left(w_{B0}+w_{S0}\right)^2}{12R}\left(\frac{A_{11}}{8}+\frac{3A_{12}}{4}+\frac{A_{22}}{8}-\frac{A_{66}}{2}\right), \tag{7.31}$$

respectively. Solutions for $w_{B0}\left(t\right)$ and $w_{S0}\left(t\right)$ can be obtained by substituting the loading functions $P_F\left(r_1,r_2,t\right)$ and $P_M\left(r_1,r_2,t\right)$, as defined in eqs. (7.6) and (7.7), respectively, into eqs. (7.30) and (7.31) and integrating the obtained differential equations numerically for $t>t_1$ by using the Phase 1 solutions, evaluated at $t=t_1$, as initial conditions,

$$w_{S0}\left(t_1\right)=w_{S0,1}\ ,\ \dot{w}_{S0}\left(t_1\right)=\dot{w}_{S0,1}\ ,\ w_{B0}\left(t_1\right)=w_{B0,1}\ ,\ \dot{w}_{B0}\left(t_1\right)=\dot{w}_{B0,1}\ . \tag{7.32}$$

Note that $P_F=P_M=0$, if impulsive loading is considered.

### 7.2.2 Underwater blast loading

In this section, the governing equations presented in Section 7.2.1 are employed to construct an approximate FSI model for predicting the response of circular elastic plates subject to underwater blast. In the process, the loading functions $P_F$ and $P_M$, as defined in eqs (7.6) and (7.7), respectively, are specialised to account for the effects of the cavitation process.

Consider a circular orthotropic plate of thickness $h$, radius $R$ and mass per unit area $\mu$, with all degrees of freedom along its boundary constrained to zero. The plate is in contact with water of density $\rho_w$ on one side and is loaded (on the wet surface) by a planar exponentially decaying pressure wave of peak pressure $p_0$ and decay time $\theta$, travelling at speed of sound in water towards the plate, $c_w$. At an arbitrary time $t$ and distance from the fluid-structure interface $z$, this wave can be written as

$$p_{in}(z,t) = p_0 e^{-(t-z/c_w)/\theta} \tag{7.33}$$

by employing the coordinate system shown in Fig. 7.1. Upon arrival of the pressure wave (7.33) at the fluid-structure interface, the wave is partly transmitted into the structure, resulting in a compressive wave, travelling in the plate in through-thickness direction, while the other part of the incident wave reflects back into the fluid. The degree of wave transmission is dictated by the discrepancy in acoustic impedance between the water, $Z_w = \rho_w c_w$, and the structure, $Z = \rho c = \sqrt{E\rho}$. The maximum pressure at time $t = 0$ at the interface between the elastic structure and the fluid is given as

$$p_{f,\max} = p(z = 0, t = 0) = 2p_0 \frac{\sqrt{E\rho}}{\sqrt{E\rho} + Z_w}. \tag{7.34}$$

For a plate made from an isotropic material of density $\rho = 2000\,\text{kgm}^{-3}$ and Young's modulus $E = 50\,\text{GPa}$ subject to loading by a pressure wave in water of density $\rho_w = 1000\,\text{kgm}^{-3}$ and speed of sound $c_w = 1498\,\text{ms}^{-1}$, the maximum pressure $p_{f,\max}$ is reduced by 13% compared to that applied on a rigid plate $(E \to \infty)$, $p_{f,\max} = 2p_0$. For the sake of simplicity, we shall neglect transverse wave propagation in the plate and assume full reflection of the incident pressure wave at the fluid-structure interface.

It merits comment that the reflection of planar waves at curved interfaces renders the formulation of the fluid pressure field in exact form extremely complicated. However, for the range of centre deflections $0 \le w_0/R < 0.25$ considered here, it can be assumed that the reflected waves remain planar and travel into the negative *z*-direction, without affecting the pressure and particle velocity fields perpendicular to the incidence angle; thus

$$p_{out}(z,t) = p_0 e^{-(t+z/c_w)/\theta} \tag{7.35}$$

the reflected wave. Upon arrival of the pressure pulse (7.33) at the fluid-structure interface, $z = 0$, at time $t = 0$, the plate is set in motion and a rarefaction wave of magnitude

$$p_{rare}(r, z, t) = -\rho_w c_w \dot{w}(r, t + z / c_w) \tag{7.36}$$

emanates from the interface and propagates into the negative $z$-direction, owing to compatibility between fluid and structure at the interface. The absolute pressure field in the fluid is given by superposition of the hydrostatic pressure field and the dynamic pressure field comprising of incident, reflected and rarefaction waves, hence

$$p(r, z, t) = p_{st} + p_0 e^{-(t - z/c_w)/\theta} + p_0 e^{-(t + z/c_w)/\theta} - \rho_w c_w \dot{w}(r, t + z / c_w) \tag{7.37}$$

In this Chapter, attention is focused on underwater blast loading of composite plates in shallow water and therefore we neglect the contributions of the hydrostatic pressure field, thus assuming $p_{st} = 0$ in the following.

The tensile term in eq. (7.37) can cause the fluid pressure to drop to the value of the vapour pressure of the fluid at a location $(r_c, z_c)$ and time $t_c$. For typical blast events in water, the vapour pressure is negligible in comparison to the peak pressure of the blast wave and therefore, we assume $p_c = 0$ in the following analysis, in line with previous studies on underwater blast loading [4, 27, 29, 30]. Both the fluid pressure field and the loads applied on surrounding structures in a blast event are significantly affected by the occurrence of cavitation and eq. (7.37) needs to be modified.

For plates of practical dimensions, the cavitation time $t_c$ is much smaller than the time it takes the flexural wave to reach the plate's centre point, $t_1$; therefore, we assume in the following $t_c < t_1$. Accordingly, the Phase 1 response is separated into two stages, namely 'Phase 1a', representing the response prior to cavitation, $t \le t_c$, and 'Phase 1b', defined as the response for $t_c < t \le t_1$.

**a) Phase 1a response** ($t \le t_c$)**.**

We now proceed to characterise structural loading for Phase 1a, by defining adequate loading functions $P_F$ and $P_M$.

As described in Section 7.2.1 and shown in Fig. 7.1, Phase 1 deformation entails propagation of a flexural wave, spanning the plate portion $(R-\zeta) \le r \le R$ and travelling inwards (i.e. towards the centre point), at velocity $\dot{\zeta}$. During Phase 1a, the plate is in contact with uncavitated water on its entire front face and thereby, the pressure at the fluid-structure interface is obtained by evaluating the fluid pressure field (7.37) at the fluid-structure interface, $z = 0$; this gives

$$p_{f,1a}(r,t) = 2p_0 e^{-t/\theta} - \rho_w c_w \dot{w}(r,t). \tag{7.38}$$

In particular, loading of the plate's undeformed central portion, $0 < r < (R-\zeta)$, can be described by

$$\hat{p}_{f,1a} = 2p_0 e^{-t/\theta} - \rho_w c_w (\dot{w}_{B0} + \dot{w}_{S0}). \tag{7.39}$$

Substituting eq. (7.39) into (7.17) yields the governing equation for transverse plate motion within the portion $0 < r < (R-\zeta)$

$$\mu(\ddot{w}_{B0} + \ddot{w}_{S0}) = 2p_0 e^{-t/\theta} - \rho_w c_w (\dot{w}_{B0} + \dot{w}_{S0}). \tag{7.40}$$

The loading functions for Phase 1a, $P_{F,1a}$ and $P_{M,1a}$, respectively, can be found by combining eqs. (7.5), (7.6), (7.7) and (7.38). After evaluating the remaining integrals, we obtain

$$\begin{aligned} P_{F,1a} = {} & 2\pi R^2 p_0 e^{-t/\theta} + \frac{\pi \rho_w c_w}{30}\Big[\zeta^2(21\dot{w}_{B0} + 25\dot{w}_{S0}) - 10R\zeta(3\dot{w}_{B0} + 4\dot{w}_{S0}) + \\ & + 10R\dot{\zeta}(3w_{B0} + 2w_{S0}) - 2\dot{\zeta}\zeta(9w_{B0} + 5w_{S0})\Big] - \pi\rho_w c_w (R-\zeta)^2(\dot{w}_{B0} + \dot{w}_{S0}) \end{aligned} \tag{7.41}$$

and

$$P_{M,1a} = \frac{R^3}{3}\hat{\varphi}p_0 e^{-t/\theta} + \frac{\rho_w c_w \hat{\varphi}}{60}\zeta\left[2\zeta^2\left(8\dot{w}_{B0}+9\dot{w}_{S0}\right) - R\zeta\left(21\dot{w}_{B0}+25\dot{w}_{S0}\right) + \right.$$
$$\left. +2R\dot{\zeta}\left(9w_{B0}+5w_{S0}\right) - 6\dot{\zeta}\zeta\left(2w_{B0}+1w_{S0}\right)\right] - \frac{\rho_w c_w \hat{\varphi}}{3}\left(R-\zeta\right)^2\left(R+2\zeta\right)\left(\dot{w}_{B0}+\dot{w}_{S0}\right). \quad (7.42)$$

Combining eqs. (7.41), (7.42), (7.23), (7.24) and (7.40) yields the governing equations of motion for Phase 1a, which can be solved for $\zeta(t)$, $w_{B0}(t)$ and $w_{S0}(t)$ via numerical integration by imposing the initial conditions given in eq. (7.25).

It can be shown analytically that the cavitation process will initiate at time

$$t_c = \frac{\ln\psi}{\psi - 1}\theta \quad (7.43)$$

uniformly within the undeformed portion of the plate $0 < r > (R-\zeta)$, causing the interface pressure to vanish[‡] ($\psi$ is a non-dimensional parameter defined as $\psi = \rho_w c_w \theta / \mu$). Subsequently, a zone of cavitated water spreads from the fluid-structure interface at time $t_c$ (7.43), spanning the plate portion $0 < r \le a_c$, with $a_c = R - \zeta(t_c)$ the radius of cavitated fluid. The ensuing cavitation process invalidates the expression for the interface pressure (7.38) and terminates the Phase 1a response at time $t_c$.

**b) Phase 1b response** ($t_c < t \le t_1$)**.**

For the response ranging between the onset of cavitation $t_c$ and the arrival of the flexural wave at the plate's centre point $t_1$, we assume that the plate remains in contact with cavitated water within $0 < r \le a_c$, causing vanishing interface pressure, while the annular portion,

[‡] For Phase 1a, the solutions of the overall central plate deflection governed by eq. (7.40) coincide with the 'Taylor solution' [5].

$a_c < r \le R$, is in contact with uncavitated water and subject to loading by the incident shock wave, hence eq. (7.38) holds:

$$p_{f,1b} = \begin{cases} 0 & \text{for } 0 < r \le a_c \\ 2\,p_0 e^{-t/\theta} - \rho_w c_w \dot{w}(r,t) & \text{for } a_c < r \le R \end{cases} \tag{7.44}$$

The loading functions $P_{F,1b}$ and $P_{M,1b}$ are obtained by substituting eq. (7.44) into eqs. (7.6) and (7.7), respectively; this gives

$$\begin{aligned} P_{F,1b} &= 2\pi \left( \int_{a_c}^{R} 2\,p_0 e^{-t/\theta} r dr - \int_{a_c}^{R} \rho_w c_w \dot{w}(r,t)\, r dr \right); \\ P_{M,1b} &= \int_{a_c}^{R} 2\,p_0 e^{-t/\theta} (R-r)\, r dr - \int_{a_c}^{R} \rho_w c_w \dot{w}(r,t)(R-r)\, r dr. \end{aligned} \tag{7.45}$$

For the sake of brevity, the evaluation of the integrals in eq. (7.45) is not carried any further here. Combining eqs. (7.23), (7.24), (7.40) and (7.45) gives the equations of motion for Phase 1b which can be solved numerically for $t_c < t \le t_1$ by imposing the initial conditions

$$\begin{gathered} \zeta(t_c) = \zeta_c \;; \qquad \dot{\zeta}(t_c) = \dot{\zeta}_c \;; \qquad w_{S0}(t_c) = w_{S0,c} \;; \\ \dot{w}_{S0}(t_c) = \dot{w}_{S0,c} \;;\; w_{B0}(t_c) = w_{B0,c} \;;\; \dot{w}_{B0}(t_c) = \dot{w}_{B0,c} \end{gathered} \tag{7.46}$$

obtained from the Phase 1a solutions evaluated at $t = t_c$.

The flexural wave continues propagating inwards and will reach the plate's centre point at $t_1$, i.e. when $\zeta(t_1) = R$. As described in Section 7.2.1, flexural wave propagation phenomena are neglected in the subsequent stage of response and the plate's deflection profile, the cavitation process as well as the structural loading histories need to be modified to adequately predict the plate's response for $t > t_1$.

**c) Phase 2 response ($t > t_1$).**

During the Phase 2 response, flexural wave propagation in the solid is neglected and the deformed shape of the plate (see eq. (7.28)) is assumed to be time-independent and similar to that of a statically loaded plate, as detailed in Section 7.2.1 (b).

As the transverse deflection $w_0$ increases, in-plane forces due to stretching of the plate's middle surface become more dominant and help resisting transverse loads. The ensuing increase in transverse stiffness has effects on FSI and structural loading during the Phase 2 response and these are handled as follows: the cavitated water in contact with the plate's central portion, $0 < r \le a_c$, collapses by propagation of a closing front (CF) and the plate is subject to continued loading by pressure waves travelling in the water layer between the fluid-structure interface and the propagating CF. Note that this scenario is qualitatively consistent with 1D analytical predictions presented in Chapter 3 for underwater blast loading of rigid, spring-supported plates. While loading histories subsequent to the cavitation collapse can be predicted for simple 1D FSI problems (see Chapter 3), exact solutions for underwater blast loading of circular plates are extremely complex and computational. Therefore, we assume that pressure wave loading during Phase 2 can be mimicked by loading the plate with an incident pressure wave $p_{in}^{1D}$ obtained from predictions performed a priori by using the 1D FSI models presented of Chapter 3.

A detailed prescription on how these 1D predictions are computed is given in Appendix A.

Now write the interface pressure applied on the wet face of the circular plate in terms of the predictions $p_{in}^{1D}$

$$p_{f,2}(r,t) = 2p_{in}^{1D}(t) - \rho_w c_w \dot{w}(r,t). \tag{7.47}$$

The corresponding loading functions $P_{F,2}$ and $P_{M,2}$ follow from substituting eq. (7.47) into eqs. (7.6) and (7.7), respectively. Upon evaluating the remaining integrals we obtain

$$\begin{aligned} P_{F,2} &= 2\pi R^2 p_{in}^{1\mathrm{D}} - \frac{\pi \rho_w c_w \left(9R^2 \dot{w}_{B0} + 15R^2 \dot{w}_{S0}\right)}{30}; \\ P_{M,2} &= \frac{R^3 p_{in}^{1\mathrm{D}} \hat{\varphi}}{3} - \frac{R \rho_w c_w \hat{\varphi} \left(5R^2 \dot{w}_{B0} + 7R^2 \dot{w}_{S0}\right)}{60}. \end{aligned} \tag{7.48}$$

Combining eqs. (7.48), (7.30) and (7.31) yields the equations of motion for Phase 2

$$\begin{aligned} &20R^2 p_{in}^{1\mathrm{D}} - 2\rho_w c_w \left(3R^2 \dot{w}_{B0} + 5R^2 \dot{w}_{S0}\right) = \mu R^2 \left(3\ddot{w}_{B0} + 5\ddot{w}_{S0}\right) + \\ &+40Ghw_{S0} + \frac{40w_{S0}\left(w_{B0} + w_{S0}\right)^2}{R^2}\left(\frac{3A_{11}}{16} + \frac{A_{12}}{8} + \frac{3A_{22}}{16} + \frac{A_{66}}{4}\right) \end{aligned} \tag{7.49}$$

and

$$\begin{aligned} &\frac{R^3 p_{in}^{1\mathrm{D}}}{3} - \frac{R\rho_w c_w \left(5R^2 \dot{w}_{B0} + 7R^2 \dot{w}_{S0}\right)}{60} = \frac{\mu}{60} R^3 \left(5\ddot{w}_{B0} + 7\ddot{w}_{S0}\right) + \\ &+\frac{9w_{B0}}{R}\left(\frac{3D_{11}}{8} + \frac{D_{12}}{4} + \frac{3D_{22}}{8} + \frac{D_{66}}{2}\right) + \frac{\left(3w_{B0} + 4w_{S0}\right)\left(w_{B0} + w_{S0}\right)^2}{12R}\left(\frac{A_{11}}{8} + \frac{3A_{12}}{4} + \frac{A_{22}}{8} - \frac{A_{66}}{2}\right), \end{aligned} \tag{7.50}$$

respectively. The governing equations, (7.49) and (7.50), respectively, can be solved numerically for $w_{B0}(t)$ and $w_{S0}(t)$ by imposing the initial conditions given in eq. (7.32).

## 7.3 Finite element models

Three-dimensional FE simulations were performed using ABAQUS/Explicit to provide more insight into FSI and to validate the analytical models described in Section 7.2. The FE method is convenient as it is able to capture all the details of FSI subsequent to first cavitation as well as flexural wave propagation in the solid.

Unless otherwise stated, the simulations were based on FE models consisting of a circular plate of thickness $h$ and radius $R$ and a water column of length $L$ and radius $R$. Due to the

symmetry of the problem, only a cirular sector with an angle of 90° was modelled by applying appropriate boundary conditions on the planes of symmetry.

### 7.3.1 Material models

For the circular plate, two different types of materials were considered as described below.

a) *Material 1: composite material with orthotropic elastic properties*

Consider a laminated composite material of total thickness $h = 8\,\text{mm}$ comprising of 24 laminas, each of thickness $h_{ply} = 0.333\,\text{mm}$. Each lamina is composed of unidirectional fibres surrounded by matrix material and can be taken as a transversely isotropic solid (Appendix B) subject to plane stress with density $\rho = 1500\,\text{kgm}^{-3}$, Young's modulus in the fibre direction $E_1 = 100\,\text{GPa}$ and $E_2 = 10\,\text{GPa}$ in the transverse direction. The Poisson's ratios are $\nu_{12} = \nu_{23} = 0.2$ and $\nu_{21} = \nu_{12} E_2 / E_1 = 0.02$ and the in-plane and transverse shear moduli are assumed to be $G_{12} = G_{13} = 10\,\text{GPa}$ and $G_{23} = E_2 / \left[ 2\left(1 + \nu_{23}\right) \right] = 4.2\,\text{GPa}$, respectively. Two different layups are considered, a *0-90 laminate* with stacking sequence $[0,90,90,0]_6$ and a *quasi-isotropic laminate* with $[0,45,90,-45]_6$.

b) *Material 2: isotropic material.*

The isotropic material is modelled with Young's modulus $E = 50\,\text{GPa}$ and Poisson's ratio $\nu = 0.25$; the density is taken to be $\rho = 2000\,\text{kgm}^{-3}$.

The constitutive response of water is modelled by using a Mie-Gruneisen equation of state with a linear Hugoniot relation to give a linear-elastic relationship between the fluid pressure

and the compressive volumetric strain, as detailed in Section 3.3; such material model is readily implemented in ABAQUS/Explicit [49]. Density and speed of sound were taken as $\rho_w = 1000\,\mathrm{kgm}^{-3}$ and $c_w = 1498\,\mathrm{kgm}^{-3}$, respectively, and the shear modulus was assumed to be zero. The pressure cut-off at $p_c = 0$ due to cavitation of the fluid is modelled by setting the tensile failure criterion in the equation of state model to zero [49].

### 7.3.2 Details on the FE models

In order to capture the anisotropic behaviour of *Material 1* as well as the 3D cavitation processes in the water, the FE simulations were based on fully coupled 3D models.

The water column was discretised by using a combination of eight-noded hexahedral brick elements (C3D8R) with reduced integration and six-noded triangular wedge elements (CRD6). It was meshed in ABAQUS with 16 elements in radial direction and 12 elements in circumferential direction, matching the mesh size of the adjoining circular plate which was tied to one end of the water column. In longitudinal direction, a mesh size of 0.15 mm was chosen to model the shock front of the incident wave with adequate accuracy (see Fig. 3.6 for a mesh sensitivity study). The circular plate was discretised using four-noded quadrilateral shell elements (S4R) with reduced integration as well as three-noded triangular elements (S3R) for the central portion. The laminated composite was modelled by assigning a composite shell section of 24 laminas (see Section 7.3.1 a) to the plate with three integration points for each lamina in through-thickness direction.

Due to the linear-elastic isotropic constistutive response of *Material 2*, FE simulations performed with this material were based on an axisymmetric model. Both plate and fluid column were discretised using four-noded axisymmetric quadrilateral elements (CAX4R,

reduced integration) with 16 elements in radial direction. Tie constraints were applied between fluid and plate nodes to enforce compatibility of fluid and plate displacements at this interface. For a typical plate of thickness $h$ = 10 mm, there were 9 elements in through-thickness direction and the element size of the fluid mesh in longitudinal direction was set to 0.15 mm.

Details on the boundary conditions are as follows. The plate was assumed to be fully clamped along its periphery with all degrees of freedom constrained to zero. For all nodes on the plate's centre line, the angle of rotation and the displacements in radial direction were set to zero; moreover, radial displacements of the nodes on the lateral area of the fluid column were forced to vanish.

To avoid excessive mesh distortion in the fluid subsequent to cavitation, the automatically calculated time step was reduced to 50%-75% and the bulk viscosity was decreased to 30% of the default values, in order to reduce artificial energy dissipation.

Underwater blast loading was performed by imposing an exponentially decaying pressure boundary condition of peak pressure $p_0$ and decay time $\theta$ according to eq. (7.33) at the free end of the water column. In all simulations, the decay time was taken to be $\theta = 0.15\,\text{ms}$ and the peak pressure $p_0$ ranged between 10 MPa and 160 MPa.

## 7.4 Comparison and discussion of results

### 7.4.1 Impulsive loading

In this section, we present results obtained from the FE and analytical models for the case of impulsively loaded circular elastic plates. First, analytical and FE predictions of central deflection histories are compared in order to assess the accuracy of the analytical models (Section 7.2.1) with effects of FSI neglected. Second, the validated analytical models are employed to construct a design chart for selecting plate geometries for a given blast impulse and with a constraint on the maximum centre deflection. Finally, we include effects of FSI in the analytical predictions by imparting the plate a velocity according to the 'Taylor impulse' [4] and we assess the quality of this assumption by comparing the predictions with results obtained from fully coupled FE simulations.

**a) Comparison between FE and analytical predictions by neglecting FSI**

Analytical and FE predictions of central deflection versus time histories of laminated composite plates (*Material 1,* $[0,90,90,0]_6$) subject to impulsive loading with $v_0 = 85\,\mathrm{ms}^{-1}$ are plotted in Fig. 7.3 (a) and (b) for two different plate geometries, ($h = 8\,\mathrm{mm}$, $R = 150\,\mathrm{mm}$) and ($h = 8\,\mathrm{mm}$, $R = 100\,\mathrm{mm}$), respectively. In the FE simulations, the water column was excluded from the FE model and loading was performed by imparting $v_0$ uniformly to the plate. For both geometries, analytical and FE predictions show that, in the initial phase of response, the plate's centre point moves in transverse direction with a constant velocity, i.e. maintaining the initially imparted velocity $v_0$. The analytical models predict that the flexural wave reaches the centre point ($r = 0$) at $t_1$, as indicated in Fig. 7.3 (a) and (b); consequently, Phase 1 terminates and in the subsequent Phase 2 response, the residual kinetic energy of the plate is

converted to elastic strain energy by further bending, stretching and shearing until the maximum central deflection $w_0^{\max}$ is reached at $t_{\max}$. In the FE simulations, $t_{\max}$ is smaller and transverse oscillations occur at a higher frequency which contribute to the overall central plate deflection. Such oscillations are not captured by the analytical models; however, the magnitude of $w_0^{\max}$ is found in excellent agreement with the FE predictions in both Fig. 7.3 (a) and Fig. 7.3 (b).

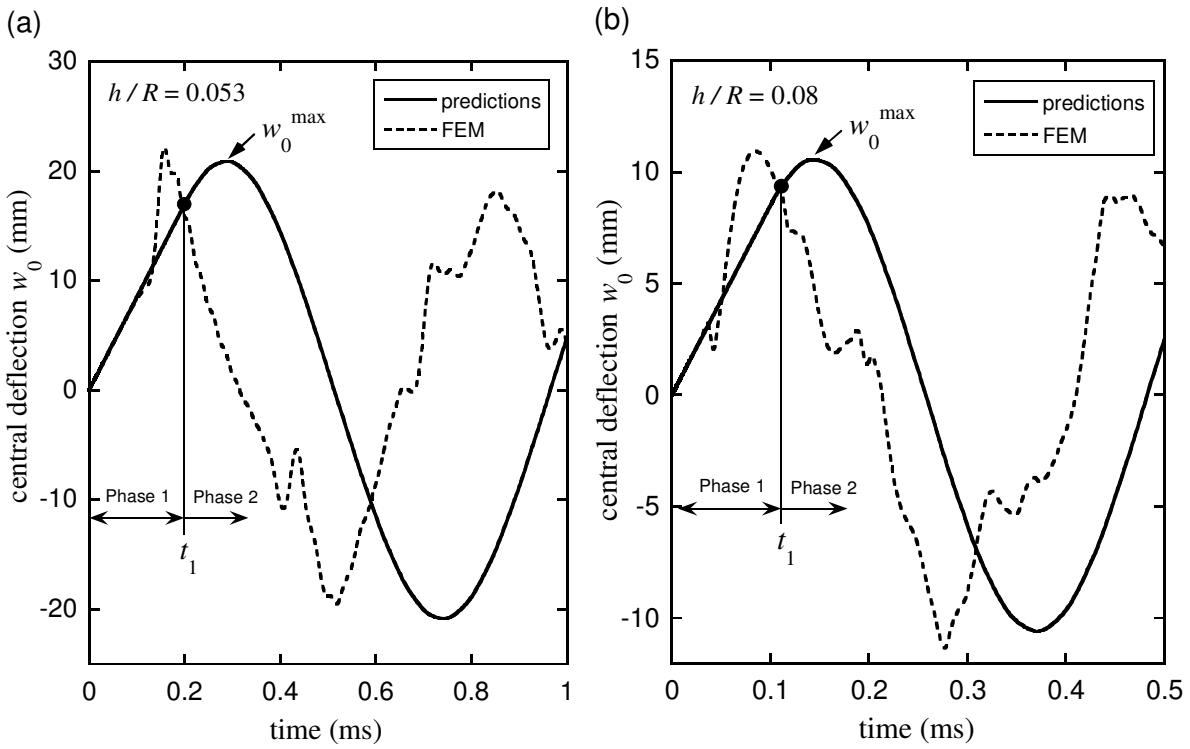



Fig. 7.3: Central deflection versus time histories of laminated composite plates (*Material 1*) subject to impulsive loading with initial velocity $v_0 = 85\,\mathrm{ms}^{-1}$ for two different geometries: (a) $R = 150\,\mathrm{mm}$, $h = 8\,\mathrm{mm}$ ($\bar{h} = 0.053$) and (b) $R = 100\,\mathrm{mm}$, $h = 8\,\mathrm{mm}$ ($\bar{h} = 0.08$); analytical predictions are compared to FE simulations.

The chart in Fig. 7.4 presents analytical and FE predictions of the maximum centre deflection $w_0^{\max} = \max_{0 \le t < \infty} \left[ w_0(t) \right]$ as functions of the imparted impulse $I = \mu v_0$ for plates made from an elastic isotropic material (*Material 2*). The predictions shown in this figure were performed

with constant plate thickness, $h = 8\,\text{mm}$, and the radius $R$ was adjusted to give four different aspect ratios, $\bar{h} = h/R$, for which contours are included in Fig. 7.4. For the range of plate geometries and loading cases considered here, FE and analytical predictions are found in good agreement; for small values of $\bar{h}$ the analytical models predict larger deflections and this over-prediction is more pronounced for large impulses $I$. This can be explained by the fact that when $\bar{h} = h/R$ is decreased, the deformation mode changes from bending dominant to stretching dominant and this is not accurately replicated by the deformation profile (eq. (7.4)) used in the analytical models.

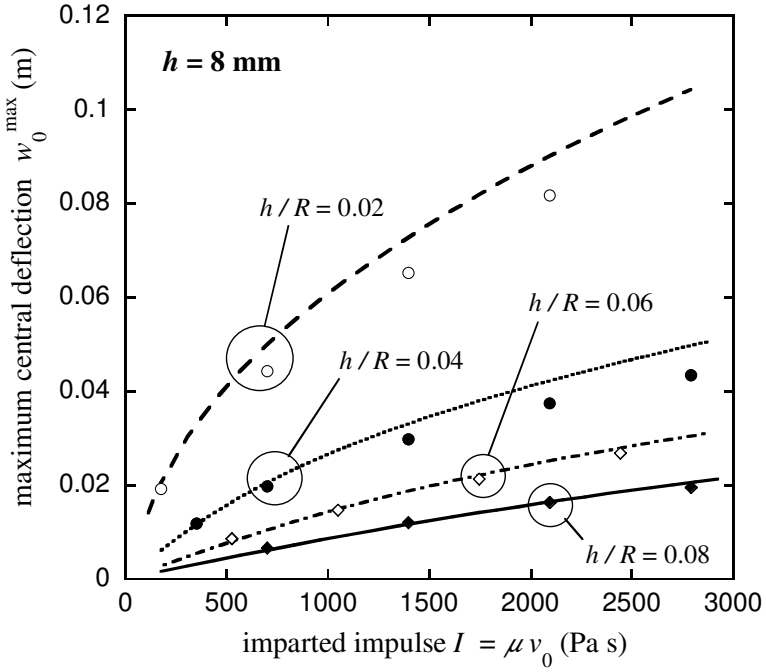



Fig. 7.4: Impulsive loading of circular plates made from elastic isotropic material (*Material 2*): analytical and FE predictions of the maximum central deflection $w_0^{\max}$ as functions of imparted impulse $I$; contours of aspect ratio $\bar{h} = h/R$ are included for four selected geometries, all of which of thickness $h = 8\,\text{mm}$.

**b) Design map**

Having shown that the analytical models are capable to predict the response of impulsively loaded plates with adequate accuracy, we now employ these models to construct a design chart which can be used to select plate geometries according to given blast impulse and maximal allowable deflection.

To help this design study, it is instructive to first decrease the number of independent material parameters associated to the orthotropic material response, $A_{ij}$ and $D_{ij}$, by incorporating an isotropic constitutive description in the governing equations. In the process, we replace the elements $A_{ij}$ of the laminate's stiffness matrix by

$$A_{11} = A_{22} = \frac{Eh}{1-\nu^2}; \qquad A_{12} = A_{21} = \frac{Eh\nu}{1-\nu^2}; \qquad A_{66} = \frac{E}{2(1+\nu)} = G \tag{7.51}$$

and employ

$$D_{11} = D_{22} = \frac{Eh^3}{12(1-\nu^2)}; \qquad D_{12} = D_{21} = \frac{Eh^3\nu}{12(1-\nu^2)}; \qquad D_{66} = \frac{Eh^3}{24(1+\nu)} \tag{7.52}$$

for the elements $D_{ij}$ of the bending stiffness matrix in eqs. (7.23), (7.24), (7.30) and (7.31).

Then we introduce the non-dimensional parameters

$$\overline{\zeta} = \zeta / R; \qquad \overline{r} = r / R; \qquad \overline{w}_{B0} = w_{B0} / R; \qquad \overline{w}_{S0} = w_{S0} / R;$$
$$\overline{t} = \frac{t}{R}\sqrt{\frac{E}{\rho}}; \qquad \overline{I} = \frac{I}{R\sqrt{E\rho}}; \qquad \overline{h} = h / R \tag{7.53}$$

representing non-dimensional wave position, radial coordinate, bending deflection, shear deflection, time, blast impulse and aspect ratio, respectively, and substitute these parameters into eqs. (7.17), (7.23), (7.24), (7.30) and (7.31) to obtain equations of motion in non-dimensional form, which are not explicitly given here for the sake of brevity.

We now employ the non-dimensional parameters of eq. (7.53) to plot a design chart for impulsively loaded circular plates made from elastic isotropic material and by neglecting the

effects of FSI, as shown in Fig. 7.5. In this chart, the aspect ratio $\bar{h}$ is plotted against the normalised impulse $\bar{I}$ and contours of the maximum central deflection $\bar{w}_0^{\max}$ are included for a range of $0.05 \le \bar{w}_0^{\max} \le 0.25$. For the purpose of choosing plate geometries with lowest possible mass per unit area, we include in Fig. 7.5 contours of $\bar{\mu}_{imp} = ER\mu / I^2$, representing the plate's areal mass in non-dimensional form (dashed curves). It can be seen that $\bar{\mu}_{imp}$ decreases along each $\bar{w}_0^{\max}$-contour for increasing values of $\bar{h}$ and $\bar{I}$. Therefore, for a circular isotropic plate of given radius $R$, imparted impulse $\bar{I}$ and maximum allowable centre deflection $\bar{w}_0^{\max}$, the areal mass of the plate can be reduced by choosing plate thickness $h$ large while keeping material density $\rho$ as well as Young's modulus $E$ low, hence increasing $\bar{I} = I / \left( R\sqrt{E\rho} \right)$ and moving upwards on the respective $\bar{w}_0^{\max}$ - contour.

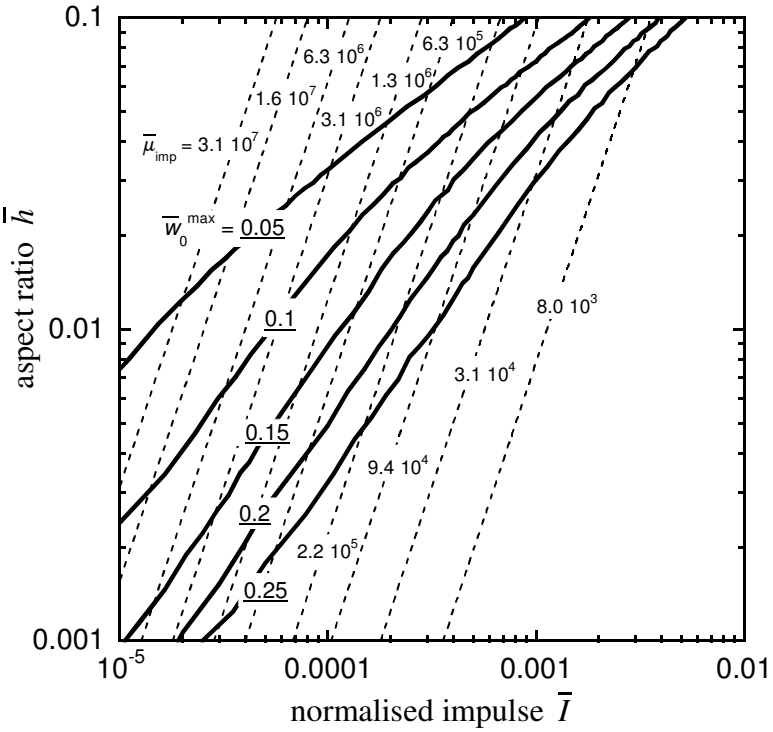



Fig. 7.5: Design chart for circular elastic plates subject to impulsive loading; contours of normalised central deflection $\bar{w}_0^{\max} = w_0^{\max} / R$ (solid curves, underlined values) and areal mass $\bar{\mu}_{imp} = ER\mu / I^2$ (dashed curves) are included.

**c) A fluid-structure interaction model based on impulsive loading**

In the event of an underwater explosion, structural components in the vicinity of the detonation point can perceive an impulse much less than that applied to a rigid stationary plate, $I_0 = 2p_0\theta$, with the reductions in impulse a consequence of interactions between the moving structure and the surrounding fluid. For a free-standing rigid plate subject to loading by exponentially decaying shock waves in water, Taylor [4] found that the momentum transmitted to the structure

$$I_t = I_0 \psi^{-\psi/(\psi-1)} \tag{7.54}$$

is dictated by a non-dimensional parameter $\psi = \rho_w c_w \theta / \mu$.

This section will investigate the adequacy of the Taylor impulse (7.54) to represent blast loading of circular elastic plates. In the process, we compare predictions obtained from fully coupled axisymmetric FE simulations (Section 7.3.2) to analytical predictions (Section 7.2.1) performed by imparting, in both these approaches, an initial transverse velocity

$$v_0 = \frac{\bar{I}_t}{\bar{h}}\sqrt{\frac{E}{\rho}} = \frac{2p_0\theta\psi^{-\psi/(1-\psi)}}{\bar{h}}\sqrt{\frac{E}{\rho}} \tag{7.55}$$

uniformly to the plates ($\bar{I}_t = I_t/I_0$ in eq. (7.55)), thus neglecting FSI subsequent to first cavitation. This comparison is performed with *Material 2* (Section 7.3.1 b) and shown in Fig. 7.6 (a), in which predictions of $\bar{w}_0^{\max} = w_0^{\max}/R$ are plotted against the normalised shock intensity $\hat{I}_t = I_t/\left(R\sqrt{E\rho}\right)$ with $I_t$ according to eq. (7.54); contours of $\bar{h} = h/R$ are included for three selected plate geometries, all of which of thickness $h = 10$ mm; the decay time of the shock wave was held fixed, $\theta = 0.15$ ms, hence $\psi = \rho_w c_w \theta / \mu = 11$. For comparison purposes, we include in Fig. 7.6 (a) analytical predictions performed with the FSI models developed in Section 7.2.2. It can be seen that the predictions computed with the FSI models

are found in excellent agreement with the FE results. In contrast, while the predictions based on impulsive loading capture the FE results for the case $\bar{h} = 0.015$ with good accuracy, discrepancies in $\bar{w}_0^{\max}$ occur when $\bar{h}$ is increased. In particular, for $\bar{h} = 0.06$, the impulsive loading case under-predicts the FE results of $\bar{w}_0^{\max}$ by more than 50%.

In Fig. 7.6 (b) we plot the corresponding predictions of the normalised structural response time defined as

$$\hat{t}_{\max} = \frac{t_{\max}}{\theta}, \tag{7.56}$$

against $\hat{I}$, with $t_{\max}$ the time at which the peak deflection $\bar{w}_0^{\max}$ is reached. For a fixed impulse $\hat{I}$, the response time $\hat{t}_{\max}$ decreases drastically by increasing $\bar{h}$ from 0.015 to 0.06. Moreover, $\hat{t}_{\max}$ decreases by increasing $\hat{I}$ when $\bar{h}$ is held fixed and this trend is more pronounced for small values of $\bar{h}$. Now compare Fig. 7.6 (a) and (b): the quality of the impulsive loading assumption is adequate only when the duration of the FSI phase is much shorter than the structural response time, thus we suggest $\hat{t}_{\max} > 10$ for the impulsive loading assumption to be valid. The reason for the discrepancies in $\bar{w}_0^{\max}$ (Fig. 7.6 a) for cases with smaller normalised response time $\hat{t}_{\max}$ can be justified by recalling that FSI phenomena subsequent to first cavitation are neglected in the impulsive loading assumption. Such phenomena become more dominant when $\hat{t}_{\max}$ is small due to the fact that elastic rebound of the plate forces the cavitation zone to collapse earlier in the response which leads to continued loading by pressure waves travelling in the reconstituted water layer. Such FSI phenomena are included in the analytical FSI models (dashed curves in Fig. 7.6 a) but are neglected in the impulsive loading cases (solid curves in Fig. 7.6 a), hence the discrepancies. The evolution

of the cavitation process, as briefly sketched above, will be examined in more detail in the following section.

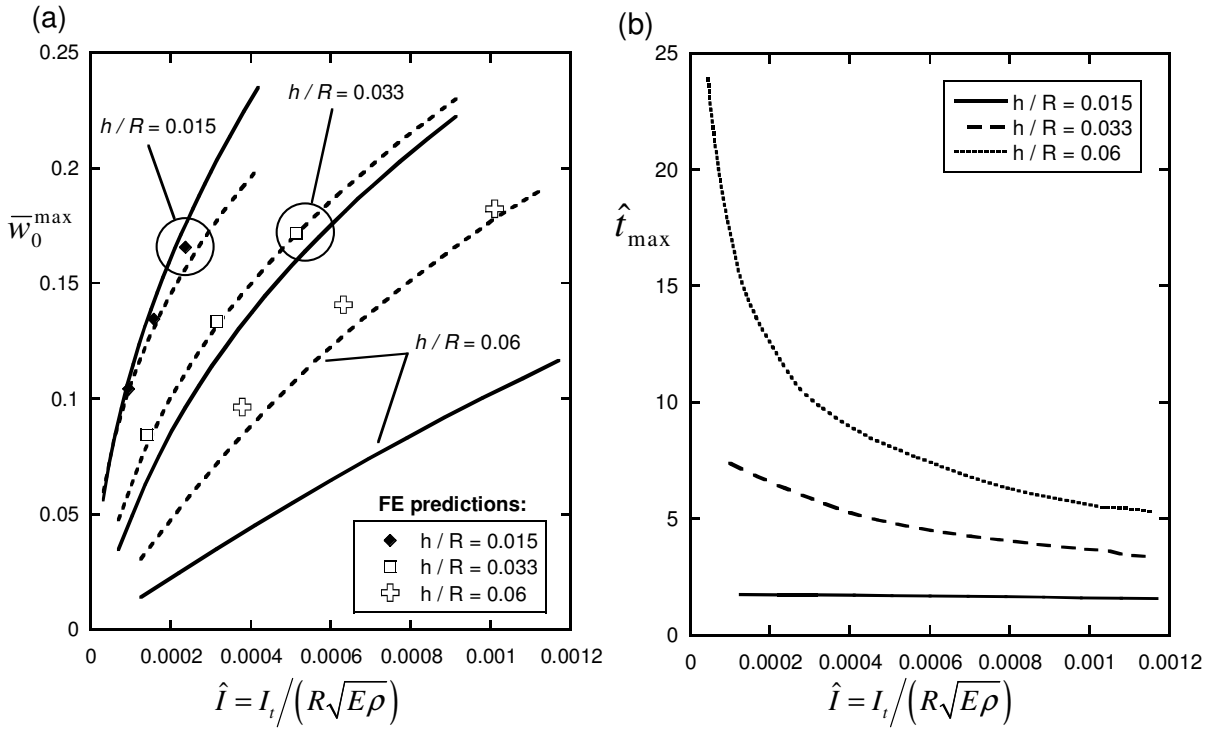



Fig. 7.6: (a) Analytical and FE predictions of the normalised maximum centre deflection $\overline{w}_0^{\max}$ as functions of the normalised impulse $\hat{I}$ for circular plates made from elastic isotropic material (*Material 2*); contours of aspect ratio $h/R$ are included for three selected geometries, all of which of thickness $h = 10$ mm. The solid curves represent analytical predictions performed by loading the plates impulsively according to the Taylor impulse, while the dashed curves denote those obtained from the analytical model developed in this thesis. (b) Analytical predictions of the response time $\hat{t}_{\max}$ as a function of $\hat{I}$ for the case of impulsive loading.

### 7.4.2 Underwater blast loading

Having demonstrated that the cavitation process can strongly affect the plate's response subsequent to first cavitation, we no longer consider underwater blast loading to be impulsive and employ the analytical FSI model developed in Section 7.2.2 to examine the response of circular elastic plates subject to underwater blast.

We now proceed with a quantitative comparison between analytical and FE predictions of centre deflection versus time histories in order to validate the accuracy of the analytical FSI models derived in Section 7.2.2. Then, the sensitivity of the plate's response to the governing non-dimensional parameters will be explored and finally, we present design charts for the selection of optimal geometries which maximise the plate's resistance to underwater blast.

**a) Comparisons of analytical and FE predictions**

Now consider the problem of a circular plate ( $h = 8\,\text{mm}$, $R = 300\,\text{mm}$ ) made from composite laminate (*Material 1*, Section 7.3.1); the plate is in contact with water on one side and loaded by an exponentially decaying shock wave of $p_0 = 75\,\text{MPa}$ and $\theta = 0.15\,\text{ms}$ on the wet face. For this problem, FE simulations (Section 7.3) and analytical calculations (Section 7.2.2) were performed and their predictions of the central deflection versus time histories are reported in Fig. 7.7 (a). Two different composite layups are considered, a *0-90 layup*, $[0,90,90,0]_6$, and a *quasi-isotropic layup*, $[0,45,90,-45]_6$. To provide insight into the cavitation process, FE contour plots of the fluid pressure field and plate deflection are illustrated in Fig. 7.7 (c) for five selected instants. The white dashed curves included in Fig. 7.7 (c) represent analytical predictions of the structural response.

As shown in Fig. 7.7 (c), the incident pressure wave reaches the fluid-structure interface at $t = 0$. Subsequently, a flexural wave starts propagating from the clamped boundary and travels towards the centre point, as observed in frame $t = 0.15\,\text{ms}$ (Fig. 7.7 c). The ensuing plate motion causes the fluid pressure in the water ahead of the propagating flexural wave to rapidly drop below zero, at time $t_c = 0.025\,\text{ms}$, as indicated in Fig. 7.7 (a), giving rise to cavitation at the fluid-structure interface and terminating the Phase 1a response. As illustrated in the contour plot for $t = 0.15\,\text{ms}$, subsequent to first cavitation in the water, the cavitated

region (dark grey area), spreads into the fluid column by propagation of a breaking front (BF), in line with what predicted theoretically (Chapter 3) and shown experimentally (Chapter 4) for 1D blast loading of rigid plates. Moreover, it can be seen in the same frame that the water contiguous to the plate's wet face just ahead of the flexural wave remains in contact with cavitated water at $p = 0$, and therefore this portion of the plate moves with constant velocity $v_c = \dot{w}_0(t_c)$ in transverse direction; this scenario is represented by the straight deflection versus time trace observed in Fig. 7.7 (a). As time elapses, the flexural wave advances further towards the plate's centre point, as shown in the frame for $t = 0.33\,\text{ms}$ and the volume of cavitated water increases by continued propagation of the BF. In Fig. 7.7 (a), the FE predictions show that the central portion of the plate starts to oscillate transversely with a higher frequency at $t \approx 0.2\,\text{ms}$ while the analytical models predict constant velocity until the flexural wave reaches the centre point at $t_1 = 0.5\,\text{ms}$, as indicated in Fig. 7.7 (a), and Phase 1b ceases. In the subsequent Phase 2 response the plate decelerates and the maximum central deflection $w_0^{\max}$ is reached at $t_{\max} = 0.8\,\text{ms}$. In the FE simulation, the termination point of Phase 1 is masked by the transverse oscillations and cannot be clearly identified; however, it can be seen that the FE predictions of $w_0(t)$ reach a maximum at $t = 0.75\,\text{ms}$ and the corresponding contour plot (Fig. 7.7 c) shows that a closing front (CF) has started to propagate into the fluid column, causing collapse of the cavitated region and leaving uncavitated water behind, qualitatively consistent with the predictions of the 1D models developed in Chapter 3. Subsequently, the CF continues propagating and plate deformaion starts to recover owing to elastic spring-back, as seen in the frame for $t = 1.2\,\text{ms}$.

In Fig. 7.7 (b), we present FE and analytical predictions of $w_0(t)$ for the same problem but with the peak pressure of the incident wave increased to $p_0 = 130\,\text{MPa}$. The trends shown in

this figure are similar to those of Fig. 7.7 (a) and described above. For both loading cases presented in Fig. 7.7 (a) and (b), respectively, the FE and analytical predictions of the maxium deflection $w_0^{\max}$ are found in excellent agreement. Moreover, the dynamic deflection profiles extracted from the FE results are captured with good accuracy by the analytical models, see Fig. 7.7 (c). In addition, it is clear from Fig. 7.7 (a) and Fig. 7.7 (b) that the effects of composite layup on the dynamic deflection histories can be neglected.

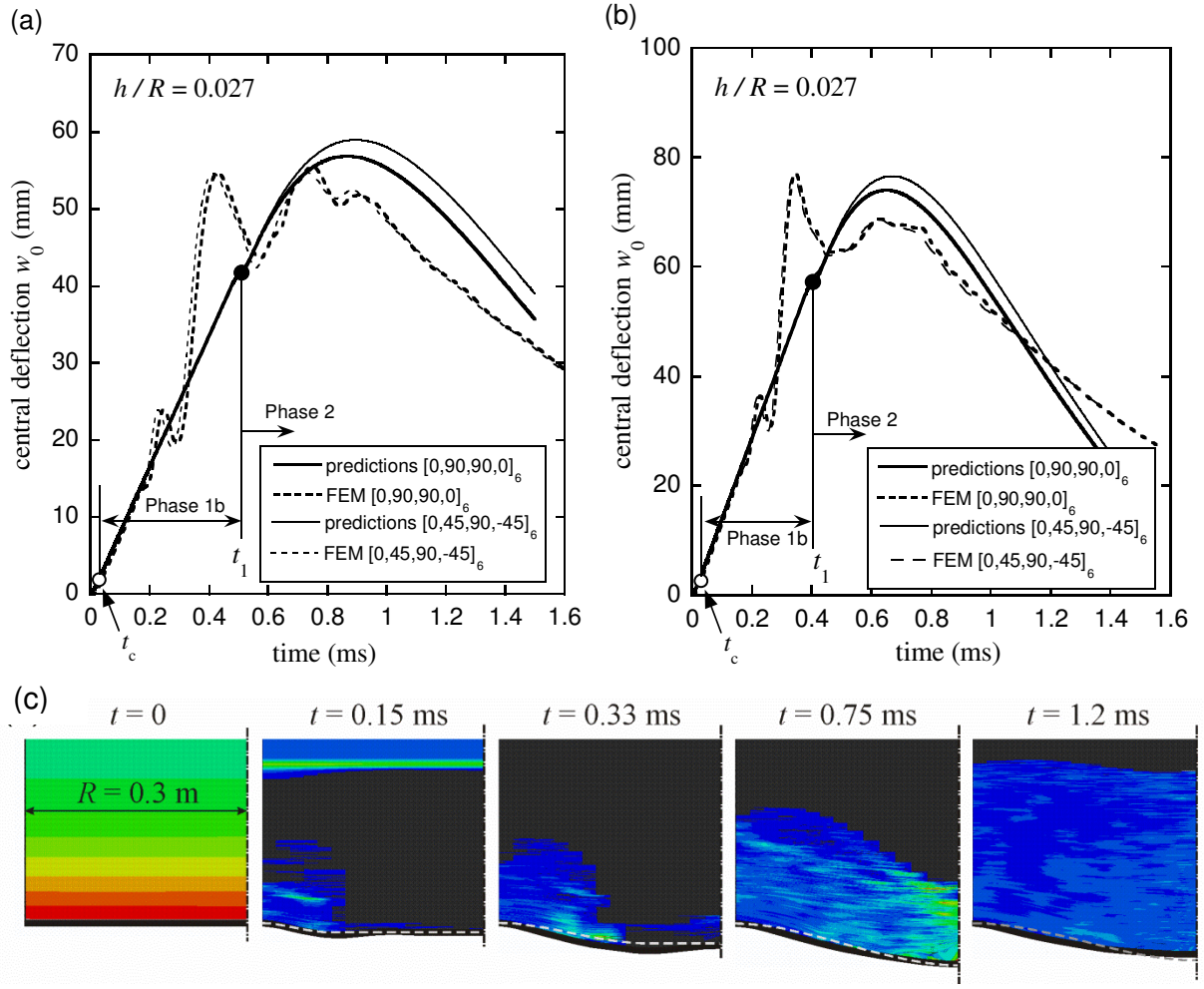



Fig. 7.7: (a) Central deflection versus time histories of circular plates made from composite laminate (*Material 1*, $h = 8\,\text{mm}$, $R = 300\,\text{mm}$) and subjected to loading by an underwater shock wave of $p_0 = 75\,\text{MPa}$ and $\theta = 0.15\,\text{ms}$; analytical predictions are compared to FE simulations for two different layups. (b) Similar information for underwater blast loading with $p_0 = 130\,\text{MPa}$ and $\theta = 0.15\,\text{ms}$. (c) Plate deformation and fluid pressure fields for five selected time frames obtained from the FE simulation corresponding to the loading case used in (a); analytical predictions (dashed curves) are included. FE scale: 75 MPa (red) – 0 MPa (blue), cavitation zones are highlighted in grey.

In the following we shall probe the accuracy of the FSI models developed in this thesis by comparing their predictions of the maximum centre deflection $w_0^{\max}$ to FE results for a practical range of aspect ratios $\bar{h} = h/R$ and blast impulses $I_0 = 2p_0\theta$.

In Fig. 7.8, analytical and FE predictions of $w_0^{\max}$ are plotted against the blast impulse $I_0 = 2p_0\theta$ with contours of $\bar{h} = h/R$ included for five selected plate geometries, all of which of thickness $h = 10\,\text{mm}$. All predictions shown here were performed on circular elastic plates with isotropic material properties (*Material 2*, see Section 7.3.1); the incident shock waves had a decay time of $\theta = 0.15\,\text{ms}$ and the peak pressures of the incident waves varied between $10\,\text{MPa} \le p_0 \le 120\,\text{MPa}$. For this range of loading cases and problem geometries, FE and analytical predictions are found in good correlation, with discrepancies not exceeding 10%. This correlation gives confidence that the established analytical models provide accurate predictions of the peak deflections produced by underwater blast loading of elastic plates.

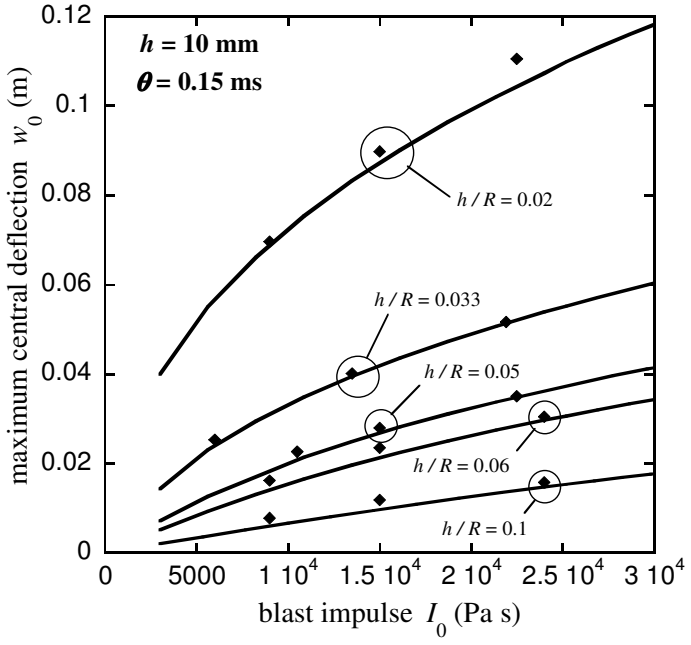



Fig. 7.8: Comparison between analytical and FE predictions of the maximum central deflection $w_0^{\max}$ plotted as functions of the impulse $I_0 = 2p_0\theta$ for underwater blast loading of elastic isotropic plates (*Material 2*, $h$ = 10 mm, $\theta = 0.15\,\text{ms}$ ); contours of $\bar{h} = h/R$ are included for five different geometries.

**b) Sensitivity of the peak centre deflection $\overline{w}_0^{\max}$ to the parameters $\overline{h}$, $\overline{R}$, $\overline{\alpha}$ and $\overline{p}_0$**

In Section 7.4.1 (b) we introduced non-dimensional parameters (eq. (7.53)) to characterise the response of impulsively loaded plates made from an elastic isotropic material. For the impulsive loading case, it can be shown that the solutions of the normalised centre deflection $\overline{w}_0 = w_0/R$ only depend on two parameters, non-dimensional impulse $\overline{I} = I\Big/\left(R\sqrt{E\rho}\right)$ and aspect ratio $\overline{h} = h/R$. Hence, one design chart is sufficient to map out the response of the plate's response, as illustrated in Fig. 7.5.

However, when underwater blast loading is considered, additional quantities ( $p_0, \theta, \rho_w, c_w$ ) appear in the equations of motion (see Section 7.2.2) and additional parameters need to be defined in order to re-write the governing equations in non-dimensional form. Analogous to the impulsive loading case, we incorporate a linear-elastic isotropic constitutive relation in our models by substituting eqs. (7.51) and (7.52) into eqs. (7.23), (7.24), (7.49) and (7.50). The obtained equations of motion as well as the loading functions (eqs. (7.41), (7.42) and (7.45)) can be recast in non-dimensional form by employing the parameters defined in eq. (7.53) as well as the non-dimensional groups

$$\overline{R} = \frac{R}{\theta}\sqrt{\frac{\rho}{E}} \quad ; \quad \overline{\alpha} = \frac{\rho_w c_w}{\sqrt{E\rho}} \quad ; \quad \overline{p}_0 = \frac{p_0}{E} \tag{7.57}$$

representing non-dimensional plate radius, acoustic impedance and peak pressure, respectively. For the sake of brevity, these non-dimensional equations are not explicitly given herein. However, it can be shown analytically that the solutions of $\overline{w}_0\left(\overline{t}\right)$ now depend on the parameters $\overline{h}$, $\overline{R}$, $\overline{\alpha}$ and $\overline{p}_0$ and the sensitivity of the maximum deflection $\overline{w}_0^{\max}$ to these governing parameters is examined in the following.

In Fig. 7.9 (a), analytical predictions of $\overline{w}_0^{\max}$ are plotted as functions of the normalised peak pressure $\overline{p}_0$ for the case $\overline{h} = 0.033$ and $\overline{\alpha} = 0.11$; contours of $\overline{R}$ are included for selected values in the range $0.085 \le \overline{R} \le 0.85$. It can be seen that the plate deflection $\overline{w}_0^{\max}$ increases with decreasing values of $\overline{R}$ when $\overline{h}$, $\overline{p}_0$ and $\overline{\alpha}$ are held fixed, indicating that plates of smaller dimensions perceive more intense structural loading in the event of an explosion in water. These observations can be addressed to FSI: the response time $t_{\max}$ of a circular plate decreases by reducing the parameter $\overline{R}$; as a consequence, elastic spring-back of the circular plate forces the cavitation zone contiguous to the fluid-structure interface to collapse earlier in the response (by propagation of a CF) and this rises the amplitude of pressure waves travelling in the water layer between the fluid-structure interface and the advancing CF, impinging on the wet face of the plate (see contour plots in Fig. 7.7 c) and providing additional loading. In Section 8.4.1 we shall explore the cavitation process associated to blast loading of composite plates in more detail, via direct observation of cavitation phenomena in laboratory-scale underwater shock experiments.

The sensitivity of $\overline{w}_0^{\max}$ to variations of $\overline{p}_0$ is shown in Fig. 7.9 (b) for $\overline{\alpha} = 0.11$ and $\overline{R} = 0.4$; contours of aspect ratio are included in the range of $0.02 \le \overline{h} \le 0.08$. For fixed parameters $\overline{R}$, $\overline{p}_0$ and $\overline{\alpha}$, the maximum deflection $\overline{w}_0^{\max}$ is reduced by increasing $\overline{h}$, as expected.

The chart in Fig. 7.9 (c) shows the variation of $\overline{w}_0^{\max}$ to changes in $\overline{p}_0$ for a given plate geometry, ($\overline{R} = 0.27$, $\overline{h} = 0.05$); contours of the non-dimensional acoustic impedance are included for selected values within $0.038 \le \overline{\alpha} \le 0.3$.

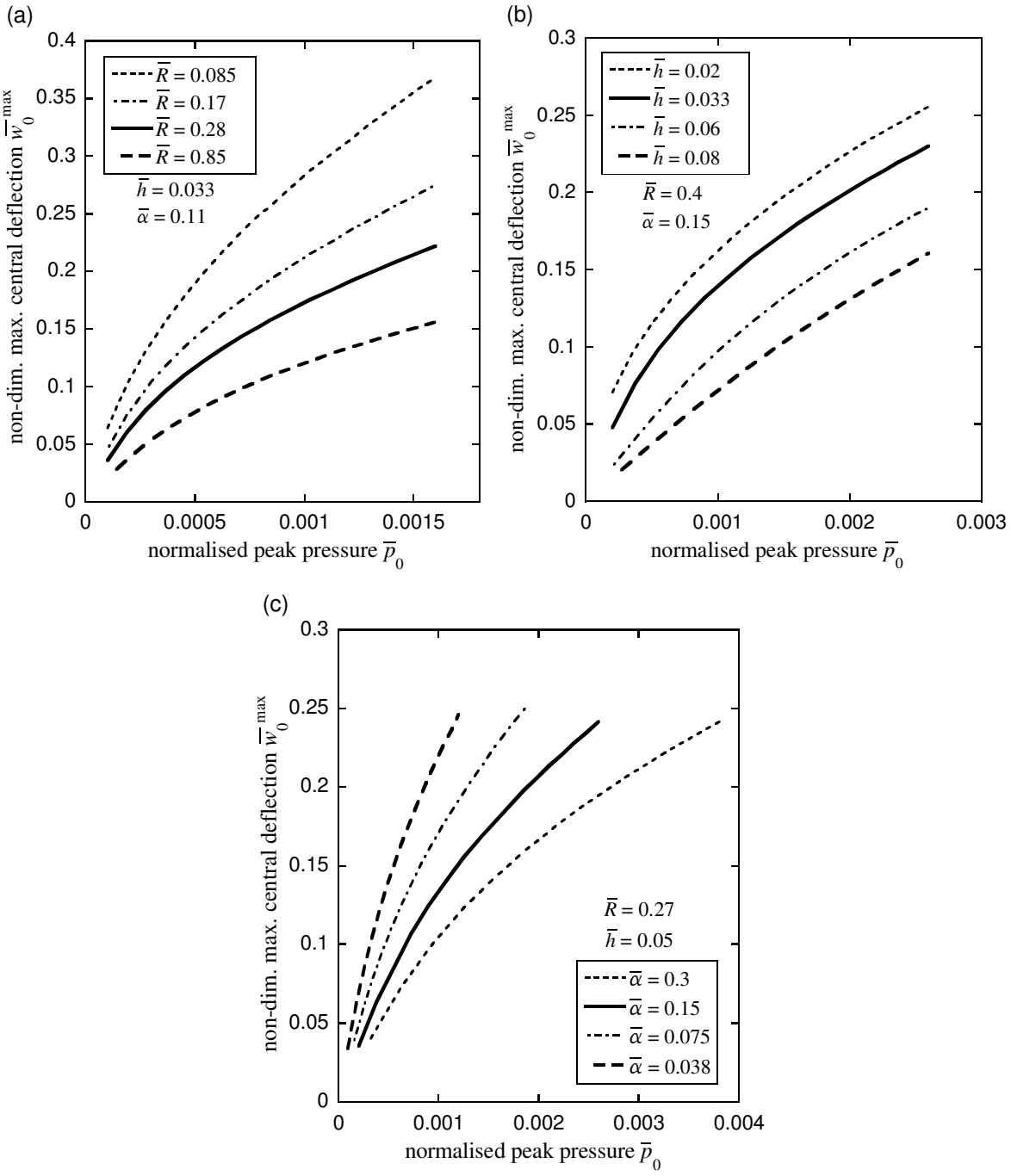



Fig. 7.9: Analytical predictions of the maximum centre deflections $\overline{w}_0$ as functions of the normalised peak pressure $\overline{p}_0$ for circular isotropic plates with contours of (a) non-dimensional radius $\overline{R}$, (b) aspect ratio $\overline{h}$ and (c) acoustic impedance $\overline{\alpha}$.

For the case of constant parameters $\bar{h}$, $\bar{R}$ and $\bar{p}_0$, Fig. 7.9 (c) shows that $\bar{w}_0^{\max}$ is reduced by increasing $\bar{\alpha}$. To help understanding this phenomenon we write $\bar{\alpha}$ in terms of the 'Taylor parameter' $\psi = \rho_w c_w \theta / (\rho h)$ [4]; this gives $\bar{\alpha} = \bar{h}\,\bar{R}\,\psi$. From the latter relationship it can be seen that for fixed parameters $\bar{h}$ and $\bar{R}$, an increase in $\bar{\alpha}$ leads to an increase of $\psi$. Taylor [4] has shown that, for the case of a free-standing rigid plate, an increase in $\psi$ allows for cavitation to occur earlier in the response and this decreases the duration of the structural loading phase as well as the momentum transmitted to the structure, recall eq. (7.54). We argue that similar FSI phenomena are operative subsequent to underwater blast loading of circular clamped plates, owing to the reductions in $\bar{w}_0^{\max}$ associated to an increase in $\bar{\alpha}$ (and thus $\psi$), see Fig. 7.9 (c).

**c) Minimal weight design**

We now proceed to determine the optimal plate designs $(\bar{h}, \bar{R})$ which maximise the underwater blast resistance of a circular isotropic plate of given areal mass and with a constraint on the maximum deflection.

In Fig. 7.10 (a) the aspect ratio $\bar{h}$ is plotted against $\bar{R}$, for a range between $0.01 \le \bar{h} \le 0.1$ and $0 < \bar{R} \le 2$, respectively, and with the constraints $\bar{w}_0^{\max} = 0.1$ and $\bar{\alpha} = 0.15$, respectively; contours of normalised peak pressure $\bar{p}_0$ (solid curves, underlined values) and non-dimensional areal mass (dashed curves), defined as $\bar{\mu} = \mu / \theta\sqrt{E\rho}$, are included for selected values within $0.0003 \le \bar{p}_0 \le 0.003$ and $0.0033 \le \bar{\mu} \le 0.13$, respectively. The arrows tracing the squares in Fig. 7.10 (a) represent the optimal path with plate geometries $(\bar{h}, \bar{R})$ such to maximise $\bar{p}_0$ for a given $\bar{\mu}$ and increasing values of $\bar{\mu}$, while the arrows tracing the circles

indicate the trajectory of the 'worst case designs' $\left(\bar{h},\bar{R}\right)_{\min}$ which minimise $\bar{p}_0$ for a given $\bar{\mu}$ and increasing values of $\bar{\mu}$. The optimal geometries $\left(\bar{h},\bar{R}\right)_{\max}$ are located at the largest possible values of $\bar{h}$, for the range of geometries plotted in Fig. 7.10 (a), while the trajectory of the designs $\left(\bar{h},\bar{R}\right)_{\min}$ is located at small values of $\bar{h}$ on each $\bar{p}_0$ contour.

Similar information is provided in Fig. 7.10 (b) for the case $\bar{w}_0^{\max}=0.2$; in contrast, the optimal path drops from large to small values of $\bar{h}$ in the low range of $\bar{R}$ but jumps back up to $\bar{h}=0.1$ as $\bar{R}$ increases. The designs $\left(\bar{h},\bar{R}\right)_{\min}$ are located midway on each $\bar{p}_0$ contour in the small $\bar{R}$ domain and move towards smallest possible values of $\bar{h}$ when $\bar{R}$ is increased.

In Fig. 7.11 the maximum normalised pressure $\bar{p}_0^{\max}$ sustained by the optimal geometries $\left(\bar{h},\bar{R}\right)_{\max}$ is plotted against the non-dimensional areal mass $\bar{\mu}$ for constrained centre deflections $\bar{w}_0^{\max}=0.1$ and $\bar{w}_0^{\max}=0.2$, according to the cases considered in Fig. 7.10 (a) and Fig. 7.10 (b), respectively. In order to determine the benefits in blast resistance offered by the optimal designs, the peak pressure $\bar{p}_0^{\min}$ sustained by the 'worst case designs', $\left(\bar{h},\bar{R}\right)_{\min}$, is included in Fig. 7.11.

For the case $\bar{w}_0^{\max}=0.2$, $\bar{p}_0^{\max}$ increases rapidly in the low $\bar{\mu}$ domain but shows a slight bend at $\bar{\mu}\approx 0.01$, owing to the drop of $\left(\bar{h},\bar{R}\right)_{\max}$ from large to small $\bar{h}$, as seen in Fig. 10b. Such drop does not occur for $\bar{w}_0=0.1$ (see Fig. 7.10 a) and in this case, $\bar{p}_0^{\max}$ increases steadily with increasing $\bar{\mu}$. Now compare the $\bar{p}_0^{\max}$ and $\bar{p}_0^{\min}$ contours for each case shown in Fig. 7.11: an increase in blast resistance of more than 40% can be achieved by employing the optimal designs.

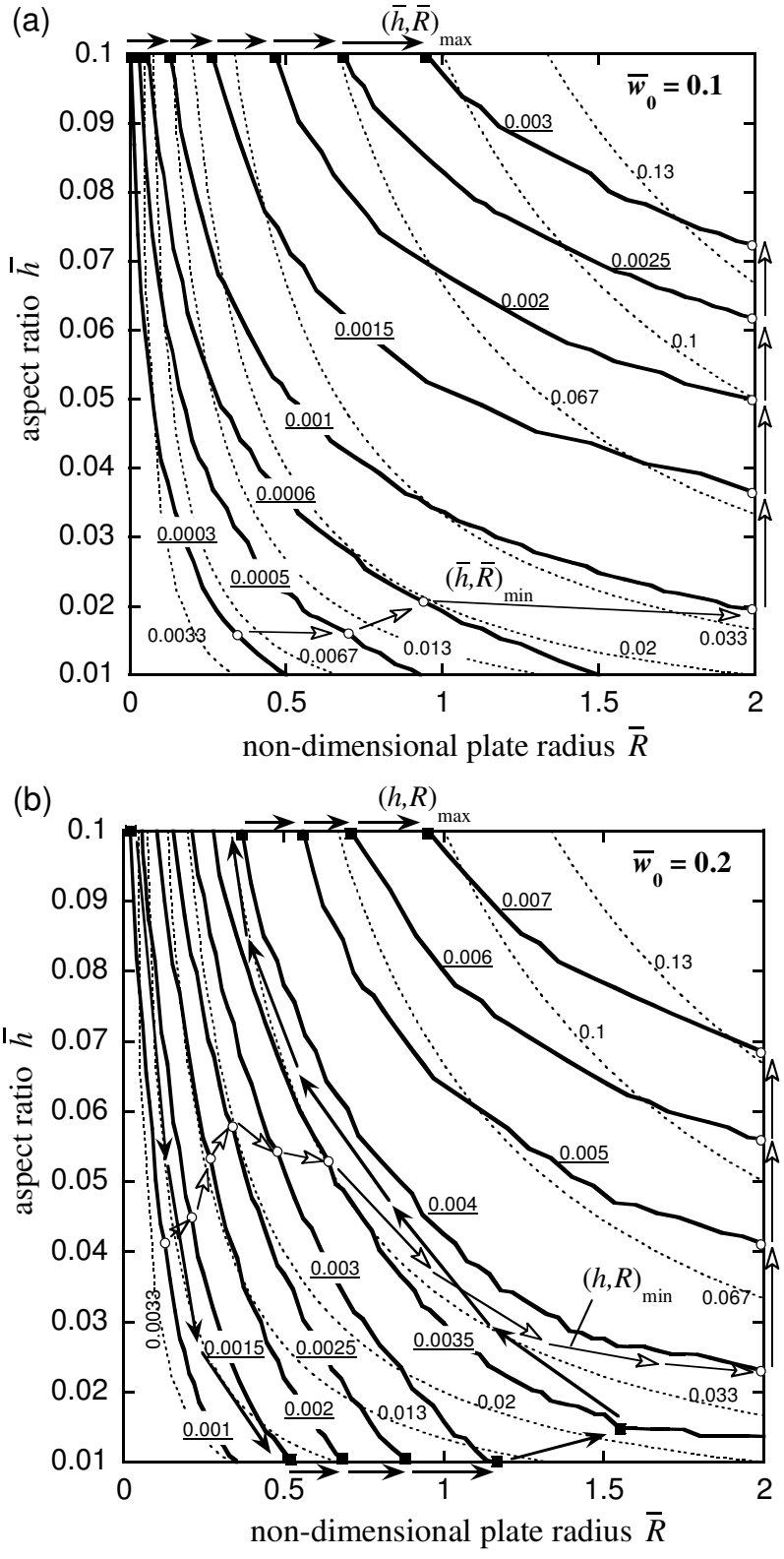



Fig. 7.10: (a) Design chart for circular isotropic plates subject to underwater blast loading with $\bar{\alpha} = 0.15$ and with constained normalised deflection $\bar{w}_0 = 0.1$; contours of non-dimensional peak pressure $\bar{p}_0 = p_0/E$ (solid curves, underlined values) and areal mass $\bar{\mu} = \mu/\left(\theta\sqrt{E\rho}\right)$ (dashed curves) are included. (b) Similar design chart for a fixed maximum centre deflection of $\bar{w}_0 = 0.2$.

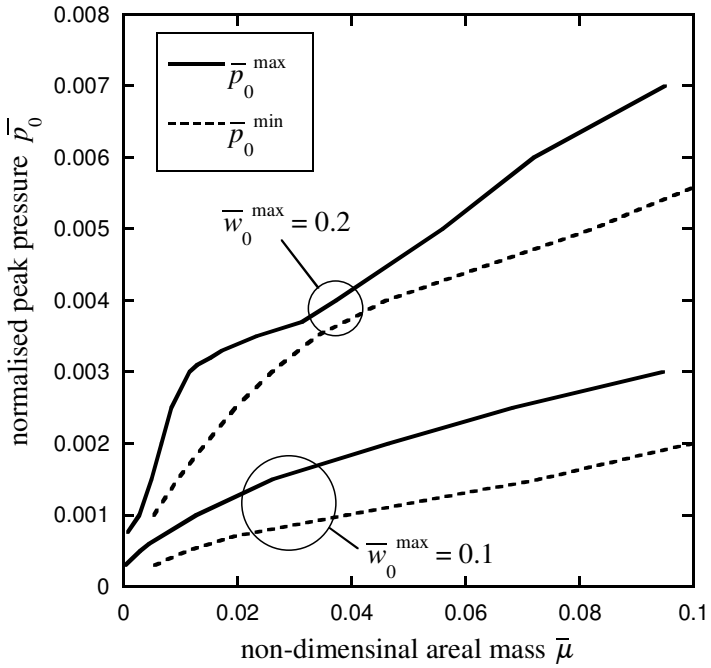



Fig. 7.11: Variation of the normalised peak pressure $\overline{p}_0$ sustained by the optimal designs and the 'worst case designs', $\overline{p}_0^{\max}$ and $\overline{p}_0^{\min}$, respectively, as a function of the non-dimensional areal mass $\overline{\mu} = \mu \big/ \left(\theta\sqrt{E\rho}\right)$ for $\overline{\alpha} = 0.15$ and fixed central deflections of $\overline{w}_0 = 0.1$ and $\overline{w}_0 = 0.2$.

## 7.5 Conclusions

Analytical models have been derived to predict dynamic deflection of fully clamped circular elastic plates subject to loading by planar, exponentially decaying underwater shock waves in water. Such models are based on a plate theory that takes into account transverse shear deformations, stretching forces due to large deflections, flexural wave propagation in the solid, FSI phenomena subsequent to first cavitation as well as the orthotropic constitutive response of composite laminates. The plate's centre deflection was found to be dictated by four non-dimensional parameters, $\overline{h}$, $\overline{R}$, $\overline{\alpha}$ and $\overline{p}_0$, respectively, representing aspect ratio, normalised plate radius, acoustic impedance and peak pressure of the incident shock wave. The analytical models were validated by comparing their predictions to those obtained from

fully coupled 3D FE simulations and both types of predictions were found to be in good agreement for a wide range of plate geometries and blast impulses. In contrast, when the plates were loaded impulsively by imparting the plate an initial velocity according to the Taylor impulse [4], large discrepancies occurred, unless the structural response time was several times larger than the duration of the phase for FSI.

The plate's response was found to be strongly affected by the problem size: for given aspect ratio, elastic properties and incident blast wave, plates of small radius respond to underwater blast with larger normalised central deflections (deflection divided by radius) due to rapid contraction of the cavitation zone in the water adjacent to the structure.

The validated analytical models were used to determine the optimal geometries that maximise the shock resistance of a circular elastic plate of given areal mass and with a constraint on the maximum centre deflection. The constructed design maps show that an increase in blast resistance of greater than 40% can be achieved by employing the optimal designs.

While the developed analytical models can be used to predict the response of circular orthotropic (and isotropic) plates subject to blast in shallow water, they do not account for the effects of an initially applied hydrostatic pressure in the fluid. Moreover, FSI at the back face of the plate is not included in the current analysis but needs to be considered when water-backed plates are subjected to underwater blast. These aspects are of drastic relevance for the design of blast resistant composite structures used in deep water applications and are left as topics for a future study.

# Chapter 8

# The Response of Circular Composite Plates to Underwater Blast: Experiments and Predictive Model Validation

## 8.1 Introduction

During the last decades, the use of composite materials in naval ships and submarines has significantly grown and their resistance to withstand underwater blast loading has gained drastic relevance. The analytical models developed in Chapter 7 of this thesis can be seen as a first step towards understanding FSI phenomena as well as dynamic deformation processes operative when composite plates are subjected to shock loading in water. However, experimental evidence is needed to gain more insight into the response of both fluid and structure to underwater blast.

As outlined in Chapter 2, several authors [39, 42, 43, 57] have developed experimental methods to probe, at laboratory scale, the underwater blast resistance of monolithic composite plates and sandwich panels made out of composite materials. Although these techniques are

capable of reproducing underwater blast loading and measuring the dynamic response of the tested structures, they do not allow observing the ensuing cavitation processes, which is vital for understanding their interactions with the loaded structure.

In this chapter, the response of submerged clamped composite plates subject to dynamic loading by exponentially decaying shock waves in shallow water is investigated. Laboratory scale underwater shock experiments are performed on (i) glass-fibre (GRP) and (ii) carbon-fibre (CRP) reinforced composites by employing the transparent water shock tube presented in Chapter 4 (and also used in Chapters 5 and 6). High-speed photography will be employed to observe the fluid response and to provide visual insight into the cavitation process. We shall also observe plate deformation and failure processes of composite plates and deduce centre deflection histories from the obtained high-speed photographs. In addition, 3D FE simulations will be performed to investigate FSI phenomena and dynamic deformation histories in more detail and their predictions will be used to validate the analytical FSI models of Chapter 7.

## 8.2 Underwater shock experiments

### 8.2.1 Description of composite specimens

Monolithic circular specimens were cut from sheets of laminated composite material; two different laminates are considered and described below.

(i) Carbon fibre/epoxy composite (CRP).

The laminates were manufactured by stacking three layers of plain woven prepregs at equal orientations and autoclave curing in a vacuum bag. The obtained sheets had a stacking

sequence $[0,90]_3$ , final thickness $h = 0.75\,\text{mm}$, density $\rho = 1500\,\text{kgm}^{-3}$ and mass per unit area $\mu = \rho h = 1.125\,\text{kgm}^{-2}$. Typical properties of carbon fibre and epoxy resin are listed in Table 8.1.

Quasi-static tensile tests were conducted at a strain rate $\dot{\varepsilon} = 10^{-4}\,\text{s}^{-1}$ on rectangular specimens cut from the laminate with fibres aligned parallel and perpendicular to the specimen's longitudinal axis; specimens had a gauge length of 100 mm and a width of 20 mm. Strains induced in the specimen in longitudinal and transverse directions were deduced from strain gauge measurements. The measured stress versus strain response in the longitudinal direction was linear elastic to failure (by fibre fracture), with stiffness of 55 GPa and failure stress of 520 MPa. Woven laminate plies can be modelled, in a first approximation, as a [0,90] stack of unidirectional (UD) composite laminas. The elastic properties for a single lamina are given in Table 8.2 and were calculated from the measurements by assuming

$$E_2 = E_1/10;\ \nu_{21} = \nu_{12}\,E_2/E_1;\ G_{12} = E_1/10 = E_2;\ G_{13} = G_{12};\ G_{23} = E_2/2(1+\nu_{23});\ \nu_{23} = \nu_{12}. \quad (8.1)$$

The indices '1' and '2' denote fibre and transverse directions, respectively. It is worth noting that the lamina properties deduced from the test results correlate with those obtained from classical lamina theory (see Appendix B).

(ii) Glass fibre/vinylester composite (GRP).

The laminate consisted of E-glass fibres infiltrated by vinylester resin and had a stacking sequence [0,45,90,-45], final thickness $h = 0.85\,\text{mm}$, density $\rho = 1550\,\text{kgm}^{-3}$ and areal mass $\mu = \rho h = 1.32\,\text{kgm}^{-2}$. Typical mechanical properties of fibres and resin are included in Table 8.1. Each lamina was taken as a transversely isotropic material; the elastic properties for a single lamina were deduced from the formulas given in Appendix B and the results are

listed in Table 8.2. These theoretical predictions were found in good agreement with results obtained from quasi-static tensile tests on similar laminates (Tagarielli et al. [11]).

Table 8.1: Constituent material properties

| | carbon fibre | epoxy resin | E-glass fibre | vinylester resin |
|---|---|---|---|---|
| Tensile modulus (GPa) | 230 | 2.46 | 76 | 3.4 |
| Shear modulus (GPa) | 92 | 0.9 | 31 | 1.3 |
| Poisson's ratio | 0.25 | 0.34 | 0.22 | 0.35 |
| Density (kg $m^{-3}$) | 1790 | 1300 | 2540 | 1050 |

Table 8.2: Elastic properties of the equivalent transversely isotropic lamina used to model CRP and GRP plates.

| | $E_1$ (GPa) | $E_2$ (GPa) | $\nu_{12}$ | $\nu_{21}$ | $G_{12}$ (GPa) | $G_{13}$ (GPa) | $G_{23}$ (GPa) |
|---|---|---|---|---|---|---|---|
| CRP | 100 | 10 | 0.2 | 0.02 | 10 | 10 | 4.17 |
| GRP | 27.8 | 5.0 | 0.3 | 0.055 | 1.86 | 1.86 | 1.9 |

### 8.2.2 Experimental technique

The experimental apparatus presented in Chapter 4 is employed here to simulate underwater blast loading of the composite specimens described in Section 8.2.1. The apparatus is sketched in Fig. 8.1 and consists of an instrumented water shock tube made from a transparent material to allow visualising the structural response as well as cavitation phenomena in the water by means of high-speed photography. The shock tube of length $L = 2\,\mathrm{m}$ was closed at one end with the circular composite specimen by adhesive bonding of the plate to the annular tube face. The shock tube was then filled with filtered tap water, in vertical position, and closed at the opposite end by a nylon piston fitted with two O-rings which provided sealing of the water column; a bleed valve was included in the piston to evacuate air bubbles in the

water column prior to the dynamic experiment. Preliminary experiments elucidated that such bubbles can lead to significant wave attenuation and distortion.

To replicate a fully clamped circular boundary condition in the blast experiment, the back face of the composite plate was supported by a clamping ring and loaded with a compressive force $F$; such force was applied by using a screw-driven loading fixture. The clamping ring was machined from a transparent acrylic rod to diameter $d = 25\,\text{mm}$; honing of the bore provided a glossy finish to enable clear observation of dynamic plate deflection by using a high-speed camera ('Vision Research' type v.7.1). The clamping plate of the fixture was machined with a vent hole to release pressurised air and water in case of plate rupture.

Blast waves emerging from explosions in shallow water (hydrostatic pressure negligible compared to the pressure induced by the blast, $p_{st} \simeq 0$) can be well approximated by an exponentially decaying pressure versus time pulse of form

$$p(t) = p_0 e^{-t/\theta} \tag{8.2}$$

with $p_0$ the peak pressure and $\theta$ the decay time of the blast wave [5]. In the experiments, such pressure wave was reproduced by firing a round steel striker of mass $M_S$ and velocity $v_S$ at the nylon piston. This technique is convenient as peak pressure $p_0$ and decay time $\theta$ can be independently tweaked by appropriate adjustment of $v_S$ and $M_S$, respectively, as described in Deshpande et al. [36]. The pressure transient in the shock tube was measured using two piezoelectric pressure gauges of type 113B23 SN 21266 (*PCB Piezoelectronics Inc.*) mounted flush on the tube at a relative distance of 1 m. The speed of pressure wave propagation in the shock tube was measured as $c_w = 1053\,\text{ms}^{-1}$. Note that this measured wave speed is significantly lower than the speed of sound in open water ($\approx 1498\,\text{ms}^{-1}$) consequent to tube bulging effects [50]. Attenuation of the pressure amplitude due to

mechanical coupling of elastic tube deformation and fluid motion was measured to be on the order of 5-10% and the rise time of the pressure wave increased by approximately 15%.

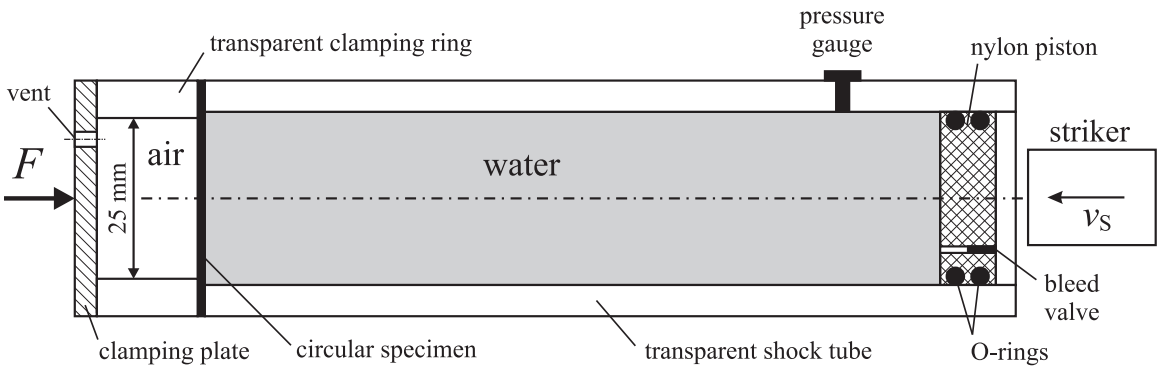



Fig. 8.1: Schematic of the experimental apparatus used to perform underwater blast experiments on circular composite plates.

## 8.3 Finite element models

In this study, 3D dynamic FE simulations were performed in accordance to the underwater shock experiments in order to gain more insight into cavitation processes and the details of dynamic plate deflection. Details on geometry, mesh, boundary conditions and loading cases are given in Section 7.3.

Thickness, stacking sequence and elastic properties of the composites were specified according to the data listed in Table 8.2; density and speed of sound in water were taken as $\rho_w = 1000\,\mathrm{kgm}^{-2}$ and $c_w = 1053\,\mathrm{ms}^{-1}$, respectively.

## 8.4 Results and Discussion

We proceed to present observations and results obtained from the FSI experiments. Details on specimen material and geometry as well as the characteristics of the loading pulses used in

each experiment are listed in Table 8.3. We include in this table the non-dimensional parameters $\bar{R} = R/\theta\sqrt{\rho/E}$ and $\bar{p}_0 = p_0/E$, representing non-dimensional plate radius and peak pressure of the incident shock wave, respectively; note that these parameters were introduced in Chapter 7 (eq. (7.57)) to characterise the underwater blast response of circular elastic plates. The quantity $E$ (included in Table 8.3) denotes the equivalent Young's modulus of the laminate under uniaxial stress conditions, hence

$$E = \frac{A_{11} - A_{12}\left(\nu_{12} + \nu_{21}\right)/2}{h}. \tag{8.3}$$

$A_{11}$ and $A_{12}$ are elements of the laminate's stiffness matrix (eq. (7.8)) and the term $\left(\nu_{12} + \nu_{21}\right)/2$ represents an average for the Poisson's ratio of the laminate (arbitrarily defined). The values of peak pressure $p_0$ and decay time $\theta$, as listed in Table 8.3, were determined by fitting curves to the pressure pulse measurements.

Table 8.3 also includes data from experiments in which failure occurred. The dominant failure mode identified in this study was shear failure at the clamped boundary and this was observed in experiments 2 and 3 performed on CRP plates with incident waves of peak pressure $p_0 \geq 9.4\,\text{MPa}$. Post-test photographs of the failed specimens are illustrated in Fig. 8.2, which show that shear-off occurred at the circular clamped boundaries over approximately one half of their circumference. In contrast, such failure process was not observed in experiments on GRP plates when subjected to similar shock loads.

Table 8.3: Details of experiments performed in this study

| test | specimen material | $E$ (GPa) | $h$ (mm) | $p_0$ (MPa) | $\theta$ (ms) | $p_0/E$ $10^{-3}$ | $\bar{R}$ | failure mode |
|---|---|---|---|---|---|---|---|---|
| 1 | CRP | 55 | 0.75 | 7.2 | 0.12 | 0.131 | 0.014 | - |
| 2 | CRP | 55 | 0.75 | 9.4 | 0.12 | 0.182 | 0.014 | shear |
| 3 | CRP | 55 | 0.75 | 10.8 | 0.14 | 0.196 | 0.017 | shear |
| 4 | CRP | 55 | 0.75 | 9.0 | 0.14 | 0.164 | 0.017 | - |
| 5 | CRP | 55 | 0.75 | 6.8 | 0.14 | 0.124 | 0.017 | - |
| 6 | CRP | 55 | 0.75 | 7.8 | 0.12 | 0.142 | 0.014 | - |
| 7 | CRP | 55 | 0.75 | 6.5 | 0.12 | 0.118 | 0.014 | - |
| 8 | GRP | 13 | 0.85 | 9.0 | 0.12 | 0.692 | 0.036 | - |
| 9 | GRP | 13 | 0.85 | 10.0 | 0.14 | 0.769 | 0.031 | - |
| 10 | GRP | 13 | 0.85 | 7.0 | 0.14 | 0.538 | 0.031 | - |
| 11 | GRP | 13 | 0.85 | 9.8 | 0.163 | 0.754 | 0.026 | - |
| 12 | GRP | 13 | 0.85 | 9.7 | 0.163 | 0.746 | 0.026 | - |
| 13 | GRP | 13 | 0.85 | 9.8 | 0.185 | 0.754 | 0.023 | - |
| 14 | GRP | 13 | 0.85 | 10.1 | 0.185 | 0.777 | 0.023 | - |

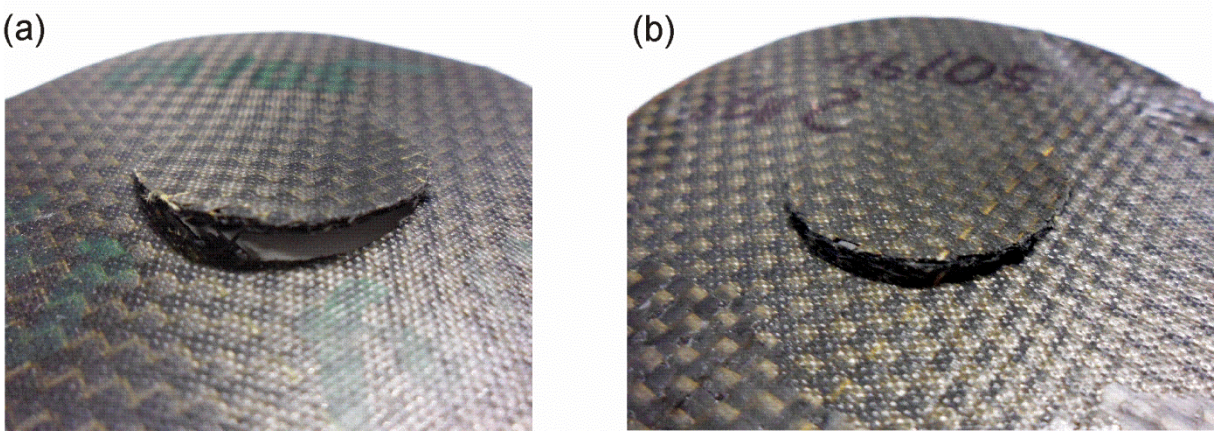



Fig. 8.2: Post-test photographs showing shear failure of CRP plates consequent to blast loading: (a) experiment 3, $p_0 = 10.8\,\text{MPa}$, $\theta = 0.14\,\text{ms}$; (b) experiment 2, $p_0 = 9.4\,\text{MPa}$, $\theta = 0.12\,\text{ms}$.

### 8.4.1 The cavitation process

In order to analyse the cavitation phenomena ensuing from underwater blast loading of circular composite plates, high-speed photographs recorded in selected experiments are

presented in this section together with contour plots obtained from corresponding FE simulations.

Experiment 1 was performed on a carbon-fibre composite plate with $p_0 = 7.2\,\text{MPa}$ and $\theta = 0.12\,\text{ms}$. A sequence of high-speed photographs recorded in this experiment is presented in Fig. 8.3 and fluid pressure contour plots extracted from the FE simulation are included for comparison (pressure scale in the FE results: $0 \le p < 7.2\text{MPa}$); in these contour plots, the patches highlighted in dark grey represent zones in which the water cavitates.

At $t = 0$, the incident pressure wave, travelling from the right to the left in Fig. 8.3 (a), reaches the wet surface of the specimen. Soon after elastic plate deformation has commenced, bubbles emerge in the water at a distance $z_c = 130\,\text{mm}$ from the fluid-structure interface, as seen in Fig. 8.3 (b). Subsequently, the cavitation zone spreads by propagation of two breaking fronts (BF). In Fig. 8.3 (c) the BF propagating away from the structure has advanced beyond the field of observation while the opposite BF has inverted its direction of motion and propagates into the cavitated water; such cavitation front is termed as closing front (CF) because it forces collapse of cavitation bubbles and leaves uncavitated water behind. This CF continues propagating and after sufficient time has elapsed, the cavitated region has completely disappeared in the field of observation and elastic plate deformation has fully recovered, as seen in Fig. 8.3 (d).

In addition, Fig. 8.3 shows that the experimental observations of the cavitation process are in good correlation with the FE predictions. The contour plots also provide further insight into the evolution of the fluid pressure field. In particular, Fig. 8.3 (b) shows that the cavitation zone separates the fluid column into a low pressure zone, just ahead of the BF, and a high pressure zone located in the fluid trapped between the cavitated region and the fluid-structure interface. The fluid pressure in the high pressure zone locally exceeds the peak pressure of the

incident wave (indicated by light grey patches), as a consequence of wave reflections at the propagating CF.

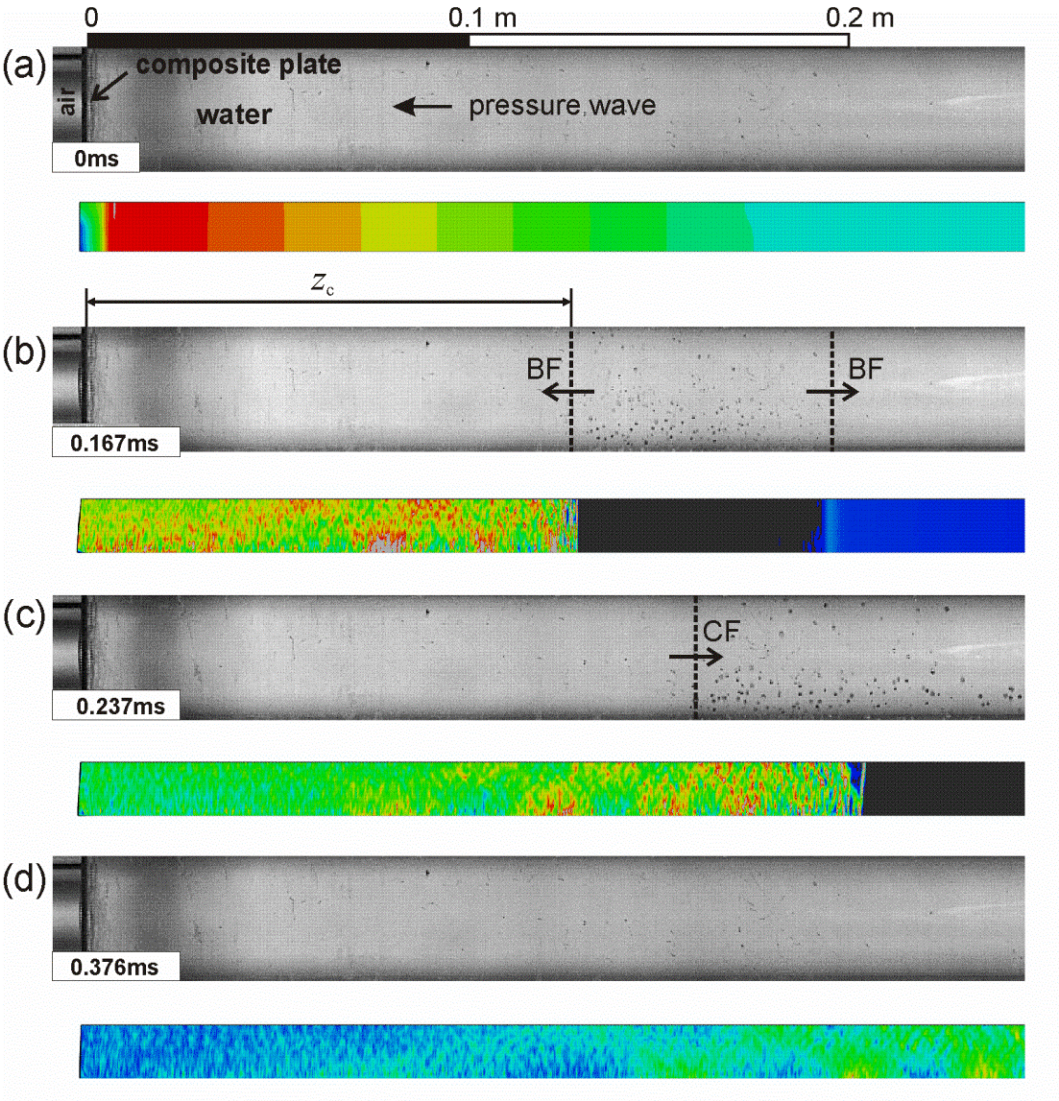



Fig. 8.3: Selected high-speed photographs for experiment 1 ( $p_0 = 7.2\,\text{MPa}$ , $\theta = 0.12\,\text{ms}$ ) performed on a CRP plate; fluid pressure contour plots extracted from corresponding FE simulations are included for comparison; FE scale: 7.2 MPa (red) – 0 MPa (blue); cavitation zones are highlighted in dark grey.

High-speed photographs for experiment 2 conducted with $p_0 = 9.4\,\text{MPa}$ and $\theta = 0.12\,\text{ms}$ are presented in Fig. 8.4. In frame (a) the incident shock wave impinges on the wet surface of the composite and leads to rapid deformation of the specimen, as seen in frame (b). At $t = 0.189$ ms (see Fig. 8.4 c), we note from careful observation of the deflected specimen that

the composite has sheared off at the clamped boundary and starts releasing water into the transparent clamping ring, leading to emergence of two cavitation zones in the water column: the cavitation zone visible at distance $z_c = 120\,\mathrm{mm}$ is a consequence of elastic plate deformation prior to the onset of failure and correlates with the fluid response observed in experiment 1 (see Fig. 8.3).

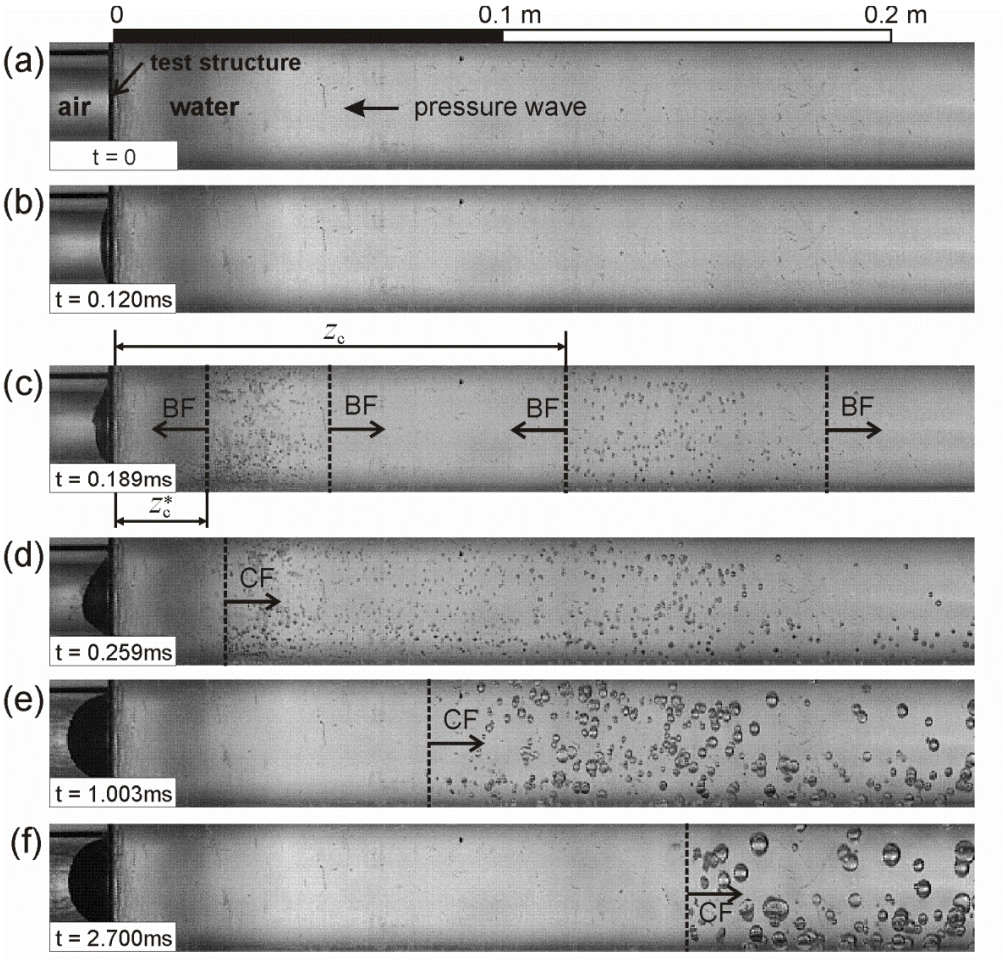



Fig. 8.4: Sequcence of high-speed photographs for experiment 2 ($p_0 = 9.4\,\mathrm{MPa}$, $\theta = 0.12\,\mathrm{ms}$) performed on a CRP composite plate: (a) incident wave reaches the specimen; (b) elastic specimen deformation; (c) plate failure and appearance of two cavitation zones, both expanding by propagation of breaking fronts (BF); (d) coalescence of both cavitation zones and emergence of a closing front (CF); (e)-(f) collapse of cavitation bubbles by propagation of a CF.

The appearance of an additional cavitation zone at distance $z_c^* = 25\,\text{mm}$ can be explained as follows: the fracture process causes a sudden increase in velocity of the fluid particles contiguous to the structure and therefore rises the amplitude of the tensile (rarefaction) wave emanated from the fluid-structure interface. Such tensile spike leads to water cavitation close to this interface (at distance $z_c^*$) and a breaking front starts propagating at supersonic speed into the fluid, closing the gap between both cavitation zones until they coalesce, as shown in Fig. 8.4 (d). In frames (d)-(f) we note that the cavitation boundary next to the structure starts propagating away from the composite plate, becoming a closing front and causing collapse of cavitation bubbles, which have grown in size due to increased strain in the cavitated fluid.

### 8.4.2 Dynamic plate deflection

The high-speed photographs also served to measure centre deflection versus time histories consequent to blast loading. Such measurements are presented in this section and compared with analytical and FE predictions. The validated analytical models are then used to explore the sensitivity of the normalised peak centre deflection $\overline{w}_0^{\max} = w_0^{\max}/R$ to the normalised peak pressure $\overline{p}_0 = p_0/E$ of the blast wave.

In order to observe dynamic plate deflection with adequate resolution, experiments 4 - 14 (see Table 8.3) were performed with the composite plate the focus of observation. Experiment 5 was performed with $p_0 = 6.8\,\text{MPa}$ and $\theta = 0.14\,\text{ms}$ and high-speed photographs obtained from this experiment are illustrated in Fig. 8.5 (a). Frame 1 shows the undeformed composite plate in a side view at the instant when the incident shock wave reaches the fluid-structure interface. In frame 2, we first observe elastic deformation of the specimen and at time $t = 0.269\,\text{ms}$ (frame 6) the maximum central deflection is reached. Subsequently, the elastic

energy stored in the deformed plate causes reverse motion and the specimen assumes its initial undeformed configuration (frames 7 and 8). At time $t = 1.470\,\text{ms}$, elastic deformation of the composite has fully recovered.

Fluid pressure contour plots extracted from the corresponding FE simulation are presented in Fig. 8.5 (b) for a narrow time frame, $5\,\mu\text{s} \le t \le 36\,\mu\text{s}$, in order to examine the early phase of plate deformation in more detail. Note that the plies of the $[0,90]_3$ composite plate are oriented parallel and perpendicular to the section plane of Fig. 8.5 (b). In frame (i), at $t = 5\,\mu\text{s}$, we note that the central portion of the plate is imparted a nearly uniform transverse velocity, causing the interface pressure to drop rapidly due to FSI. The ensuing dynamic deformation process entails propagation of a flexural wave, travelling in radial direction from the clamped boundary towards the centre point. Ahead of the wave front, i.e. within $0 \le r \le (R - \zeta)$, the plate remains nearly undeformed and is imparted a uniform velocity, as seen in frames (i) and (ii). Plate acceleration continues until the water cavitates at the fluid-structure interface in the central portion, $0 \le r \le (R - \zeta)$; this is observed in frame (ii) at $t = 12\,\mu\text{s}$. The flexural wave reaches the centre point, approximately $20\,\mu\text{s}$ after the impact of the incident wave, as illustrated in frame (iii). At time $t = 20\,\mu\text{s}$ the central patch of the plate is still in contact with cavitated water; however, this cavitation zone soon collapses (at $t \approx 36\,\mu\text{s}$) and the ensuing response produces pressure spikes in the water adjacent to the specimen, as illustrated in frame (iv). It merits comment that the limited spatial and temporal resolution of the high-speed camera used in the experiments (inter-frame time of 20 μs, pixel size of 120 μm) did not allow observing flexural wave propagation phenomena in the solid which occur within time frames of approximately $20\,\mu\text{s}$ for the plate geometries considered here.

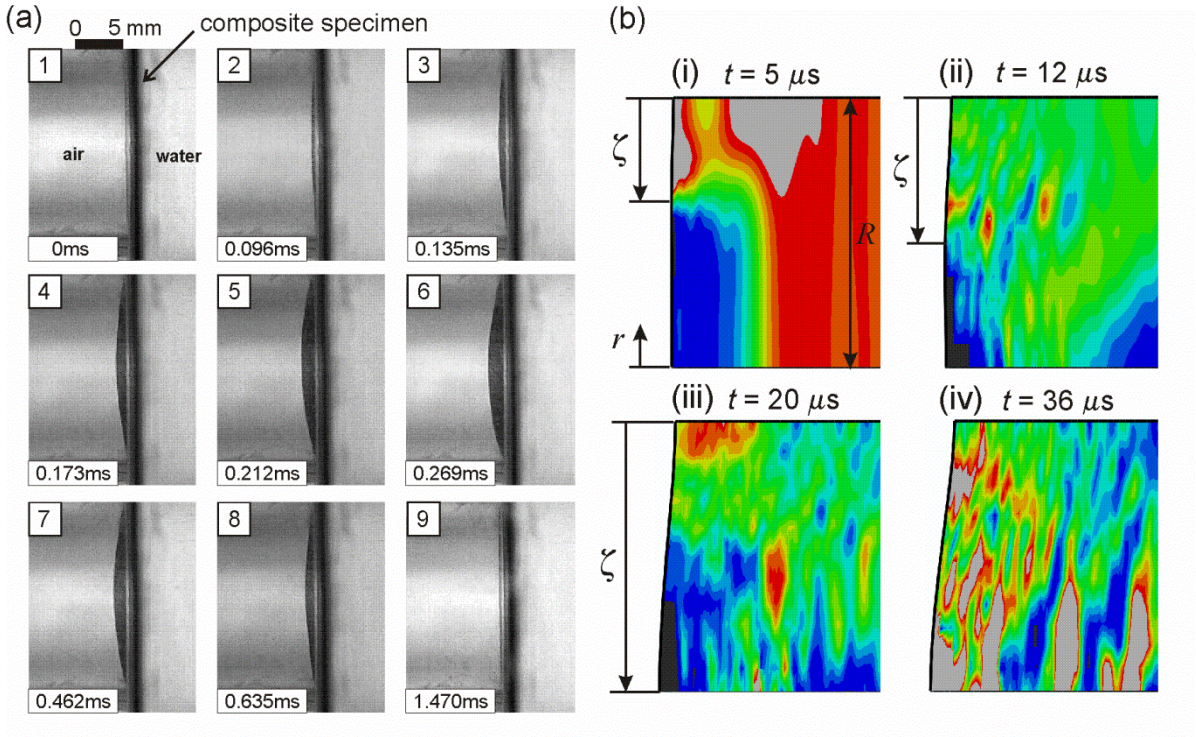



Fig. 8.5: (a) High-speed photographic sequence for experiment 5 ( $p_0 = 6.8\,\text{MPa}$, $\theta = 0.14\,\text{ms}$ ) showing the dynamic elastic deformation of a CRP plate; (b) contour plots of fluid pressure obtained from the corresponding FE simulations for four selected time frames; composite plies are oriented parallel and perpendicular to the section plane; FE scale: 6.8 MPa (red) – 0 MPa (blue); cavitation zones are highlighted in dark grey.

High-speed photographs, such as shown in Fig. 8.5 (a), allow measuring time histories of the plate's centre deflection. In Fig. 8.6 (a) we present such measurements obtained from experiment 8 (GRP composite, $p_0 = 9.0\,\text{MPa}$, $\theta = 0.12\,\text{ms}$ ) together with the corresponding FE predictions. In addition, we include in Fig. 8.6 predictions performed with the analytical models presented in Chapter 7. Analytical predictions and measurements are found in excellent agreement up to the point when the plate reaches its maximum centre deflection $w_0^{\max} = w_0(t_{\max})$. Larger discrepancies occur for $t > t_{\max}$, however, this phase of response is of minor practical relevance. In the initial response, $0 \le t \le 20\,\mu\text{s}$, the FE models also correlate with the measurements and analytical predictions but predict an increase in plate velocity at the instant when the flexural wave arrives at the plate's centre point, $t = 20\,\mu\text{s}$, recall

frame (iii) in Fig. 8.5 (b). Moreover, the FE results underpredict the peak deflection by approximately 10-15%. Similar information is shown in Fig. 8.5 (b) for experiment 10, conducted with $p_0 = 7.0\,\text{MPa}$ and $\theta = 0.14\,\text{ms}$.

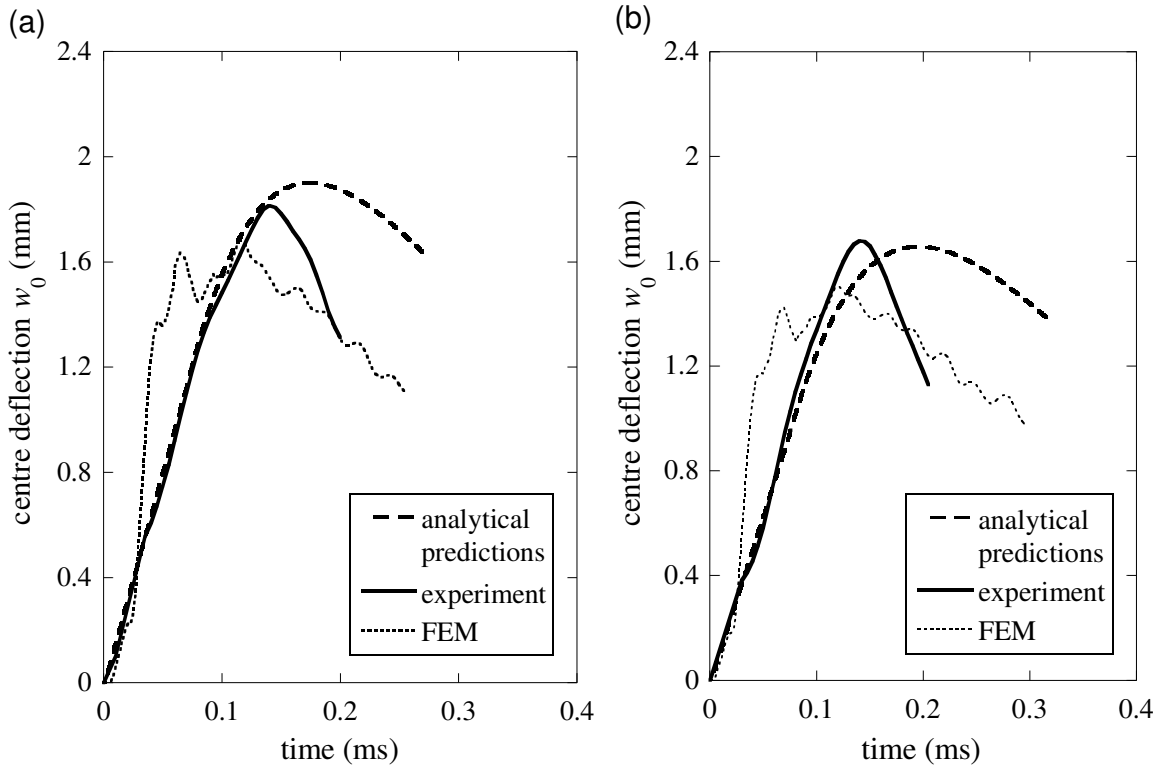



Fig. 8.6: Time histories of the measured centre deflection for two selected experiments performed on GRP plates: (a) experiment 8, $p_0 = 9.0\,\text{MPa}$, $\theta = 0.12\,\text{ms}$; (b) experiment 10, $p_0 = 7.0\,\text{MPa}$, $\theta = 0.14\,\text{ms}$; analytical and FE predictions are included for comparison.

In the following, the non-dimensional parameters introduced in Chapter 7 (see eq. (7.57)) are employed to assess the blast resistance of the CRP and GRP plates under investigation.

The non-dimensional chart in Fig. 8.7 shows analytical predictions of the peak centre deflection $\overline{w}_0^{\max} = \max_{0 \le t < \infty} \left[ w_0(t)/R \right]$ as a function of the normalised peak pressure of the incident shock wave, $\overline{p}_0 = p_0/E$, with contours of non-dimensional radius $\overline{R} = R/\theta\sqrt{\rho/E}$. These predictions were performed in accordance to the plate geometries and pressure pulse

characteristics used in experiments 4 – 14 (see Table 8.3) by employing the analytical models presented in Chapter 7. For comparison purposes, measurements obtained from the latter experiments are included in Fig. 8.7 and are indicated by markers. The predictions show that $\overline{w}_0^{\max}$ increases progressively by increasing $\overline{p}_0$; for fixed values of $\overline{h}$, $\overline{p}_0$ and $\overline{\alpha} = (\rho_w c_w)/\sqrt{E\rho}$ (normalised acoustic impedance), $\overline{w}_0^{\max}$ increases with decreasing $\overline{R}$. The broken and dotted curve in the centre of Fig. 8.7 represents predictions for a GRP plate with reduced thickness $h = 0.75\,\text{mm}$ to match the aspect ratio $\overline{h} = 0.06$ of the CRP composite used in the experiments. Now compare the contours of GRP and CRP specimens for the case ($\overline{h} = 0.06$, $\overline{R} = 0.017$): the parameter $\overline{\alpha}$ of GRP plates is nearly double that of CRP plates; the effect of increasing $\overline{\alpha}$ is to shift the curves in Fig. 8.7 to higher values of $\overline{p}_0$, indicating that plates with large $\overline{\alpha}$ can take higher peak pressures $\overline{p}_0$ for given $\overline{w}_0^{\max}$, $\overline{R}$ and $\overline{h}$. The experimental results are found in good agreement with the predictions and show that GRP plates sustained centre deflections up to $\overline{w}_0^{\max} = 0.2$. In contrast, the centre deflections of CRP plates were limited to $\overline{w}_0^{\max} = 0.12$ due to the occurrence of shear failure, see Fig. 8.2.

We now employ the analytical models of Chapter 7 to aid interpretation of the onset of shear failure observed in experiments 2 and 3, both of which performed on CRP specimens. In the process, we analyse the through-thickness shear stress histories at the clamped plate boundary, $\tau_{rz}(r = R, t)$, in order to predict the maximum shear stress induced in the composite specimen during the dynamic experiment. Evaluating eq. (7.15) at $r = R$ gives the transverse shear force at the clamped boundary

$$Q_{rz}\big|_{r=R} = -\frac{2G_{rz}h}{\zeta(t)} w_{S0}(t) \tag{8.4}$$

where $G_{rz}$ represents the shear stiffness of the laminate in the *r*-*z* plane, $w_{S0}(t)$ denotes the centre deflection of the plate due to shearing and $\zeta(t)$ is the flexural wave position. For the CRP composites under investigation, the shear stiffness $G_{rz}$ is a function of the circumferential coordinate, i.e. $G_{rz} = G_{rz}(\varphi)$; however, in a first approximation, we employ a mean shear stiffness

$$G_{rz} = \frac{G_{13} + G_{23}}{2} \tag{8.5}$$

calculated from the shear stiffnesses $G_{13}$ and $G_{23}$ corrsponding to a single CRP lamina (see Table 8.2). Employing eqs. (8.4) and (8.5), the shear stress at the clamped boundary can be expressed as

$$\tau_{rz}(t) = (G_{13} + G_{23}) \frac{w_{S0}(t)}{\zeta(t)}. \tag{8.6}$$

For both experiments 2 and 3 (see Table 8.3), solutions of $w_{S0}(t)$ and $\zeta(t)$ were performed using the analytical models of Chapter 7 and eq. (8.6) was employed to compute the maximum shear stress $\tau_{rz}^{\max} = \max_{0 \le t < \infty} \left[ \tau_{rz}(t) \right]$; we obtained $\tau_{rz}^{\max} = 55$ MPa and $\tau_{rz}^{\max} = 65$ MPa for experiments 2 and 3, respectively. Note that these values are on the order of magnitude of the shear strength of typical CRP composites, see e.g. [58].

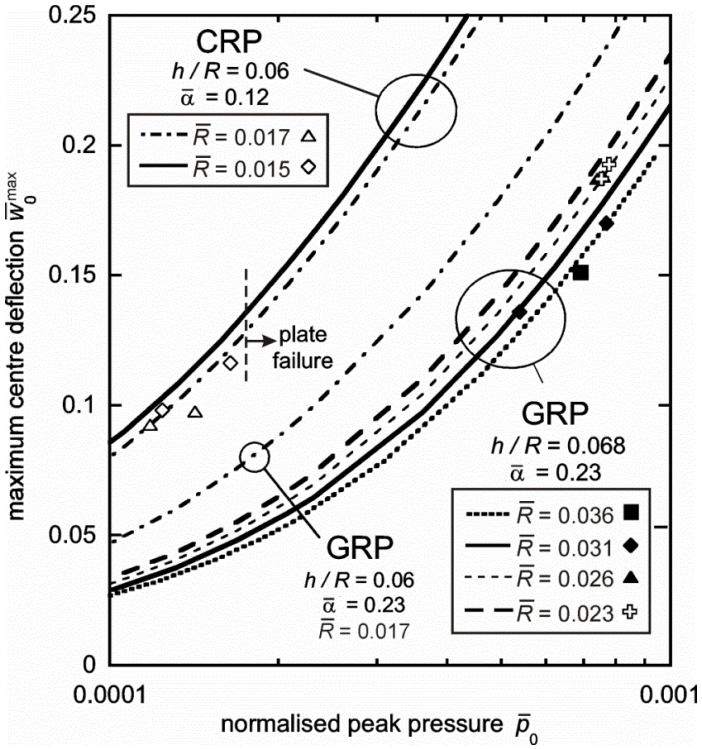



Fig. 8.7: Analytical predictions of maximum centre deflection $\bar{w}_0^{max}$ as a function of the non-dimensional peak pressure of the incident shock wave $\bar{p}_0 = p_0/E$ for the plate geometries and pressure pulse characteristics used in experiments 4 – 14; experimental measurements obtained from these experiments are included for comparison (full and empty markers).

## 8.5 Conclusions

The response of clamped circular composite plates subject to loading by exponentially decaying underwater shock waves has been investigated. Underwater blast experiments were performed on laminated carbon-fibre (CRP) and glass-fibre (GRP) reinforced composite plates by employing the transparent shock tube presented in Chapter 4. High-speed photography was employed to observe dynamic plate deflection, failure processes and cavitation phenomena in the liquid.

The observations revealed that cavitation bubbles first appeared in the water at a finite distance from the specimen and subsequently, the cavitation zone expanded by propagation of two breaking fronts. An additional cavitation zone appeared in the water close to the fluid-

structure interface in case of plate failure. Soon after the first cavitation bubbles became visible, the plate's peak deflection was reached and the cavitated water rapidly collapsed by propagation of a closing front due to the ensuing elastic spring-back of the plate.

The high-speed photographs were also used to measure centre deflection versus time histories and the experimental results were compared to results obtained from 3D FE simulations and to predictions performed with the analytical models of Chapter 7. Both types of predictions were found in good correlation with the experimental evidence and we conclude that these models are accurate and capable of replicating the response of submerged composite plates subject to shock loading in water.

The measurements showed that the GRP specimens sustained larger normalised peak deflections (peak deflection divided by plate radius) than those made from CRP. The reason for the limited maximum deflection of the CRP plates was the occurrence of shear failure at the clamped plate boundary. The onset of shear failure in these experiments has been confirmed by analytical calculations.

The experiments presented in this study provide valuable insight into the interaction between an elastically deforming composite plate and the surrounding fluid when the structure is subjected to loading by an exponentially decaying shock wave. However, this study has only addressed the response of relatively small composite plates. With increasing dimensions, the plate's response time rises and this affects the flexural wave propagation phenomena in the solid as well as the evolution of the cavitation process in the fluid. Therefore, further experiments on larger scale are necessary in order to determine the size effect in the response of composite plates. We shall start to investigate this in a future study.

# Chapter 9

# Conclusions

The work presented in this thesis has addressed the response of various structural systems subject to blast loading in deep and shallow water and has unveiled and explored the ensuing cavitation phenomena initiated by FSI. Analytical models were developed to examine the 1D response of both water-backed and air-backed rigid spring-supported plates loaded by exponentially decaying shock waves in deep or shallow water. In order to provide experimental evidence for the theoretical findings, an experimental apparatus was developed capable of simulating 1D underwater blast loading in initially pressurised water. Subsequently, the developed experimental apparatus was used to investigate the underwater blast response of monolithic plates, sandwich panels and double-walled structures. Finally, the underwater blast response of circular elastic plates were investigated via experimentation, analytical and numerical modelling.

The work presented in this thesis gives valuable insight into the main FSI phenomena associated to underwater blast loading and provides useful guidelines for the design of structural components resistant to blast in deep and shallow water. In the following we summarise the main conclusions drawn from each part of this thesis and provide directions for possible future work.

## 9.1 The one-dimensional response of rigid plates subject to blast in deep and shallow water

Analytical models have been derived to predict the response of a spring-suppported, rigid plate, in contact with water on one or both sides and loaded by an exponentially decaying shock wave (Chapter 3). Such models account explicitly for the evolution of cavitation phenomena in the fluid, including propagation of breaking fronts and closing fronts as well as for the effect of an initial hydrostatic pressure in the fluid. The system response was found to depend only on three non-dimensional parameters: non-dimensional spring stiffness, plate mass and initial static fluid pressure. The analytical models were validated by comparing their predictions to those obtained from detailed dynamic FE simulations and both types of predictions were found to be in excellent agreement.

It has been a long-accepted paradigm that a reduction in structural mass (hence an increase of $\psi$) leads to a reduction in the imparted impulse; the results presented in Chapter 3 clearly show that a decrease in the plate's mass can increase the severity of structural loading (hence the imparted impulse) for particular choices of spring stiffness and static pressure (see Fig. 3.11b).

The analytical predictions also showed that the application of an initial static pressure in the fluid affects substantially cavitation phenomena; specifically, the point of first cavitation in the front water is found at increasing distance from the structure and the cavitation zone contracts faster, as the static pressure is increased. This results in a reduction of the impulse imparted to the plate for an increase in initial static pressure. At a sufficient level of initially applied pressure, cavitation in the fluid is entirely suppressed.

In order to provide experimental evidence for the theoretical findings, a novel experimental method has been developed to produce controlled blast loading in liquids subject to an initial hydrostatic pressure (Chapter 4). The apparatus consists of a transparent shock tube and allowed visualising for the first time the emergence and propagation of cavitation fronts triggered by FSI in a blast event and their interaction with the loaded structure. It also allowed observing the structural motion as well as measuring the impulse imparted to the structure consequent to blast loading. This technique has been employed to mimic the response of monolithic air-backed and water-backed plates subject to blast in deep water and to measure the effects of increased initial hydrostatic pressure on the evolution of the cavitation process as well as on the structural response.

The main conclusions of this experimental study are the following:

- For given incident blast wave and initial static pressure, air-backed plates are imparted less impulse than water-backed plates; the impulse imparted to air-backed plates can be greatly reduced by reducing the mass of the plate, while a smaller reduction in imparted impulse is observed by reducing the mass of water-backed plates.
- The peak impulse imparted to air-backed plates is insensitive to the initial hydrostatic pressure while that imparted to water-backed plates decreases with increasing static pressure.

The experimental results obtained with the shock tube apparatus were found in good agreement with predictions obtained from the theoretical models developed in Chapter 3 and this allows concluding that these models are accurate and capable of capturing the response of both fluid and structure to underwater blast in deep water.

## 9.2 The one-dimensional response of sandwich plates subject to blast in deep and shallow water

The 1D response of both air-backed and water-backed sandwich plates subject to blast loading in initially pressurised water has been investigated by experimentation and FE modelling (Chapter 5). Underwater blast experiments were performed on foam-cored sandwich specimens with metallic face sheets by using the shock tube apparatus developed in Chapter 4. Face sheet motion, core compression and cavitation processes were observed by means of high-speed photography and the impulse imparted to the structure was deduced from the measurements. The obtained high-speed photographs showed that the cavitation process inititates at a finite distance $x_c$ from the fluid-structure interface, in line with the findings of previous theoretical studies on underwater blast loading of sandwich plates.

The results of permanent core compression, imparted impulse and cavitation front trajectories were adequately captured by the corresponding dynamic FE simulations and yielded the following conclusions:

- Both air-backed and water-backed sandwich plates outperform rigid plates of equal mass in terms of the impulse imparted to the structure in a blast event. For given core collapse strength and shock wave characteristics, the permanent core compression of water-backed sandwich plates is larger than that of air-backed sandwiches and thus impulse reductions are more pronounced when sandwich plates are loaded in water-backed configuration.
- For the case of blast loading of water-backed sandwich plates, the impulse imparted to a rigid plate of mass equal to the front face sheet cannot be taken as a lower bound for the impulse imparted to a sandwich structure.

- The impulse imparted to water-backed sandwich plates can be drastically reduced by increasing the initial hydrostatic pressure in the surrounding fluid; impulse reductions of up to 70% (in relation to the unpressurised loading case) can be achieved when the initially applied fluid pressure is on the order of the core's collapse strength.

The experiments presented in this study give great insight into the main phenomena of the cavitation process and how these affect the dynamic response of sandwich plates. However, to improve the current understanding of FSI in underwater blast loading of sandwich constructions, rigorous 1D analytical models are needed, which account for all the details of the cavitation process in the fluid, without the need of simplifying assumptions. This is left as a topic for a future study.

## 9.3 The one-dimensional response of double-walled structures to underwater blast

Chapter 6 has investigated the 1D response to underwater blast loading of double-walled hulls comprising of a monolithic inner pressure hull, an outer shell and a water gap located between both structures. Laboratory scale underwater shock experiments were performed by using the shock tube apparatus presented in Chapter 4. Structural motion as well as ensuing cavitation phenomena were observed using high-speed photography and the impulse imparted to the structure was deduced from the performed measurements. The experimental results were found in good agreement with the predictions obtained from detailed FE simulations and the main findings of this study are the following:

- The loading histories applied on outer skin and inner hull in a blast event are only scarcely sensitive to variations of the water gap width.
- When sandwich construction is employed for the outer skin structure, cavitation processes initiate in the water very close to the front face sheet and this substantially mitigates the intensity of the loads imparted to outer skin and inner hull in a blast event.
- The blast performance of monolithic double-hulls can be enhanced by increasing the mass ratio between outer skin and inner hull.

The experimental results give valuable visual insight into the cavitation process and provide practical guidelines for the design of double-walled hulls resistant to underwater blast. However, the effect of a non-negligible static fluid pressure on the system response has not been addressed in this study but will be examined in a future study.

## 9.4 The response of circular elastic plates to underwater blast

In Chapter 7, analytical models have been derived to predict dynamic deflection of fully clamped circular elastic plates subject to loading by planar, exponentially decaying underwater shock waves in water. Such models are based on a plate theory that takes into account transverse shear deformations, stretching forces due to large deflections, flexural wave propagation in the solid, FSI phenomena subsequent to first cavitation as well as the orthotropic constitutive response of composite laminates. The analytical models were validated by comparing their predictions to those obtained from fully coupled 3D FE simulations and both types of predictions were found to be in good agreement for a wide range of plate geometries and blast impulses. In contrast, when the plates were loaded impulsively by imparting the plate an initial velocity according to the Taylor impulse [4],

large discrepancies occurred, unless the structural response time was several times larger than the duration of the phase for FSI.

The validated analytical models were then used to determine the optimal geometries that maximise the shock resistance of a circular elastic plate of given areal mass and maximum allowable centre deflection. The constructed design maps show that an increase in blast resistance of greater than 40% can be achieved by employing the optimal designs.

The developed analytical models can be used to predict the response of circular elastic plates subject to blast in shallow water, they do not account for the effects of an initially applied hydrostatic pressure in the fluid. Moreover, FSI at the back face of the plate is not included in the current analysis but needs to be considered when water-backed plates are subjected to underwater blast. These aspects are of crucial importance for the design of blast resistant composite structures used in deep water applications and are left as topics for a future study.

In order to investigate dynamic deformation and failure processes of circular composite plates subject to underwater blast and to gain deeper insight into the evolution of the ensuing cavitation phenomena, FSI experiments were performed on carbon-fibre (CRP) and glass-fibre (GRP) reinforced composite laminates by employing the transparent shock tube described in Chapter 4. High-speed photography was employed to observe and analyse dynamic plate deflection, failure processes and cavitation phenomena in the water.

For the pressure pulses and plate geometries used in the experiments, the high-speed photographs showed that a cavitation zone spreads in the water a finite distance away from the fluid-structure interface and collapses soon after by propagation of a closing front owing to the elastic spring-back of the circular plate.

The high-speed photographs were also used to measure centre deflection versus time histories and the experimental results were compared to results obtained from 3D FE simulations and

to predictions performed with the analytical models of Chapter 7. Both types of predictions were found in good correlation with the experimental evidence.

The measurements showed that the GRP laminates sustained larger normalised peak deflections (peak deflection divided by plate radius) than those made from CRP. The reason for the limited maximum deflection of the CRP plates was the occurrence of shear failure at the clamped boundary. The onset of shear failure in these experiments has been confirmed by analytical calculations.

The experiments presented in Chapter 8 provide valuable insight into the interaction between an elastically deforming composite plate and the surrounding fluid consequent to dynamic loading by underwater shock waves. However, this study has only addressed the response of relatively small composite plates. With increasing dimensions, the plate's response time rises and this affects flexural wave propagation phenomena in the solid as well as the evolution of the cavitation process in the fluid. Therefore, further experiments on larger scale are necessary in order to determine the size effect in the response of composite plates. We shall start to investigate this in a future study.

# Appendix A. Description of structural loading subsequent to first cavitation (Phase 2 response)

In this Appendix we describe a procedure which makes use of the analytical models derived in Chapter 3 in order to approximate structural loading of circular orthotropic plates during the Phase 2 response, i.e. for $t > t_1$. First, we derive the governing equations of a simplified analytical model for the response of a circular plate made from an elastic transversely isotropic solid and loaded by exponentially decaying shock waves in water. Such equations allow extracting characteristic parameters which are then fed into the theoretical models of Chapter 3 in order to perform predictions able to represent FSI and structural loading of circular orthotropic plates during the Phase 2 response.

Now consider a circular transversely isotropic plate of thickness $h$ and radius $R$ with a fully clamped boundary. The plate is in contact with water on one side and loaded by an exponentially decaying pressure shock wave, travelling in the water towards the structure, as given in eq. (7.33). Upon neglecting transverse shear deformations (i.e. $G \to \infty$, $w_{S0} \to 0$) and flexural wave propagation phenomena (i.e. $\zeta = R$, $\dot{\zeta} = 0$) the deformation profile of the plate can be approximated by a third-order polynomial

$$w(r,t) = w_0(t)\left[3\left(1-\frac{r}{R}\right)^2 - 2\left(1-\frac{r}{R}\right)^3\right]. \tag{A.1}$$

Angular momentum conservation for a circular plate sector of angle $\hat{\varphi}$ dictates

$$\begin{aligned}&\hat{\varphi}\int_0^t\left[\int_0^R 2p_0 e^{-t/\theta}(R-r)\,r\,dr - \int_0^R \rho_w c_w \dot{w}(r,t)(R-r)\,r\,dr\right]dt = \\ &= \int_0^R \mu\dot{w}(r,t)(R-r)\,r\,dr\,\hat{\varphi} - \int_0^t \tilde{M}_r\big|_R\, R\hat{\varphi}\,dt + \int_0^t\int_0^R \tilde{M}_t\hat{\varphi}\,dr\,dt + \int_0^t\int_0^R \tilde{N}_t\hat{\varphi}w\,dr\,dt\end{aligned} \tag{A.2}$$

Substituting eqs. (7.21), (7.22) and (A.1) into eq. (A.2), evaluating the space integrals with respect to the coordinate $r$ and differentiating the obtained equation with respect to time $t$ gives

$$\mu\ddot{w}_0 + \frac{54w_0}{R^4}\left(\frac{3D_{11}}{8} + \frac{D_{12}}{4} + \frac{3D_{22}}{8} + \frac{D_{66}}{2}\right) + \frac{3w_0^{\,3}}{2R^4}\left(\frac{A_{11}}{8} + \frac{3A_{12}}{4} + \frac{A_{22}}{8} - \frac{A_{66}}{2}\right) = 4p_0 e^{-t/\theta} - \rho_w c_w \dot{w}_0 \quad \text{(A.3)}$$

Equation (A.3) represents the equation of motion for the central deflection $w_0(t)$ and can be re-written as

$$\mu\ddot{w}_0 + k_{eq}w_0 + c_{eq}w_0^3 = 2p_{eq}e^{-t/\theta} - \rho_w c_w \dot{w}_0 \quad \text{(A.4)}$$

where $p_{eq}$, $k_{eq}$ and $c_{eq}$ denote equivalent peak pressure, linear stiffness and cubic stiffness, respectively, and are given by

$$p_{eq} = 2p_0;\ k_{eq} = \frac{54}{R^4}\left(\frac{3D_{11}}{8} + \frac{D_{12}}{4} + \frac{3D_{22}}{8} + \frac{D_{66}}{2}\right);\ c_{eq} = \frac{3}{2R^4}\left(\frac{A_{11}}{8} + \frac{3A_{12}}{4} + \frac{A_{22}}{8} - \frac{A_{66}}{2}\right). \quad \text{(A.5)}$$

The parameters defined in eq. (A.5) can be used to solve the equivalent 1D problem of a rigid plate (mass per unit area $\mu$) in contact with water (density $\rho_w$, speed of sound $c_w$) on one side (front face), supported by a linear spring of stiffness $k_{eq}$ at the back face and loaded by an exponentially decaying shock wave of peak pressure $p_{eq}$ and decay time $\theta$ on the front face. This problem can be solved by using the analysis derived in Chapter 3.

One note of caution: eq. (A.4) comprises a cubic term $c_{eq}w_0^3$ representing membrane forces induced by stretching of the plate's middle surface. The effect of a cubic stiffness $c_{eq}$ is not included in the analytical models of Chapter 3 but needs to be accounted for if the plate undergoes large deflections, i.e. $w_0/R > 0.1$. This is treated in our calculations as follows.

The plate displacement at the onset of cavitation, $t = t_c$, is very small for the loading cases considered in this work and therefore the influence of the cubic term $c_{eq}w_0^3$ can be neglected,

thus $c_{eq} = 0$ for $t \le t_c$. In contrast, for $t > t_c$, the governing equation (3.39) for the 1D problem is modified to account for the effect of $c_{eq}$. To achieve this, numerical integration for $t > t_c$ is performed with

$$\mu\ddot{u} + k_{eq}u + c_{eq}u^3 = 2\,p_{in}^{eq}(t) - \rho_w c_w \dot{u}\ , \tag{A.6}$$

i.e. replacing eq. (3.39) by eq. (A.6).

The solutions of $p_{in}^{eq}(t)$ (eq. (A.6)) represent magnitudes of the equivalent incident pressure wave evaluated at the fluid-structure interface, i.e. $p_{in}^{eq}(z=0,t)$, and includes the contributions of pressure wave reflections at the propagating closing front. Note that the pressure values are scaled in the 1D calculations by $p_{eq} = 2p_0$, see eq. (A.5) (recall that $p_0$ is the peak pressure of the shock wave impinging on the circular elastic plate); hence $p_{in}^{1D}(t) = p_{in}^{eq}(t)/2$ the incident wave to be substituted into eq. (7.47) in order to characterise structural loading during the Phase 2 response

## Appendix B. Review of lamina theory

In this appendix we briefly summarise the formulas used for computing the elastic properties of unidirectional (UD) continuous composites with perfectly aligned but randomly located fibres (f) embedded in matrix material (m).

If density $\rho$ of the composite material is known, the volume fraction of fibres can be calculated using the rule of mixtures; hence

$$\varphi_f = \frac{\rho - \rho_m}{\rho_f - \rho_m}. \tag{B.1}$$

UD composite materials can be taken as transversely isotropic elastic solids. The relationship between strains and stresses follows from symmetry considerations and can be written as

$$\begin{pmatrix} \varepsilon_{11} \\ \varepsilon_{22} \\ \varepsilon_{33} \\ \gamma_{23} \\ \gamma_{31} \\ \gamma_{12} \end{pmatrix} = \begin{pmatrix} E_1^{-1} & -\nu_{21}E_2^{-1} & -\nu_{21}E_2^{-1} & 0 & 0 & 0 \\ -\nu_{12}E_1^{-1} & E_2^{-1} & -\nu_{23}E_2^{-1} & 0 & 0 & 0 \\ -\nu_{12}E_1^{-1} & -\nu_{23}E_2^{-1} & E_2^{-1} & 0 & 0 & 0 \\ 0 & 0 & 0 & G_{23}^{-1} & 0 & 0 \\ 0 & 0 & 0 & 0 & G_{12}^{-1} & 0 \\ 0 & 0 & 0 & 0 & 0 & G_{12}^{-1} \end{pmatrix} \begin{pmatrix} \sigma_{11} \\ \sigma_{22} \\ \sigma_{33} \\ \tau_{23} \\ \tau_{31} \\ \tau_{12} \end{pmatrix}. \tag{B.2}$$

The indices ‘1‘ and ‘2‘ denote the fibre and transverse directions, respectively. Isotropy in the 2-3 plane and symmetry of the compliance matrix (eq. (B.2)) yields

$$G_{23} = \frac{E_2}{2(1+\nu_{23})}\ ;\ \frac{\nu_{12}}{E_1} = \frac{\nu_{21}}{E_2}. \tag{B.3}$$

In general, deformation of a UD composites results in complex stress distributions in the constituent materials. In order to find such stress distributions, a full stress analysis is required. However, approximate analysis on simplified stress fields can yield simple expressions for estimating the elastic properties of UD composites and such relations are summarised in the following.

First, let us assume isotropic behaviour for fibres (f) and matrix (m) material. A widely used approximation for the axial modulus $E_1$ and Poisson's ratio $\nu_{12}$ of a UD composite is the rule of mixtures; hence

$$E_1 = \varphi_f E_f + \left(1-\varphi_f\right) E_m \; ; \nu_{12} = \varphi_f \nu_f + \left(1-\varphi_f\right)\nu_m . \tag{B.4}$$

Upon assuming no stress amplifications in the direction of applied stress and no axial constraint, the transverse modulus $E_2$ can be computed using inverse rule of mixture

$$\frac{1}{E_2} = \frac{\varphi_f}{E_f} + \frac{1-\varphi_f}{E_m} \tag{B.5}$$

and the Poisson's ratio $\nu_{21}$ follows immediately from eq.(B.3).

Similarly, inverse rule of mixture can be employed for computing the shear modulus

$$\frac{1}{G_{12}} = \frac{\varphi_f}{G_f} + \frac{1-\varphi_f}{G_m} \tag{B.6}$$

by neglecting stress concentrations in the constituent materials.

# References


1. Swisdak, M.M., *Explosion effects and properties: part II - explosion effects in water.*, 1978, Naval surface weapons centre: Dahlgren, Virginia, USA.
2. Mouritz, A.P., et al., *Review of advanced composite structures for naval ships and submarines.* Composite Structures, 2001(53): p. 21-41.
3. Kennard, E.H., *Cavitation in an elastic liquid.* Physical review, 1943. **63**: p. 172-181.
4. Taylor, G.I., *The pressure and impulse of submarine explosion waves on plates*, in *The scientific papers of GI Taylor*. 1941, Cambridge University Press: Cambridge.
5. Cole, R.H., *Underwater Explosions*. 1948, New York: Dover Publications Inc.
6. Slifko, J.P., *Pressure-pulse characteristics of deep explosions as functions of depth and range*, 1967, United States Naval Ordnance laboratory: White Oak, Maryland. p. 67-87.
7. Hudson, G.E., *A Theory of the Dynamic Plastic Deformation of a Thin Diaphragm.* Journal of Applied Physics, 1951. **22**: p. 1-11.
8. Wang, A.J. and H.G. Hopkins, *On the plastic deformation of built-in circular plates under impulsive load.* Journal of the Mechanics and Physics of Solids, 1954. **3**: p. 22-37.
9. Jones, N., *Structural Impact*. 1989, Cambridge, UK: Cambridge University Press.
10. Tagarielli, V.L., V.S. Deshpande, and N.A. Fleck, *The dynamic response of composite sandwich beams to transverse impact.* International Journal of Solids and Structures, 2007. **44**: p. 2442-2457.
11. Tagarielli, V., L., *The static and dynamic response of sandwich beams to transverse loading*, in *Department of Engineering*2005, University of Cambridge: Cambridge.
12. Hoo Fatt, M.S. and L. Palla, *Analytical Modeling of Composite Sandwich Panels under Blast Loads.* Journal of Sandwich Structures and Materials, 2009. **11**: p. 357-380.
13. Boteler, J.M. and G.T. Sutherland, *Tensile failure of water due to shock wave interactions.* Journal of Applied Physics, 2004. **96**: p. 6919-6924.
14. Brennen, C.E., *Cavitation and Bubble Dynamics*. 1 ed. 1995, New York: Oxford University Press.
15. Bleich, H.H. and I.S. Sandler, *Interaction between structures and bilinear fluids.* International Journal of Solids and Structures, 1970. **6**: p. 617-639.
16. Wadley, H.N.G., *Multifunctional periodic cellular metals.* Philosophical Transactions of the Royal Society, London, Ser.A, 2005. **364**: p. 31-68.
17. Arezoo, S., et al., *The mechanical response of Rohacell foams at different length scales.* Journal of Materials Science, 2011. **46**: p. 6863-6870.
18. Arezoo, S., et al., *Compressive Deformation of Rohacell Foams: Effects of Strain Rate and Temperature.* Polymer, 2012: p. submitted Feb 2012.
19. Tagarielli, V.L., V.S. Deshpande, and N.A. Fleck, *The high strain rate response of PVC foams and end-grain balsa wood.* Composites: Part B, 2008. **39**: p. 83-91.

20. Ashby, M.F., et al., *Metal Foams: A Design Guide*. 2000, London: Butterworth-Heinemann.
21. Wadley, H.N.G., N.A. Fleck, and A.G. Evans, *Fabrication and structural performance of periodic cellular metal sandwich structures.* Composite Science and Technology, 2003. **63**: p. 2331-2343.
22. Xue, Z. and J.W. Hutchinson, *A comparative study of impulse-resistant metal sandwich plates.* International Journal of Impact Engineering, 2004. **30**: p. 1283-1305.
23. McShane, G.J., V.S. Deshpande, and N.A. Fleck, *The underwater blast resistance of metallic sandwich beams with prismatic lattice cores.* Journal of Applied Mechanics, 2007. **74**: p. 352-364.
24. Tilbrook, M.T., V.S. Deshpande, and N.A. Fleck, *Underwater blast loading of sandwich beams: Regimes of behaviour.* International Journal of Solids and Structures, 2009. **46**: p. 3209-3221.
25. Fleck, N.A. and V.S. Deshpande, *The resistance of clamped sandwich beams to shock loading.* Journal of Applied Mechanics, 2004. **71**: p. 386-401.
26. Qiu, X., V.S. Deshpande, and N.A. Fleck, *Dynamic response of a clamped circular sandwich plate subject to shock loading.* Journal of Applied Mechanics, 2004. **71**(5): p. 637-646.
27. Deshpande, V.S. and N.A. Fleck, *One-dimensional response of sandwich plates to underwater shock loading.* Journal of the Mechanics and Physics of Solids, 2005. **53**: p. 2347-2383.
28. Hutchinson, J.W. and Z. Xue, *Metal sandwich plates optimized for pressure impulses.* International Journal of Mechanical Sciences, 2005. **47**: p. 545-569.
29. Liang, Y., et al., *The response of metallic sandwich panels to water blast.* Journal of applied mechanics, 2007. **71**: p. 81-99.
30. McMeeking, R.M., et al., *An analytical model for the response to water blast of unsupported metallic sandwich panels.* International Journal of Solids and Structures, 2007. **45**: p. 478-496.
31. ONR, *Underwater explosion research: a compendium of Britisch and American reports*. Vol. 3. 1951, Washington, D.C.
32. Hall, D.J., *Examination of the effects of underwater blasts on sandwich composite structures.* Composite Structures, 1989. **11**(2): p. 101-120.
33. Mouritz, A.P., D.S. Saunders, and S. Buckley, *The damage and failure of GRP laminates by underwater explosion shock loading.* Composites, 1994. **25**(6): p. 431-437.
34. Ramajeyathilagam, K. and C.P. Vendhan, *Deformation and rupture of thin rectangular plates subjected to underwater shock.* International Journal of Impact Engineering, 2004. **30**: p. 699-719.
35. Rajendran, R., J.K. Paik, and J.M. Lee, *Of Underwater Explosion Experiments on Plane Plates.* Experimental Techniques, 2007. **31**: p. 18-24.
36. Deshpande, V.S., A. Heaver, and N.A. Fleck, *An underwater shock simulator.* Proceedings of the Royal Society A, 2006. **462**: p. 1021-1041.

37. Kazemahvazi, S., et al., *Mechanics of Materials and Structures.* Journal of Mechanics of Materials and Structures, 2007. **2**: p. 2007-2023.
38. McShane, G.J., V.S. Deshpande, and N.A. Fleck, *Underwater blast response of free-standing sandwich plates with metallic lattice cores.* International Journal of Impact Engineering, 2010. **37**: p. 1138-1149.
39. Espinosa, H.D., S. Lee, and N. Moldovan, *A novel fluid structure interaction experiment to investigate deformation of structural elements subjected to impulsive loading.* Experimental Mechanics, 2006. **46**(805-824).
40. Mori, L.F., et al., *Deformation and fracture modes of sandwich structures subjected to underwater impulsive loads.* Journal of Mechanics of Materials and Structures, 2007. **2**(10): p. 1981-2006.
41. Mori, L.F., et al., *Deformation and failure modes of I-core sandwich structures subjected to underwater impulsive loads.* Experimental Mechanics, 2009. **49**(2): p. 257-275.
42. Latourte, F., et al., *Failure mechanisms in composite panels subjected to underwater impulsive loads.* Journal of the Mechanics and Physics of Solids, 2011. **59**: p. 1623-1646.
43. LeBlanc, J. and A. Shukla, *Dynamic response and damage evolution in composite materials subjected to underwater explosive loading: An experimental and computation study.* Composite Structures, 2010. **92**: p. 2421-2430.
44. Wadley, H., et al., *Compressive response of multilayered pyramidal lattices during underwater shock loading.* International Journal of Impact Engineering, 2008. **35**: p. 1102-1114.
45. Benjamin, T.B. and A.T. Ellis, *The collapse of cavitation bubbles and the pressures thereby produced against solid boundaries.* Philosophical Transactions of the Royal Society, London, Ser.A, 1966. **260**: p. 221-240.
46. Lauterborn, W. and H. Bolle, *Experimental investigations of cavitation-bubble collapse in the neighbourhood of a solid boundary.* Journal of Fluid Mechanics, 1975. **72**(2): p. 391-399.
47. Tomita, Y. and T. Kodama, *Interaction of laser-induced cavitation bubbles with composite surface.* Journal of Applied Physics, 2003. **94**(5): p. 2809-2816.
48. Ross, C.T.F., *A conceptual design of an underwater vehicle.* Ocean Engineering, 2006. **33**: p. 2087-2104.
49. Abaqus, *Analysis User's Manual 6.8*, 2008, Dassault Systemes Simulia Corp.
50. Korteweg, D.J., *Uber die Fortpflanzungsgeschwindigkeit des Schalles in elastischen Rohren.* Annalen der Physik, 1878. **5**(12): p. 525-542.
51. Schiffer, A., et al., *The Response of Submerged Rigid Plates to Blast Loading: Analytical Models and Finite Element Predictions.* Journal of Applied Mechanics, 2012. **79**: p. 061014.
52. Qiu, X., V.S. Deshpande, and N.A. Fleck, *Finite element analysis of the dynamic response of clamped sandwich beams subject to shock loading.* European Journal of Mechanics - A/Solids, 2003. **22**(6): p. 801-814.

53. Chen, C. and N.A. Fleck, *Size effects in the constraint deformation of metallic foams.* Journal of the Mechanics and Physics of Solids, 2002. **50**: p. 955-977.
54. Deshpande, V.S. and N.A. Fleck, *Isotropic Constitutive Model for Metallic Foams.* Journal of the Mechanics and Physics of Solids, 2000. **48**: p. 1253-1276.
55. Dannemann, K.A. and J. Lankford, *High strain rate compression of closed-cell aluminium foams.* Materials Science and Engineering A, 2000. **293**: p. 157-164.
56. Radford, D.D., V.S. Deshpande, and N.A. Fleck, *The use of metal foam projectiles to simulate shock loading on a structure.* International Journal of Impact Engineering, 2005. **31**: p. 1152-1171.
57. Avachat, S. and M. Zhou, *Effect of Facesheet Thickness on Dynamic Response of Composite Sandwich Plates to Underwater Impulsive Loading.* Experimental Mechanics, 2012. **52**: p. 83-93.
58. Soden, P.D., M.J. Hinton, and A.S. Kaddour, *Lamina properties, lay-up configurations and loading conditions for a range of fibre-reinforced composite laminates.* Composite Science and Technology, 1998. **58**: p. 1011-1022.